



**HAL**  
open science

# Towards the generation of entangled sources from single quantum dots in photonic crystal cavities

Matthieu Larqué

► **To cite this version:**

Matthieu Larqué. Towards the generation of entangled sources from single quantum dots in photonic crystal cavities. Atomic Physics [physics.atom-ph]. Université Pierre et Marie Curie - Paris VI, 2009. English. NNT: . tel-00431849

**HAL Id: tel-00431849**

**<https://theses.hal.science/tel-00431849>**

Submitted on 13 Nov 2009

**HAL** is a multi-disciplinary open access archive for the deposit and dissemination of scientific research documents, whether they are published or not. The documents may come from teaching and research institutions in France or abroad, or from public or private research centers.

L'archive ouverte pluridisciplinaire **HAL**, est destinée au dépôt et à la diffusion de documents scientifiques de niveau recherche, publiés ou non, émanant des établissements d'enseignement et de recherche français ou étrangers, des laboratoires publics ou privés.

**THESE DE DOCTORAT DE  
L'UNIVERSITE PIERRE ET MARIE CURIE**

Spécialité

Physique quantique  
(Ecole doctorale de Physique de la Région Parisienne ED107)

Présentée par

**M. Matthieu LARQUE**

Pour obtenir le grade de

**DOCTEUR de l'UNIVERSITÉ PIERRE ET MARIE CURIE**

# **Towards the generation of entangled sources from single quantum dots in photonic crystal cavities**

soutenue le 16 Octobre 2009

devant le jury composé de :

M. Claude FABRE	Président du Jury
M. Philippe GRANGIER	Rapporteur
M. Valéry ZWILLER	Rapporteur
M. Izo ABRAM	Directeur de Thèse
M. Philippe LALANNE	Examineur
M. François LARUELLE	Examineur
Mme Isabelle ROBERT-PHILIP	Invitée



# Abstract / Résumé

**Titre français** Vers la création de sources de paires de photons intriquées à partir de boîtes quantiques en cavité à cristal photonique

**English title** Towards the generation of entangled sources from single quantum dots in photonic crystal cavities

**Thèse préparée au / PhD work held in** Laboratoire de Photonique et de Nanostructures - CNRS UPR 20 - Route de Nozay - 91460 Marcoussis - France

**Abstract** Cryptography is the art of making a message only understandable by the recipient of the message, provided it has the proper equipment with the correct key to decrypt it, that is, to make it again understandable. Quantum cryptography is a way for the two communicating parties, usually called Alice and Bob, to securely exchange this key with the laws of quantum mechanics. The bits forming the key are then encoded on quantum states, such as the polarization of a single photon. The presence of a spy is then revealed on the bits exchanged and measured by the devices of Alice and Bob, without their having to monitor every inch of their online communications, and that holds true whatever the means possessed by the spy. Today the simplest protocol of quantum key communication remains the first proposed by Charles H. Bennett and Gilles Brassard in 1984 (hence the name BB84). This is a point to point communication where each bit sent by Alice to Bob is encoded on the polarization of a single photon. Because the coding bases chosen by Alice is one of two random and incompatible polarization bases (horizontal-vertical on the one hand, and diagonal - anti-diagonal on the other), and because this choice of bases cannot be known by any spy beforehand, it is impossible for the spy to make a measurement that is always transparent to Bob's detectors. This guarantees the security of the key. The fact that the bits are encoded on single photons guarantee that the eavesdropper cannot separate the encoding media in two and keep one of these parties for its own use, because a photon is indivisible. The no-cloning principle also ensures that it is impossible for the spy to duplicate information.

This protocol has now been implemented over long distances (240km), in public telecommunications networks, and networks. However, to achieve better performances, the implementation of quantum relays is necessary. These relays use pairs of entangled photons, and / or indistinguishable single photons. Here the fact that we use pairs of single photons, rather than a larger number of photons is essential. Otherwise the security protocol is not as efficient, but also its efficiency in terms of generated key rate is reduced. These protocols have been demonstrated in the laboratory using parametric sources, however, these sources display Poissonian statistics in the number of generated pairs of entangled photons, and are therefore unsuitable. To ensure successful implementation of these protocols, a deterministic source of entangled photon pairs is necessary.

Among the current best hope for achieving such sources include quantum dots. These objects are small clusters of semiconductor material placed in another semiconductor, in our case, InAs in a

GaAs matrix. These dots are obtained by molecular beam epitaxy, by growing a few monolayers of InAs on GaAs, which is then covered with GaAs. During the growth of InAs, the difference in crystal lattices between these two materials creates stress, which in appropriate conditions, relaxes and leads to the formation of InAs islands. The difference of material creates a three-dimensional quantum well in the conduction band and valence. The well's size of a few nanometres, smaller than the spatial extent of electrons and holes creates a discretization of the energy levels in these wells. The first level of excitement of a dot is the exciton consisting of a trapped electron and a trapped hole. The second level is the biexciton consisting of two trapped electron-hole pairs. The discretization of these energy levels is responsible for the deterministic aspect of the radiative recombination mechanism of these electron-hole pairs. This deterministic aspect has been demonstrated experimentally, and the spectroscopy of these boxes is becoming well known. Also the fact that these sources are made of semiconductors allows both to benefit from the mature technology in this area and to hope in the longer term to integrate these sources into more complex systems.

Two patterns of entanglement are studied. The first uses the radiative cascade biexciton-exciton to emit a pair of photons entangled in polarization. The biexcitonic photon is then sent to a first remote recipient, Alice, and the other photon to Bob. The second pattern of entanglement, called "time-bin", uses two photons emitted successively by the excitonic level, entanglement is then obtained at a beam splitter where are kept only the cases where one photon is sent to Alice and the other to Bob. The encoding bit is then on the date of the photon (in a naive view). Some very recent experiments in the laboratory have demonstrated the feasibility of using these two schemes for quantum dots as a source of deterministic pairs of entangled photons. However, because of imperfections inherent in these sources, these experiences are lacking in performance and cannot be directly used for the communication of quantum key. These shortcomings are a lack of light signal collected, and loss of coherence related to interactions of the dot with its crystalline surroundings. The perturbations impacting the degree of entanglement are different depending on the format used. This thesis examines quantitatively the impact of these phenomena in both schemes.

In the case of time-bin, provided that the dot is optically pumped in a quasi-resonant way, it is shown that an acceleration by a factor 30 of the radiative emission leads to a radiative lifetime faster than the processes degrading the entanglement. These processes are dephasing processes of the excitonic level. This acceleration of the radiation time, called Purcell effect is obtained by placing a photonic crystal cavity around the quantum dots. It is shown that this type of cavity is best suited to this problem, thanks to their small modal volume. Moreover such a cavity, when properly chosen, can effectively redirect light toward the collecting objective and significantly increase the brightness of the source. The development of simulation tools adapted to the pursuit of such cavities is presented and so are the results of these numerical and experimental studies.

In the case of the biexciton radiative cascade, it is shown that using the Purcell effect is necessary but insufficient. While it helps offset the decoherent mechanisms and the spin flip, it cannot fully compensate the fine structure splitting of the excitonic level. Indeed this splitting of the intermediary level of the biexcitonic radiative cascade greatly degrades or even destroys the entanglement. However, although this intermediary level is degenerated, a cavity degenerated in polarization with a Purcell factor of 10 on the excitonic level is required. Our calculations indicate that cavities in carefully designed photonic crystals can meet these criteria. When well chosen, they can also as before, significantly increase the brightness of the source. The exact requirements of spectral and spatial agreement between the source and the cavity are discussed. It is thus demonstrated that it is necessary to locate precisely the quantum dot in the centre of the cavity, which is a technology still under development today. However, the use of the Purcell effect is not sufficient to compensate for the native splitting of usual quantum dots. This thesis explores the possibility of reducing the splitting by using a tuneable vertical electric field. This solution was chosen for its technological compatibility with the photonic crystal cavities and the future integrability of the system. The electric field is obtained by placing the

quantum dot in the intrinsic part of a vertical pin diode used in the blocking regime. By gradually straightening the electronic bands, the electric field can be tuned. To maintain compatibility with the photonic crystal technology, the total thickness of the pin diode is  $180\text{nm}$ , which raised some difficulties in developing the manufacturing process of these diodes. Finally, a spectroscopic study of these dots demonstrates a variation of  $10\mu\text{eV}/V$  of the splitting on a usable voltage range of  $0.5V$  applied to the diode.

This thesis concludes on the technological feasibility of these two processes of entanglement, and their potential for future development requirements.

**Keywords** entangled photons, semi-conductor, quantum dots, photonic crystal, Purcell effect, collection efficiency, radiation pattern, pin diode

**Résumé court** Les boîtes quantiques sont des systèmes de choix pour générer des états quantiques de la lumière. Il est possible de créer avec ces objets des sources de photons uniques ainsi que des sources de paires de photons intriqués. Ces deux types de sources sont cruciaux pour les futurs réseaux de communications quantiques, et pour des applications à faible échéance comme la distribution de clés quantiques. Les boîtes quantiques en semi-conducteur III-V ont l'avantage d'utiliser une technologie de fabrication éprouvée et qui permet de contrôler leurs propriétés optiques ainsi que de les intégrer dans des cavités à cristaux photoniques, afin de créer des sources compactes et intégrables. Bien que ces boîtes quantiques aient été intensément étudiées pendant ces dix dernières années, et bien que l'émission de photons uniques par ces structures ait été démontrée, une source efficace et pure de paire de photons intriqués n'a pas encore été obtenue malgré des efforts expérimentaux conséquents. Plusieurs phénomènes ont été proposés comme responsables de cette dégradation des états intriqués émis, mais sans en faire une description quantitative.

Le but de cette thèse est la création à partir de boîtes quantiques uniques, de sources qui émettent de manière déterministe des paires de photons intriqués. Deux procédés d'intrication différents sont proposés, qui sont l'intrication en polarisation de photons émis lors de la cascade radiative du bi-exciton, et l'intrication temporelle de deux photons indistinguables. Le degré d'intrication est numériquement calculé afin d'évaluer quantitativement l'impact des différents phénomènes déphasants, qui sont la levée de dégénérescence de la structure fine de l'exciton, le renversement de spin, et l'interaction de l'exciton avec son environnement. Il est démontré que l'intrication peut être restaurée dans les deux procédés en accélérant la durée de vie radiative de la raie excitonique, à l'aide de l'effet Purcell. Un moyen approprié pour obtenir cet effet est une cavité à cristal photonique gravée dans une membrane suspendue contenant la boîte quantique. Une telle structure de taille nanométrique peut en effet accélérer le processus d'émission et le rendre plus rapide que les processus déphasants. Elle peut aussi rediriger l'émission et augmenter significativement le signal collecté. Le problème d'obtenir une grande efficacité de collection tout en maintenant le confinement optique est abordé. Les requis technologiques en termes d'alignement entre la boîte quantique et la cavité sont aussi étudiés. Même si les effets de cavité sont capables de corriger la majeure partie des points faibles des boîtes quantiques, ceux-ci sont insuffisants pour corriger la levée de dégénérescence de la structure fine de l'exciton. Cette levée de dégénérescence peut être réduite en appliquant un champ électrique variable dans la direction de croissance des boîtes. La technologie pour produire des diodes PIN compatibles avec la technologie des cristaux photoniques sur membrane suspendue a été développée et ont permis de démontrer cette dernière affirmation.

**Mots clés** Photons intriqués, semi-conducteur, boîtes quantiques, cristal photonique, effet Purcell, efficacité de collection, diagramme de rayonnement, diode pin

**Résumé long** La cryptographie est l'art de rendre un message uniquement compréhensible par le destinataire du message. Pour cela les deux interlocuteurs s'accordent sur un algorithme et une clé de cryptage. La sécurité est garantie par le fait que l'espion, Eve, n'est pas en possession de la clé, même s'il connaît l'algorithme sous-jacent. La distribution de clé quantiques, appelé aussi cryptographie quantique permet pour la première fois que Alice et Bob sécurisent l'échange de leur clé grâce aux lois de la mécanique quantique. Pour cela ils codent le bit à échangé sur un qubit (quantum bit), qui peut être par exemple la polarisation d'un photon unique. La présence d'un espion est alors révélée sur les bits échangés et mesurés par les appareils d'Alice et de Bob, sans que ceux-ci aient à surveiller chaque centimètre de leur ligne de communication, et ce, quels que soient les éventuels moyens de l'espion. Aujourd'hui le protocole le plus simple de communication de clé quantique, reste le premier proposé par Charles H. Bennett et Gilles Brassard en 1984 (d'où le nom BB84 du protocole, figure 1). Il s'agit d'une communication point à point où chaque bit envoyé par Alice à Bob est codé sur la polarisation d'un unique photon. Parce que la base de codage choisie par Alice est aléatoire parmi deux bases de polarisations non-orthogonales (horizontal - vertical d'une part, et diagonal-anti-diagonal d'autre part), et que l'espion n'as pas la connaissance de cette base, il lui est impossible d'effectuer une mesure de la valeur du qubit tout évitant de perturber le système. C'est cette perturbation qui est mesurée par Alice et Bob qui permet la sécurité du protocole d'échange. Le principe garantissant cette sécurité est le principe de non clonage, unique en mécanique quantique ne permettant pas à l'espion de dupliquer l'information.

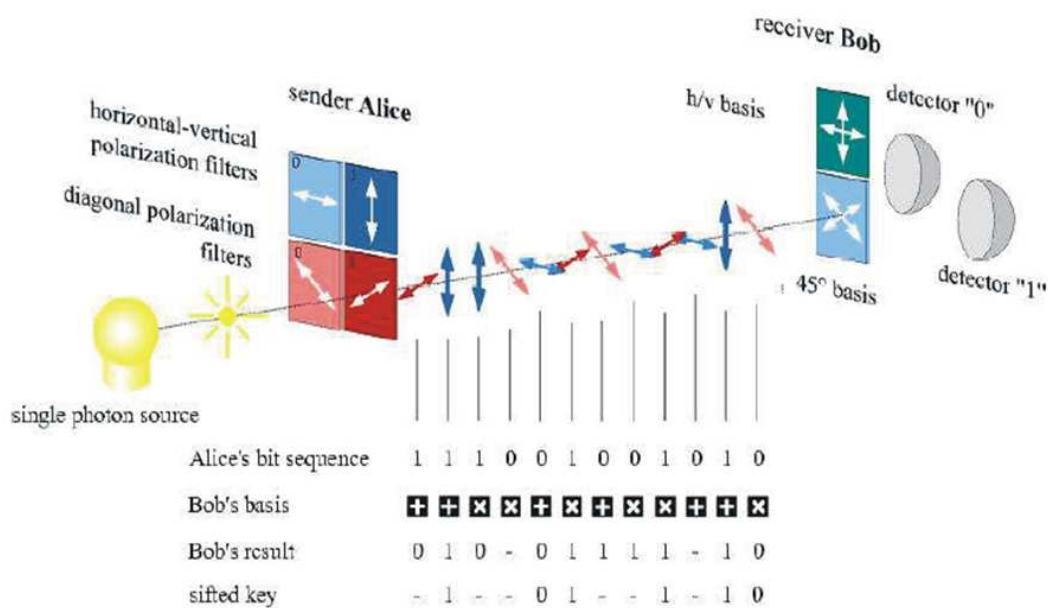


Figure 1: Principes du protocole BB84.

Ce protocole a aujourd'hui été mis en œuvre sur de grandes distances (100km) expérimentalement, dans des réseaux de télécommunications publics, et un réseau complet de 5 nœuds fut démontré dernièrement. Cependant, pour atteindre de meilleures performances, la mise en place de relais quantiques est nécessaire. La base d'un relais quantique est l'intrication de paires de photons. Le développement de sources de paires de photons intriqués à l'aide de la conversion paramétrique à permis la démonstration de principe de tels relais. Néanmoins ces sources ne sont pas parfaites, et le nombre de paires créés n'est pas déterministe, mais suis une distribution Poissonienne. Ceci a comme effet d'augmenter le taux d'erreur du relais quantique, rendant son application impossible. Pour cela,

expérimentalement, on diminue la probabilité de créer une paire, ce qui impact le débit réel. Pour permettre une mise en œuvre performante de ces protocoles, une source déterministe de paires de photons intriqués est nécessaire.

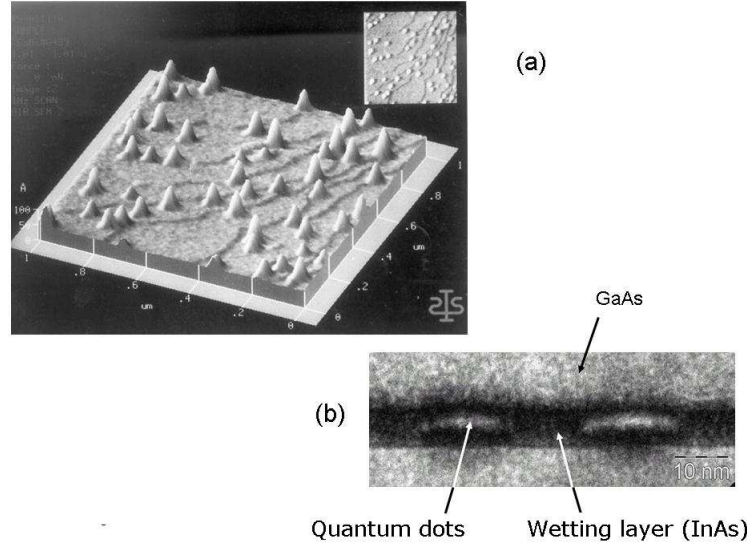


Figure 2: (a) Vue au microscope à force atomique de la surface épitaxiée d'un échantillon contenant des boîtes auto-organisées, avant recouvrement par du GaAs. (b) Coupe au microscope électronique en transmission de boîtes quantiques.

Parmi les meilleurs espoirs actuels pour réaliser de telles sources figurent les boîtes quantiques (figure 2). Ces objets sont de petits îlots de semi-conducteur placés dans un autre semi-conducteur, en l'occurrence de l'InAs dans une matrice de GaAs. Ces boîtes sont obtenues par épitaxie par jet moléculaire, en faisant croître quelques monocouches d'InAs sur du GaAs, ensuite recouvert de GaAs. Lors de la croissance de l'InAs, la différence de maille cristalline entre ces deux matériaux crée des contraintes, qui, dans les conditions adéquates, se relâchent et amènent à la formation d'îlots d'InAs. La différence de matériau crée un confinement tridimensionnel dans les bandes de conduction et de valence. La taille de quelque nanomètre de ce puits, plus petite que l'extension spatiale des électrons et des trous crée une discrétisation des niveaux électroniques. Le premier niveau d'excitation d'une boîte est l'exciton, constitué d'un électron et d'un trou piégés. Le second niveau est le biexciton, constitué de deux paires électron - trou piégées. La discrétisation de ces niveaux d'énergie est responsable de l'aspect déterministe du mécanisme radiatif de recombinaison de ces paires électron - trou. Cet aspect déterministe a été démontré expérimentalement, et la spectroscopie de ces boîtes commence à être bien connue. De plus le fait que ces sources soient faites en semi-conducteur permet à la fois de bénéficier de toute la technologie mature dans ce domaine, et d'espérer pouvoir à plus long terme, intégrer ces sources dans des systèmes plus complexes.

Deux schémas d'intrication sont étudiés. Le premier utilise la cascade radiative biexciton - exciton pour émettre une paire de photons intriqués en polarisation (figure 3). Le photon biexcitonique est alors envoyé à un premier destinataire distant, Alice, et l'autre photon à Bob. La conservation du moment total impose la présence de deux chemins de désexcitations différents, passant par un niveau excitonique intermédiaire différent qui correspondent à la structure fine de l'exciton. Si ces niveaux excitoniques sont identiques, et qu'aucune autre grandeur physique n'est couplée à la polarisation des photons émis, alors ces photons sont intriqués en polarisation. Le moment total de la paire est nul

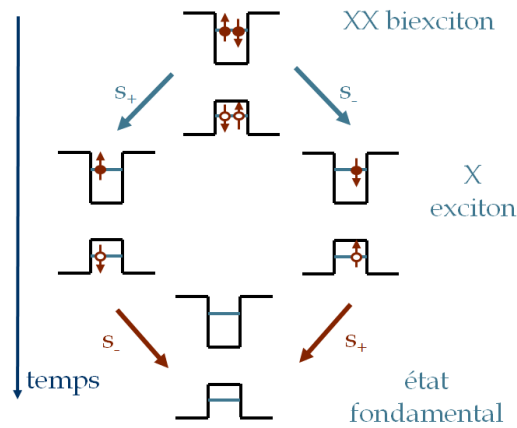


Figure 3: Schéma de la cascade radiative biexcitonique.

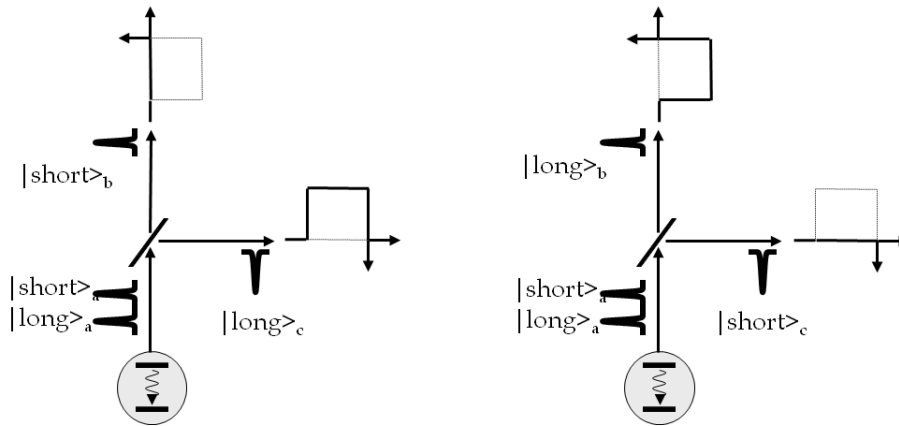


Figure 4: Schéma de l'intrication temporelle de deux photons excitoniques. Les deux chemins qui interfèrent et qui sont utilisés pour la communication de clé quantique sont représentés, avec en traits pleins, le trajet pris par chaque photon.

car les spins du biexciton et de l'état fondamental (boîte quantique vide) le sont aussi. L'état créé est donc idéalement  $|\psi^+\rangle = (|\sigma^+, \sigma^-\rangle + |\sigma^-, \sigma^+\rangle)/\sqrt{2}$  où le premier photon est celui envoyé à Alice et le second à Bob. La phase égale à 1 entre ces deux états est déterminée par les coefficients de Clebsh-Gordan. Le second schéma d'intrication, dit "time-bin" (figure 4), utilise deux photons émis successivement par le niveau excitonique (à la pulsation  $\Omega$ ); l'intrication est alors obtenue au niveau d'une lame séparatrice où ne sont gardés que les cas où l'un des photons est envoyé à Alice et l'autre à Bob. L'état ainsi sélectionné est alors  $|\phi^+\rangle = (|Long_b, Short_c\rangle + |Short_b, Long_c\rangle)/\sqrt{2}$ , où le premier photon est celui qui prend la sortie (b) de la lame séparatrice (vers Alice par exemple), et le second la sortie (c) (vers Bob); *Short* désigne le premier photon émis, et *Long* le second. Le décalage temporel  $T$  d'émission est grand devant l'extension temporelle des photons, de sorte qu'ils n'interfèrent pas sur, par exemple, la lame séparatrice. Naïvement, le codage de bit est sur la date d'émission du photon. Quelques expériences très récentes en laboratoire ont démontré la possibilité d'utiliser dans ces deux schémas, des boîtes quantiques comme sources déterministes de paires de photons intriqués. Cependant à cause d'imperfections inhérentes à ces sources, ces expériences manquent en performance

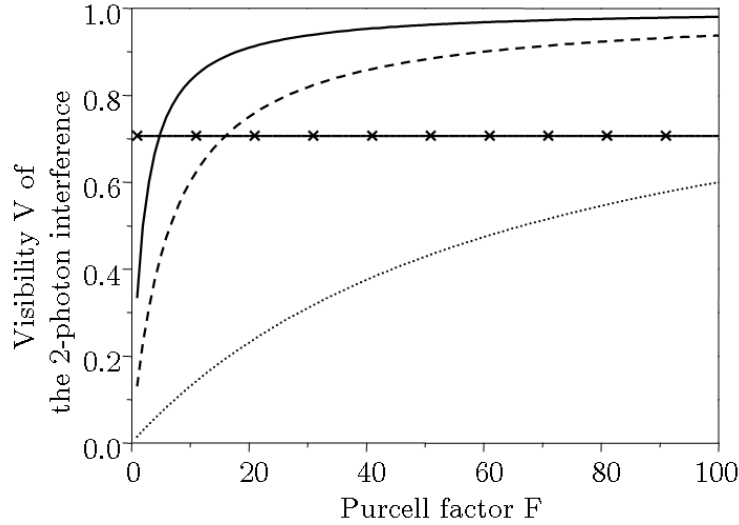


Figure 5: Visibilité maximale des interférences à 2 photons en fonction de l’effet Purcell subit par l’exciton, selon trois régimes de pompage optique: non résonant (courbe pointillée), quasi-résonant (courbe tirets) et résonant (courbe continue).

et ne peuvent être directement utilisées pour la communication de clé quantique. Ces imperfections sont un manque de luminosité du signal collecté et des pertes de cohérence liées aux interactions de la boîte émettrice avec son environnement cristallin. Les phénomènes mis en jeu et impactant le degré d’intrication sont différents selon le schéma utilisé. Cette thèse étudie quantitativement l’impact de ces différents phénomènes dans les deux schémas.

Dans un point de vue plus rigoureux sur le time-bin, il s’agit d’interférences délocalisées entre deux chemins possibles dans les appareils de mesure d’Alice et de Bob. Ces appareils sont des interféromètres stabilisés, déséquilibrés, dont la différence  $c \times d\tau_{b,c}$  de longueur de bras correspond à la durée séparant l’émission des deux photons  $T \sim d\tau_{b,c}$  et plus grand que l’extension spatiale du paquet d’onde du photon, c’est à dire la durée de vie de l’émetteur. Ne sont gardées que les situations où le photon *Short* s’est propagé dans le bras court d’un interféromètre (que ce soit celui d’Alice ou de Bob), et le photon *Long* dans le bras long de l’autre interféromètre, de sorte que les deux photons arrivent simultanément sur les lames séparatrices de sorties des deux interféromètres, puis sont détectés. Il n’est alors plus possible, si les deux photons sont identiques hormis leur date d’émission, de les distinguer. Les deux chemins possibles (dans lequel des deux interféromètres s’est propagé le photon *Short*, et réciproquement *Long*?) interfèrent. Ces interférences varient comme  $V \cos(\Omega(d\tau_b - d\tau_c))$ . La visibilité  $V$  des interférences est fonction de la durée de vie  $T_1 \sim 1ns$  et du temps de cohérence  $T_2$  du niveau excitonique, elle approche de son maximum  $V \simeq T_2/(2T_1)$  dans le cas où les deux interféromètres sont effectivement avec un déséquilibre proche du décalage d’émission  $T$  (à quelques centaines de  $\mu m$ ). Ce ratio  $T_2/(2T_1)$  est aussi la profondeur du “dip” lors de la mesure d’indiscernabilité de Hong-Ou-Mandel, ce qui permet notamment d’évaluer plus aisément la qualité d’une telle source. La valeur du temps de décohérence dépend, comme démontré expérimentalement par de nombreux groupes, de la méthode de pompage. Un pompage adapté est par exemple u pompage quasi-résonant. Dans ce cas  $T_2 \sim 230ps$ , mais ce ratio reste trop faible pour atteindre le régime intriqué ( $V > 1/\sqrt{2}$ ). Une accélération d’un facteur 30 de la vitesse d’émission est suffisante pour que le processus radiatif soit suffisamment plus rapide que les processus dégradants ce procédé d’intrication, qui sont ces processus déphasant sur le niveau excitonique (figure 5).

Cette accélération de l'émission, appelée effet Purcell, est obtenue en plaçant une cavité autour de la boîte quantique. La cavité modifie l'environnement électromagnétique de la source, et donc l'interaction entre celle-ci et le champ électromagnétique environnant, pouvant, selon les conditions, augmenter ou diminuer l'intensité de cette interaction, et donc la durée de vie radiative de l'émetteur. L'effet Purcell maximal est obtenu lorsque la source est au maximum du mode de cavité avec lequel il est en résonance. L'amplitude maximale de l'effet Purcell ne dépend que des caractéristiques de ce mode, à savoir son volume modal et son facteur de qualité. Il est démontré que les cavités à cristal photonique sur membrane suspendue (figure 6) sont parmi les mieux adaptées à la problématique de cette thèse, notamment grâce à leur très faible volume modal. De plus une telle cavité, lorsqu'elle est proprement choisie, permet de rediriger efficacement la lumière vers l'objectif collecteur et ainsi augmenter la luminosité de la source. Ces cavités sont en fait un défaut dans un maillage périodique bidimensionnel de trous creusés dans une membrane qui contient la (ou les) boîte(s) quantique(s). La lumière émise par la boîte à l'intérieur de la cavité ne peut se propager dans la membrane car les trous dans cette dernière créent une alternance périodique de l'indice de réfraction, ce qui réfléchit la lumière lorsque celle-ci est à la bonne longueur d'onde (comme un miroir de Bragg). Le confinement vertical est obtenu par réfraction interne totale sur l'interface semi-conducteur/air de la membrane. Le développement d'outils de simulation adaptés à la recherche de telles cavités est présenté. Il est ainsi possible de calculer efficacement la longueur d'onde de résonance, le volume modal, le facteur de qualité, le diagramme de rayonnement et l'efficacité de collection, de différents dessins de cavité et d'en optimiser les performances. Certains des résultats obtenus lors de ces études numériques sont expérimentalement testés. Il est notamment démontré que l'absorption de la couche de mouillage, qui est le puits quantique résiduel lors de la croissance des boîtes, et qui est pourtant hors résonance avec la cavité (à plus de  $70nm$ ), est responsable d'une forte limitation du facteur de qualité expérimental des cavités à cristal photonique sur GaAs vers  $950nm$ .

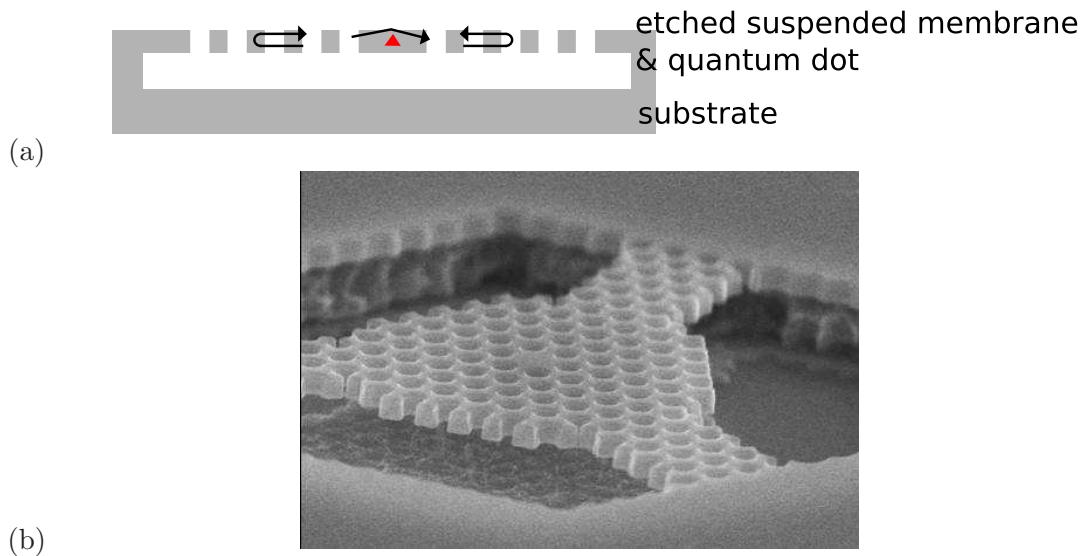


Figure 6: a: Schéma d'une cavité à cristal photonique sur membrane suspendue: coupe verticale. b: Image au microscope à balayage électronique d'une cavité à cristal photonique sur membrane suspendue.

Le problème d'obtenir un pompage quasi-résonant d'une boîte quantique placée dans un cristal photonique est étudié. La solution proposée consiste à créer un second mode de cavité de polarisation perpendiculaire au mode résonant avec l'exciton (qui est responsable de l'effet Purcell). Ce second mode doit être de faible facteur de qualité et spectralement environ  $30nm$  en deçà du mode résonant

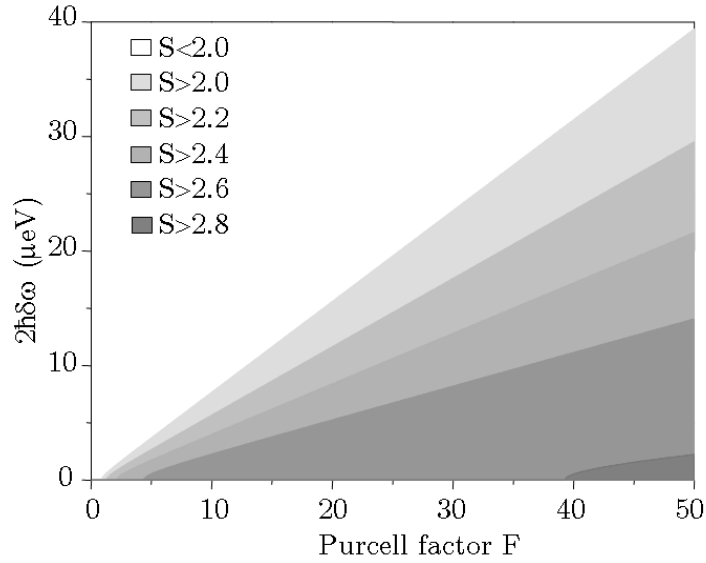


Figure 7: Degré d'intrication en polarisation de la paire de photon émise lors de la cascade radiative du biexciton, en fonction de la levée de dégénérescence  $\delta\omega$  de la structure fine de l'exciton, et de l'effet Purcell subit par celui-ci.

avec l'exciton, afin de permettre l'accès au laser de pompe à la boîte. Ce second mode est alors en résonance avec le susdit laser. Différentes géométries de cavités à cristal photonique sont étudiées pour répondre à ce problème.

Dans le cas de la cascade radiative du biexciton, il est démontré que l'utilisation de l'effet Purcell est nécessaire mais insuffisant (figure 7). S'il permet de compenser les mécanismes de pertes de cohérence ou de retournement de spin, il ne peut compenser pleinement la levée de dégénérescence du niveau excitonique. En effet, le niveau intermédiaire de la cascade radiative, le niveau excitonique, présente une levée de dégénérescence de la structure fine du spin qui dégrade fortement, voire même détruit, l'intrication. Les autres effets, qui sont suffisamment lents pour être pris de vitesse en accélérant l'émission de l'exciton, sont: le retournement de spin de l'exciton, la décohérence de ce spin, et la perte de cohérence entre les deux niveaux excitoniques créée par des processus déphasant sensibles à la polarisation de l'exciton. Cependant, même si ce niveau relais est dégénéré, une cavité dégénérée en polarisation avec un facteur de Purcell de 10 reste nécessaire. Nos calculs indiquent que des cavités à cristal photoniques judicieusement dessinées peuvent satisfaire ces critères. Bien choisies, elles permettent aussi comme précédemment, d'augmenter sensiblement la luminosité de la source. Grâce au faible volume modal de la cavité, il est possible d'obtenir un couplage non-résonant avec la raie biexcitonique tout en gardant l'effet Purcell désiré sur la raie excitonique. Ce couplage avec le biexciton permet d'augmenter l'efficacité de collection sur le biexciton, et donc l'efficacité de collection de l'ensemble de la paire. Ceci permet aussi d'éviter la recherche, garantie de peu de succès, du dessin d'une cavité présentant deux modes dégénérés en polarisation distants spectralement de quelques nanomètres et ayant des intensités du champ électromagnétique qui coïncident au niveau de la source.

Les conditions de pompage de ce système sont discutées. Les conditions exactes d'accord spectral et spatial entre la source et la cavité sont discutées. Il est ainsi démontré qu'il est nécessaire de pouvoir localiser précisément la boîte quantique au centre de la cavité, technologie encore en développement aujourd'hui.

Par ailleurs une tomographie quantique des paires de photons émises s'avère être un moyen

de mesurer l'ensemble des paramètres phénoménologiques de ce modèle. Le modèle développé permet aussi d'expliquer les résultats obtenus expérimentalement par un autre groupe. Dans ces expériences, il a été possible d'augmenter la fidélité de l'état intriqué en effectuant une sélection temporelle des photons émis dans un temps court devant les temps de déphasage caractéristiques.

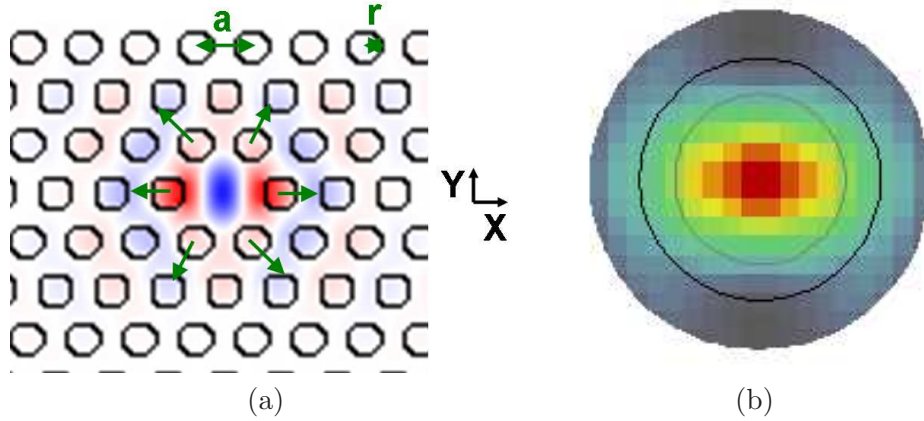


Figure 8: a: Schéma d'une cavité H1 modifiée. b: Diagramme de rayonnement calculé d'une cavité H1 modifiée de sorte à satisfaire les besoins pour une source de paire de photons intriqués en polarisation; rouge: intensité maximale, gris: nulle. Intérieur du cercle gris (resp. noir, ou la totalité du disque): signal collecté par un objectif d'ouverture numérique 0.5 (resp. 0.7 et 1) placé au-dessus de la cavité et focalisé sur celle-ci.

Il est aussi mis en avant un autre problème jusque là ignoré, qui impacte le degré d'intrication des paires émises. En effet, le diagramme d'émission de la polarisation H et V ne se recouvrent pas ce qui crée un chemin de discernabilité au détriment de l'intrication. Dans le pire cas, si la direction d'émission des photons est très fortement couplée à la polarisation de ces photons, il est alors possible de prédire la polarisation du photon à partir du mode spatial de propagation des photons collectés. Les paires de photons émises lors de la cascade radiative du biexciton, par une boîte, même parfaite, placée dans une telle cavité ne sont plus intriqués. Durant ces travaux, nous avons recherché l'existence de cavités en cristaux photoniques permettant une parfaite indiscernabilité des diagrammes de rayonnement. Une telle cavité est proposée (figure 8). Elle est formée d'un trou manquant dans une maille triangulaire de trous, et les six trous autour de ce trou manquant sont éloignés du centre de la cavité. Une telle géométrie de cavité, communément appelée H1, a déjà été étudiée, mais uniquement dans une optique d'optimiser le facteur de qualité. Il est démontré que cette optique et celle de cette thèse, à savoir trouver une cavité avec un facteur de Purcell suffisant mais non trop élevé, avec une bonne efficacité de collection, et une sensibilité nulle à la polarisation, sont incompatibles.

Toutefois, le recours à l'effet Purcell ne suffit pas à compenser la levée de dégénérescence usuelle des boîtes quantiques natives. Cette thèse explore la possibilité de réduire la levée de dégénérescence à l'aide d'un champ électrique vertical réglable. Cette solution a été choisie pour sa compatibilité technologique avec les cavités à cristaux photoniques et la future intégrabilité du système mis en œuvre. Le champ électrique est obtenu en plaçant la boîte quantique dans la partie intrinsèque d'une diode pin verticale utilisée dans le régime bloquant. En redressant progressivement les bandes il est ainsi possible de faire varier ce champ électrique. Afin de garder la compatibilité avec la technologie à cristal photonique, l'épaisseur totale de la diode pin est de 180nm, ce qui a soulevé des difficultés dans le développement du procédé de fabrication de ces diodes. En effet le métal utilisé pour faire le contact avec la partie supérieure de la diode doit être non diffusif pour ne pas être en contact ohmique avec la partie inférieure de la diode située seulement 140nm sous la surface. Afin de mener une première

étude, la diode est recouverte d'un masque métallique opaque optiquement percé de trous. Une grande attention a été portée pour que ces trous, de diamètre entre  $0.5\mu m$  à  $2\mu m$  soient parfaitement ronds afin de ne pas déformer en polarisation le signal de photoluminescence émis par les boîtes situées juste en-dessous. Ces trous permettent d'effectuer une sélection spatiale des boîtes quantiques et de mener une étude spectroscopique de boîtes individuelles. Cette étude a permis de démontrer une variation de  $10\mu eV/V$  de la levée de dégénérescence, sur une plage utile de  $0.5V$  en tension appliquée à la diode. Cependant la valeur initiale des boîtes quantiques de l'échantillon étudié, qui est de  $70\mu eV$ , est trop importante pour permettre d'approcher la valeur de cette levée de dégénérescence suffisamment proche de zéro pour le but de cette thèse. Une diode de type *nin* peut être produite avec le même procédé technologique et devrait être adapté.

Cette thèse conclue sur la faisabilité technologique de ces deux procédés d'intrication, ainsi que sur leurs possibilités d'évolution futures respectives. Les progrès récents dans la technologie des boîtes quantiques InP émettant dans la longueur d'onde des télécommunications ( $\sim 1500nm$ ), et le faible nombre de difficultés aujourd'hui envisagées pour obtenir une source déterministe et efficace de paires de photons intriqués en *time-bin*, permet d'avoir de grands espoirs sur la réalisation d'une telle source. A l'opposé, l'autre schéma d'intrication nécessite encore aujourd'hui d'importants efforts technologiques en termes de positionnement spectral et spatial de la boîte, et dans le contrôle de la levée de dégénérescence du niveau excitonique. Sur ce second point, le développement de diodes verticales fines a permis de mettre en évidence la variation de cette dégénérescence avec un champ électrique vertical, et ce dans une structure compacte et compatible avec la technologie des cristaux photoniques.



# Thanks

I would like to thank many people I interacted with, during these three years, for their help, their efforts, and their time.

First I would like to thank Jean-Yves Marzin, head of the LPN, and Izo Abram, former head of the PEQ team, for having given me the great opportunity to spend these three industrious years within the friendly PEQ team. This PhD work has been supervised mostly by Isabelle Robert-Philip and Alexios Beveratos. They provided me with numerous pieces of advice that I have lost count (if I ever started to count). Thank you both for your patience, your availability to discuss (and digress) on all the topics I encountered, and for having borne with my loud rages against the variety of software I had to fight in order to obtain the expected behaviour. Your enthusiasm, even during the times when everything had mischievously decided not to work as I intended, has been very much welcome. I want also to thank Remy Braive for his help in mastering the optical setup, as well as for all the photonic crystal samples he kindly produced for me. The PEQ team would not have been so pleasant without Richard Hostein, Tiffany Elsass, Sylvain Barbay and Robert Kuszelewicz. Thank you all for your help, your good moods, the discussions of everything but physics during the lunch time. Thanks also to Alexandre Bazin and Arnaud Risper for their help during the optical measures I performed during this last year.

My work led me to strongly cooperate with another team of the LPN, lead by Paul Voisin, whose research topics include the spectroscopy of the excitonic fine structure of the exciton. This is not the place to explain that: I kindly refer you to this manuscript to know more about it. I would like to thank them for having welcomed in their team, and helped me on this subject. Most particularly Olivier Krebs, who gave me numerous explanations on this topic, and taught me how to use his optical setup intelligently. Many thanks also to Jan Suffczynski who spared me lots of time by performing for me a great amount of the measures on this particular aspect. Thanks to Paul for his explanations (on physics and to decipher the sometimes-too-obscure explanations of Olivier). From the GOSS team, but on another topic, I would like to thank Pascale Senellart for her help and advice on how to anneal the samples in the hope to obtain GaAs dot room temperature photoemission in photonic crystal cavities. Despite all our attempts it did not work, but only because the laws of physics did not wish it, and absolutely not through lack of enthusiasm on her part.

On the topic of photonic crystal cavity simulations, I mostly interacted with Alexios Beveratos and Timothy Karle. Thanks to Timothy, I avoided and resolved many practical difficulties in the use of FDTD software, but also understood the obtained results and why the computed data went wrong. Tim, it is always a pleasure to discuss with you. The LPN invested lots of funds in order to develop this capacity to compute photonic crystals. Thank you for that. Thanks also to Lorenzo Bernardi who managed the technical aspect of the huge computer called Avengers.

Thanks to Nadia Belladas for her help in conceiving and stabilizing the two interferometers I created in the first year of my PhD work. At that time, I hoped to use them to perform the experiment, but we did not find the source within the allotted time. I might have been too ambitious to expect that to happen. Nevertheless, I have been promised they will be used at some point in the future, and that part of our common work will not be in vain.

To finish this tour of the "optical experiments" part of my work, I would like to thank Jean-François Roch and Dominique Chauvat, both from the LPQM in Cachan, for their advice and their interest in measuring the radiative patterns of the photonic crystal cavities. I am sorry we did not find a way to perform this experiment in the LPQM as we first intended to. Your expert explanations on the obtained results were very reassuring.

This kind of work which involves, amongst other things, the development of semi-conductor processes in a clean room environment, can obviously be performed only with the active day-to-day help of many people. I would like to thank all of them, and to apologize if I forget to name them specifically below.

I would like to thank first Isabelle Sagnes who supervised my work during these three years, and whose dynamism and enthusiasm are very overwhelming. Thanks also to Aristide Lemaitre, for the samples he produced for me, and the advice he gave me on the diode process.

I mostly discovered how to work in the clean room with Edmond Cambril, with whom I developed the process to lift-off big squares of metal with suitably shaped little holes. Edmond, thank you for your time, your patience, and so many things. Two other people have been of great help in my learning process of the clean room: Christophe Dupuis and Christophe Roblin, who, among other things, taught me and helped me to perform and check the UV-lithographic steps of my process. Thank you, both of you, for the lively atmosphere you provide in this part of the clean room. When none of you is around, the place is really not the same.

Thanks also to Laurent Couraud for the numerous metal evaporations he performed for me, and for the advice he gave me to help me find the right metal to deposit. Thanks also to Nathalie Bardou for her help in our attempt to use the tungsten.

Thanks to Patrick Hisope for his support in providing me all the things I asked him, amongst which are the He cylinders—but this is far from being all that he provided. Thanks to the staff of the mechanics workshop for all the mechanical pieces, and to have so kindly satisfied all my weird requests. Thanks to the administration staff, for all their hard and necessary work, which we sometimes do not appreciate enough.

Thanks to Claude Fabre, Philippe Grangier, Valéry Zwiller, Izo Abram, Philippe Lalanne and Isabelle Robert-Philip for attending my PhD defence and showed such a great interest in my work. Thanks to François Laruelle, who had an impossibility to be present, for accepting to be part of my jury.

Thanks to my fiancée Alette and my parents, for their support and their desire to understand what I was doing.

Thanks to the Sun who has the courage and never forget to rise every day, to let us see and play with the wonders of the world.

# Contents

<b>Foreword</b>	<b>xx</b>
<b>1 Why a quantum dot in a cavity, and what for?</b>	<b>1</b>
1.1 Brief introduction to cryptography	1
1.2 Quantum cryptography : principles, examples and technical challenges	4
1.2.1 Principles	4
1.2.2 The example of the BB84 protocol	4
1.2.3 The example of the EPR protocol	6
1.2.4 Quantum relays	8
1.3 Quantum dots as candidates for deterministic sources of quantum states of light	9
1.3.1 Photon sources for quantum cryptography	9
1.3.2 Single semiconductor quantum dots	11
1.4 Cavity effects	15
1.4.1 Purcell effect	15
1.4.2 Coupling and collection efficiency	17
1.4.3 Impact of light absorption on the cavities optical quality factors	19
1.4.4 Overview on different semiconductor cavities	20
1.5 Conclusion	22
Bibliography	23
<b>2 Design of bi-dimensional photonic crystal cavities</b>	<b>29</b>
2.1 Confinement in 2D photonic crystals slab cavities	30
2.1.1 Hybrid confinement : photonic-crystal effects and index guiding	30
2.1.2 Cavity designs	31
2.2 Fabrication of GaAs photonic crystal slabs	32
2.3 Numerical treatment of photonic crystals	34
2.3.1 Numerical tools to treat photonic crystals	34
2.3.2 The Finite Difference Time Domain (FDTD) tool	34
2.3.3 The monomode excitation condition	37
2.3.4 Far-field calculations: Young's setup test	39
2.3.5 Collection efficiency	43
2.4 Optical properties of photonic crystal cavities	43
2.4.1 Important characteristics of the cavity	43
2.4.2 Defect photonic crystal cavities	44
2.4.3 Impacts of the cavity geometry on the optical properties of the cavities	46
2.4.4 Impacts of the absorption on the optical properties of the cavities	57
2.5 Experimental wavelength resonance and quality factors of photonic crystal cavities	58
2.5.1 Experimental setup	58
2.5.2 Wavelength resonance of "modified" L3 cavities	59

2.5.3	Quality factor of modified L3 and H1 cavities . . . . .	59
2.6	Experimental far-field patterns of photonic crystal cavities . . . . .	61
2.6.1	Choice of the material . . . . .	61
2.6.2	Experimental setup . . . . .	61
2.6.3	Far-field measurements . . . . .	63
2.7	Conclusion . . . . .	66
	Annex: From Scanning Electron Microscopy images to simulation . . . . .	66
	Bibliography . . . . .	66
<b>3</b>	<b>Time-bin entanglement</b>	<b>71</b>
3.1	The model . . . . .	73
3.1.1	Single photons with phase diffusion . . . . .	73
3.1.2	Propagation . . . . .	74
3.2	Entanglement on a beamsplitter . . . . .	75
3.2.1	Two photons travelling through two different interferometers . . . . .	76
3.2.2	Entanglement and indistinguishability . . . . .	77
3.2.3	Conditions for creating and observing entanglement . . . . .	78
3.3	Cavity design for restoring entanglement . . . . .	82
3.3.1	The need of quasi-resonant pumping . . . . .	82
3.3.2	Excitation schemes . . . . .	83
3.4	Conclusion . . . . .	86
	Annex: Calculation details of the visibility . . . . .	86
	Annex: Preparation of the time-bin experimental setup . . . . .	87
	Bibliography . . . . .	89
<b>4</b>	<b>Polarization entanglement</b>	<b>93</b>
4.1	The model . . . . .	94
4.1.1	The four-level system . . . . .	94
4.1.2	Dynamics of the four levels system . . . . .	96
4.2	Polarization entanglement from the biexciton cascade . . . . .	97
4.2.1	Experimental setup . . . . .	97
4.2.2	Joint photodetection probability . . . . .	99
4.2.3	Quantifying two-photon entanglement and density matrix . . . . .	100
4.2.4	Quantum dot spectroscopy from quantum tomography . . . . .	102
4.2.5	Other entanglement criteria . . . . .	103
4.2.6	Further developments of the model . . . . .	104
4.3	Restoration of entanglement . . . . .	104
4.3.1	Ingredients degrading entanglement . . . . .	105
4.3.2	Controlling the fine structure splitting . . . . .	106
4.3.3	Exploiting the Purcell effect . . . . .	106
4.4	Cavity design for restoring entanglement . . . . .	109
4.4.1	Optimization of the Purcell effect and the collection efficiency . . . . .	109
4.4.2	Farfield discernability . . . . .	111
4.4.3	Impact of the dot's position . . . . .	112
4.5	Conclusion . . . . .	114
	Bibliography . . . . .	115

<b>5</b>	<b>Fine-tuning of the excitonic splitting</b>	<b>121</b>
5.1	Fine structure splitting of the exciton . . . . .	121
5.1.1	Quantum dot anisotropy . . . . .	121
5.1.2	Control of the quantum dot anisotropy . . . . .	122
5.2	Control of fine structure splitting . . . . .	124
5.2.1	Vertical electric field . . . . .	124
5.2.2	Quantum confined Stark effect . . . . .	125
5.2.3	Field-induced carrier escape . . . . .	125
5.3	Device for vertical field . . . . .	126
5.3.1	Design of the structure . . . . .	126
5.3.2	Processing of the structure . . . . .	127
5.4	Experimental results . . . . .	133
5.4.1	Experimental setup . . . . .	133
5.4.2	Fine-tuning of the exciton splitting in dots with high asymmetry . . . . .	134
5.4.3	Towards a fine-tuning of the exciton splitting in dots with high asymmetry . . . . .	137
5.5	Conclusion to this study . . . . .	139
	Bibliography . . . . .	140
<b>6</b>	<b>Conclusions and perspectives</b>	<b>143</b>
6.1	Summary . . . . .	143
6.1.1	Towards photon entanglement from a single quantum dot . . . . .	143
6.1.2	Time-bin entanglement . . . . .	144
6.1.3	Polarization entanglement . . . . .	144
6.1.4	Polarization entanglement versus time-bin entanglement? . . . . .	145
6.2	Perspectives . . . . .	145
6.2.1	Towards entanglement at telecommunication wavelengths . . . . .	145
6.2.2	Towards entanglement from two single dots . . . . .	146
	Annex: Personnal publications . . . . .	147



# Foreword

Quantum key distribution was the very first component of a quantum network allowing for the secure distribution of secret keys between two partners Alice and Bob. In over twenty years of active research, quantum key distribution is now a commercial system, allowing for short distance communications. In classical communications, the optical amplifiers was the key element allowing longer distances and at higher bit rates giving rise to the current communications networks. A quantum counterpart of such amplifier is the quantum relay based on quantum teleportation or quantum entanglement swapping. The aforementioned protocols require deterministic sources of entangled photons which are yet to be obtained. Quantum dots are a system of choice when it comes generating quantum states of light. From such systems, it is possible to create single photon sources or sources of entangled photon pairs. Both sources are crucial for future quantum communication networks, and for near future applications such as quantum key distribution. Semiconductor quantum dots based on III-V elements take advantage of the mature processing technology, allowing the control of their emission properties and their integration in photonic crystal cavities giving rise to compact and integrated sources. Although quantum dots have been extensively studied during the last ten years, and single photon emission was demonstrated, an efficient and pure source of entangled photons is still an open problem despite important experimental efforts. Several mechanisms, responsible for the degradation of the entangled state, have been proposed, but without any quantitative description.

This manuscript is divided in 5 chapters. The first chapter presents to the motivations to design and study sources made of a unique quantum dots embedded in a bi-dimensional photonic crystal cavities. Mainly two kinds of motivations appear: to obtain sources with better performances than the current ones, and to study decoherence effects in solid state deterministic sources. This introduction also leads to the definition of two kinds of bit encoding for secured communications: the time-bin and the polarization. In both schemes, the desire to improve existing sources implies some benchmarks, which in turn, justify the use of the photonic crystal cavity. The second chapter begins with a short presentation of these optical nano-structures, and then develops the simulation tools to obtain cavities with the specific requirements of these sources. Simulation and experimental results are compared. The time-bin scheme and its specific requirements are the topic of the following chapter, and chapter 4 performs the same but for the polarization scheme. It also highlights the insufficiency of cavity effects to obtain efficient polarization entangled sources with quantum dots, and motivates the work reported in chapter 5 on the tuning of the excitonic splitting. The last chapter concludes on the current possibilities to solve the original problem.



# Chapter 1

## Why a quantum dot in a cavity, and what for?

This chapter introduces one of the motivations of our work, which is the engineering of a practical source for quantum cryptography. Cryptography is the art of rendering a message unintelligible to any unauthorized party. To achieve this goal, an algorithm (also called a cryptosystem or cipher) is used to combine a message with some additional information (the key) and produce a cryptogram. In this process, the key management, i.e. the generation and distribution of secret keys is the weak link in the chain. Quantum Key Distribution, also called quantum cryptography, is a method for secure key exchange over an insecure channel based on individual quantum objects, like for example photons. In such systems, any attempt to intercept the key during the exchange will inevitably give away the presence of a spy.

In this chapter, we will first give a short overview of the context of modern cryptology and introduce shortly the principles of quantum cryptography. This will allow us to bring to light some main technological challenges to implement such protocols, in particular the engineering of a practical, efficient, deterministic and reliable source of quantum states of light. The chapter continues with a presentation of semiconductor quantum dots as possible candidates for the engineering of such a source. We will show that these single emitters may be valuable candidates, if and only if they are subjected to cavity quantum electrodynamics effects. The chapter ends with a brief description of the involved cavity effects.

### 1.1 Brief introduction to cryptography

Cryptography is the practice and science of rendering a message incomprehensible to any party, without a special secret knowledge, the latter referred to the "key". It includes encryption, which is the process of converting ordinary information into unintelligible message (a cipher text), and decryption, which converts the unintelligible cipher text back to plaintext. Secure communication is the most straightforward use of cryptography, but other applications such as authentication are based on cryptographic protocols. The two parties involved in such communications are generally called Alice and Bob. In order to guarantee the privacy of the communications (for various reasons: personal, military, economical or commercial reasons for instance), they encrypt their message in such a way that Eve, the eavesdropper, cannot decipher the message. A less strict definition consists in rendering the message incomprehensible by Eve for a finite period in time, at least as long as the information it contains is valuable. This latter definition eases the absolute security necessary in communications. For example, the number of a personal VISA card exchanged over a secure site has a lifetime of only two years, and revealing this information to Eve after the expiration date has no impact on Alice or

Bob.

Cryptography generally uses a mathematical algorithm. Encryption and decryption require the use of some secret information shared by Alice and Bob, referred to as a key, which Eve does not know. The complexity of the used algorithms has steadily increased over time ranging from Caesar code to the famous Enigma machine of the German army. While all these algorithms had intrinsic loopholes making the decryption a simple task, even without the knowledge of the key, mathematicians have proved that there exist a simple algorithm allowing for unconditional security. This code is named Vernam code or one-time pad code. The one-time pad is an encryption algorithm in which the plaintext is combined with a secret random key or pad, which is at least as long as the message and which is used only once. By "as long as", we mean that the length of the message is measured in number of bits, possibly compressed, and the pad must be a totally random sequence containing the same number of bits. In order to cipher and decipher the message, a modular addition is typically used to combine plaintext elements with pad elements. Perfect secrecy can only be achieved however with perfectly random one-time pads, and if the key is used only once. Randomness is needed in order to prevent Eve to deduce part of the key (and of the message) by use of some repetition (or more generally correlations) in the bits sequence composing the key. If Alice and Bob want their message to be kept secret for a finite period of time and if they have certain knowledge of Eve's resources, then they can use shorter keys and pseudo-random algorithms to extend the length of this key to the length of their message. The resulting key will obviously contain non random aspects, but the information contained in these correlations may be time consuming to be deduced. In order to circumvent these practical problems, mathematicians have developed new cryptographic techniques, which consist in replacing the modular addition in the one-time pad technique by complex operations between the key and the message. It becomes therefore almost impossible to decipher the cipher text or even to deduce the "key" from the plaintext and cipher text, even if the key is much shorter than the message. One such example is the Advanced Encryption Standard (or AES) used in most modern communications.

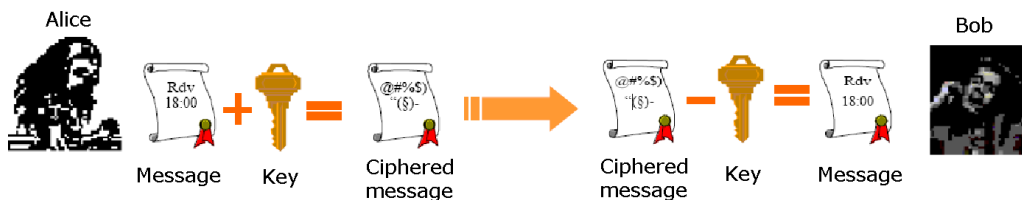


Figure 1.1: The basic principles of cryptography.

In every case, the need to share a secret is replaced by the need to possess beforehand a random sequence of bits of sufficient length, this length depending of the quantity of data you may have to share secretly and of your practical knowledge of Eve's resources. In traditional cryptography, the sender and receiver of a message know and use the same secret key, used to encrypt and decrypt the message. This method is known as secret key or symmetric cryptography. The main challenge here is getting the sender and receiver to agree on the secret key without anyone else finding out. The simplest way for Alice and Bob to share this secret key is to meet and exchange from hand to hand a huge quantity of random bits. This method, still in use today, relies on the reliability of the entities involved and the ability to securely store this information. We will here focus more on the situation in which Alice and Bob are in separate physical locations and have to trust a transmission medium to exchange the key while preventing its disclosure. Eve in this case may intercept the communication during the key generation and may later read, modify, and forge all messages encrypted using that key. Consequently, key management (generation, transmission and storage) becomes a critical issue

in such cryptosystems.

In order to solve the key management problem, the concept of public-key cryptography was introduced in 1976. In this system, each entity gets a pair of keys, one called the public key and the other called the private key. The public key is published, while the private key is kept secret. The need for Alice and Bob to share secret information is eliminated; all communications involve only public keys, and no private key is ever transmitted or shared. The only requirement is that public keys be associated with their users in a trusted (authenticated) manner. Alice can then send a confidential message to Bob by just using public information, but the message can only be decrypted with a private key, which is in the sole possession of Bob. However, in such cryptosystem, the private key is always linked mathematically to the public key. Therefore, it is always possible to attack a public-key system by deriving the private key from the public key. Typically, the defence against this is to make the operation as difficult as possible. For instance, some public-key cryptosystems are designed such that deriving the private key from the public key requires the attacker to factor a large number, so that it is computationally infeasible to perform the derivation. This is the idea behind the RSA public-key cryptosystem, invented in 1977 by R. Rivest, A. Shamir and L. Adleman. RSA stands for the first letter in each of its inventors' last names. Indeed, if it is easy to multiply two huge prime numbers, it is much more complicated to deduce these two numbers from the value of their product. Given the power of modern computers and progress of factorization algorithms, security is achieved by lengthening the key. For serious commercial use, 1024 bits keys are now recommended. A 640-bits RSA key has already been factorized in a few months [1]. This however does not logically exclude the possibility of a new efficient factoring algorithm being discovered, or the existence of a secret factoring algorithm, or the invention of technology capable of running current factoring algorithms at high speed. This latter may become possible for instance by use of quantum computing.

Quantum computing is a new field in computer science based on our understanding of quantum mechanics. Conversely to classical computers that manipulate bits, a quantum computer manipulates quantum bits or qubits. Conversely to classical bits that have a discrete range and can represent either a zero state or a one state, a qubit can be in a linear superposition of the two states. Because of superposition, a phenomenon known as quantum parallelism allows many computations to take place simultaneously, thus vastly increasing the speed of computation. This increasing advantage over classical computers suppose however to find algorithms that can solve problems based on quantum mechanical phenomena, such as superposition and entanglement. One example of quantum algorithm is Shor's algorithm [2], that will be able to factor huge numbers. Unfortunately, one of the most important problems in implementing such algorithm is a phenomenon called quantum decoherence, which results from the coupling between the qubits and their environment and affects the interactions that generate the required quantum superpositions. Consequently, such an algorithm has yet to be implemented on a sufficiently large number of bits to be of practical use (see [3] for an example of implementations).

If quantum information processing could be used to break the code, it could also be used to generate the key. Quantum mechanics provide a way to distribute a key (in this case called "quantum key"), the security of which is absolute as it is warranted by the laws of physics, and not by some mathematical assumptions on the complexity of the factorization problem. The next paragraph will give an overview of the principles that warrant secure communication in quantum cryptography (or quantum key distribution - QKD). It will list various protocols that can be used, focusing only on the ones in which the qubits are encoded on single photons. This short introduction to QKD techniques will reveal the technical needs to be able to implement efficiently these protocols. My goal here is not to make a review of this topic (see [4, 5]), but to focus on one of the major issues in implementing those protocols, which is the engineering of a reliable source which emits deterministically and efficiently quantum states of light.

## 1.2 Quantum cryptography : principles, examples and technical challenges

### 1.2.1 Principles

Quantum cryptography (or quantum key distribution) is a technique that exploits properties of quantum mechanics to guarantee the secure exchange of secret keys. In this cryptosystems, Alice and Bob will generate and exchange a random sequence of bits on a “quantum” absolutely secure channel, that will be further used as a key to encrypt and decrypt a message. The support of information on this “quantum” channel are quantum systems, like, for example, individual photons. The security of this key distribution is then warranted by the laws of quantum mechanics, among which :

- Every measurement perturbs the system
- One cannot duplicate an unknown quantum state

Hence, if Eve tries to eavesdrop on the key, she will not get any information about the communication without introducing perturbations which will reveal her presence. Consequently, after exchanging the photons, Alice and Bob can check whether someone “was listening”: they simply compare a randomly chosen subset of their data using a public channel. If Bob received the randomly chosen subset unperturbed, then the key can be produced and is guaranteed to be secure. Alice and Bob can safely use this key to encode messages. Conversely, if the key turns out to be perturbed, no secure key is possible and communication is aborted. Quantum cryptography is only used to produce and distribute a key, not to transmit any message data. This key can then be used with any chosen encryption algorithm to encrypt (and decrypt) a message, which can then be transmitted over a standard communication channel. The algorithm most commonly associated with QKD is the AES.

The quantum systems, usually photons, on which the information is encoded, are called quantum bits or qubits. The information is then encoded on any variable of the quantum system, like the photons polarization [6], or photons arrival times [7], or on the quadrature amplitudes of the quantized electromagnetic field. Different protocols have been proposed, depending on the nature of the quantum systems (discrete variables such as the photon polarization, we could also mention protocols based on continuous lasers in which the single photons are extracted at the detection stage [8], or protocols using continuous variables such as the quadrature amplitudes of the quantized electromagnetic field [9, 10]...). The former are called discrete variable protocols, while the latter continuous wave protocols. In the following, we shall describe two of these protocols based on discrete variables.

### 1.2.2 The example of the BB84 protocol

The simplest QKD scheme has been proposed in 1984 by Charles H. Bennett and Gilles Brassard, hence the name BB84 under which this protocol is recognized nowadays [6]. In this protocol, the qubits are encoded on the polarization of single photons. Alice sends individual photons to Bob in polarization states chosen at random among four basic states depending on the direction of polarization: horizontal ( $H$ ), vertical ( $V$ ), diagonal ( $D$ ) or antidiagonal ( $A$ ). On his side, Bob performs a measure of the photon polarization in one of the two bases ( $H, V$ ) or ( $A, D$ ).

Let us first consider Alice and Bob use the same polarization basis  $\{H, V\}$  to respectively encode and measure the photon polarization state. The horizontal polarization encodes the bit “0”, and the vertical one refers to “1”. If the communication channel does not perturb the photon polarization (for example has no birefringence or is compensated [11]), if the communication channel has no losses, and if the Bob’s detectors are ideal (no noise, total efficiency), then they get perfectly correlated results: each bit sent by Alice, and chosen randomly, is read unambiguously by Bob. Any loss of bits impacts only the rate of the communication, and not the content of the transferred message as it is

random, as soon as Alice and Bob are able to recover which photons Bob received (by synchronizing themselves for example). This is not yet a secured communication. Eve can intercept Alice's photons, perform a measure of the photon polarization and send again to Bob a photon with the polarization she measured. Conversely, if Alice and Bob choose randomly for each photon the two possible polarization basis  $(H, V)$  or  $(A, D)$  and do not tell publicly which basis they have chosen before the whole key exchange, then Eve can no more act like a transparent repeater as previously [12].

(figure 1.2). In that case, after exchanging the whole sequence of qubits, for each photon, Bob announces publicly in which basis he measured the corresponding qubit (but he does not tell the result he obtained). Alice then only tells whether she used or not the same basis to encode the photons. If they used the same basis, they keep the bit, if not they disregard it (see table 1.3). In this way 50% of the bit string is discarded. Let us suppose now Eve intercepts the qubits propagating from Alice to Bob. She measures each qubits in one of the two bases, precisely as Bob does. Then, she resends to Bob another qubit in the state corresponding to her measurement result. However, in half of the cases, Eve will choose a basis incompatible with the state prepared by Alice, will measure a wrong result with probability failure of  $1/2$ , erase on the Alice's photon the polarization information and will send to Bob a right copy in only 50 % of the cases. These errors will introduce differences between Bob's measures and Alice's data, which they can discover by performing a public comparison of a part of the key. Using some classical algorithm and knowing the errors rate, they can generate a shorter secured key [4]. Eve also cannot create a copy of Alice's photons, in order to keep a copy of the photons Alice sent to Bob and wait for the public announcement of the used basis to perform her own measure.

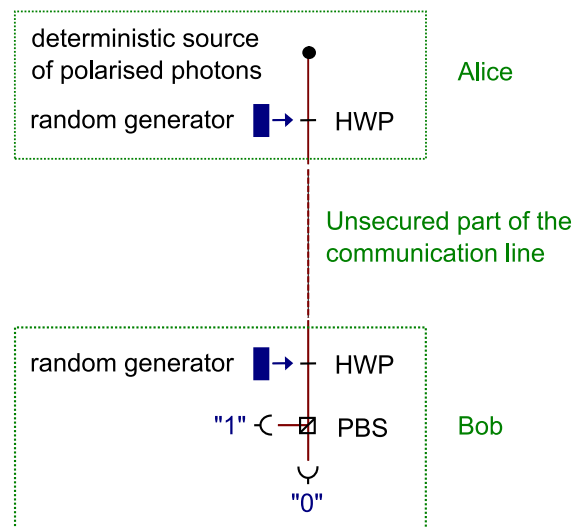


Figure 1.2: Schematic example <sup>1</sup> of a direct quantum key distribution setup : the BB84 protocol [6]. The classical (and unsecured) communication channel between Alice and Bob is not represented here.

The security of this protocol is therefore based on rules in quantum mechanics:

- according to the No-Cloning Theorem of Quantum Mechanics, Eve won't be able to duplicate the quantum information [13] (or divide a particle [14]), keep a copy without leaving the "original" unaffected);

<sup>1</sup>For all the schematics: HWP = half wave plate, QWP = quarter wave plate, BS = 50/50 beam splitter, PBS = polarized beam splitter.

Alice's random bits	0	0	0	1	1	0	1
Alice's random basis	$\{H, V\}$	$\{A, D\}$	$\{A, D\}$	$\{H, V\}$	$\{A, D\}$	$\{H, V\}$	$\{A, D\}$
Polarization sent	H	A	A	V	D	H	D
Bob's random basis	$\{H, V\}$	$\{H, V\}$	$\{A, D\}$	$\{H, V\}$	$\{A, D\}$	$\{A, D\}$	$\{H, V\}$
Bob's measure	H	V	A	V	D	A	H
Identical basis?	yes	no	yes	yes	yes	no	no
Kept bits	0		0	1	1		

Figure 1.3: Example of a direct quantum key distribution.

- according to the Heisenberg Uncertainty Principle, she won't be able to completely measure a quantum state.

The security of the technique however relies on an ideal implementation of the protocol, one that uses single-photon sources. Let us suppose that Alice sends to Bob more than one photon with the same polarization instead of one single photon, without neither Alice nor Bob's knowledge. Eve then can split off the extra photons and transmit the remaining single photon to Bob. This is the basis of the photon number splitting attack, where Eve stores these extra photons in a quantum memory until Bob detects the remaining single photon and Alice reveals the encoding basis. Eve can then measure her photons in the correct basis and obtain information on the key without introducing detectable errors. While the BB84 protocol has already been implemented and tested in a European wide effort [15] and is even now proposed as a commercial product by IdQuantique (Switzerland), MagiqTech (USA), SmartQuantum (France), most of these implementations use attenuated laser pulses that contain less than one photon per pulse, such as to keep the probability of multiphoton pulses very low. In fact, the number of photons in a laser pulse follows a Poissonian statistics. The probability that the pulse contains  $n$  photons reads  $p_n^{\text{laser}} = e^{-\mu} \mu^n / n!$  where  $\mu$  is the mean number of photons per pulse. The probability to have two or more photons is therefore  $p_{\geq 2}^{\text{laser}} = \frac{\mu^2}{2} = \frac{(P_1^{\text{laser}})^2}{2}$  in the limit of a small number of photons per pulses ( $\mu \ll 1$ ). This inherent distribution of photons in laser light imposes to operate with very faint laser pulses that mostly contain no photons ( $P_0^{\text{laser}} \sim 1 - \mu$ ), which reduces consequently the rates of secured key generation. While such imperfection is not a limit for short distance communications, it becomes a limiting factor for long distance quantum key distribution. For such links, an efficient source of deterministic single photons would be of great importance. Moreover, the key used in the one-time-pad must be perfectly random. The later point proves to be delicate in practice. How Alice "chooses at random" her polarization basis, is not straightforward. There exist classical algorithms which generate pseudo-random sequences of bits, but they however introduce correlations whereas we look for an absolutely secured protocol. Another possibility to generate a random sequence is to rely again on the polarization measurement result in the  $\{H, V\}$  basis of a diagonally polarized photon or a similar system such as [16], but these methods suffers from the low detection efficiency which lowers the random number generation rate. One much more interesting way to obtain this randomness is to let the physics make the choice.

### 1.2.3 The example of the EPR protocol

The possibility to use entangled photon pairs for quantum cryptography was first proposed by Ekert in 1991 [12]. The idea consists in replacing the quantum channel carrying single qubits from Alice to Bob by a channel carrying two entangled qubits from a common source, usually named Charlie, one qubit to Alice and one to Bob. In such scheme, Alice and Bob choose randomly their measurement basis. While the output of Alice's detector will always be random, her result will always be correlated

with Bob's measurement in case he chooses the same basis. The rest of the protocol, i.e. the error correction and privacy amplification is the same as for the single photon BB8 protocol. The main advantage of such a system, is that Alice and Bob can use passive detection schemes, and hence avoid the use of random generators. Such scheme (figure 1.4) has already been used in quantum key distribution experiments [17].

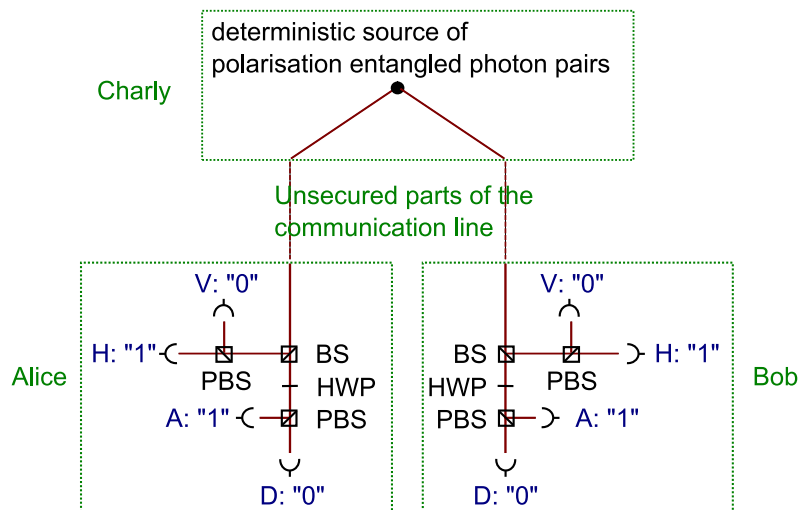


Figure 1.4: Schematic example of quantum key distribution setup with a source of polarization entangled photon pairs and no needs for random generators.

This technique also allows extending the achievable distances in QKD systems by the use of entangled photons and of entanglement swapping. Yet, it will not allow an increase of the key generation rate for a fixed distance. Let us consider the situation in which Alice and Bob are at different locations separated by a distance  $D$ . “Charlie” is the source placed at mid-distance between them, which delivers entangled photon pairs. For each photon pairs, he sends one photon to Alice and one to Bob. Alice and Bob perform the same kind of measurement as the one Bob only performed previously in the single photon setup. The communication line has a loss of  $w$  per length of propagation. The detection efficiency of one detector is  $\eta$ . In the first described scheme, the probability to obtain a secured communicated bit, that is, the probability for Bob to detect the photon emitted by Alice, is  $p_{\text{direct}} = \eta e^{-wD}$  if we do not consider any detector noise. If Alice and Bob use a pair of entangled photons (Charlie) to communicate, with a same distance  $D$  as previously, the probability to obtain a secured bit, that is, the probability for Alice and Bob to detect the pair, is  $p_{\text{entangled}} = (\eta e^{-wD/2})^2 = \eta p_{\text{direct}}$  which is lower than previously. Consequently, for a fixed distance, the use of quantum relays as Charlie is not favourable, at least when the noise is negligible. Conversely, if noise becomes important compared to the detection probability, the effective rate of secured key (including error correction and privacy amplification) abruptly drops down at some distance. The use of Charlie as a quantum relay becomes here worthwhile [18]. This subject is rigorously developed in [19, 20, 18] for example.

The generation of entangled photons has been demonstrated using single atoms [21] but for quantum communication applications mostly rely on parametric down conversion [22]. In this process, one photon injected in a  $\chi^{(2)}$  non-linear material can spontaneously split into two photons conserving total energy and momentum. By nature, this photon pair creation process is probabilistic and quite inefficient. Typically the conversion efficiency ranges from  $10^{10}$  [23] to  $10^6$  [24] as a function of the material used. Consequently, the number of photon pairs per excitation pulse (or coherence length [8]) is randomly distributed following a Poissonian distribution [25, 26]. In addition to the security issue,

these statistics of the entangled photons pairs raises another issue: if two pairs are generated, then four photons are emitted. If the two detected photons by Alice and Bob do not belong to the same pair, then the detected pair is not entangled [26]. This degrades the rate of correlated measurements performed by Alice and Bob, and thus the key generation rate. As a consequence, the deterministic generation of entangled photon pairs, is needed.

Different classes of QKD experiments takes advantage of entangled photon pairs. They can be polarization-entangled photon pairs, as described in the EPR protocol previously. While these experiments are very interesting in the context of free space quantum cryptography, they are limited to very short distances of a few kilometres on optical fiber. Polarization is not robust enough to decoherence in optical fibers. In addition, the polarization state transformation induced on usual fibers often fluctuates. Another class of experiments takes advantage of time-bin entangled photons which can be simply summarized as follows. Let us consider a single photon travelling through an unbalanced interferometer with an arm length difference greater than the coherence length of the photon. At the exit, the photon will be in a superposition of two possible arrival times,  $|t\rangle + |t + \Delta T\rangle$ . We note  $|0\rangle$  and  $|1\rangle$  the two different arrival times respectively. In order to encode an information, one can apply a small change on the interferometer arm length difference so that it corresponds to a small change in the phase between  $|0\rangle$  and  $|1\rangle$ . Such encoding is not yet secured, as only one basis is given to measure the arrival time. In order to introduce some non determination in the measurement process which will reveal Eve's presence, this time encoding is transformed into photon interferences. Bob's measurement setup consists into an unbalanced interferometer with an optical path difference of  $c\Delta t$ . The two possibilities "0" and "1" will thus interfere. Depending on the exact phase between the states  $|0\rangle$  and  $|1\rangle$  that Alice chose, and the exact unbalance of the Bob's interferometer, the two interferometer's paths will interfere constructively or destructively at the output of the interferometer. This kind of coding is called "time-bin" and was first used over long distance in quantum key distribution protocols [23, 7] and group velocity dispersion compensation [27].

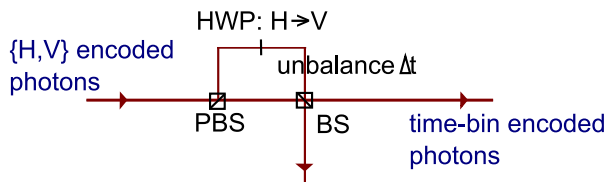


Figure 1.5: Schematic example to convert the polarization encoding basis into the time-bin encoding basis. We keep only the cases where the photons take the desired output, which lowers the conversion efficiency to 50% per photon.

Let us mention that it is possible to perform a conversion from the time-bin encoding to the polarization encoding and reversely (figure 1.5). The most simple setup to do so is a  $\Delta t$ -unbalanced interferometer with a half wave plate in one of its arm (let us say the longer one). If the state  $|1\rangle$  (i.e. arrives first) takes the long arm and the state  $|0\rangle$  the short one, then the basis  $\{|0\rangle, |1\rangle\}$  is transformed into  $\{H, V\}$  (if the polarization of the time-bin states is  $V$ ). Such transformation cannot be performed with a complete efficiency. With linear optics, the theoretical maximal efficiency is  $1/2$ .

#### 1.2.4 Quantum relays

Experiments up till now have demonstrated that keys can be exchanged over distances of a few dozen kilometres at rates at least of the order of a thousand bits per second, even up to  $240km$  [28]. Presently quantum cryptography is still very limited in distance and in secret-bit rate. One of the reasons

resides in the quantum channel losses (see [18, 20] for example). In classical communications, such losses are compensated by using amplifiers (Erbium Doped fiber Amplifiers EDFA, or Semiconductor Optical Amplifier SOA) in mid-distance allowing for an effective re-amplification of the signal. Such systems are of course not compatible with single photon level quantum communications. First, the non-cloning theorem forbids the perfect copy of an unknown quantum state, so photons cannot be amplified without introducing errors, and secondly if the photon is lost before the amplifier, there is nothing to be amplified. Quantum relays [18] are the quantum equivalent of classical amplifiers. These relays are based on protocols such as quantum teleportation or quantum entanglement swapping in order to map the incoming qubit on another distant one, without reading, even in principle, the actual information. The simplest example is quantum teleportation. In this scheme, Bob and a third party, David <sup>2</sup>, share each one photon of an entangled photon pair (emitted by another party called Charly). Alice, wishes to communicate a qubit to Bob using the quantum relay. She sends her qubit to David, who makes a Bell-State projection using Alice's photon and his own. David then communicates the output of his measurement to Bob, who by applying a unitary transformation on his photon, recovers the qubit Alice had send, without even measuring it. In order to succeed, it is necessary that both Alice's photon and Charlie's photon are indistinguishable.

Table 1.6 lists different quantum communications schemes based on polarization encoding. In this table, we added elements on the sources requirements to implement such protocols. Another important issue is the number of photons to be detected, which is related to the number of segments. Already in the second scheme, it is necessary to detect two photons. The efficiency to detect N photons evolves obviously as the efficiency of one detector to the power of N. In the same way, the efficiency of secret key distribution will be generally related to the quantum efficiency per emitted photon of the sources to the same power of N. In order to obtain sufficient secured key generation rates, luminous sources are obviously necessary.

### 1.3 Quantum dots as candidates for deterministic sources of quantum states of light

The very first demonstration of quantum cryptography was a tabletop experiment performed at the IBM laboratory in the early 1990's over a distance of 30 cm [29]. Since then, impressive experimental improvements have been achieved during the last years. Yet, some technical challenges still remain: the effective generation of quantum states of light, the efficient transmission of quantum states of light and the efficient detection of quantum states of light. In the following, we shall focus on the first challenge, in the framework of quantum cryptography with discrete variables.

#### 1.3.1 Photon sources for quantum cryptography

Optical quantum cryptography is based on the use of single photon or single entangled photon pair states. Unfortunately, these states are difficult to realize experimentally. Nowadays, practical implementations rely on weak laser pulses or entangled photon pairs, where both the photon or photon-pair number distribution obey Poisson statistics. Hence, both possibilities suffer from a small probability of generating more than one photon or photon pair at the same time. For large losses in the quantum channel even small fractions of these multi-photons can have important consequences on the security of the key [26].

---

<sup>2</sup>This entity is also usually called Charly. The point is that they are too many Charlies in this story. I will call Charlie only those who possess a source of entangled photons, and call David the ones who perform Bell's measurement and swapping.

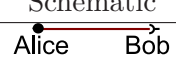
	Schematic	Segments	Source's requirements
Direct		1	Deterministic source of single polarized photons
Direct with no active choice		1	Deterministic source of entangled photon pairs
Entangled		2	Deterministic source of entangled photon pairs
Entangled + teleportation		3	one deterministic source of single photon and one deterministic source of entangled photon pairs. Indistinguishability between the photons from the first source and one photon from the second one
2 Entangled + swapping		4	Two deterministic sources of entangled photon pairs. Indistinguishability between two photons, one from each source
etc			

Figure 1.6: Quantum cryptography distribution schemes with increasing complexity on the requirements on the sources, but increasing potential distance.

The ideal single photon source is a device that, when one pulls the trigger, and only then, emits one and only one photon. Although such behaviour, called photon anti-bunching, has been demonstrated already years ago by use of single atoms [30], a practical and handy device is still awaited. The main idea here is to work with a single two-level quantum system that can obviously not emit two photons at a time. The manipulation of single trapped atoms [21] or ions requires a much too involved technical effort. Single organics dye molecules [31, 32] are easier to handle but only offer limited stability at room temperature. Promising candidates, however, are nitrogen-vacancy centres in diamond [33, 34, 35], although their emission spectrum is not compatible with telecommunication applications. Heralded single photon sources where the detection of one photon of a photon pair announces the second one [36] are also an interesting solution, but their production rate is limited to the detection rate of the announcing detector, generally limited to less than  $10MHz$ .

Single semiconductor quantum dots are a promising candidate for the realization of single photon sources as well as entangled photon sources. Their semiconductor solid state nature makes them compatible with highly mature semiconductor manipulation techniques allowing for example to embed them in solid-state microcavities. Several experiments and theoretical predictions in this direction have been performed in the last 10 years demonstrating single photon emission [37, 38, 39, 40, 41], emission of indistinguishable single photons [42, 43, 44] and steps towards the generation of entangled photon

pairs [45, 46, 47, 48, 49, 50, 51, 52, 53, 54].

### 1.3.2 Single semiconductor quantum dots

I will now describe the radiative mechanisms of these quantum dots structures, in particular why they are deterministic. This part continues with a short description on how they are grown, and finishes with the advantages of these sources. During this report I will return to various aspects of these sources, in particular dephasing processes.

Quantum dots are tiny regions (of the order of  $600 \text{ nm}^2$ ) of a smaller band gap semiconductor surrounded by a larger band gap semiconductor, in which conduction-band electrons and holes (missing electrons in the valence band) can be trapped. The confinement is in all three dimensions. The size of this region is small enough that quantized (discrete) energy levels occur. Optical transitions between the valence band and the conduction band can thus occur only at discrete energies.

#### Quantum dots fabrication

Quantum dots are grown by Molecular Beam Epitaxy (MBE) or Metalorganic Vapour Phase Epitaxy (MOVPE) by a strain induced process known as Stransky-Krastanov growth. While the former growth technique is the most advanced for InAs/GaAs quantum dots, dots grown by MOCVD are under investigation, since they would allow the growth of quantum dots compatible with telecommunications wavelength. The dots I used during my PhD were grown by MBE. In MBE, one begins with a high-quality substrate, heated and placed in an ultra-high vacuum. Sources of pure elements are heated so that a small flux of atoms evaporates and travels toward the substrate in a beam. These beams are turned on and off using shutters. Some of the atoms that strike the substrate stick to it, and due to the high temperature of the substrate, these atoms move across the surface until they find an energetically favourable resting place, typically along an atomic step. These steps propagate across the sample surface as single monolayers are deposited onto the substrate. Optimal crystal growth depends on the atomic beam-flux ratios, the substrate temperature, and the absence of contaminants. The formation of InAs quantum dots occurs in a different way, known as Stranski-Krastanov growth. Quantum dots form when InAs is grown on top of GaAs, due to the lattice size mismatch (the natural lattice size of InAs is 7% larger). The first one or two monolayers of InAs match the underlying GaAs lattice, but are under mechanical strain. This initial, smooth layer of InAs is called the “wetting layer”. After a critical thickness (typically less than 2 monolayers), it becomes energetically favourable for the InAs layer to form islands. These are typically 4-7 nm thick and 20-40 nm in diameter, depending on the growth parameters (see Fig. 1.7). The density of islands depends on both the growth temperature and the amount of indium deposited, but can vary from  $10 \mu\text{m}^{-2}$  to  $500 \mu\text{m}^{-2}$ . To complete the quantum dot structures, a GaAs capping layer is grown on top.

#### Optical properties

The optical properties of quantum dots depend heavily on the growth process. The emission wavelength depends on both the size and the composition (how much GaAs is mixed into the InAs island). The energy-level spacing depends on these same factors. The cleanliness of the growth might affect whether quantum dots start out neutral, or with extra charges...

Self-assembled InAs/GaAs quantum dots are appealing as optical emitters for several reasons. The band gaps of the two materials line up such that a large potential well is formed for both electrons and holes. InAs has a direct band gap, which allows for efficient optical transitions. The dipole moments of the particles (electron and hole) in the dot effectively add up to create a single dipole with large oscillator strength. Finally, the energy of transitions between confined states in the dots lies in the near infrared, where the unique photon detection efficiency is not too bad. One principle

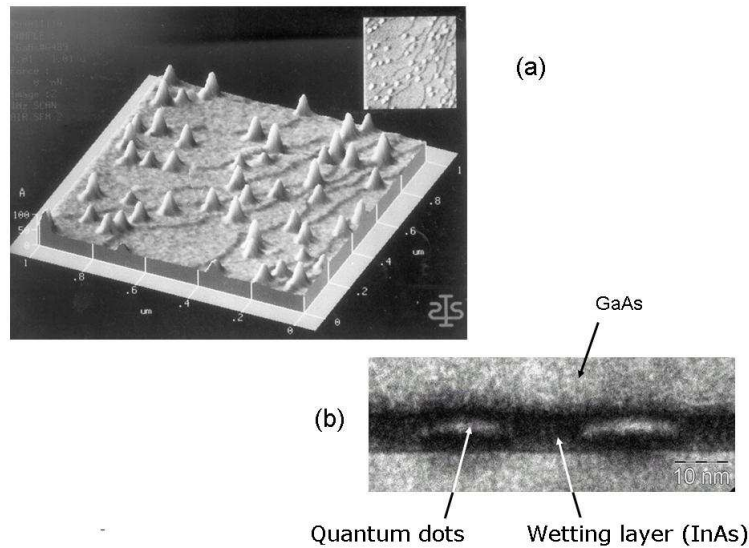


Figure 1.7: (a) Atomic force microscope view of the surface of the epitaxied sample with Stranski-Krastanov quantum dots before being capped with GaAs. (b) Cross-section of quantum dots observed with a Transmission Electron Microscope.

tool for investigating optical emission from quantum dots is photoluminescence (PL). An intense laser light ( $\sim 50mW$ ) is directed toward the sample, leading to the production of electron-hole pairs. The energy of the incident light may be larger than the GaAs band gap; this is what we call above-band excitation. In this case, many electron-hole pairs are created in the GaAs matrix surrounding the dot. The carriers diffuse toward the dots. At low temperature, they are rapidly trapped by the dots, and quickly relax to the lowest-energy confined states. They then recombine to emit a photon with a characteristic energy level. A typical spectrum of a set of quantum dots is presented on Figure 1.8. We can distinguish at lower wavelength a 25 nm wide peak around 870 nm corresponding to emission from one-dimensionally confined states in the wetting layer. A broader peak is observed around 960 nm. It comes from the quantum dots. Since the dots are formed through a self-assembly process, they have a distribution of sizes and shapes. This leads to a variation in the confined energy levels, reflected in the large inhomogeneous linewidth. Two broad peaks can be seen, most probably due to the existence of two quantum dot families, characterized by a different high.

In order to recover the narrow homogeneous linewidth, we must isolate a single quantum dot from the set. Several techniques have been explored to isolate the luminescence of a single quantum dot. A small volume of the sample can be selectively excited by cathodoluminescence, current injection by a scanning tunnelling microscope, or near-field scanning optical microscopy. Alternatively, microscopic holes can be patterned into a metal layer deposited on the sample. When the sample is illuminated from above, only dots below the holes are excited, and only the light that escapes through the holes is collected. Perhaps the simplest way to isolate the luminescence from a single quantum dot, though, is to remove all the other dots. This can be done by etching mesas into the sample. If the mesas are made small enough, and the dot density is low enough, then the average number of dots per mesa can be less than one. Mesas can then be found that contain only a single quantum dot. The PL spectra of a particular single quantum dot under above-band excitation present several narrow emission lines, corresponding to different charge configurations of the dots. The total energy of the quantum-dot system is indeed modified by Coulomb interaction among the carriers: the optical transition of a

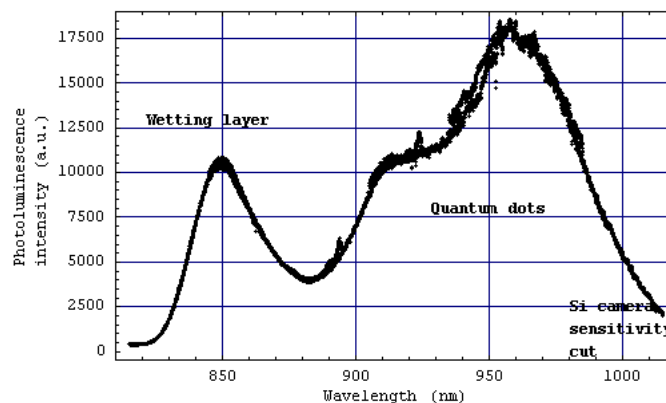


Figure 1.8: Typical photoluminescence spectrum of an ensemble of GaAs quantum dots cooled at 4 K.

trapped electron-hole pair will depend on the number of carriers trapped in the dot (see Fig. 1.9). A single electron and single hole trapped on the fundamental levels of the dot will form a quasi-particle known as an exciton<sup>3</sup>. The energy-level structure of the exciton is dominated by quantum confinement. Due to Pauli's principle, the fundamental level of the electron can be occupied by no more than two electrons, with opposite spin. The same stands for the holes. Therefore at first sight, a quantum dot should be able to contain simultaneously two excitons at the same energy, and therefore should be susceptible to emit two photons and not one at a time. Yet, the second electron-hole pair, called biexciton, interacts electromagnetically with the first one. This interaction modifies the energy level of the excitonic pairs, by an amount called "binding energy". Therefore the recombination of the first electron-hole pair release a photon at a different energy than the one released by a dot containing a single exciton. In the dot's spectrum, a second line appears, called biexcitonic line. Likewise, higher-number multiexciton states can be formed, as well as charged excitons, consisting of two holes and an electron, one hole and two electrons, etc. Since each spectral line correspond to the recombination of one electron and one hole in a single dot's configuration, at most one photon is released under pulsed excitation at the exciton line for instance. After emitting a single photon at the excitonic energy, the dot has to trap another electron-hole pair to emit another single photon. Let us mention that such behaviour occurs generally at low temperatures, which insures the stability of the trapped excitons. In the InGaAs/GaAs system, the holes are not well confined and partially maintained in the dot by the electron's electronic attraction.

### Quantum dots for quantum cryptography

Even if these InAs/GaAs dots emit around 950 nm which is not adapted for optical communications (low-loss fibres at these wavelengths have not been developed) and require an operation at the temperature of liquid helium (4K), they remain valuable systems, more particularly with the development of quantum dots in the C-band ( $\lambda \sim 1.5\mu m$ , wavelength at which losses are minimal in optical fibres) and operating at higher temperatures (at least liquid nitrogen temperature). InAsP quantum dots on InP, studied also in the laboratory, are good candidates for such expectations. Whatever the exact composition of the dot and its surroundings, the radiative processes remain approximately the same. More details on these InP dots can be found in R. Hostein's PhD [55]. Other groups have reported

<sup>3</sup>More usually an exciton is an electron-hole pair maintained in pair by their mutual electromagnetic attraction, but free to propagate within the material, or at least in a two dimensional quantum well. Here, I will use the "exciton" term to design a captured pair in an otherwise empty dot.

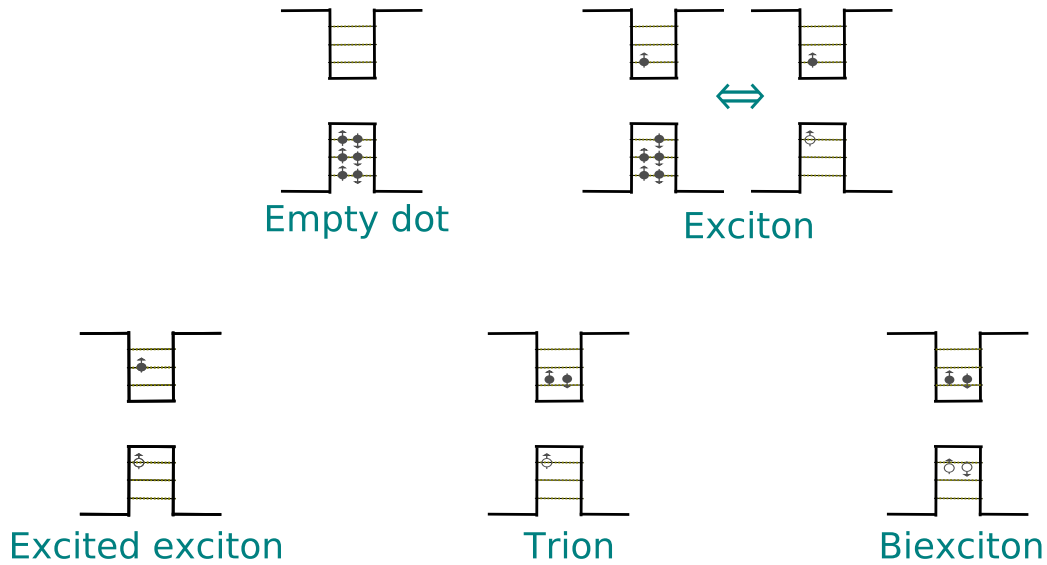


Figure 1.9: Excitation levels of a quantum dot.

similar works, such as InAs/GaAs dots emitting at  $950\text{nm}$  at liquid nitrogen temperature [56]. In the following, if I do not specify the composition of the considered dot, I will refer to GaAs dots. For other dots composition, I will specify their type.

A deterministic source of polarized single photons based on a single GaAs quantum dot was already demonstrated in many groups, and in particular at LPN [46]. Such a polarized source could be of practical use in the BB84 protocol for instance, if the extraction efficiency of the emitted single photons were sufficiently high. This is unfortunately not the case [43, 42]: dots are embedded in a high refractive index material and most of the photons are guided into the semiconductor matrix. This particular problem was one of the focuses in my study (chapter 2). Indistinguishable single photons have also been generated by use of dots embedded in microcavities [42, 43, 44].

Entangled photons could also be produced by self-assembled quantum dots. A first evidence has already been obtained by use of linear optics and of the phenomenon of quantum interference of indistinguishable photons with deterministic single-photon sources [48]. This technique relies on a conversion of a time-bin encoding into a polarization one<sup>4</sup> such as on figure 1.5. Despite the persistent problem of photon extraction, this source could be adequate for a 2-segment quantum key distribution protocol (table 1.6). The experimentally obtained degree of entanglement however does not allow a high key generation rate, because the emitted photon pairs are not highly entangled. Increased polarization entanglement visibility is not out of reach however and solutions will be presented in chapter 4. Chapter 5 will focus on possible experimental implementations of our proposed scheme. Time-bin entangled photons can also be produced. Chapter 3 will present solutions that could lead to the engineering of practical sources of possible use in a 2-segment protocol (table 1.6), or even in a 4-segment protocols.

If dots may be valuable candidates for the engineering of practical sources for QKD, they are however embedded in a solid state matrix and will suffer from decoherence processes. In a first step,

<sup>4</sup>For comparison to other values given in chapter 5, the Bell test they performed gives a value of  $2.38 \pm 0.18$ , which demonstrates entanglement. I will define this Bell test in chapter 5. Such results put strong benchmarks on the quest of quantum dot based polarization entangled photon sources, at least in the prospect of quantum key distribution. Since encoding basis conversion cannot increase the degree of entanglement, the experimental realization of such value is a strong indication of the possibility to obtain not-strongly time-bin entangled photons with quantum dots.

dots can be simply and approximately modelled as artificial solid-state atoms. This approximation is however too strong. These nanostructures range in size up to several million atoms and are buried in a crystalline material. They will likely be subject to many dephasing mechanisms. From this point of view, the Grail consisting in producing entanglement from dots will require a further understanding on the underlying dephasing mechanisms and how they can affect the degree of entanglement of the emitted photon pairs. We will see that the underlying decoherent mechanism which impacts the degree of entanglement is strictly different in the time-bin encoding and the polarization one.

## 1.4 Cavity effects

As we will see in chapters 3 and 4 (respectively for each encoding basis), one possible way to avoid these decoherent effects is to force the dot to emit its photons before the decoherent processes impact the dot. Chapter 4 also demonstrates that this strategy is not sufficient to produce polarization entangled photons, which is the reason of the study presented in chapter 5 about the excitonic splitting (defined in chapter 4). Because this spontaneous emission acceleration is needed for both types of entanglement (time-bin and polarization), I chose to present it here. This will allow us to define some of the characteristics needed in the design of the cavities in which the dots are to be placed. Chapter 2 will be more focused on the design of the cavity in order to reach these cavities' figures of merit.

### 1.4.1 Purcell effect

When embedding a single emitting dipole in an appropriate cavity, it becomes possible to accelerate its spontaneous emission dynamics. This effect is called "Purcell effect" [57]. In order to express the amplitude of this acceleration, I will consider a point-emitting dipole embedded in an unspecified semiconductor cavity. In order to quantify the modification induced by the cavity, I will also consider the "free space" case in which the source is not inside a cavity but in an homogeneous medium, that is, for a quantum dot, in the semiconductor material of refractive index  $n$ .

Our point source emits at a pulsation  $\omega_0$  with a radiative decay in free space  $\Gamma_0$ . It is placed inside a single mode cavity. The cavity mode has a pulsation  $\omega_c$  and a decay rate  $\Gamma_c$  (i.e. a quality factor  $Q = \omega_c/\Gamma_c$ ). In practice, cavities are not monomode. The other cavity modes will be supposed to be sufficiently out of resonance with the dipole, so that they will weakly affect its radiative properties. The source may also emit in any leaky modes, the amplitude of which is non-zero at the dipole's location. Terms underscored with "c" (respectively "0") will refer to the cavity (resp. to the source in free space). The source is coupled to its electromagnetic environment by the Hamiltonian  $\hat{H}_{int} = -\hat{\vec{d}} \cdot \hat{\vec{E}}$  where the operator  $\hat{\vec{d}}$  describes the dipole, and  $\hat{\vec{E}}$  the electric field at the position of the dipole. We consider as the initial state  $|i\rangle$  referring to the configuration in which the mode is empty and the source excited, and as the final state  $|f\rangle$  to the configuration in which the source is in its fundamental state and the photon is emitted into the mode. The coupling coefficient between these two states is  $g = \langle f | \hat{H}_{int} | i \rangle = -\vec{d} \cdot \vec{E}$ , with  $\vec{d}$  being the dipole between the fundamental and excited states of the point source.  $\vec{E}$  is the field amplitude in the usual field quantification scheme. For a free space mode at pulsation  $\omega$  and polarization  $\vec{u}$  ( $|\vec{u}| = 1$ ) that propagates in a material of refractive index  $n$ ,  $\vec{E} = \mathcal{E}\vec{u} = \sqrt{\hbar\omega/2\epsilon_0 n^2 V} \vec{u}$  where  $V$  is the quantification volume. Conversely, for a spatially localized mode inside a cavity where the refractive index is spatially modulated, we define the volume as

$$V_c = \frac{\int_{\text{whole space}} d^3r \epsilon_0 \epsilon_r(\vec{r}) |\vec{E}(\vec{r})|^2}{\max \left[ \epsilon_0 \epsilon_r(\vec{r}) |\vec{E}(\vec{r})|^2 \right]} \quad (1.1)$$

The quantification relation

$$\int_{\text{whole space}} d^3r \epsilon_0 \epsilon(\vec{r}) \left| \vec{E}(\vec{r}) \right|^2 = \frac{1}{2} \hbar \omega_c \quad (1.2)$$

leads to the relation

$$V_c \max \left[ \epsilon_0 \epsilon_r(\vec{r}) \left| \vec{E}(\vec{r}) \right|^2 \right] = \frac{1}{2} \hbar \omega_c \quad (1.3)$$

For the cavities I will consider further, the maximum of the electrical field's energy  $\epsilon_0 \epsilon_r(\vec{r}) \left| \vec{E}(\vec{r}) \right|^2$  is achieved at the maximum of the field's amplitude  $\left| \vec{E}(\vec{r}) \right|$  inside the semiconductor. Thus if we define  $\vec{E} = \mathcal{E}_c u(\vec{r}) \vec{u}$  with  $\vec{u}$  referring to the polarization of the mode and  $u(\vec{r})$  its spatial modulation normalized to a maximal value of 1, the quantified field's amplitude is again  $\mathcal{E}_c = \sqrt{\hbar \omega_c / 2 \epsilon_0 n^2 V_c}$ .

The framework of this study is the so-called weak-coupling regime. The emitted photon is not reabsorbed by the emitting dipole: the characteristic time for the photon to be reabsorbed ( $1/|g|$ ) is much longer than the characteristic time for the photon to escape the cavity ( $1/\Gamma_c$ ). We will also suppose that the coupling between the dipole and cavity mode does not strongly affect the dipole ( $|g| \ll \Gamma_0$ ). In such cases, the system can be treated by means of the perturbation theory with the use of the Fermi's Golden Rule to calculate the new radiative decay rate of the dipole. By separating the cavity's field and the fields of the leaky modes, one obtains:

$$\Gamma = \frac{2\pi}{\hbar^2} \int_{\text{all modes}} d\omega \left| \langle f | \hat{H}_{int} | i \rangle \right|^2 \rho(\omega) \delta(\omega - \omega_0) \quad (1.4)$$

$$= \Gamma_{\text{leaky}} + \frac{2\pi}{\hbar^2} \int_{\text{cavity mode}} d\omega |g|^2 \rho_c(\omega) \delta(\omega - \omega_0) \quad (1.5)$$

with:

- $\rho(\omega)$  spectral density of electromagnetic states,
- $\rho_c(\omega)$  spectral density of the cavity mode,
- $\Gamma_{\text{leaky}}$  radiative decay rate into the leaky modes.

As usually, numbering of the modes in the free space volume  $V$  leads to

$$\rho(\omega) d\omega = \frac{2V n^3 \omega^2 d\omega}{\pi^2 c^3} \quad (1.6)$$

The spectrum of the cavity mode gives the spectral density

$$\rho_c(\omega) d\omega = \frac{\Gamma_c}{2\pi} \frac{d\omega}{(\omega - \omega_c)^2 + (\Gamma_c/2)^2} \quad (1.7)$$

In free space, all the angles of polarization are averaged, whereas in the cavity, we need to introduce the angle  $\theta$  between the dipole  $\vec{d}$  and the mode's field polarization. This finally leads to:

$$\Gamma_0 = \frac{4}{3} \frac{d^2}{4\pi\epsilon_0} \frac{n\omega_0^3}{c^3} \quad (1.8)$$

$$\Gamma = F\Gamma_0 + \Gamma_{\text{leaky}} \quad (1.9)$$

$$F = F_p \frac{1}{1 + 4Q^2 \left( \frac{\lambda_0 - \lambda_c}{\lambda_0} \right)^2} \cos(\theta)^2 |u(r)|^2 \quad (1.10)$$

$$F_p = \frac{3}{4\pi^2} \frac{Q}{V_c / (\lambda_c / n)^3} \quad (1.11)$$

$F$  is the overall enhancement of the spontaneous emission rate due to the presence of the cavity. It is the product of four dimensionless terms:

- the Purcell factor  $F_p$  named after E. M. Purcell who first formulated this effect of lifetime modification by cavity effect [57]. It depends only of the properties of the cavity's mode itself and is the maximal achievable value of spontaneous emission exaltation by use of this cavity.
- the Lorentzian part reflects the resonant character of the Purcell effect : the dot must be spectrally coupled to the cavity mode
- the spatial term  $u(\vec{r})$  describes the impact of the dot location with respect of the cavity field spatial distribution : the dot has to be located on an antinode of the electric field. Oppositely, if it is at a node of the electric field, the emission within the mode will be slowed down. If moreover the cavity does not sustain any leaky modes ( $\Gamma_{\text{leaky}} \sim 0$ ), spontaneous emission can be inhibited.
- the emitting dipole must be collinear to the cavity mode electric field polarization.

During this report I will address, at least theoretically, each of these problems, but for this chapter we will focus on the mode's property, that is, the Purcell factor  $F_p$  and the impact of  $F$  on the collection efficiency. Additional requirements on the cavity designs will be presented in the chapters 3 and 4.

### 1.4.2 Coupling and collection efficiency

The collection efficiency is a crucial characteristic in the systems we want to engineer if we want to develop a source with competing performances compared to laser-based sources. Such requirements are even important for demonstrative experiments because most of the measures involve at least two-photon correlations. The intensity of the photon cross-detection signal is proportional to the efficiency to emit a photon pair and the square of the probability to collect and detect one photon. The detection efficiency is determined by the characteristics of the used photodetector. For a chosen wavelength, the detection efficiency does not depend on the source obviously. Thus in order to compare two different kinds of sources, the parameter of importance is the luminosity of the source [58].

The emission efficiency, (the probability to emit one photon per pulse or excitation cycle) is a characteristic of the emitter, but the collection efficiency  $\eta$  (the probability to collect the emitted photon in the desired direction) depends on the electromagnetic surroundings of the emitter. The luminosity is the product of these two. I will separate the collection efficiency into two contributions: the collection efficiency  $\eta_c$  of the light emitted by the source inside the cavity mode, and the collection efficiency  $\eta_{\text{leak}}$  of the light emitted by the source inside the other leaky modes. The balance of each of these contribution is determined by the coupling coefficient  $\beta$  defined as the probability to emit the photon inside the cavity mode:  $\eta = \beta\eta_c + (1 - \beta)\eta_{\text{leaky}}$ . I will evaluate each term of this expression.

The coupling efficiency  $\beta$  is given by

$$\begin{aligned} \beta &= \frac{\text{Photons emitted in the mode}}{\text{Total of emitted photons}} \\ &= \frac{\int_0^\infty F\Gamma_0(1 - e^{-t/T_1})dt}{\int_0^\infty \Gamma(1 - e^{-t/T_1})dt} \\ &= \frac{F}{F + \gamma} \end{aligned} \tag{1.12}$$

with  $T_1$  being the lifetime of the source in the cavity (including radiative and non-radiative decays). Let  $\gamma = \Gamma_{\text{leaky}}/\Gamma_0$  be the acceleration into the leaky modes. In the theoretical case of a monomode

cavity, there should be no leaky mode ( $\gamma = 0$ ). Usually the cavity mode is not inside a wide complete band gap (i.e. there exist free propagating modes with a non-zero value at the position of the source and at its energy), and for the cavities we will study here,  $\gamma$  stands around 0.8. Therefore the emission into the leaky modes is poorly modified by the presence of the cavity, and the collection efficiency of the leaky modes is of the same order of the collection efficiency in the free space case. This latter can be approximately estimated as following.

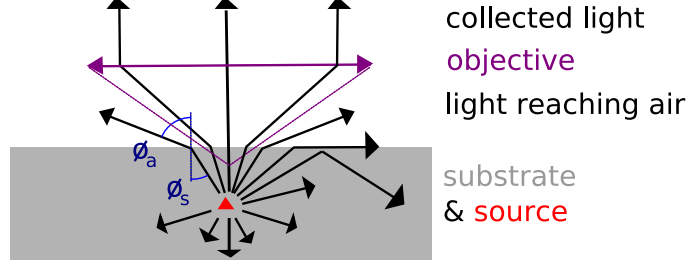


Figure 1.10: Light emitted by a source in a semiconductor substrate: some of it propagates into the air, part of it is then collected through the objective.

The source is placed at a distance  $d$  from the surface of the semiconductor of refractive index  $n$  (figure 1.10) and emits isotropically. Part of the light is collected by the objective with a numerical aperture  $NA$  located above the source. The light emitted in the vertical direction is subject to the Snell's law at the interface semiconductor/air. A ray which impinges the interface at an angle  $\phi_s$  sufficiently small, is partially reflected ( $R = \left(\frac{n-1}{n+1}\right)^2 \sim 0.3$ ) and the remaining ( $1 - R \sim 70\%$ ) is refracted at the angle  $\phi_a$  such as  $n \sin(\phi_s) = \sin(\phi_a)$ . The maximal value of  $\phi_s$  to obtain refraction is  $\sin \phi_s^{\max} = 1/n$ . From all the emitted light within a solid angle  $4\pi$ , only the light in the cone within this angle  $\phi_s^{\max}$  escapes the semiconductor. This corresponds to a solid angle  $2\pi/n$  within the semiconductor. Therefore  $(1 - R) \times (2\pi/n)/(4\pi) = (1 - R)/2n$  of the light emitted by the source reaches the air. This escaping light, after propagating through the interface and being deviated by the refraction, covers a solid angle  $2\pi$ . Part of it is collected by the objective. This corresponds to a solid angle  $2\pi NA$ , thus the proportion of light which is collected of the light which reaches the air is  $(2\pi NA)/(2\pi) = NA$ . The total collected light funnelled into the leaky modes is therefore

$$\eta_{\text{leaky}} = \frac{(1 - R) \times NA}{2n}. \quad (1.13)$$

$$\sim 4\% \text{ with } NA = 0.4 \quad (1.14)$$

Considering the strong assumptions made in this calculation, the effective value is probably smaller. I will retain that the collection efficiency of the light coupled into the leaky modes is a few percent.

When the source is in a cavity, the contribution of the leaky modes to the collected efficiency is negligible as soon as the total efficiency reaches about tenth percents. In this case the collection efficiency is  $\eta = \beta \times \eta_c$ . Independently of the need to accelerate the emission of the dot for producing entangled photons, the need to engineer a luminous source has therefore two consequences:

- the quantum dot must undergo a sufficiently high acceleration effect to couple predominantly to the cavity mode, assuming we have an acceleration into the leaky mode fixed around 0.8. For example, a coupling efficiency of  $\beta = 90\%$  implies a Purcell factor of 8.

- the cavity mode must display an appropriate emission pattern that allows for a good collection efficiency  $\eta_c$  by an objective placed above the cavity. Moreover if we want to couple the source to a monomode telecommunication fiber, the emission pattern must be close to a  $TEM_0$  mode.

Note that for sources based on parametric down conversion, the collection efficiency of each photon is generally limited to 25% [8], except for fibered sources based on four-wave mixing [59]. This gives a value of comparison for the collection efficiency for both entanglement schemes.

### 1.4.3 Impact of light absorption on the cavities optical quality factors

In practice, semiconductor cavities may also present absorption effects : part of the light emitted by the point dipole in the cavity mode may be absorbed by the surrounding material with a rate  $\Gamma_{\text{abs}}$ . I will not focus on the mechanisms of this absorption, nor where this appears spatially. The rate of optical losses from the cavity is still equal to  $\Gamma_c$ . In such case, the quality factor of the cavity may be limited by the absorption. The decay rate of the photonic population in the cavity mode is  $\Gamma_{\text{abs}} + \Gamma_c$ , and the quality factor of the mode is modified as  $Q = \omega_c / (\Gamma_{\text{abs}} + \Gamma_c)$ . Let the intrinsic quality factor of the cavity mode be the quality factor of the mode without absorption  $Q_c = \omega_c / \Gamma_c$  and the absorption factor  $Q_{\text{abs}} = \omega_c / \Gamma_{\text{abs}}$  (A high absorption factor means a small absorption).  $Q_c$  is also called the cold cavity quality factor. We have [60]

$$\frac{1}{Q} = \frac{1}{Q_c} + \frac{1}{Q_{\text{abs}}} \quad (1.15)$$

For small intrinsic quality factors, the absorption is negligible; but for higher intrinsic values  $Q_c$ , the effective quality factor is limited by the absorption effect. In this last picture most of the light is absorbed by the material. Indeed the proportion of outgoing light is

$$\begin{aligned} \eta_{\text{out}} &= \int_0^{\infty} \Gamma_c (1 - e^{-(\Gamma_{\text{abs}} + \Gamma_c)t}) dt \\ &= \frac{\Gamma_c}{\Gamma_{\text{abs}} + \Gamma_c} \\ &= \frac{Q_{\text{abs}}}{Q_c + Q_{\text{abs}}} \end{aligned} \quad (1.16)$$

For a fixed absorption factor, a high intrinsic quality factor will reduce the quantities of outgoing light compared to a situation with a lower quality factor, because part of the light trapped inside the cavity will be absorbed. Moreover in the Purcell factor picture the quality factor characterizes the spectral spreading of the mode around the source linewidth. Therefore we must use in the expression of the Purcell factor, the final quality factor  $Q$  and not the intrinsic one. It is counterproductive to look for quality factors higher than the absorption factor: it does not increase the emission acceleration of the source and it decreases by a factor  $\eta_{\text{out}}$  the collection efficiency.

The reasons for the presence of a strong absorption in the photonic crystals made of GaAs around  $950\text{nm}$ , even at 4 Kelvin, are not clear still today. It cannot be explained by the intrinsic absorption of the GaAs itself. It has been suspected to come from absorption mechanisms into the wetting layer or the quantum dots. High quality factors and low absorption losses have been already obtained on cavities, the resonance of which is around  $1.3$  to  $1.5 \mu\text{m}$  in passive cavities (without emitting material inside such as quantum wells or quantum dots) [61, 62]. For now on, we will remember that it is unproductive to look for intrinsic quality factors higher than a few  $\sim 10000$ 's, which is about the highest values observed on GaAs around  $950\text{nm}$  at LPN. Higher values will only lead to sources with poorer characteristics, in terms of collection efficiency without any increase of the Purcell factor.

#### 1.4.4 Overview on different semiconductor cavities

Since the Purcell factor is proportional to the ratio  $Q/V_c$ , we have to design cavities with reasonable quality factors (no more than 10000) and a very small mode volume (about  $\lambda^3$ ). In the following, I will express the mode volume in  $(\lambda_c/n)^3$  units as it appears in the expression of  $F_p$ . For example a Purcell factor of 30 with an ultimate mode volume of 1 requires a quality factor of 500. In order to anticipate the spectral, polarization orientation and spatial mismatch of the dot, and any technological limitations, a higher quality factor must however be aimed at. Considering also the limitations due to the absorption, Purcell factors of more than 30 on 4K-GaAs at 900nm are mandatory. Different geometries can be used to process semiconductor cavities, the dimensions of which are of the order of the optical wavelength (named microcavities).

A semiconductor is a high refractive index material, which allows the efficient use of the total refraction effect to confine light (figure 1.11), provided the mode propagates inside the cavity so that it impinges the interfaces semiconductor/air at large angles with respect to normal incidence. The minimal angle of incidence to achieve total internal reflection at the interface between GaAs and air is  $16^\circ$ . Another strategy to confine light exploits the destructive interference between optical waves impinging on a medium with a periodically modulated index of refraction, so-called photonic crystals: for waves at a wavelength close to the period of modulation, the scattering of light on the photonic crystal combines with destructive interference. This interference cancels out light of certain wavelengths and the photonic crystal acts as a high-quality reflector: like the electronic band gap in semiconductors, such periodic structures exhibit a certain frequency range where light cannot propagate through the structure. This frequency range is known as the photonic band gap. Photonic crystals can be divided into three categories, namely one-dimensional (1D), two-dimensional (2D) and three-dimensional (3D) crystals according to the dimension of the periodicity. A not very new one-dimensional photonic crystal is the Bragg mirror composed of multiple layers of dielectric films. 2D and 3D photonic crystals employ the Bragg reflection in more than one spatial direction.

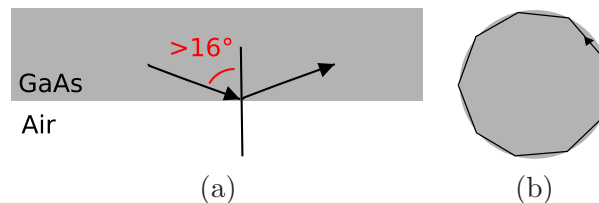


Figure 1.11: a: Intern total reflection of light on the interface semiconductor/air. b: A gallery mode where confinement of light is obtained by intern total reflection only.

One can use total internal reflection to make three-dimensionally confined resonators. This is achieved with the “whispering-gallery” resonators. They are essentially microdisks [63, 64] (figure 1.12), microtoroids [65] or microspheres [66, 67] in which the light circulates around close to the dielectric interface. The curvature at the interface is sufficiently small for the light to impinge on the border at angles higher than the total internal reflection angle with respect to normal incidence. The losses are usually due to surface roughness [68]. The emission is not directive but mostly in all directions in the plane of the mode, usually parallel to the substrate. Thanks to the substrate, part of this emission is redirected upward, but it remains a small part of the whole emitted light. This kind of cavity is thus not fitted for an upward light collection. It remains possible to create a local defect in order to create a dominant leaking way, and collect in this direction [69]. Another possibility, mostly used, is to approach a tapered optical fiber; if the evanescent coupling between the resonator and the fiber is sufficiently strong, this will be the dominant way of losses from the cavity [70]. These cavities made of III-V semiconductors have usually a mode volume of about 6 and a quality factor of the order

of 12000<sup>5</sup> leading to record Purcell factors above 150. However, the mode is spatially confined close to the semiconductor-air interface and dots on the field antinode may be affected by defects induced along this interface. These structures may however be a good candidate for the time-bin entanglement scheme, if used with a fiber to collect the light, and with a vertically incident laser to pump the dot as requested. I did not work on this possibility.

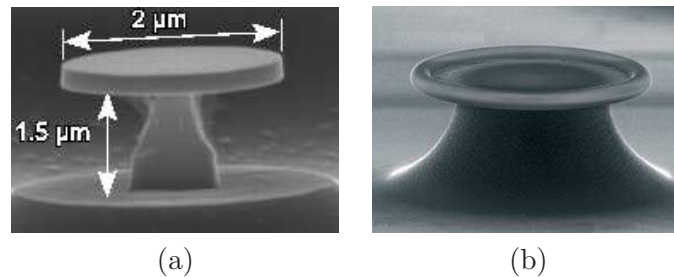


Figure 1.12: Electronic microscope images of two designs to confine light by internal total reflection only: (a) a microdisk [63] and (b) a microtor [71]

Another strategy to confine light in the three directions of space would be to isolate a point defect, such as one or more missing periods, into a three-dimensional photonic crystal [72, 73]. However, it is far from trivial to reach a full photonic band gap in the near-infrared and visible spectral range. The three-dimensional photonic crystals actually produced suffer from these disorders, that result in a strong degradation of the quality of the stop band (both its width and its rejecting power) [74]. The technology for these kind of three dimensional photonic crystal cavities still has to progress to be of interest for the current topic, even if very recently 3D photonic crystal cavities have been obtained [75].

In view of the difficulties in fabricating such deterministic photonic defects into 3D photonic crystal structures, a lot of efforts have been devoted to less demanding structures involving a hybrid confinement: In this context, light confinement combines total internal reflection in one or two spatial directions and interference effects in the other directions of space. Such cavities are more sensitive to fabrication than three-dimensional photonic crystals resonators, but retain or approximate many of the latter's desirable properties, such as 3D confinement of light.

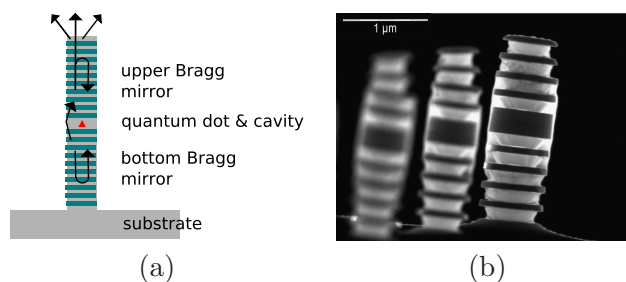


Figure 1.13: a: Schematic of a micropillar. b: Electronic microscope image of a micropillar produced at the LPN.

One example is the micropillar cavity [37, 76, 42] (figure 1.13). The transverse mode confinement results from total internal reflection at the semiconductor/air interface, while confinement in the vertical direction is provided by Bragg reflections. Thanks to the high quality factors obtained in

<sup>5</sup>at  $1\ \mu\text{m}$  [64], greater at higher wavelengths [70].

pillars with a diameter about the wavelength, experimental Purcell factors of about 5 are currently observed in those structures, but it is insufficient for our needs. This technology has been developed at LPN by S. Varoutsis [77] during his PhD, and it is still currently used.

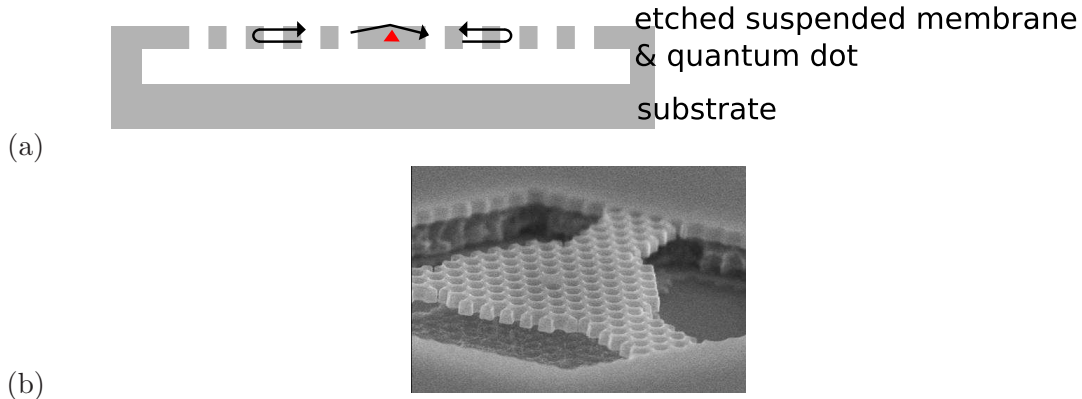


Figure 1.14: a: Schematic of a 2D photonic crystal slab cavity. b: Electronic microscope image of a 2D photonic crystal slab cavity.

Another example is the 2D photonic crystal cavity in a slab waveguide, consisting of a 2D array of holes perforated through a thin membrane. In these cavities, the photonic-band gap effect is used for strong light confinement in the transverse directions, and total internal reflection at the air-slab interface insures light confinement in the longitudinal direction. This is the geometry retained in our group. In these structures, the cavity is formed by the introduction of a point defect in the 2D photonic crystal. The simplest cavity geometry consists in removing a finite number of holes in a perfect array of holes. For instance, the  $L_n$  cavities are formed by a line of  $n$  missing holes in a triangular array of holes. These microcavities are highly valuable candidates for achieving high quality factors with wavelength-sized modal volumes, by finely tuning the holes position and/or radius at the cavity termination. For instance,  $Q$  factors of 45000 with ultra small volumes close to  $(\lambda/n)^3$  have been measured in a  $L3$  microcavity etched in a Si membrane, by slightly shifting the position of the holes surrounding the defect region [78]. The technological developments needed to produce these resonators, are the main PhD results of S. Laurent [79] and R. Braive [80]. The technological process will be exposed in summary form in the next chapter. For a quite recent and good review on various possibilities to form photonic crystal cavities, please refer to [81].

## 1.5 Conclusion

Entangled photons are attractive carriers of Quantum Information. Once produced, they can be reliably manipulated and can travel long distances unaffected. They are the main components of quantum communication protocols, and it is likely that they will even play a major role in the development of quantum computers.

However, because of some intrinsic limitations of existing single and entangled photon sources, extensive work is currently aiming at generating bright and deterministic entangled photons sources. Among all possible candidates in this field, quantum dots may be attractive. They can produce deterministically single photons or photons pairs. And they can be easily embedded in optical microcavities. The use of cavity effects and more particularly the Purcell effect, allows tailoring the emission of the dots, in particular to fully control the single photon pulse temporal amplitude and propagation direction. Indeed, placing a quantum dot in a micro-cavity has two effects: it changes the

light emission pattern and affects the exciton radiative decay rate. By redirecting the light emission, it can help improving the light collection efficiency which is the major source of photon loss in current systems. Also, it can reduce the photon temporal width, lowering the impact of potential exciton state dephasing on the quantum indistinguishability of photons. Another practical effect of small cavities is to isolate a few quantum dots so they can be dealt with individually.

Different cavity designs can be used in semiconductor physics: microdisks, micropillars and photonic crystal slab cavities for instance. Besides the capability of offering high quality factor and ultra small modal volume, the inherent flexibility and diversity in cavity design makes photonic crystal nanocavities a very promising device for tailoring of cavity-mode wavelength, polarization, and directionality through fine adjustments in lattice structures. However, due to the large variety of possible designs in such resonators, it is necessary to investigate theoretically the underlying physics of the spatial and modal redistribution of light in these resonators, in order to obtain an appropriate design for the desired functionalities. This investigation will be described in the next chapter, more particularly on the issue of photon collection efficiency.

## Bibliography

- [1] Announcement of rsa-640 factorisation. <http://www.rsa.com/rsalabs/node.asp?id=2964>.
- [2] P. W. Shor. Polynomial-time algorithms for prime factorization and discrete logarithms on a quantum computer. *IEEE International conference on Computers, Systems, and Signal Processing*, 124, 1994.
- [3] X. Peng, Z. Liao, N. Xu, G. Qin, X. Zhou, D. Suter, and J. Du. Quantum adiabatic algorithm for factorization and its experimental implementation. *Phys. Rev. Lett.*, 101:220405, 2008.
- [4] N. Gisin, G. Ribordy, W. Tittel, and H. Zbinden. Quantum cryptography. *Rev. Mod. Phys.*, 74:145, 2002.
- [5] V. Scarani, H. Bechmann-Pasquinucci, N. J. Cerf, M. Dusek, N. Lutkenhaus, and M. Peev. A framework for practical quantum cryptography. *Arxiv*, page 0802.4155, 2008.
- [6] C. H. Bennett and G. Brassard. Quantum cryptography: Public key distribution and coin tossing. *Proc IEEE Int. Conf. on Computers, Systems and Signal Processing*, page 175, 1984.
- [7] G. Ribordy, J.-D. Gautier, N. Gisin, O. Guinnard, and H. Zbinden. Fast and user-friendly quantum key distribution. *Journ. Mod. Opt.*, 47:517, 2000.
- [8] M. Halder, A. Beveratos, N. Gisin, V. Scarani, C. Simon, and H. Zbinden. Entangling independent photons by time measurement. *Nat. Phys.*, 3:692, 2007.
- [9] F. Grosshans, G. Van Assche, J. Wenger, R. Brouri, N.J. Cerf, and P. Grangier. Quantum key distribution using gaussian-modulated coherent states. *Nature*, 421:238, 2003.
- [10] S. Lorenz, N. Korolkova, and G. Leuchs. Continuous-variable quantum key distribution using polarization encoding and post selection. *Appl. Phys. B*, 79:273, 2004.
- [11] G. B. Xavier, N. Walenta, G. Vilela de Faria, G. P. Temporao, N. Gisin, H. Zbinden, and J. P. von der Weid. Experimental polarization encoded quantum key distribution over optical fibres with real-time continuous birefringence compensation. *New. J. Phys.*, 11:045015, 2009.
- [12] A. Ekert. Quantum cryptography based on bell's theorem. *Phys. Rev. Lett.*, 67:661, 1991.

- [13] W. K. Wootters and W. H. Zurek. A single quantum cannot be cloned. *Nature*, 299:802, 1982.
- [14] J. F. Clauser. Experimental distinction between the quantum and classical field-theoretic predictions for the photoelectric effect. *Phys. Rev. D*, 9:853, 1974.
- [15] A. Poppe, M. Peev, and O. Maurhart. Outline of the secoqc quantum key distribution network in vienna. *International Journal of Quantum Information*, 6:209, 2008.
- [16] M. Stipcevic and B. M. Rogina. Quantum random number generator based on photonic emission in semiconductors. *Rev. Sci. Instrum.*, 78:045104, 2007.
- [17] T Jennewein, C Simon, G Weihs, H Weinfurter, and A Zeilinger. Quantum cryptography with entangled photons. *Phys. Rev. Lett.*, 84:4729, 2000.
- [18] D. Collins, N. Gisin, and H. de Riedmatten. Quantum relays for long distance quantum cryptography. *J. Mod. Opt.*, 52:735, 2005.
- [19] H.-J. Briegel, W. Dur, J. I. Cirac, and P. Zoller. Quantum repeaters: The role of imperfect local operations in quantum communication. *Phys. Rev. Lett.*, 81:5932, 1998.
- [20] H. de Riedmatten, I. Marcikic, W. Tittel, H. Zbinden, D. Collins, and N. Gisin. Long distance quantum teleportation in a quantum relay configuration. *Phys. Rev. Lett.*, 92:047904, 2004.
- [21] A. Aspect, P. Grangier, and G. Roger. Experimental realization of einstein-podolsky-rosen-bohm gedankenexperiment: A new violation of bell's inequalities. *Phys. Rev. Lett.*, 49:91, 1982.
- [22] W. Tittel, J. Brendel, H. Zbinden, and N. Gisin. Violation of bell inequalities by photons more than 10 km apart. *Phys. Rev. Lett.*, 81:3563, 1998.
- [23] P. G. Kwiat, K. Mattle, H. Weinfurter, A. Zeilinger, A. V. Sergienko, and Y. Shih. New high-intensity source of polarization-entangled photon pairs. *Phys. Rev. Lett.*, 75:4337, 1995.
- [24] S. Tanzilli, W. Tittel, H. de Riedmatten, H. Zbinden, P. Baldi, M.P. De Micheli, D.B. Ostrowsky, and N. Gisin. Ppln waveguide for quantum communication. *Eur. Phys. Journ. D*, 18:155, 2002.
- [25] H De Riedmatten, V. Scarani, I Marcikic, A. Acino, W. Tittel, H. Zbinden, and N. Gisin. Two independent photon pairs versus four-photon entangled states in parametric down conversion. *Journ. Mod. Opt.*, 51:1637, 2004.
- [26] V. Scarani, H. de Riedmatten, I. Marcikic, H. Zbinden, and N. Gisin. Four-photon correction in two-photon bell experiments. *Eur. Phys. Journ. D*, 32:129, 2005.
- [27] S. Fasel, N. Gisina, G. Ribordy, and H. Zbinden. Quantum key distribution over 30 km of standard fiber using energy-time entangled photon pairs: a comparison of two chromatic dispersion reduction methods. *Eur. Phys. Journ. D*, 30:143, 2004.
- [28] D. Stucki, N. Walenta, F. Vannel, R. T. Thew, N. Gisin, H. Zbinden, S. Gray, C. R. Towery, and S. Ten. High rate, long-distance quantum key distribution over 250 km of ultra low loss fibres. *New. J. Phys.*, 11:075003, 2009.
- [29] C. H. Bennett, F. Bessette, G. Brassard, L. Salvail, and J. Smolin. Experimental quantum cryptography. *Journal of Cryptology*, 5:3, 1992.
- [30] H. J. Kimble, M. Dagenais, and L. Mandel. Photon antibunching in resonance fluorescence. *Phys. Rev. Lett.*, 39:691, 1977.

- [31] F. Treussart, A. Clouqueur, C. Grossman, and J.F. Roch. Photon antibunching in the fluorescence of a single dye molecule embedded in a thin polymer film. *Opt. Lett.*, 26:1504, 2001.
- [32] B. Lounis and W.E. Moerner. Single photons on demand from a single molecule at room temperature. *Nature*, 407:491, 2000.
- [33] A. Beveratos. *Réalisation expérimentale d'une source de photons uniques par fluorescence de centres colorés dans le diamant : application à la cryptographie quantique*. PhD thesis, 2002.
- [34] A. Beveratos, R. Brouri, T. Gacoin, A. Villing, J.-P. Poizat, and P. Grangier. Single photon quantum cryptography. *Phys. Rev. Lett.*, 89:187901, 2002.
- [35] R. Alleaume, F. Treussart, G. Messin, Y. Dumeige, J.-F. Roch, A. Beveratos, R. Brouri-Tualle, J.-P. Poizat, and P. Grangier. Experimental open-air quantum key distribution with a single-photon source. *New. J. Phys.*, 6:92, 2004.
- [36] S. Fasel, O. Alibart, A. Beveratos, S. Tanzilli, H. Zbinden, P. Baldi, and N. Gisin. High quality asynchronous heralded single photon source at telecom wavelength. *New. J. Phys.*, 6:163, 2004.
- [37] J. M. Gerard, B. Sermage, B. Gayral, B. Legrand, E. Costard, and V. Thierry-Mieg. Enhanced spontaneous emission by quantum boxes in a monolithic optical microcavity. *Phys. Rev. Lett.*, 81:1110, 1998.
- [38] C. Becher, A. Kiraz, P. Michler, A. Imamoglu, W. V. Schoenfeld, P. M. Petroff, Lidong Zhang, and E. Hu. Nonclassical radiation from a single self-assembled inas quantum dot. *Phys. Rev. B*, 63:121312(R), 2001.
- [39] C. Santori, D. Fattal, M. Pelton, G. S. Solomon, and Y. Yamamoto. Polarization-correlated photon pairs from a single quantum dot. *Phys. Rev. B*, 66:045308, 2002.
- [40] R. M. Thompson, R. M. Stevenson, A. J. Shields, I. Farrer, C. J. Lobo, D. A. Ritchie, M. L. Leadbeater, and M. Pepper. Single-photon emission from exciton complexes in individual quantum dots. *Phys. Rev. B*, 64:201302(R), 2001.
- [41] D. C. Unitt, A. J. Bennett, P. Atkinson, D. A. Ritchie, and A. J. Shields. Polarization control of quantum dot single-photon sources via a dipole-dependent purcell effect. *Phys. Rev. B*, 72:033318, 2005.
- [42] S. Varoutsis, S. Laurent, P. Kramper, A. Lemaitre, I. Sagnes, I. Robert-Philip, and I. Abram. Restoration of photon indistinguishability in the emission of a semiconductor quantum dot. *Phys. Rev. B*, 72:041303(R), 2005.
- [43] S. Laurent, S. Varoutsis, L. Le Gratiet, A. Lemaitre, I. Sagnes, F. Raineri, A. Levenson, I. Robert-Philip, and I. Abram. Indistinguishable single photons from a single-quantum dot in a two-dimensional photonic crystal cavity. *Appl. Phys. Lett.*, 87:163107, 2005.
- [44] C. Santori, D. Fattal, J. Vuckovic, G.S. Solomon, and Y. Yamamoto. Indistinguishable photons from a single-photon device. *Nature*, 419:594, 2002.
- [45] O. Benson, C. Santori, M. Pelton, and Y. Yamamoto. Regulated and entangled photons from a single quantum dot. *Phys. Rev. Lett.*, 84:2513, 2000.
- [46] E. Moreau, I. Robert, L. Manin, V. Thierry-Mieg, J. M. Gérard, and I. Abram. Quantum cascade of photons in semiconductor quantum dots. *Phys. Rev. Lett.*, 87:183601, 2001.

- [47] N. Akopian, N. H. Lindner, E. Poem, Y. Berlatzky, J. Avron, D. Gershoni, D. Gerardot, and P. M. Petroff. Entangled photon pairs from semiconductor quantum dots. *Phys. Rev. Lett.*, 96:130501, 2006.
- [48] D. Fattal, K. Inoue, J. Vuckovic, C. Santori, G. S. Solomon, and Y. Yamamoto. Entanglement formation and violation of bell's inequality with a semiconductor single photon source. *Phys. Rev. Lett.*, 92:037903, 2004.
- [49] A. J. Hudson, R. M. Stevenson, A. J. Bennett, R. J. Young, C. A. Nicoll, P. Atkinson, K. Cooper, D. A. Ritchie, and A. J. Shields. Coherence of an entangled exciton-photon state. *Phys. Rev. Lett.*, 99:266802, 2007.
- [50] R. J. Young, R. M. Stevenson, A. J. Hudson, C. A. Nicoll, D. A. Ritchie, and A. J. Shields. Bell-inequality violation with a triggered photon-pair source. *Phys. Rev. Lett.*, 102:030406, 2009.
- [51] R. M. Stevenson, R. M. Thompson, A. J. Shields, I. Farrer, B. E. Kardyna, D. A. Ritchie, and M. Pepper. Quantum dots as a photon source for passive quantum key encoding. *Phys. Rev. B*, 66:081302(R), 2002.
- [52] R.J. Young, R. M. Stevenson, P. Atkinson, K. Cooper, D. A Ritchie, and A. J. Shields. Improved fidelity of triggered entangled photons from single quantum dots. *New. J. Phys.*, 8:29, 2006.
- [53] S. M. Ulrich, M. Benyoucef, P. Michler, N. Baer, P. Gartner, F. Jahnke, M. Schwab, H. Kurtze, M. Bayer, S. Fafard, Z. Wasilewski, and A. Forchel. Correlated photon-pair emission from a charged single quantum dot. *Phys. Rev. B*, 71:235328, 2005.
- [54] R. Hafenbrak, S. M. Ulrich, P. Michler, L. Wang, A. Rastelli, and O. G. Schmidt. Triggered polarization-entangled photon pairs from a single quantum dot up to 30k. *New. J. Phys.*, 8:315, 2007.
- [55] R. Hostein, A. Michon, G. Beaudoin, N. Gogneau, G. Patriache, J.-Y. Marzin, I. Robert-Philip, I. Sagnes, and A. Beveratos. Time-resolved characterization of inasp/inp quantum dots emitting in the c-band telecommunication window. *Appl. Phys. Lett.*, 93:073106, 2008.
- [56] X. M. Dou, X. Y. Chang, B. Q. Sun, Y. H. Xiong, Z. C. Niu, S. S. Huang, H. Q. Ni, Y. Du, and J. B. Xia. Single-photon-emitting diode at liquid nitrogen temperature. *Appl. Phys. Lett.*, 93:101107, 2008.
- [57] E. Purcell. Resonance absorption by nuclear magnetic moments in a solid. *Phys. Rev.*, 69:37, 1946.
- [58] M. Halder, A. Beveratos, R. T. Thew, C. Jorel, H. Zbinden, and N. Gisin. High coherence photon pair source for quantum communication. *New J. Phys.*, **10:023027, 2008.**
- [59] **J. Fulconis, O. Alibart, J. L. O'Brien, W. J. Wadsworth, and J. G. Rarity. Nonclassical interference and entanglement generation using a photonic crystal fiber pair photon source. *Phys. Rev. Lett.*, 99:120501, 2007.**
- [60] C. Kreuzer, J. Riedrich-Möller, E. Neu, and C. Becher. Design of photonic crystal microcavities in diamond films. *Opt. Expr.*, 16:1632, 2008.
- [61] R. Herrmann, T. Sunner, T. Hein, A. Löffler, M. Kamp, and A. Forchel. Ultrahigh-quality photonic crystal cavity in gaas. *Opt. Lett.*, 31:1229, 2006.

- [62] E. Weidner, S. Combrie, N.-V.-Q. Tran, A. De Rossi, J. Nagle, S. Cassette, A. Talneau, and H. Benisty. Achievement of ultrahigh quality factors in gas photonic crystal membrane nanocavity. *Appl. Phys. Lett.*, 89:221104, 2006.
- [63] E. Petter. *Couplage fort exciton-photon pour une boite quantique de GaAs en microdisque*. PhD thesis, 2006.
- [64] B. Gayral, J.-M. Gerard, A. Lemaitre, C. Dupuis, L. Manin, and et J.-L. Pelouard. High-q wet-etched gas microdisks containing inas quantum boxes. *Appl. Phys. Lett.*, 75:1908, 1999.
- [65] D. K. Armani, T. J. Kippenberg, S. M. Spillane, and K. J. Vahala. Ultra-high-q toroid microcavity on a chip. *Nature*, 421:925, 2003.
- [66] Y.-S. Park, A. K. Cook, and H. Wang. Cavity qed with diamond nanocrystals and silica microspheres. *Arxiv*, page 0608493, 2006.
- [67] I.H. Agha, J.E. Sharping, M.A. Foster, and A.L. Gaeta. Optimal sizes of silica microspheres for linear and nonlinear optical interactions. *Appl. Phys. B: Laser and Optics*, 43:2, 2006.
- [68] M. Borselli, K. Srinivasan, P. E. Barclay, and O. Painter. Rayleigh scattering, mode coupling, and optical loss in silicon microdisks. *Appl. Phys. Lett.*, 85:3693, 2004.
- [69] V. M. Apalkov and M. E. Raikh. Directional emission from a microdisk resonator with a linear defect. *Phys. Rev. B*, 70:195317, 2004.
- [70] K. Srinivasan, M. Borselli, T. J. Johnson, P. E. Barclay, O. Painter, A. Stintz, and S. Krishna. Optical loss and lasing characteristics of high-quality-factor algaas microdisk resonators with embedded quantum dots. *Appl. Phys. Lett.*, 86:151106, 2005.
- [71] Results worthy of notes, about microtores at the cea. <http://www-dsm.cea.fr/fr/Vie-scientifique/Faits-marquants-DSM/24-decembre-2008>.
- [72] M. Qi, E. Lidorikis, P. T. Rakich, S. G. Johnson, J. D. Joannopoulos, Erich P. Ippen, and Henry I. Smith. A three-dimensional optical photonic crystal with designed point defects. *Nature*, 429:535, 2004.
- [73] P. Lodahl, A. Floris van Driel, I. S. Nikolaev, A. Irman, K. Overgaag, D. Vanmaekelbergh, and W. L. Vos. Controlling the dynamics of spontaneous emission from quantum dots by photonic crystals. *Nature*, 430:654, 2004.
- [74] S. Matthias, R. Hillebrand, F. Muller, and U. Gosele. Macroporous silicon: Homogeneity investigations and fabrication tolerances of a simple cubic three-dimensional photonic crystal. *Journ. Appl. Phys.*, 99:113102, 2006.
- [75] A. Tandaechanurat, S. Ishida, K. Aoki, D. Guimard, M. Nomura, S. Iwamoto, and Y. Arakawa. Demonstration of high-q ( $\approx 8600$ ) three-dimensional photonic crystal nanocavity embedding quantum dots. *Appl. Phys. Lett.*, 94:171115, 2009.
- [76] S. Reitzenstein, C. Hofmann, A. Gorbunov, M. Strauss, S. H. Kwon, C. Schneider, A. Löffler, S. Höfling, M. Kamp, and A. Forchel. Alas/gaas micropillar cavities with quality factors exceeding 150.000. *Appl. Phys. Lett.*, 90:251109, 2007.

- [77] S. Varoutsis. *Génération de photons uniques indiscernables par une boîte quantique semi-conductrice dans une microcavité optique*. PhD thesis, 2005.
- [78] Y. Akahane, T. Asano, B.-S. Song, and S. Noda. High-q photonic nanocavity in a two-dimensional photonic crystal. *Nature*, 25:944, 2003.
- [79] S. Laurent. *Cavités à bande interdite photonique bidimensionnelle et application à une source de photons uniques indiscernables*. PhD thesis, 2006.
- [80] R. Braive. *Contrôle de l'émission spontanée dans les cristaux photoniques*. PhD thesis, 2008.
- [81] S. Noda, M. Fujita, and T. Asano. Spontaneous-emission control by photonic crystals and nanocavities. *Nat. Phot.*, 1:449, 2007.

## Chapter 2

# Design of bi-dimensional photonic crystal cavities

One-dimensional photonic crystals of periodic multi-electric stacks, known as Bragg mirrors, have been first studied by Lord Rayleigh in 1887. In such devices each material interface reflects a small part of the incoming light (at an angle normal to the surface). When the periodicity of these interfaces corresponds to one half of the wavelength, those reflected beams interfere constructively, and with a sufficient number of layers all the light can be reflected over some bandwidth. But the concept of photonic crystals and the associated concept of photonic band gap only appeared in 1987 in two articles published independently by E. Yablanovitch [1] and S. John [2]. Since this date, the interest for these types of structures, and the panel of domains for which they are studied, has never ceased to grow. I do not intend to make here a global review of these domains, nor of how each of them is studied, but to focus on the one of interest here: suspended bi-dimensional photonic crystal cavities.

The major goal of this chapter is to propose appropriate designs of cavities, in order to build deterministic sources for quantum cryptography, by coupling a single quantum dot to the optical mode of such resonators. The subsequent acceleration of the exciton lifetime, will then allow us to restore entanglement between single photons emerging from the dot, as we shall see in chapters 3 and 4. The cavity should also allow an increase in the collection efficiency of the generated quantum states of light.

In this chapter, we will first introduce the mechanisms allowing a three-dimensional confinement of light in photonic-crystal slabs. The chapter will continue with a short presentation of the fabrication procedure to etch such resonators. In order to find the appropriate design of the cavity, the Finite-Difference Time-Domain (FDTD) computational electrodynamics modelling technique is used. Modelling correctly photonic crystal structures and understanding the optical underlying optical phenomena is a quite delicate problem and is even a research field by itself [3]. If various simulation tools have been developed, I will limit myself however to present them from a user point of view. This chapter continues with an analysis of the different cavity properties we have simulated (field distribution, quality factor, Purcell factor, radiation diagram...). Comparisons with experimental results on processed cavities are then presented, first with respect to the wavelength resonance, quality factor, and finally radiation pattern of the cavity's modes.

## 2.1 Confinement in 2D photonic crystals slab cavities

### 2.1.1 Hybrid confinement : photonic-crystal effects and index guiding

Photonic crystals are periodically structured electromagnetic media, generally possessing photonic band gaps which are frequency ranges in which light cannot propagate through the structure. This periodicity is the electromagnetic analogue of a crystalline atomic lattice, where the latter acts on the electron's wave function to produce the familiar band gaps of solid-state physics. Indeed, even if the basic laws are not the same (Maxwell's laws for the light and equation of movement for an electron inside a potential), the introduction of periodicity within the system (resp. the refractive index and the potential created by the crystal) leads to permitted and forbidden bands of propagation (resp. of the light or of the electrons and holes) [4].

Let us first consider a two dimensional problem, and forget the third dimension of space. We will consider a 2D photonic crystal composed of holes etched in a high refractive index material. The key to understanding photonic crystals in two dimensions is to realize that the fields in 2D can be divided into two polarizations by symmetry: TM (transverse magnetic), in which the magnetic field is in the photonic crystal plane and the electric field is parallel to the holes axis; and TE (transverse electric), in which the electric field is in the photonic crystal plane and the magnetic field is perpendicular. The band gap of 2D photonic crystals consisting of holes etched in a high refractive index material is usually not complete, and appears only for transverse electric (TE) modes. This absence of TM gap implies strong technological constraints, since any deviation in the holes verticality (with a slight tilt or conical shape) will introduce a coupling between TE and TM modes and thus degrade the confinement. Considering the quite good verticality of the holes flanks obtained with the process available at LPN [5], we will consider that these two polarization modes are not mixed. For all the simulations, the holes are supposed to be perfectly vertical and to display a cylindrical shape of radius  $r$  without any kind of position disorder <sup>6</sup>. I will also only consider crystals made of triangular lattice of holes and not square lattice <sup>7</sup>. Since the band gap is wider in the first case and leads to more numerous possibilities to get a complete cavity effect with better confinement, it has been more extensively studied by the community and is more suited to my problem.

Typical band diagrams of such 2D photonic crystal are shown in Fig. 2.2. As for electron standing waves in a crystal, the band diagram represents the allowed frequencies (bands) and forbidden frequencies (band gaps) for an optical standing wave propagating in the periodic medium. It allows the survey of all the dispersion characteristics  $\omega(k)$  of the photonic crystal. Because of the symmetries of the crystal, one can as in solid-state physics restrict the calculation of  $\omega(k)$  to  $k$ 's contained in a limited region of the reciprocal space referred to as the irreducible Brillouin zone. The direct and reciprocal lattice along with the irreducible Brillouin zone are shown on Figure 2.1 and the photon energy band structure for a triangular lattice photonic crystal is shown in Fig. 2.2 left, where the unit cell of the lattice is shown in the inset, and the naming of the high symmetry points follows the terminology of semiconductor physics. It can be seen that the reciprocal lattice is also triangular, but rotated relative to the original lattice by  $30^\circ$ . It also reveals the presence of a robust and large (resp. small) photonic band gap for the TE (resp. TM modes).

The photonic crystal slab is a 2D photonic crystals etched on high refractive index suspended material. In such suspended bi-dimensional photonic crystals, since the structure is neither periodic nor infinite in the third dimension, photons incident to the semiconductor/air interface between the

<sup>6</sup>A design made of lattices of holes with a cylindrical shape is obviously not the only possibility. Cylindrical shapes have the advantage to be quite simple to produce. For example, it would be technologically difficult to obtain sharp edges and etch squared holes. Moreover use of other shapes may not be worthwhile compared the cylindrical one, see for example [6].

<sup>7</sup>Triangular and square lattices are not also the sole possible arrangement of holes. See for example [7] for other lattices study.

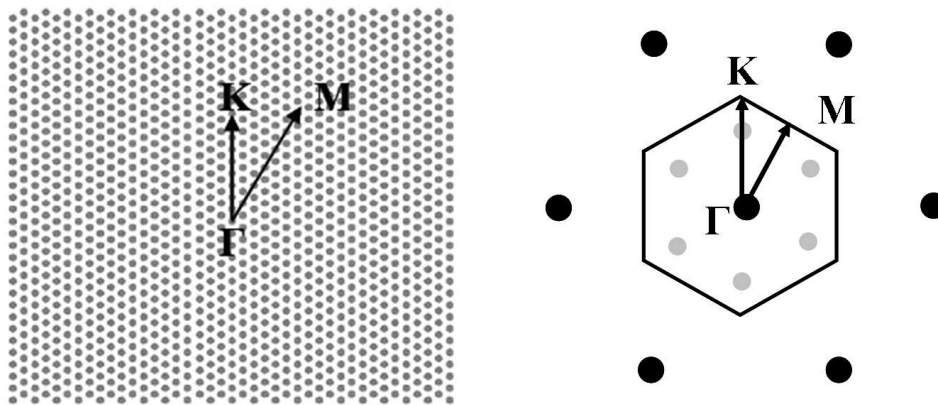


Figure 2.1: Left: direct space with the directions  $\Gamma - M$  and  $\Gamma - K$ . Right: reciprocal space and Brillouin zone with the directions  $\Gamma - M$  and  $\Gamma - K$ . Gray points correspond to air holes.

semiconductor slab and air under angles smaller than the total internal reflection critical angle can escape from the structure and couple to the continuum radiation modes. To take into account these radiation losses in the analysis of planar photonic crystal slabs we use the notion of the light line (light cone). This is indicated by the solid red line in Fig. 2.2 right. The region above the light line corresponds to the leaky modes, which are not confined in the membrane by refractive index guiding effects. The modes below the light line can be guided in the slab and are called guided modes. This confinement is analogous to total internal reflection, and is due to the guided modes seeing a higher effective index in the slab compared to its surroundings.

### 2.1.2 Cavity designs

A very promising application of photonic crystals is to realize optical nanocavities that can trap the light in very small mode volumes and for a long period of time. Photonic crystal nanocavities can be formed by modifying one or more holes (i.e., by changing the hole size or the refractive index or by removing one hole) in an otherwise perfectly periodic lattice. Such a break in the periodicity of the lattice introduces new energy levels within the photonic band gap. This is analogous to the creation of energy levels within the semiconductor energy band gap by the addition of dopant atoms in semiconductor crystals. An increase in the holes' size increases the energy of the modes supported in the slab and pulls up defect states from the dielectric band into the band gap, or other kind of localized crystal defects. Such bound states exist close to the dielectric band and show similarity to the acceptor levels in semiconductors. Because of that, the modes created in this way are called the acceptor modes. Similarly, the reduction of the holes' size decreases the energy of the mode and pulls down defect states from the air band into the band gap. Such types of defect modes are referred to as the donor modes.

The crystal can thus form a kind of perfect optical “insulator” which can confine light within wavelength-scale cavities, among other novel possibilities for control of electromagnetic phenomena. However, as we have mentioned above, the vertical confinement in the slab is achieved by index guiding. Therefore, the defect modes in the band gap will suffer from radiation losses due to their coupling to the continuum of radiation modes that exist within the light cone. Indeed since the cavity mode is localized in real space, it is extended in the reciprocal space as governed by the uncertainty principle. It consists of  $k$  vector components that, for some of them, are positioned within the light

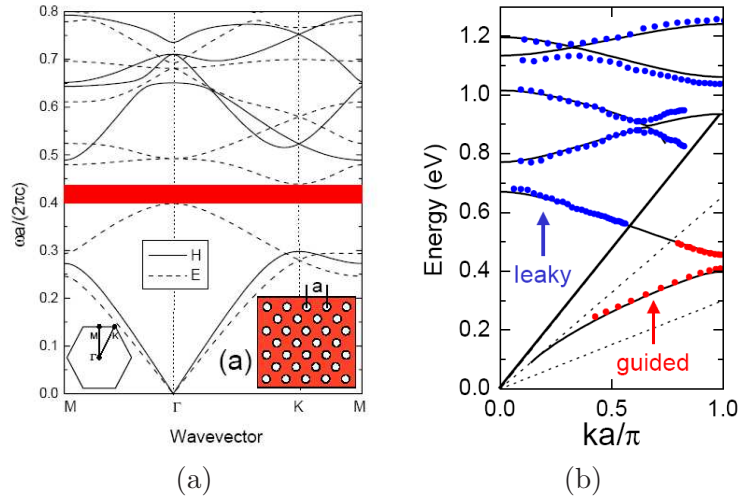


Figure 2.2: a: Band diagram of a triangular lattice of holes in a semiconductor, calculated in two dimensions. H (resp. E): Bloch modes with the electric (resp. magnetic) component normal to the plane (TE, resp. TM, modes). b: Band diagram of the same kind of structure, taking not account the third dimension, along the  $\Gamma - K$  Brillouin line. Only TE modes are shown. The vertical dimension makes appear the light line. (Source: [8])

cone components contribute to the out-of-plane losses of the cavity. The problem of high  $Q$  cavity design has therefore attracted much attention and several designs were proposed in order to minimize the proportion of these  $k$  vectors components within the light cone. We will present some of these designs in this chapter.

In all cases, in investigating the quality factor of such cavities, two radiation losses channels will have to be taken into account. The first one is radiation losses due to the mode coupling to the continuum of radiation modes that exist within the light cone. This vertical (out-of-plane) loss can be described by  $Q_{ver}$ . In addition, the light can leak laterally due to the finite number of holes surrounding the defect. This lateral (in-plane) loss can be described by  $Q_{lat}$ . The total  $Q$  factor of the cavity can then be written as the superposition of these two factors as follows:  $1/Q = 1/Q_{ver} + 1/Q_{lat}$ . Obviously, one of the goals in designing high- $Q$  cavities consists in reducing the impact of the vertical losses and extending the crystal over huge numbers of periods to reduce the lateral losses. For a laterally infinite size perfect crystal the lateral losses of such cavities are null. But this is not our goal here, since  $Q$  factors of the order of 2000 will be sufficient for the intended functionalities. We will therefore consider in the following that the main loss channel is vertical losses and that lateral losses are much smaller than out-of-plane losses. For example, a photonic crystal cavity with a quality factor of about 1000 does not suffer from planar losses as soon as the defect is surrounded by only 5 ranks of holes.

## 2.2 Fabrication of GaAs photonic crystal slabs

The LPN had already developed cutting-edge technologies to process photonic crystal cavities on a suspended GaAs membrane and whose resonance is centred around  $950nm$  [9]. Lasing has already been observed on such structures [10]. All the samples I have been working on during my PhD, were grown by Aristide Lemaître and processed by Isabelle Sagnes and Rémy Braive. I will just give here a short description of the main processing steps, which are depicted in figure 2.3. For more details, please refer to [9, 5].

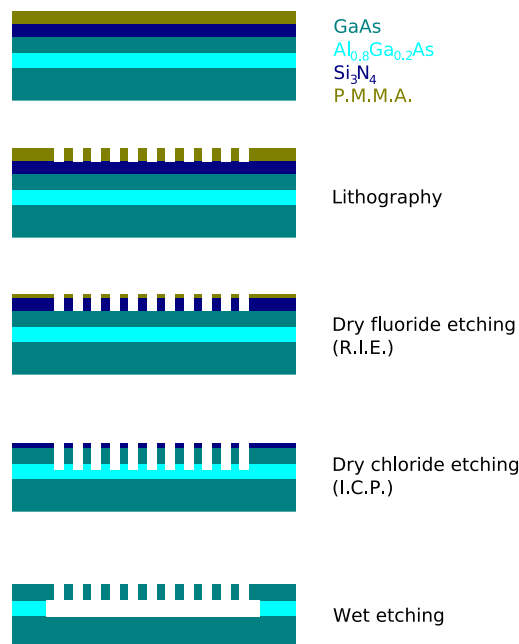


Figure 2.3: Successive steps of the processing of suspended bi-dimensional photonic crystals.

The first step is the epitaxy of the whole structure. Our samples consist of a  $180\text{ nm}$ -thick GaAs membrane incorporating a  $1\text{ }\mu\text{m}$ -thick  $Al_{0.8}Ga_{0.2}As$  sacrificial layer under the GaAs membrane. The growth is carried out by molecular beam epitaxy on an n-doped GaAs substrate. A single layer of self-assembled InAs quantum dots, the density of which is of the order of  $4 \cdot 10^{10}\text{ cm}^{-2}$  is grown at the membrane vertical center plane. The low temperature emission is centred around  $945\text{ nm}$  at  $4\text{ K}$  with an inhomogeneous broadening of about  $30\text{ nm}$  (§ 1.3.1).

A  $300\text{ nm}$ -thick  $Si_3N_4$  layer is deposited on the sample by P.E.C.V.D (Plasma Enhanced Chemical Vapour Deposition), and is subsequently covered by a  $450\text{ nm}$ -thick polymethylmethacrylate layer (P.M.M.A.), an electronic resist deposited by centrifugation and annealed at  $150^\circ\text{C}$ . The photonic crystal pattern is then printed by electron-beam lithography on the P.M.M.A. layer. The regions of resist insulated by electronic lithography are removed by wet etching.

The P.M.M.A. layer on which the photonic crystal pattern is printed cannot be used as the hard etching mask for the subsequent chlorine-based semiconductor etching because it is quickly removed during the dry-etching process. The pattern has to be transferred to a hard dielectric mask, the etching selectivity of which in the semiconductor dry-etching process is higher. After the development of the exposed resist, the pattern composed of holes is consequently transferred by a fluorine based dry-etching process into the  $Si_3N_4$  layer that acts as a mask in the subsequent chlorine-based dry-etching of the semiconductor.

The next step is the chlorine-based etching of the semiconductor in an Inductively Coupled Plasma - Reactive Ion Etching (I.C.P.-R.I.E.) reactor. The holes are drilled by a combination of physical sputtering and chemical etching. The etching depth reaches the AlGaAs layer. Finally the sacrificial layer of AlGaAs is removed by selective wet etching.

The final structure is a  $180\text{ nm}$  thick membrane of GaAs suspended in air. The substrate of GaAs is  $1\text{ }\mu\text{m}$  below the membrane. The active region is in the middle of the membrane. Obviously all this region contains a dense quasi-continuous distribution of independent sources in the limit of no interactions between the quantum dots. If the dots' density is very low, at most a few dots lie in

the cavity, but their position is random and it remains possible to separate them spectrally. In order to simulate a high number of incoherent sources, one usually requires a great number of repetitions of the same computation with varying phases for each source. Here I only want to study the cavity's modes, and only need to put some energy into them. One coherent source inside the cavity is sufficient whatever its position, as long as it is not on a node of the mode under study.

As explained further I will also usually put aside the substrate and only simulate the propagation of light inside the membrane surrounded by air.

## 2.3 Numerical treatment of photonic crystals

### 2.3.1 Numerical tools to treat photonic crystals

Many different numerical methods have been used to investigate various aspects of electrodynamicics in photonic crystals. These methods fall into two broad categories :

- Finite-domain techniques where Maxwell's equations are solved by formulating an eigenvalue problem. The photon eigenvalue equation is then solved to obtain the allowed photon states and their energies. The advantages provided by these methods are that they directly provide the band structure. One example is the Plane wave expansion method (PWE) which is used in the MIT Photonic Bands (MPB) package, a free program developed at the Massachusetts Institute of Technology (MIT) by Steven G. Johnson. Another one is the Transfer Matrix Method.
- Time-domain techniques which calculate the temporal evolution of the input electromagnetic field propagating through the crystal. Then the band structure is calculated by the Fourier transform of the time-dependent field to the frequency domain. A widely used time-domain method is Finite Difference Time Domain (FDTD).

In contrast to the Finite-domain methods which work in Fourier space, in the Finite-difference time-domain (FDTD) method, the temporal evolution of electromagnetic fields in real space is calculated. The FDTD method calculates the time evolution of the electromagnetic waves by a direct discretization of the Maxwell equations. In this method, the differentials in the Maxwell equations are replaced by finite differences on a spatial and temporal grid to connect the electromagnetic fields in one time interval to the ones in the next interval. In other words time and space are discretized. The electric and magnetic fields evolutions are step-by-step calculated from the four discretized Maxwell laws [4, 11]. As a rule of thumb the spatial grid size should be on the order of about  $a/10$  to  $a/20$  to ensure sufficient representation of the dielectric distribution while keeping the necessary amount of computational time bearable,  $a$  being the lattice constant of the photonic crystal. The choice of the grid depends on the geometry studied. The advantage of this method is that results for a large frequency range can be obtained in a single run.

### 2.3.2 The Finite Difference Time Domain (FDTD) tool

All simulations described below are obtained on a 20 processor cluster using the open source program Meep, developed by the group of J. Johanolopoulos [12, 13]. While other commercial software packages are available, none of them had the required flexibility.

From all the different strategies to simulate photonic crystals [3], FDTD software have the advantages to be well developed, easily understandable and close to the experiment we perform, even if it may not be the best tool to accurately simulate those structures [14]. The time evolution of the electromagnetic field is simulated within a finite volume; this allows seeing immediately what happens in time within the studied structure. In practice, we start our computation with a situation with no

energy at all inside the resonator: all fields are set to zero. The simulation is performed into two parts. First a short pulse of light with a duration  $T_{\text{source}}$  is emitted inside a cavity. Once the pulse is sent, we study how the fields freely evolve during a time  $T_{\text{free}}$ . The time envelop of the source is a Gaussian centred at  $t = T_{\text{source}}/2$ , with a width  $T_{\text{coh}}$  about a sixth of  $T_{\text{source}}$ , as recommended by Meep's designers. From these numerical measures, we can deduce the desired cavity's characteristics. This kind of simulation is performed many times for various sets of parameters in the photonic crystal design in order to study their impact on the optical properties of the whole structure.

## 2D FDTD versus 3D FDTD

Let us point out that bi-dimensional simulations are not fitted for the study of photonic crystal slab resonators. It could be possible to ignore the vertical dimension and use simplified propagation equations in the plane of the membrane. This kind of simulation is obviously much faster than a three-dimensional one. With some corrections (in the effective refractive index felt by the propagating wave for example), it is possible to obtain a good estimation of the wavelength of the cavity with bi-dimensional simulations. However, this method does not include the effects of coupling with the light cone, which governs as explained in the paragraph before, the loss rate and the radiation diagram out of the cavity. A three-dimensional simulation is needed to take into account these effects. Since I had to simulate many cavities' designs, I focused on techniques allowing me to reduce the computational time per design. The simulation of one structure calculated on one processor usually lasted between 3 to 6 hours <sup>8</sup>.

The minimum useful variation of each parameter was dictated by the resolution on the spatial discretization, limited to about  $a/10$ . A smaller step in the variation would not lead to any significant change on the simulation. While an option exist in Meep to take in account smaller steps using sub-pixel calculation of the index map, it introduced numerical instabilities, a bug which has been only solved in a latter version of the software.

## Simulated volume

Obviously the FDTD method can be used to describe electromagnetic fields in a finite area in space. The simulated volume (figure 2.4) is a finite three dimensional box. Ideally one should look into border conditions for which it is possible to simulate free propagation outgoing from the simulated volume without any waves coming in. This should apply for any waves whatever the angle at which they impinge on the border. For 3D calculations such mathematical conditions while keeping the linear aspect of the Maxwell's equations, do not exist (see [11] for a complete explanation). Problems in unbounded regions can be simulated by including absorbing boundary conditions to the edges of the calculation domain. The best performance is attained by using the perfectly matched layer (PML) boundary conditions are strongly absorbing layers adjacent to the finite computation box, hence greatly reducing the back reflected waves. The three dimensional box is thus enclosed by PMLs, the role of which is to replace the free propagation of the fields that should escape the box. Outgoing light is attenuated before reflecting on the border of the computational cell (where we use null fields conditions, i.e. perfect mirrors) and attenuated again by its second propagation into the PMLs. This attenuation evolves exponentially with the thickness of the PMLs. The adjunction of the Perfect Matched Layers induces consequently an increase of the computational volume. A PML thickness

---

<sup>8</sup>I experienced strong fluctuations on the computational time without finding the reasons. Meep software allows also parallel computation of the fields' time evolution on one structure, that is, to run the calculation on more than one processor. The LPN's calculators were first chosen for such an eventuality, with high performance communication speed rates between the processors to fully use the computational power in parallel processing. At least with Meep software, the computed volume proved to be small and it was then not worthwhile to run the calculation on more than one processor. It appears however much more efficient to simulate several designs simultaneously, each on one processor.

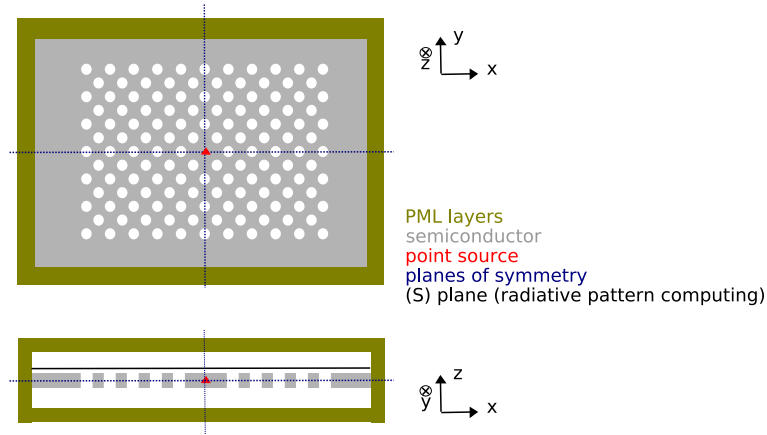


Figure 2.4: Schematic of the calculated cell. Horizontal and vertical cut views.

of about the lattice constant was sufficient, but it nevertheless increased strongly the volume to be computed (and the time needed to compute it).

Midway is placed the semiconductor membrane, surrounded above and below by air, and pierced with holes of cylindrical shape to constitute the photonic crystal cavity. The vertical axis will be referred to as  $Z$ , the plane of the membrane is denoted  $(XY)$ . The source is a point source at the center of the structure and acts as an electric dipole linearly polarized in the  $X$  or  $Y$  direction depending on the polarization we want to study.

On figure 2.4 the border of the calculated cell is some distance away from the border of the crystal (2 lattice constants between the crystal's borders and the PMLs). The region of non patterned membrane provides a matching region between the crystal and the PMLs. Indeed instabilities may appear if the holes were also drilled in the membrane covered by the PMLs.

As explained later § 2.3.4, in order to compute the collection efficiency, I will have to consider a virtual plane (S) placed just above the surface of the semiconductor. This plane has no material reality and is just a region of space where the fields' data will be registered at the end of the simulation. To be accurate, these data should contain the fields' value of only one single mode. This implies that only one mode must be excited, or that any other mode must contain negligible energy compared to the studied one at least at the end of the simulation. I call this situation "monomode excitation condition". This will be the topic of the next section.

### Spatial and temporal grid

In order to simulate accurately the structure, the space grid must be a fraction of the lattice constant  $a$  (about  $\lambda/n$ ) of the crystal, at least  $a/15$ . The choice of  $a/15$  results from a compromise between simulation time and resolution. Indeed, in order to avoid numerical instabilities, the time is also discretized proportionally. Therefore the computer memory required to store the fields data and the number of values to be calculated at each time-step, are proportional to the cubic of the resolution, leading to a simulation time proportional to the resolution raised to the power four. On the opposite, a coarser discretization was no more accurate, in particular with the variation of the position of some holes of the design. Last, if the triangular lattice constant spans over  $N$  pixels (15 here), then the lines of holes are separated by a distance equal to  $N\sqrt{3}/2$ , which is obviously not an integer number of pixels. Even with an algorithm which adapts the values of the refractive index and which does not impose the holes to be centred on the discretization lattice, this non-superposition between the discretization lattice and the holes lattice can still induce a breaking of any mode's degeneracy induced

by the triangular symmetry <sup>9</sup> (as for the H1 cavity I will present in § 2.4.2). The choice of  $N = 15$  gives  $N\sqrt{3}/2 = 12.990$ . This is one of the values giving the smallest deviation from an integer value, thus with the smallest impact on the triangular symmetry <sup>10</sup>.

### 2.3.3 The monomode excitation condition

	Y	Odd (-1)	Even (+1)
X			
Odd (+1)			
Even (-1)			

Figure 2.5: X component of the electric field created by a continuous point source, with different plane symmetries in X and Y directions. X: horizontal, Y: vertical. Numbers in parenthesis are the phase to be applied to the field.

In order to infer accurate values, only one mode must be excited in the cavity during the simulation. Two tools can be used to satisfy this monomode excitation condition.

First, it is possible to reduce the spectral width of the source, so that it is only resonant with the studied mode. This has two drawbacks. The time length of the source, and thus the computational time, increases as the spectral width decreases. Moreover, (1) the use of spectrally narrow sources does not warrant that we excite only one mode, since there may be a second mode expected to lie too spectrally too close to the first, and (2) it requires to have a higher understanding of the studied design in order to accurately choose a source's wavelength sufficiently close to the desired mode's wavelength to be resonant with it. Another method that can be used to decrease the number of excited modes exploits symmetry conditions. If for example a plane of symmetry in the  $X$  direction is set (and crosses the cavity dividing it in two), only fields with an odd or even parity in the  $X$  direction can be sustained. The figure 2.5 illustrates this point. When the parity in all three directions is set, the number of modes susceptible to be excited is highly reduced. Moreover each used symmetry plane obviously divides the volume to be computed, and thus the computational time, by two. Apart from the simulations where I studied the effect of the substrate, the simulated structure was supposed to stand freely in air. This allows us to position one plane of symmetry at the center of the membrane, parallel to the photonic crystal. I relied quite exclusively on the parity selection, as I most often chose sources with a temporal width of only  $N_{\text{oscil}} = 10$  light oscillations ( $T_{\text{coh}} = N_{\text{oscil}}\lambda/c \sim 33fs$ , a spectral width of about  $\Delta\lambda = 0.44\lambda^2/cT_{\text{coh}} = 0.44\lambda/N_{\text{oscil}} \sim 44nm$  at  $\lambda \sim 1\mu m$ ).

I will now explain how the monomode excitation condition allows for a simple and accurate computation of both the wavelength and the quality factor of the mode, and how it is possible to check if this condition is satisfied. For this, the time evolution of the electric field component, at the position of the source, is registered at each step of the simulation. More precisely we register the component with the same polarization as the one of the source, since it is the one with the highest amplitude, thus the less sensitive to numerical errors. All the analysis is based on this field's component only. Figure 2.6 illustrates some different situations that may appear and that I will discuss in the following.

<sup>9</sup>This problem is not proper to the simulation, and also appears during the lithographic step when processing the cavities.

<sup>10</sup>There exist more accurate ways to respect this symmetry, as to use a triangular lattice of discretization, or to use adapted rectangular lattices (with a height  $\sqrt{3}/2$  times the width). The first software I used (CrystalWave), implements

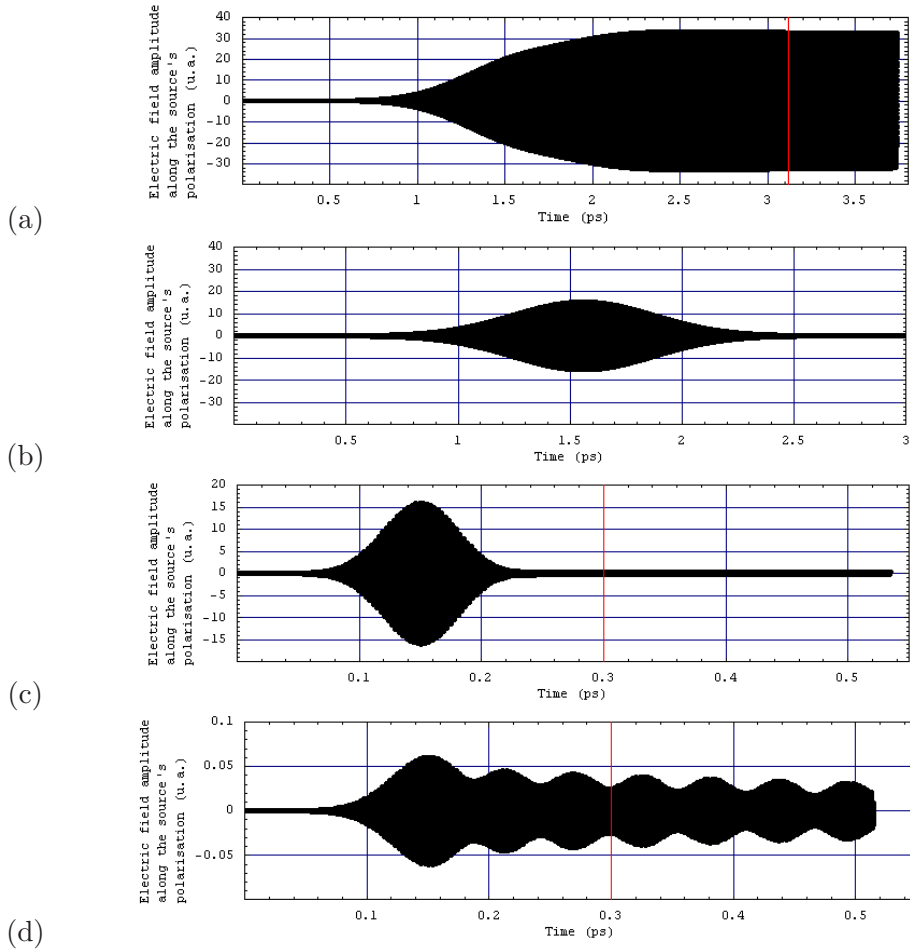


Figure 2.6: Component of the electric field amplitude, along the source’s polarization, at the center of a photonic crystal cavity during various FDTD simulations, a: with a long resonant pulse ( $N_{\text{oscil}} = 100$ ), b: with a long out-of-resonance pulse ( $N_{\text{oscil}} = 100$ ), c: with a short pulse ( $N_{\text{oscil}} = 10$ ), d: with a short quasi-resonant pulse ( $N_{\text{oscil}} = 10$ ) and beating effects. The red line indicates when the source is turned off (b: simulation was stopped at this stage because of the non resonant behaviour). Due to the high number of oscillations, the curves here appear as black regions and not as curves.

The spectral mismatch between the source and the mode is reflected by the amplitude of the field after the pulse. I managed to maintain this mismatch approximately close to zero by anticipating the spectral shift of the mode between different cavity designs. Too small amplitudes for the field which may become sensitive to the numerical errors, are thus avoided. If the mismatch is too important, the field amplitude is too low (1/10000 of the maximal amplitude obtained in the run shown on figure 2.6 (b) and the simulation is stopped.

If the monomode excitation condition is satisfied, the light oscillates at the cavity wavelength independently of the source’s wavelength. The times at which the electric field component drops and equals zero are linearly extrapolated from the calculation steps. We can deduce from this the oscillation frequency and its standard variation. If only one mode is excited, this standard variation should be null, but if two or more modes oscillates, the frequency is not well defined and the standard variation rises. I will further call “standard wavelength deviation” this first of the two indicators

---

this second possibility. This is one of the reasons we first chose this software.

used to check the monomode condition. Are also registered each time at which the field component reaches a maximum, as well as the corresponding amplitude of the field at these times<sup>11</sup>. This allows us to build, with a good approximation, the time envelop of the field, which is an exponential decay at the rate  $\Gamma_c/2$  ( $\Gamma_c$  for the intensity) if only one mode is excited. If not, beating between the two (or more) modes is observed (figure 2.6 (d)), and the time envelop is no more an exponential decay. The figure 2.6 (d) is a textbook case of beating effects I obtained once. Thus a linear fit in log-linear scale will give the decay rate (the slope of the line obviously). This also gives us an indication that the monomode excitation condition is satisfied, by looking to  $\sigma$  the reduced square of the fit (with maximal, and best, value of 1). I mostly used this method, by setting a condition of  $\sigma > 0.9$ , which proved to be necessary. To give an idea of the strength of this requirement, if  $\sigma = 0.9$  then it becomes difficult to extract from the curve a beating effect and to separate accurately the (at least) two beating components, because of the reduced number of beating oscillations and/or the small amplitude of the beats. I will further call this second indicator “ $\sigma$  value”.

Let me mention that it is not necessary to register the data on all the light oscillations as I described above. About 200 light oscillations is highly sufficient, corresponding to a simulated time of evolution of less than  $T_{\text{free}} < 1ps$ . Most often the excitation pulse duration  $T_{\text{source}}$  is much longer than that, in order to be as monochromatic as possible (figure 2.6).

The time evolution of the fields can also be used to compute the spectrum of the cavity modulated by the spectrum of the source, but the spectral resolution is proportional to the length of the simulation time. Direct calculations of the quality factor by fitting the field’s envelope is more accurate as soon as it exploits the monomode excitation condition.

### 2.3.4 Far-field calculations: Young’s setup test

In order to compute the collection efficiency, it is first necessary to obtain the complete far-field radiation pattern of the mode under study. I will first present the methods I tested to compute it, and how I validated them. Then I will explain how I deduced the collection efficiency and I will apply the chosen method to the studied cavities. During this whole discussion, the monomode excitation condition is considered to be satisfied, which warrants the accuracy of the data registered on the plane (S) from which these data are inferred.

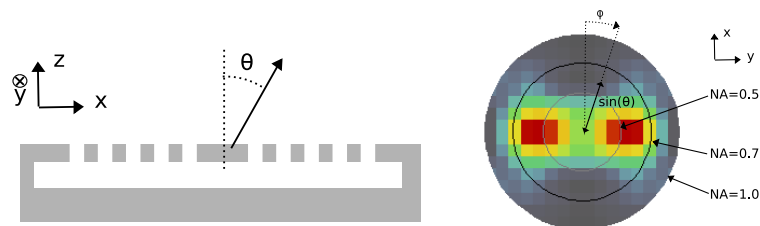


Figure 2.7: Used conventions of far-field representation. Left : cross section of the membrane. Right: Example of radiation pattern in the azimuthal and longitudinal coordinates. Circles indicate the region collected by an objective with a numerical aperture NA.

The “far-field” or “radiation pattern” is an intensity map of the light emitted by the mode under study, at infinite distance from the cavity in a direction identified by its azimuthal  $\theta$  and

<sup>11</sup>On the contrary to the data used to calculate the frequency’s cavity, the dates at which the field is maximum, and the corresponding value of the field is not extrapolated. The kept values are the steps for which the previous and the successive steps present a field’s value smaller than the current one. Because the time values are here not extrapolated, they are lesser accurate values to compute the mode’s frequency than the extrapolated times at which the field crosses zero.

longitudinal  $\phi$  coordinates (figure 2.7). Emission in direction  $\theta = 0$  is in the direction normal to the membrane, and  $\theta = \pi/2$  is the light emitted in the plane of the membrane (but out of it). In the band diagram formalism, light emitted at  $\theta = 0$  had an in-plane null wavevector in the cavity. Therefore it is also called "emission at  $\Gamma$  point". This "far-field" is also the intensity map of the beam outgoing from an objective focused on the cavity with numerical aperture (NA) of 1 without diffraction effects on the objective's aperture. Emission in the direction  $\theta = 0$  is the intensity at the center of this beam, while emission at  $\pi/2$  is the intensity at its border.

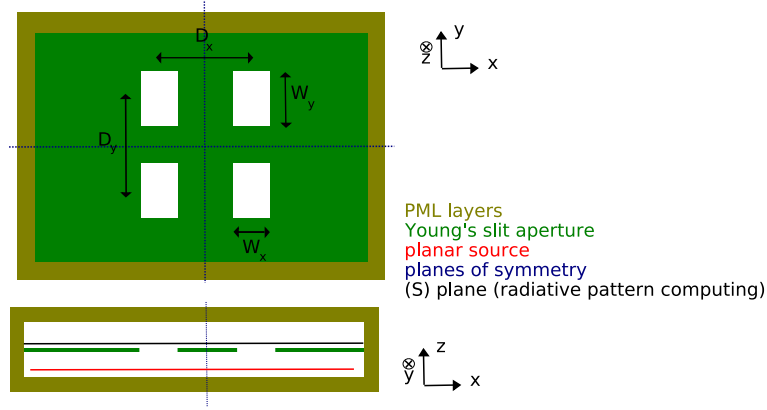


Figure 2.8: Schematic of the calculated cell for Young's slit tests.

I tested different methods to implement the computation of this far-field. The experiment I used to validate my method is Young's experiment: a plane wave goes through an aperture made of four rectangular slits positioned on a square (figure 2.8). I used a continuous monochromatic source with the form of a plane placed below the aperture, creating a plane wave propagating in the vertical direction as in a usual Young's setup. The FDTD program I used allows such numerical experiment, by using a perfect metallic material as the aperture. This material is a domain of the computational cell where all fields are set and maintained to zero (i.e. the refractive index is infinite). The slits have a width  $W_x$ , a length  $W_y$ , and are separated by a distance  $D_x$  (resp.  $D_y$ ) in the X direction (resp. Y). Z is the vertical direction of propagation. The FraunHoffer diffraction theory gives the intensity in the  $(\theta, \phi)$  direction from such apertures:

$$I(\theta, \phi) = I_0 \frac{\sin(2D_x\alpha)}{\sin(D_x\alpha)} \text{sinc}(W_x\alpha) \frac{\sin(2D_y\beta)}{\sin(D_y\beta)} \text{sinc}(W_y\beta) \quad (2.1)$$

$$\alpha = \frac{\pi \sin(\theta) \cos(\phi)}{\lambda} \quad (2.2)$$

$$\beta = \frac{\pi \sin(\theta) \sin(\phi)}{\lambda} \quad (2.3)$$

We shall see that the radiation pattern can be deduced from the real and imaginary values of the electric and magnetic field. The field's values used to compute the radiative pattern are those measured on the plane ( $S$ ) parallel to the membrane (or the aperture in the Young's slit experiment). I varied the distance between this plane ( $S$ ) and the membrane from less than  $\lambda/50$  to  $2\lambda$  without noticing any differences, therefore I kept it close to the membrane in order to minimize the simulated volume and to minimize errors when calculating the field emitted close to  $\theta = \pi/2$ . In order to calculate the different values of the field, I used two methods. In the first one, I recorded the real and imaginary parts of the field. This had the disadvantage of being very slow, since the calculation of the imaginary part is twice as slow as the calculation of the real parts. The second method consists

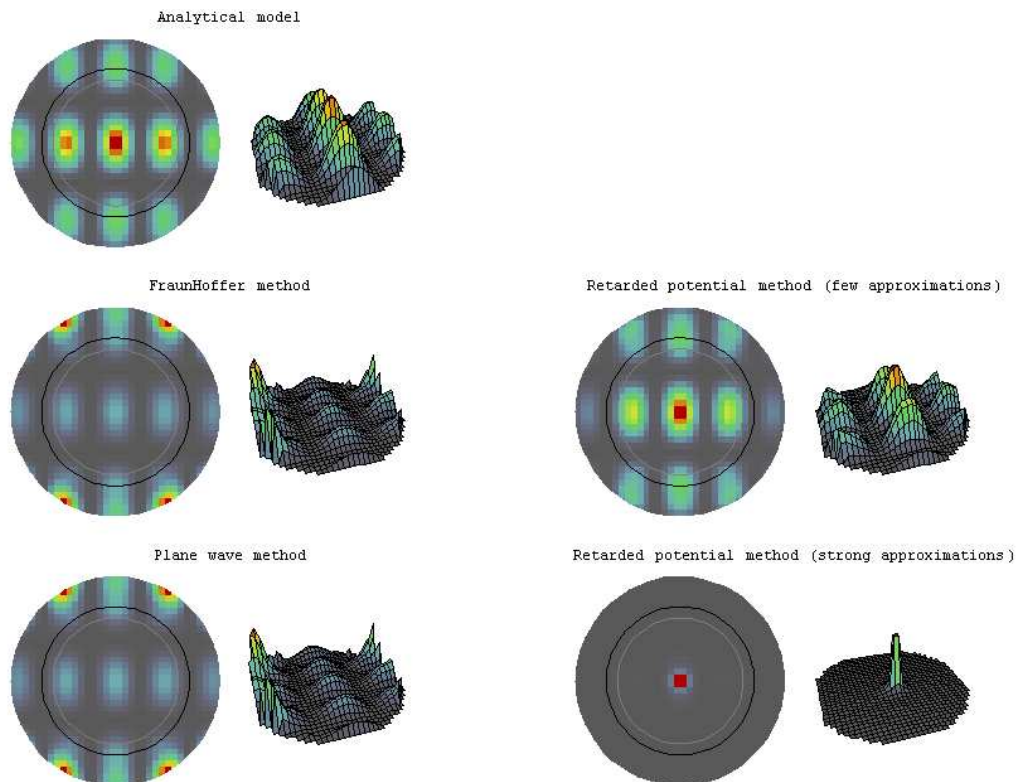


Figure 2.9: Radiative patterns, in map and in 3D representations, for the analytical model of the 4-slit Young' setup, and for various attempts to compute it using FDTD data.

in registering twice at the end of the calculation the real parts of the field, at times separated by a quarter of light oscillation <sup>15</sup>. Since light is monochromatic at the end of the simulation, this gives both quadratures of the fields [15], from which we can deduce its imaginary expression after correcting from any damping during this quarter of oscillation. This method allows us to run the simulation only on the real parts of the fields, thus saving much computational time.

### FraunHoffer diffraction theory

A first idea to compute the far-field radiation pattern consists in using the FraunHoffer diffraction theory to compute the mode's radiative pattern: from the real and imaginary values of the electric and magnetic fields  $E$  and  $B$  on the plane ( $S$ ) we should be able to deduce the intensity of the field emitted in any direction. The fields components at the infinite are the spatial 2-dimensional Fourier transform of the fields on ( $S$ ) (written  $TF_{(S)}$ ), and the Pointing's vector at the infinite is  $\vec{\pi} = TF_{(S)}(\vec{E}) \times TF_{(S)}(\vec{B}) / 2\mu$ . Theoretically the plane ( $S$ ) should be infinite in the  $X$  and  $Y$  directions. The fields' amplitude decreases sufficiently quickly (exponentially when the distance from the cavity center increases) so that we can consider that the fields outside the computational cell are null. The PMLs provide also a good regularization at the border of ( $S$ ) to avoid problems of frequency cutting.

The field at the infinite in the  $(\theta, \phi)$  direction is a plane wave propagating in the  $Z$  direction far from the membrane, and the Pointing's vector should be pointing in this direction. However, by using this method, we observed a deviation of Pointing's vector direction from the  $Z$  direction. This deviation was too strong to be explained by numerical errors. If I consider only the component in the

expected direction, I nevertheless obtain something quite similar to the expected result given by the analytical. Figure 2.9 gives the patterns obtained for the analytical model and the different numerical methods I tested in the configuration of Young's slit experiment. This first method shows that the amplitude of the field is not correct, with an exaltation of the field propagating close to the membrane.

### Plane wave method

A second method, following [16], is to consider the light at the infinite as plane waves and deduce their value by Fourier-transforming the near field on (S) as previously. For any plane waves, their intensity is proportional to the squared amplitude of the imaginary electric (or magnetic) field:  $K \sim |TF_{(S)}(\vec{E})|^2$ . This method is the one used in [16], but we ended up with the same deviations as previously (see figure 2.9).

### Theory of retarded potential

A third method, following [17] is to first deduce the equivalent surface electric and magnetic currents on the plane (S), and then to apply the theory of retarded potentials to compute the far-field. The expression of the radiation intensity (power per unit solid angle), is then [17]<sup>12 13 14</sup>:

$$K(\theta, \phi) = \frac{\eta_0}{8\lambda_c^2} \left( \left| N_\theta + \frac{L_\phi}{\eta_0} \right|^2 + \left| N_\phi - \frac{L_\theta}{\eta_0} \right|^2 \right) \quad (2.4)$$

$$N_\theta = -TF_{(S)}(H_y) \cos \phi \cos \theta + TF_{(S)}(H_x) \sin \phi \cos \theta \quad (2.5)$$

$$N_\phi = TF_{(S)}(H_y) \sin \phi + TF_{(S)}(H_x) \cos \phi \quad (2.6)$$

$$L_\theta = TF_{(S)}(E_y) \cos \phi \cos \theta - TF_{(S)}(E_x) \sin \phi \cos \theta \quad (2.7)$$

$$L_\phi = -TF_{(S)}(E_y) \sin \phi - TF_{(S)}(E_x) \cos \phi \quad (2.8)$$

$$\eta_0 = \sqrt{\frac{\mu_0}{\epsilon_0}} \quad (2.9)$$

If I use this expression, this method leads to far-fields patterns almost identical to the pattern obtained analytically in the Young's slit experiment. Two side peaks are a little too small with this method. Conversely, a more approximated version of this formula [18] gives wrong patterns (see Fig. figure 2.9).

<sup>12</sup>Here I give the formula in usual units. Meep software uses dimensionless units (for ex.  $c = 1$ ,  $\eta_0 = 1$  and  $a = 1$ ) which modifies the expression of the prefactor in  $K(\theta, \phi)$ . We are only interested in the collection efficiency, which is a ratio without dimension. The fields' amplitude and the total emitted power (see § 2.3.5) are first calculated in Meep's units. It is therefore more suitable to perform the whole computation in these units by using the values of the various terms of the formula in these units (the decay  $\Gamma_c$ , the wavelength  $\lambda_c$ , the cavity's energy  $W_c$  (§ 2.3.5) ...).

<sup>13</sup>One obviously also has to be careful with the discretization steps in the computation:  $dxdy$  in  $TF_{(S)}$  becomes  $(1/\text{resolution})^2$ , which here equals to  $1/15^2$  (§ 2.3.2).

<sup>14</sup>Moreover the solid angle unit is  $(\sin \theta)d\theta d\phi = \frac{dk_x dk_y}{\cos \theta}$  where  $dk_x dk_y$  corresponds to the reciprocal basis of (S), in which the radiative patterns are represented (figure 2.7). The radiative pattern is not naively the central part of the Fourier transform of the (S) plane's fields.

<sup>15</sup>Here I speak of the light oscillations at the excited mode wavelength and not at the source wavelength. To do so, it is necessary to compute the resonant wavelength at the end of the simulation but before registering the fields data on the (S) plane. The script language used by Meep allows the computation of evolved algorithms during the simulation, such as the computation of this wavelength and the quality factor to correct of the damping operation, and to save the fields' data on (S) accordingly. I had to write my own scripts for that. This language is today unusual and not as friendly as others, as it is similar to LISP.

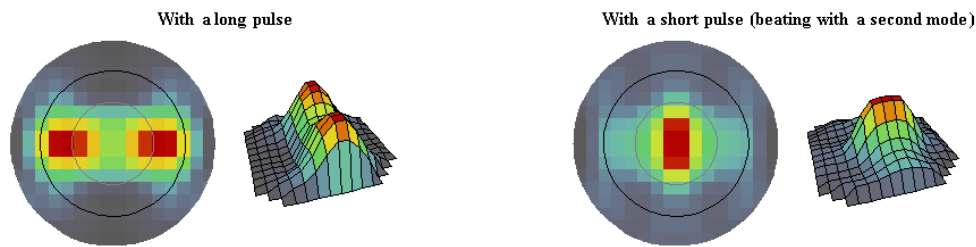


Figure 2.10: Radiative patterns of the same cavity and using same simulation parameters apart from the duration of the source pulse. In the case of a short excitation pulse, a second mode is excited. For indication the regression quality is 0.9996 in the long pulse case and 0.502 in the short one.

All of the radiative patterns I will show in the following are obtained by this last method. As I already said, if two or more modes are excited, the results given by this algorithm are not correct. Figure 2.10 gives an example illustrating the importance of this condition: two computed radiative patterns are given here. The cavity design is the same in both diagrams and we are supposed to study the same mode in both cases. The diagram on the right corresponds to the situation in which the monomode excitation conditions is not satisfied (another mode is excited in addition to the studied one), whereas on the left, only one mode is excited.

### 2.3.5 Collection efficiency

The collection efficiency is the ratio between the power emitted in the solid angle of the objective and the total emitted power. Let us stress that in the configuration in which where the substrate is not taken into account, the maximal calculated collection efficiency is 50%.

In order to evaluate the power emitted in the solid angle of the objective, one can integrate from the radiation pattern the flux in the solid angle of the objective. A more delicate task is the evaluation of the total emitted power. In the case of vertical symmetry (i.e. with simulation forgetting the substrate), the total emitted power is the sum of two times the total flux of the radiative pattern (up and down) and of the flux escaping into the membrane due to the finite size of the crystal. This fraction of energy funnelled in the membrane appears to be difficult to evaluate numerically. Moreover this method is inadequate for simulations taking into account the substrate. The method to deduce the total emitted power is based on the quality factor. I registered the energy  $W_c$  inside the cavity at the same time as the fields amplitude used to extract the radiative pattern. These data  $W_c$  combined to the intensity decay rate of the cavity ( $\omega_c/Q$ ) allows to deduce the total emitted power as  $P = W_c \omega_c / Q$ . In the case of photonic crystal cavities, the border of the cavity is badly defined, thus it is difficult to determine in which volume the energy of the cavity must be measured. By taking the whole computational volume to measure it, and assuming the border of the computational volume is at a distance  $d$  from the border of the cavity, the error made in evaluating the energy is  $P(1 + d/c)$  (with  $c$  the speed of light) instead of  $P$ . Since the computational volume is small, the error is negligible.

## 2.4 Optical properties of photonic crystal cavities

### 2.4.1 Important characteristics of the cavity

I have already listed two important characteristics which depend only on the cavity: the Purcell factor  $F_p$  and the collection efficiency  $\eta_c$ . Depending on the entanglement scheme, some extra conditions

appear. Before continuing on the study on some photonic crystal cavity design, I would like to summarize here the various characteristics I looked for the two entanglement schemes.

For the time-bin entanglement scheme, we look for a unique polarized mode with a Purcell factor of 30. A way to introduce the laser inside the cavity, at an energy about  $30meV$  above the energy's mode is also needed. One good solution should be a second mode, orthogonally polarized to the other, spectrally wide (i.e. low quality factor), non nodal at the maximum of amplitude of the other one, and with a good radiative pattern to allow a good penetration of the laser. More explanations of these are given in chapter 3.

For the polarization entanglement scheme, a Purcell factor of about 10 is sufficient (see § 4.3.3), but the cavity must be energetically degenerated in polarization. I will also compare the radiative pattern of both polarizations. The reason will be explained in § 4.4.2. More precisely I will look by how much their radiative pattern differs from the polarization, and quantify this by the overlap factor defined as  $K = \int d\theta d\phi K_x(\theta, \phi)K_y(\theta, \phi)$  where  $K_u(\theta, \phi)$  ( $u = x, y$ ) is the radiative pattern of the mode with polarization  $u$  on an orthogonal polarization basis  $(x, y)$  and normalized such has  $\int d\theta d\phi K_u(\theta, \phi) = 1$ . For indistinctive radiative patterns the overlap factor equals its maximal value 1, whereas for totally distinctive ones it equals 0. For these kind of cavities I will look for non distinctive radiative patterns ( $K \sim 1$ ).

Note that for sources based on parametric downconversion, the collection efficiency of each photon is generally limited to 25% [19], except for fibered sources based on four-wave mixing [20]. This gives a value of comparison for the collection efficiency to look for in both entanglement schemes.

## 2.4.2 Defect photonic crystal cavities

### The H1 cavity

The simplest cavity defect in a bi-dimensional photonic crystal consists of removing one hole [21] in a perfect triangular lattice of holes. This cavity, called H1, is unchanged by a rotation of  $\pi/3$  (i.e.  $C_6$  symmetry). Such a cavity sustains monopole, dipole, quadripole and hexapole modes [22]. The hexapole mode has been thoroughly studied [22] since it made possible to obtain a directive emission pattern, but it is not adapted for the generation of entangled photons. In fact, this mode is much like a whispering gallery mode with a null electrical field in the cavity center and the field maxima near the etched holes. Consequently, for the generation of entangled photons, the quantum dot placed on a maximum will be subject to strong charge fluctuations due to the vicinity of the etched surface.

The dipole mode is more adapted to our situation: the generation of entangled photon pairs. From its  $C_6$  symmetry, the cavity sustains two energy degenerate orthogonally polarized modes and the mode maximum is located in the center of the cavity. Hence the quantum dot will be placed on a symmetry axis of the structure.

In such a cavity, the  $X$  polarized mode has a wave vector mostly in the  $Y$  direction, and vice versa<sup>16</sup>. This implies that the two modes have their fields nodes at different positions, implying that their respective radiation patterns will not perfectly overlap. On the other hand, their electric field maxima are positioned at the same place, leading to the same Purcell factor for both polarizations (see § 4.4.3 for a complete discussion of this problem).

The aim of this paragraph is to find a design that satisfies the conditions for the generation of a polarization entangled photon source. The main issue is to keep the  $C_6$  symmetry in order to keep the polarization degeneracy, but at the same time increase the mode overlap of the emission diagrams. In fact, due to the intrinsic symmetry of the cavity, the radiative pattern of the  $X$  polarized mode is the same as the one on  $Y$  with a rotation of 90 deg around the propagation axis ( $\theta = 0$ )<sup>17</sup>.

<sup>16</sup>This is not the case for example for the micropillar, where both modes propagates mostly in the vertical direction  $z$

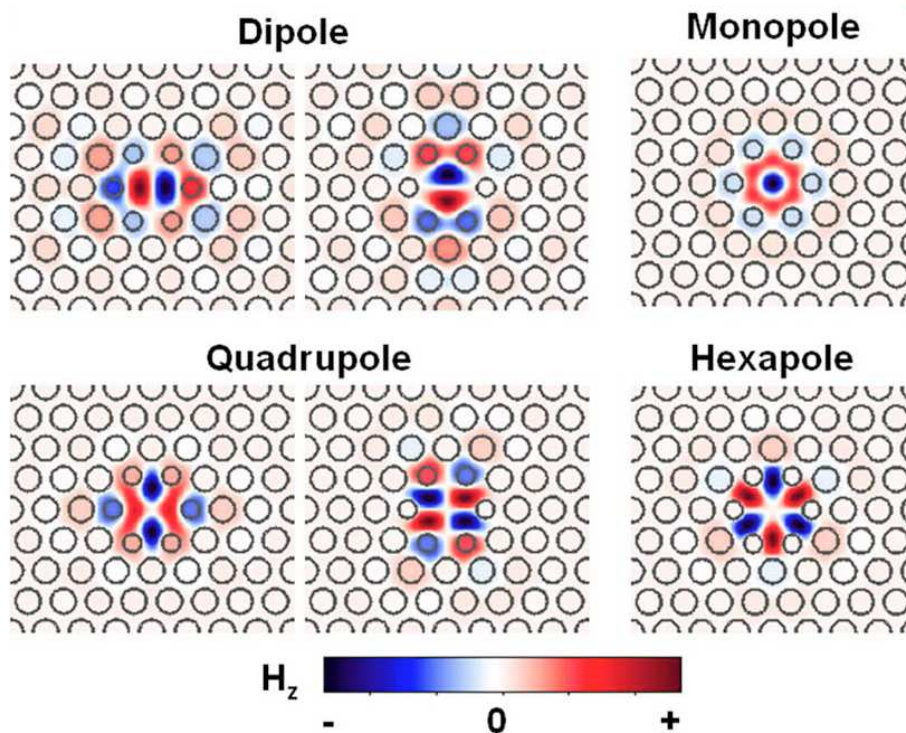


Figure 2.11: Various modes in a “modified” H1 single-defect cavity. The term “modified” indicates the radius of the six holes surrounding the cavity is slightly smaller than the other holes composing the photonic crystal. The dipole and quadrupole modes are doubly degenerate while the monopole and hexapole modes are not degenerated. Here is plotted the  $H_z$  component. From [22].

### The L3 cavity

Another cavity of interest, this time for the time-bin entangled scheme, is the  $L_n$  linear cavity. This cavity consists in removing  $n$  holes in the  $\Gamma - K$  direction of a perfect photonic crystal with a hexagonal structure. Such cavity can in a first approximation (for  $n \geq 3$ ) be considered as a Fabry-Perot cavity. Cavities with  $n \leq 3$  can also be seen as simple Fabry-Perot cavities, but the emission wavelength does not exactly match the size of the cavity. Such cavities can display high quality factors in small volumes and only one polarization mode is sustained [23], which makes them a cavity of choice for the generation of time-bin entangled photons. Ultimate L0 cavities have also been studied [24, 25].

These designs are obviously not the only ones to obtain cavity effects. Notably designs based on the waveguides formed by the removal of one line of holes in the  $\Gamma - K$  direction (named W1) have been studied and have permitted to experimentally reach record quality factors in semiconductor physics (more than  $10^8$  for mode volumes of the order of 1 [26, 27]). As already explained, the high values of the quality factors of those last designs tends to indicate that their emission pattern is far from being directive, which makes them uninteresting for the current topic.

---

and are reflected by the Fabry-Perot Bragg mirrors above and below the quantum dot.

<sup>17</sup>After carefully checking this assertion by simulating both polarizations, only one polarization was calculated for every set of parameters

### 2.4.3 Impacts of the cavity geometry on the optical properties of the cavities

Most work on H1 or L3 cavities was aimed at maximizing the quality factor while minimizing the cavity volume. Since the fraction of coupled light in the cavity is linked to the Purcell effect, high Purcell factors were sought in order to obtain a  $\beta \approx 1$ . The most important basic idea to get high quality factors is to adjust the profile of the mode inside the cavity to the profile of the mode in the mirrors formed by the holes, at the interface between the cavity and the crystal. This mode matching is obtained either (1) by shifting the holes at the border of the cavity [28, 29], or (2) by changing the radius of the holes surrounding the cavity or part of them in order to attenuate the geometrical difference between the region without holes (the cavity) and the region with holes (the crystal) [30], or (3) by changing their shape [31, 32], or (4) by combining some of these different techniques simultaneously [33, 30, 34]. This reduction of the optical losses also corresponds to a displacement of the locked wavevector of the mode away from the light cone and/or to a decrease of the wavevector distribution around the mode wavevector. In both cases this means that the proportion of wavevectors around the  $\Gamma$  point is reduced, and the quantity of light emitted upwards accordingly. Thus optimized design to reach high quality factors seem incompatible with designs allowing for good collection efficiency with an emission mostly in the vertical direction. Lately, a structuration of the surrounding photonic crystal was proposed, which allows for an efficient collection by band folding coupled wavevectors of the K direction to the  $\Gamma$  point [35].

In our case, one of the figures of merit of our cavities will not be their quality factors, since quality factors of around  $Q=10000$  are enough. Our goal is to obtain relatively moderate  $Q$  factors while increasing significantly the fraction of collected light. In the case of the H1 cavities, one also seeks an important mode overlap of the two polarizations. The above conditions can be achieved by changing slightly some of the geometrical parameters of the photonic crystal cavity: the geometrical characteristics of the holes surrounding the cavity (position and radius), the period of the lattice of holes, the proportion of air within a unit cell (or filling factor), the membrane thickness and the distance to the substrate for instance.

#### Position of the nearest-neighbour air holes around the cavity

Let us first focused on a “modified” H1 cavity in which all six air holes surrounding the cavity are shifted away from the center of cavity along the lines of symmetry. The results obtained here are part of an article we published in New Journal of Physics [36]. The hole displacement  $d$  is expressed in lattice constant  $a$  units and depicted on figure 2.12. A displacement of  $d = 0$  corresponds to the unmodified H1 cavity.

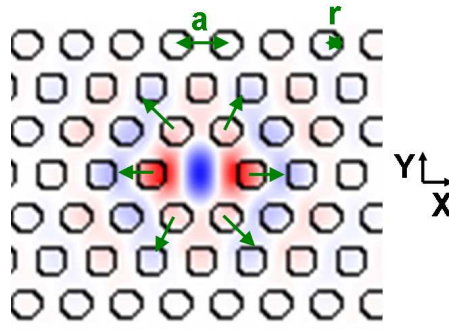


Figure 2.12: Displacement of the six holes surrounding the H1 design <sup>18</sup>.

<sup>18</sup>A positive value of the displacement always means that the holes are shifted away from the cavity center.

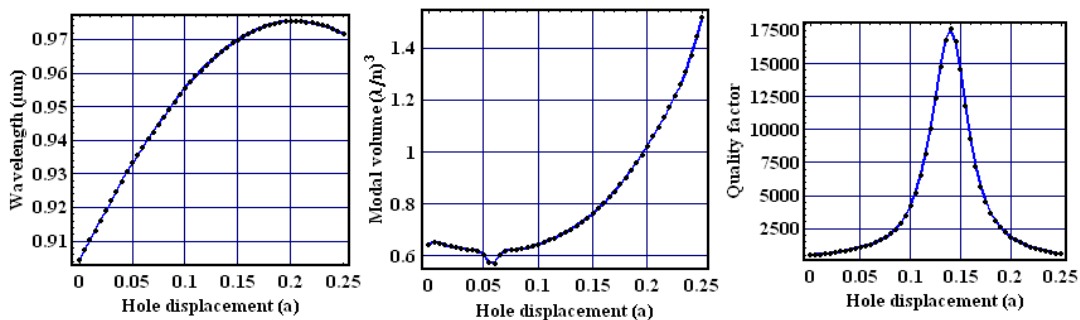


Figure 2.13: Wavelength, mode volume and quality factor of the dipole mode of a H1 cavity when shifting the first cavity neighbour holes away from the cavity center along the lines of symmetry <sup>19</sup>.

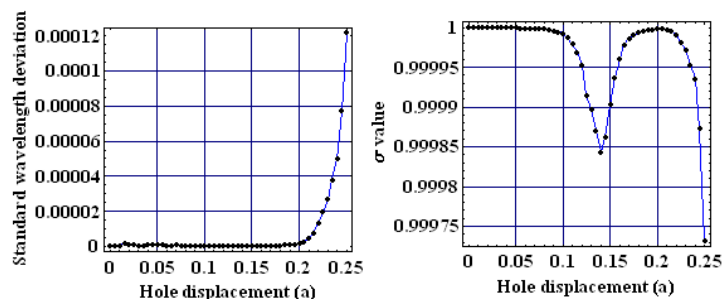


Figure 2.14: Two criteria used to check the monomode excitation condition when displacing the six neighbour holes in a H1 cavity. Left: standard deviation of the resonance wavelength of the dipole mode as a function of  $d$ . Right:  $\sigma$  parameter as a function of  $d$  <sup>19</sup>.

Figure 2.13 depicts the most straight forward results, mainly the emission wavelength, modal volume and quality factor of the cavity. As expected, the emission wavelength and the modal volume increase as the holes are shifted away from their initial position. For a displacement of more than  $d = 0.2$  a decrease of the emission wavelength is observed. In fact, for such important displacements, the H1 cavity tends towards an H2 design consisting of seven missing holes. The quality factor of the cavity also increases and reaches its maximum for a displacement of  $d = 0.14a$ . This likely results from a better mode matching between the cavity dipole mode and the mode of the photonic crystal forming the in-plane mirror : when the holes displacement is increased, the planar wavevector points to the direction moving away from the  $\Gamma$  point. For higher shifts ( $d > 0.16$ ), the quality factor begins to drop again and the mode wavelength tends to saturate and decrease. This might be correlated to the fact that a second mode progressively appears when the holes displacement becomes too large since the H1 cavity tends towards an H2. The onset of this second mode can be checked by testing the validity of the monomode excitation condition (see Fig. 2.14). For the studied range of displacements, the standard deviation of the resonance wavelength and the  $\sigma$  parameter indicate that only one mode is indeed excited for  $d < 0.2a$ . Above  $d > 0.2a$ , the standard deviation of the resonance wavelength increases and above  $d > 0.25a$ , both criteria degrade, indicating a beating between two emission modes.

The conditions sought in this paragraph are to obtain a maximum mode overlap of the two

<sup>19</sup>For reference purpose, the other design parameters' values are: refractive index  $n = 3.45$  (GaAs at 4K), lattice constant  $a = 270nm$ , holes' radius  $r = 80nm$ , filling factor  $f = 0.65$  and membrane thickness  $h = 140nm$ .

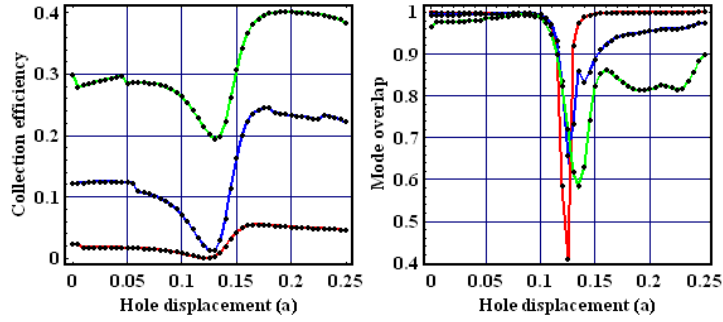


Figure 2.15: Collection efficiency and mode overlap as a function of the displacement  $d$  of the holes in a H1 cavity for numerical apertures  $NA = 0.2$  (red curve) 0.5 (blue) and 0.8 (green) <sup>19</sup>.

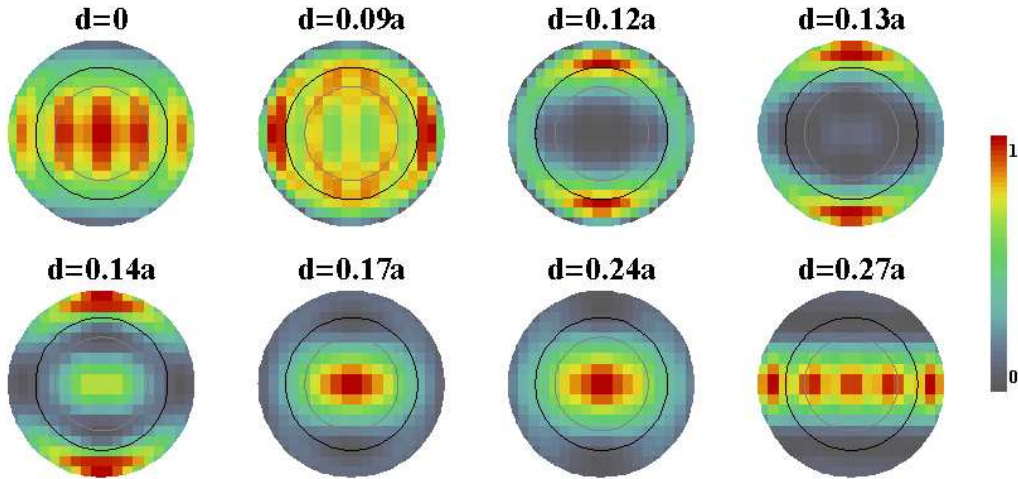


Figure 2.16: Radiation patterns of H1 cavities with different hole displacements  $d$  <sup>19</sup>. Each pattern is normalized to its maximum independently of the other cavities.

polarization modes with the maximum possible collection efficiency. Of course this should not be done at the expense of the quality factors and modal volume.

Figure 2.15 displays the collection efficiency (with a maximum of 0.5 as explained previously) and the mode overlap in an experiment where the light is collected above the membrane through a microscope objective with three different numerical apertures. One can differentiate three operating domains

- For small hole displacements ( $d \leq 0.09a$ ), the mode overlap is almost unity (more than 95%), but the collection efficiency is low, below 15% for standard microscope objective and does not exceed 30% for a numerical aperture of  $NA = 0.8$ . The emission diagram (see Fig. 2.16) for a hole displacement of  $d = 0.09a$  clearly explains the situation. The mode is almost uniformly distributed in all directions giving rise to a high mode overlap, and the collection efficiency scales as the objective numerical aperture. Consequently, even if most of the signal escapes from the cavity, the isotropic radiation pattern prevents from an efficient collection of the photons.
- For holes displacements ranging from  $0.11a$  to  $0.15a$ , the quality factor reaches its maximum.

However, the mode overlap drops down to 40% for an objective with  $NA = 0.8$ , which is the minimum overlap affordable to engineer an entangled photon pairs source (see § 4.4.2). The collection efficiency drops also down to 20 % at most. This decrease of the collection efficiency results from a better confinement of the light inside the photonic crystal slab as indicated by the increase of the quality factor due to a reduction of the optical losses at the  $\Gamma$  point and thus an increase of  $Q_{vert}$ .

- For even larger hole displacements ( $0.15 \leq d \leq 0.25a$ ) the photon collection efficiency increases abruptly reaching 25% for a  $NA = 0.5$  (and  $d = 0.18a$ ), corresponding to a 2-fold increase compared to the standard H1 cavity. At the same time, the mode overlap increases up to 95% reaching almost the values obtained at low values of  $d$ . The mode profile (2.16) is almost  $TE_{00}$  in the propagation direction perpendicular to the membrane allowing for an efficient coupling in an optical fiber.

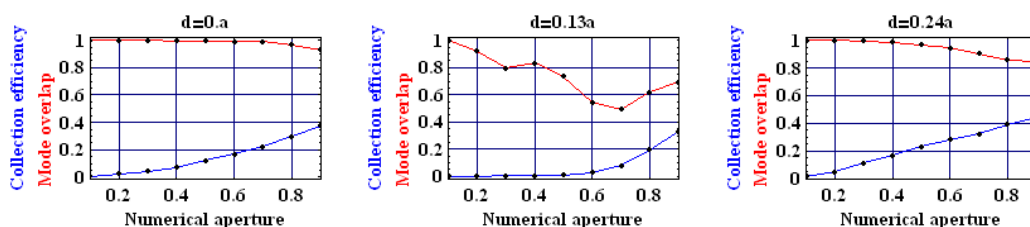


Figure 2.17: Collection efficiency and mode overlap as a function of the numerical aperture of the objective, for H1 cavities with three different hole displacements <sup>19</sup>.

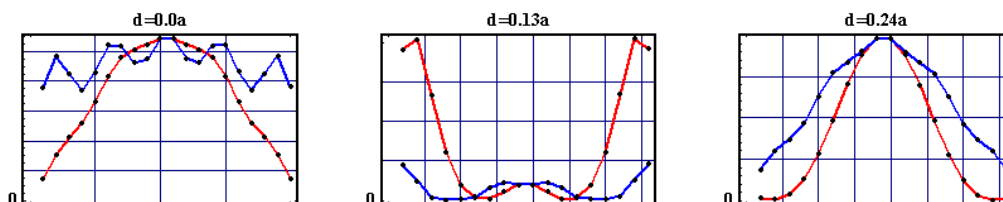


Figure 2.18: Cross-section of the radiation patterns of H1 cavities with three different hole displacements. Red: along  $k_y$ , blue: along  $k_x$ . The ordinate values are intensity fluxes in arbitrary units <sup>19</sup>.

In order to illustrate the effect of spatial selection by the aperture of the objective, I plotted both collection efficiency and mode overlap as a function of the numerical aperture for three different holes displacements  $d$  (see Figure 2.17). Using an objective with a numerical aperture of  $NA = 0.2$  increases the mode overlap up to almost 100% for every cavity but at the cost of a low collection efficiency. On the other hand, a numerical aperture  $NA = 0.7$  increases the collection efficiency by a factor of 1.5 (for  $d = 0.18a$ ) compared to an experiment with a numerical aperture of  $NA = 0.5$ , but the mode overlap does not exceed 83% indicating that almost half of the energy is astigmatic. This astigmatism is clearly visible for a displacement of 0.13, both on Figure 2.17 and on its far-field distribution (see Fig. 2.16). The strong astigmatism observed for  $d = 0.13$  strongly impacts the variation of the mode overlap as a function of the numerical aperture, compared to the two other examples. The non-linear increase of the collection efficiency as a function of the numerical aperture

for such cavity design directly reflects the directivity of the emission at large angles : the collection significantly increases only for numerical apertures greater than 0.6, whereas for more directive cavities with respect to normal incidence, the collection efficiency increases more rapidly at low numerical apertures. For  $d = 0.24a$  the collection efficiency increases linearly with the numerical aperture, as for the "free space" case (§ 1.4.2), apart from the fact that most of the light is lost into the substrate in the "free space" case while a large fraction of light is now confined and emitted outside the membrane in the "cavity" case. The far-field of the  $d = 0.24a$  design displays a distribution similar to  $\sin(\theta)$  function (at least in the  $k_x$  direction, in the  $k_y$  direction the profile resembles more a Gaussian function, 2.18 which is even better!).

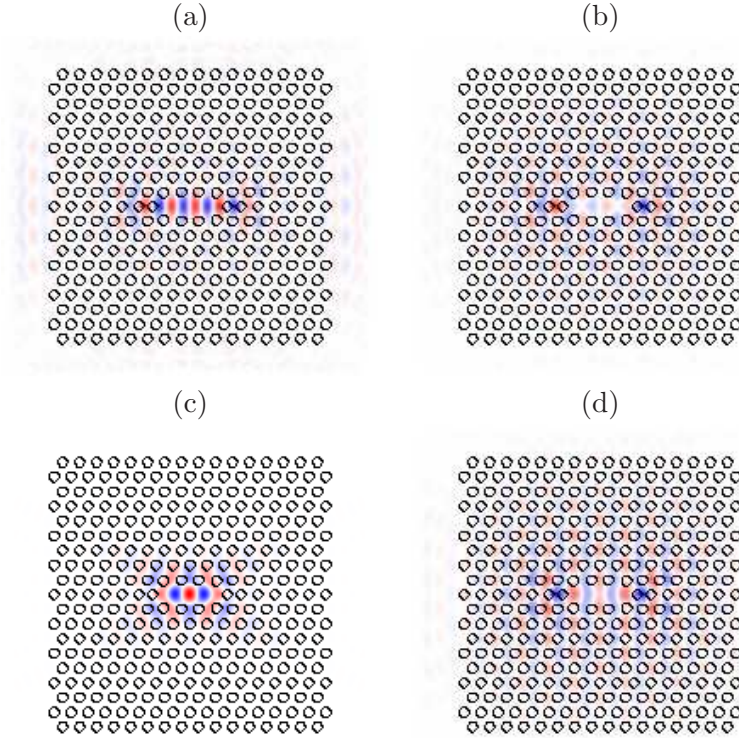


Figure 2.19: Even and odd modes of the L3 cavity with shifted holes (same design for the four patterns). (a): even mode at 922nm (rejected by symmetry), (b) even mode at 972nm (rejected by symmetry), (c): odd mode at 935nm (the studied one), (d): odd mode at 974nm (the one which creates problems).

The same kind of behaviour is obtained for L3 cavities. Following the previous studies on L3 cavities aiming at increasing the quality factors [28, 25, 29], only the two holes bounding the cavity in the  $\Gamma - K$  direction are moved. As the design is modified in only one direction, one does not expect to get directive emission in both directions, but only in the  $\Gamma - K$  one. The spatial distribution of the mode of interest is described on Figure 2.19 (c). Its field is maximum at the center of the cavity. The main problem with such modified L3 cavities is the onset of another mode with the same symmetries as the one of interest, the wavelength of which is close to the investigated mode (at least for some parameters). This mode is in fact composed of two independent uncoupled modes localized between the shifted hole and the next hole in the  $\Gamma - K$  direction <sup>21</sup> (see Fig. 2.19 (d)). I also observed experimentally this mode, the resonance wavelength of which varies spectrally over a broad range of

<sup>20</sup>Other parameters are:  $n = 3.45$ ,  $a = 270nm$ ,  $r = 80nm$ ,  $h = 260nm$ .

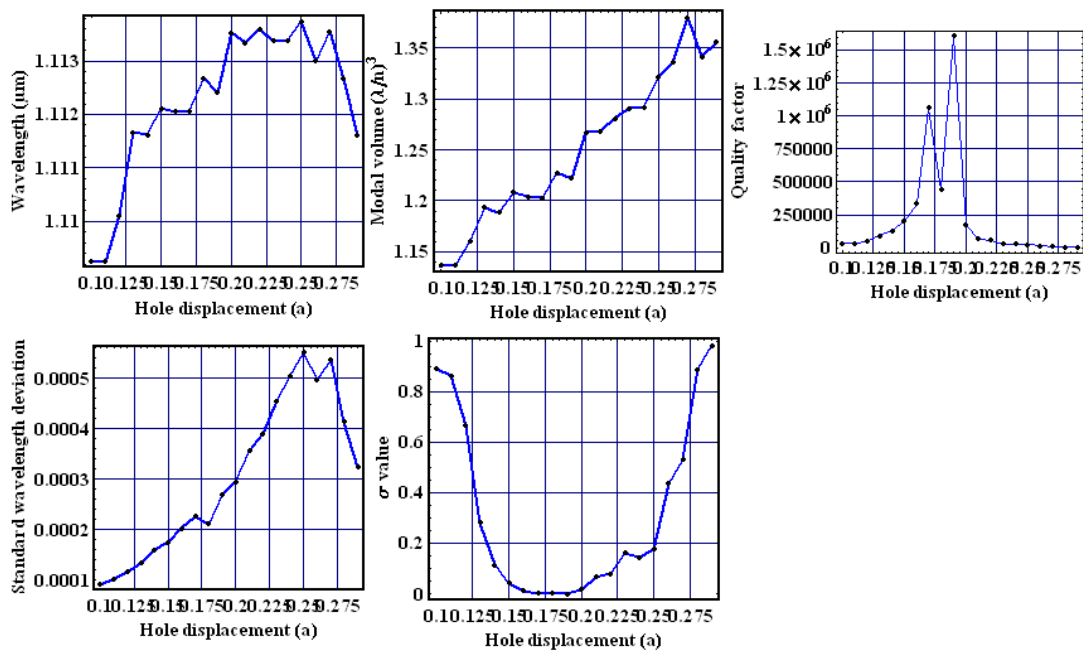


Figure 2.20: Characteristics of the fundamental mode of an L3 cavity as a function of the displacement  $d$  of the two holes bounding the cavity in the  $\Gamma - K$  direction <sup>20</sup>.

wavelength, from 10 nm below to 40 nm above the one of the investigated mode, depending on the hole shift. Figure 2.20 gathers the different values of various figures of merit of such cavities, as a function of the hole displacement. The two criteria used to check the monomode excitation condition are clearly not satisfied over a broad range of holes shift. This is due to the beating between two or more modes. As explained previously (§ 2.3.3), this beating creates noise on the calculated wavelength and alters the inferred value of the quality factors. The effect appears in the region of holes displacement, where the quality factor reaches its maximum. However, the region is not the region of interest in our case: we do not aim to get high quality factors but moderate ones combined to high collection efficiency. Consequently, since in the region of moderate  $Q$ s the monomode excitation condition is fulfilled, we did not bother about this beating and limited our studies to holes shift regions where only the mode of interest is excited.

### Radius of the nearest-neighbour air holes around the cavity

An additional possible geometrical modification in the cavity design consists in reducing the radius of the holes or of some of the holes around the cavity. Let us first focus on the “modified” H1 cavity and denote  $v$  the amplitude of the hole radius reduction: in this case, the radius of the six nearest-neighbour air holes around the cavity is equal to  $v \times r$ . We can combine the reduction of the holes to a displacement  $d$  of these holes as previously. Figure 2.21 gathers different optical characteristics of the cavity dipole mode (more particularly the ratio between the quality factor  $Q_c$  and mode volume  $V_c$  as

<sup>21</sup>For a complete list of the modes of the unmodified L3, see for example [37].

<sup>22</sup>I plotted  $Q_c/V_c$  instead of the Purcell factor because the highest Purcell values obtained here are not achievable in practice, since such Purcell factors would be limited by absorption effects or the dot-cavity system would shift into the strong coupling regime, before reaching such values. As an indication  $F_p \sim 0.08Q_c/V_c$  which should give here the maximal value of  $F_p \sim 10000$ .

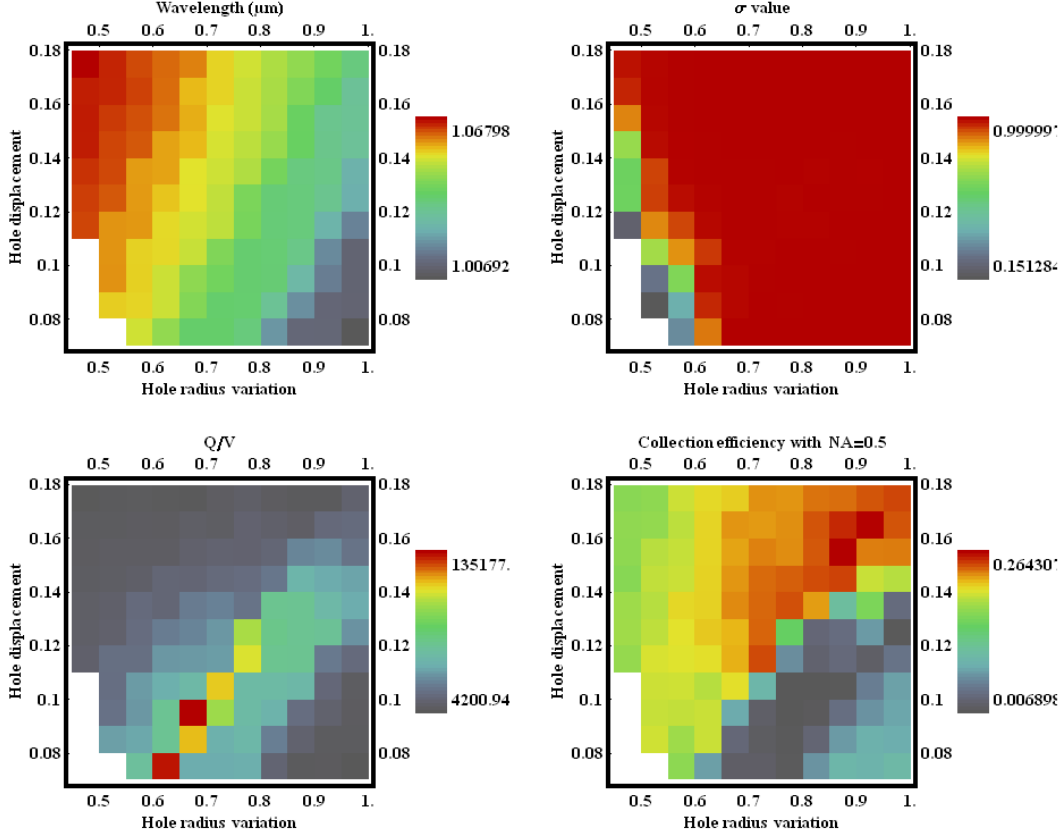


Figure 2.21: Characteristics<sup>22</sup> of the dipole mode of a modified H1 cavity as a function of the radius and the displacement of the six surrounding holes. White domains correspond to regions where the monomode excitation condition is far from being satisfied.

well as the collection efficiency), as a function of  $d$  and  $v$ . In the range of  $v$  and  $d$  values investigated here, the mode volume gets roughly constant (at most a factor 2 of variation). Conversely, for a fixed hole displacement  $d$ , one can find values of hole radius reduction  $v$  allowing for a strong increase of the quality factor compared to the cavity with  $v = 1$ . The maximal value of  $Q^{23}$  is obtained for coupled values of  $d$  and  $v$  verifying the linear equation  $v \sim 5.0d + 0.25$ . For a fixed displacement  $d$ , if one further reduces the hole radius compared to the one leading to a maximal value of  $Q_c$ , one observes a reduction of the quality factor and an enhancement of the collection efficiency. Again, the maximal value of the collection efficiency is obtained for coupled values of  $d$  and  $v$  verifying the linear equation<sup>24</sup>  $v \sim 4.28d + 0.22$ . Thus, for fixed values of  $d$ , the highest collection efficiency is achieved for values of  $v$  smaller than the ones exalting the quality factors. As previously, reaching the maximum of the collection efficiency requires stronger modifications of the photonic crystal geometry compared to the modifications required to maximize the quality factor: the collection efficiency enhancement is achieved for smaller holes and/or larger shifts. The variation of the collection efficiency varies significantly around this line defined by  $v \sim 4.28d + 0.22$ . Below this line (smaller shifts and larger holes), the emission is mostly in-plane, whereas above this line (larger shifts and smaller holes), part of the emission is directed upward. Below this line, the peak at the  $\Gamma$  point vanishes leading to only

in-plane emission.

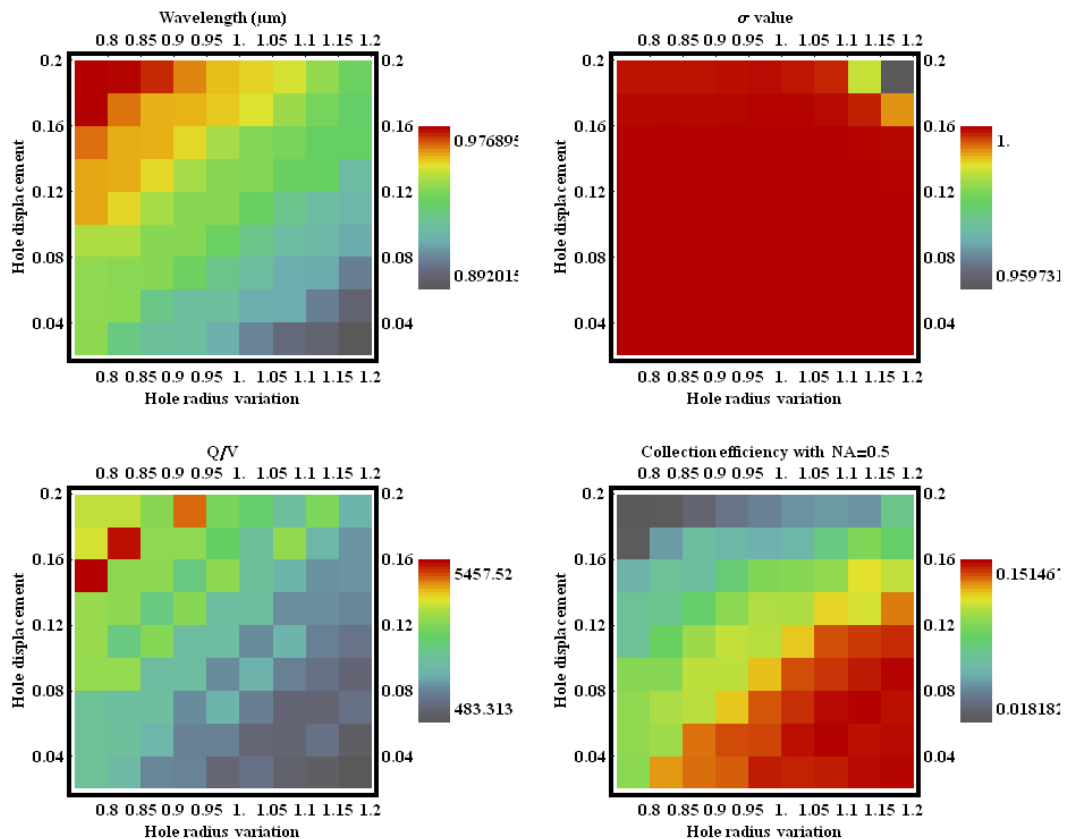


Figure 2.22: Characteristics of the L2 fundamental mode as a function of the holes radius and holes shift of the two holes bounding the cavity in the  $\Gamma - K$  direction <sup>25</sup>.

We could also expect in “modified” H1 cavities, that an increase of  $v$  above one would lead to a further decrease of the quality factor. The impact of values of  $v > 1$  has however been studied on other cavities: “modified” L2 cavities, consisting in removing 2 holes on a line in the  $\Gamma - K$  direction in a perfect triangular lattice of holes. The geometrical modifications are a shift and a radius reduction of the two holes bounding the cavity in the  $\Gamma - K$  direction. The main advantage of the “modified” L2 cavities compared to the “modified” H1 cavities is their high quality factor even achieved for  $v = 1$  and  $d = 0$  (see Fig. 2.22). For a fixed value of  $d$ , we observe a similar variation of the quality factor as a function of  $v$  for values of  $v < 1$ : the quality factor increases and then decreases when reducing

<sup>23</sup>This kind of simultaneous modification of the holes radius and holes shift has already been studied by D. G. Gevaux *et al* [33]. They considered the impact of these values on the quality factor, but for only coupled values of  $v$  and  $d$  verifying  $r = d \times a + v \times r$ . They also inferred an optimal value for the coupled values  $(v, d)$  maximizing the  $Q_c$  factor. However, my calculations indicate that this value of  $Q_c$  is not the absolute maximum achievable, which is achieved for values of  $v$  and  $d$  that do not verify the relation  $r = d \times a + v \times r$ .

<sup>24</sup>From a technological point of view, this linear relation  $v \sim 4.28d + 0.22$  is of great importance. Large shifts can suffer from proximity effects, which may induce a distortion of the hole shape or even a merging of the shifted holes with the next row of holes. For smaller holes, the required holes shift to optimize the collection efficiency is smaller. It is then more easy, technologically speaking, to reduce the holes radius and the hole displacements, than using designs with large holes and large displacements.

<sup>25</sup>Other parameters are:  $n = 3.45$ ,  $a = 270nm$ ,  $r = 80nm$ ,  $h = 180nm$ .

$v$ . For values of  $v > 1$ , we observe as expected a reduction of  $Q_c$ . Conversely, the variations of the collection efficiency are quite different, since the directivity of the emission is modified in only one direction when changing  $v$  and  $d$  in the “modified” L2 cavity. One notice however that for values of  $v > 2.9d + 0.73$  (right bottom corner of 2.22), the collection efficiency greatly increases. However, the quality factor is very low and not sufficient for the implementation of entangled photon sources.

### Membrane thickness

Photonic crystal cavities are scale invariant, that is, if the whole design is homothetically shrink in the three direction of space by a factor  $h$ , then its wavelength is also reduced by the same factor  $h$  whereas any other dimensionless characteristics are unmodified, such as the quality factor, the normalized mode volume, or the collection efficiency. Naively we might think it gives us the possibility to tune the wavelength of any photonic crystal cavity. However, from a technological point of view, this scaling is not so simple. Shrinking homothetically the whole design means to shrink also the membrane thickness. This would imply at least to grow a large number of samples. In practice, we deal with a membrane, the thickness of which is fixed during the growth and a homothetic modification of the design is thus impossible [38]. One thus has to investigate the impact of the membrane thickness on the optical properties of the cavities and check whether it is possible to make a homothetic modification of the cavity without modifying the effective membrane thickness while preserving the optical properties presented previously.

Figure 2.23 explores the effect of the membrane thickness  $h$  combined with the displacement  $d$  of the six holes in a “modified” H1 cavity. As usual, the maximal quality factor is not achieved for the same values of  $d$  and  $h$  as the maximal collection efficiency. However, the optimal values of  $d$  to maximize the quality factors do not depend significantly on the membrane thickness and the previous discussion on the effect of  $d$  stands for a wide range of thickness values. However the maximum achievable value of  $Q_c$  depends strongly on the membrane thickness. The variations of the collection efficiency as a function of the membrane thickness are much stronger: for a fixed holes shift  $d$  of about 0.17, corresponding to the configuration where the emission is highly directive, the collection efficiency increasing for smaller values of the membrane thickness. We also observe significant variations of the resonance wavelength.

### Constant lattice and filling factor of the photonic crystal

In order to tune the cavity wavelength, the scale invariance is not amenable to fabrication. Another parameter we can play with hopefully, is the filling factor  $f$  of the whole crystal, i.e. the proportion of air within a unit cell. The parameter  $f$  is related to the hole radius  $r$  and lattice period  $a$  by:

$$r = a\sqrt{f}\sqrt{\frac{3\sqrt{3}}{8\pi}} \quad (2.10)$$

This parameter is not easy to control technologically. Two techniques can be used to circumvent this problem: either processing cavities with various filling factors and constant electron beam dose during lithography, or processing cavities with constant filling factors and various electron beam doses during lithography. This should allow us to process on the same sample various cavities with various resonance wavelengths. Let us see here theoretically the impact of the variation of the filling factor on the cavities optical properties. All previous results were obtained with a filling factor of about 0.45. Figure 2.24 displays the characteristics of modified H1 cavities for varying filling factors and hole displacements. Even if the optimal displacement does not change much with the filling factor,

<sup>26</sup>These computations were made on InP ( $n = 3.17$ ). Other parameters' values are: lattice constant  $a = 400nm$  and membrane thickness  $h = 262nm$ .

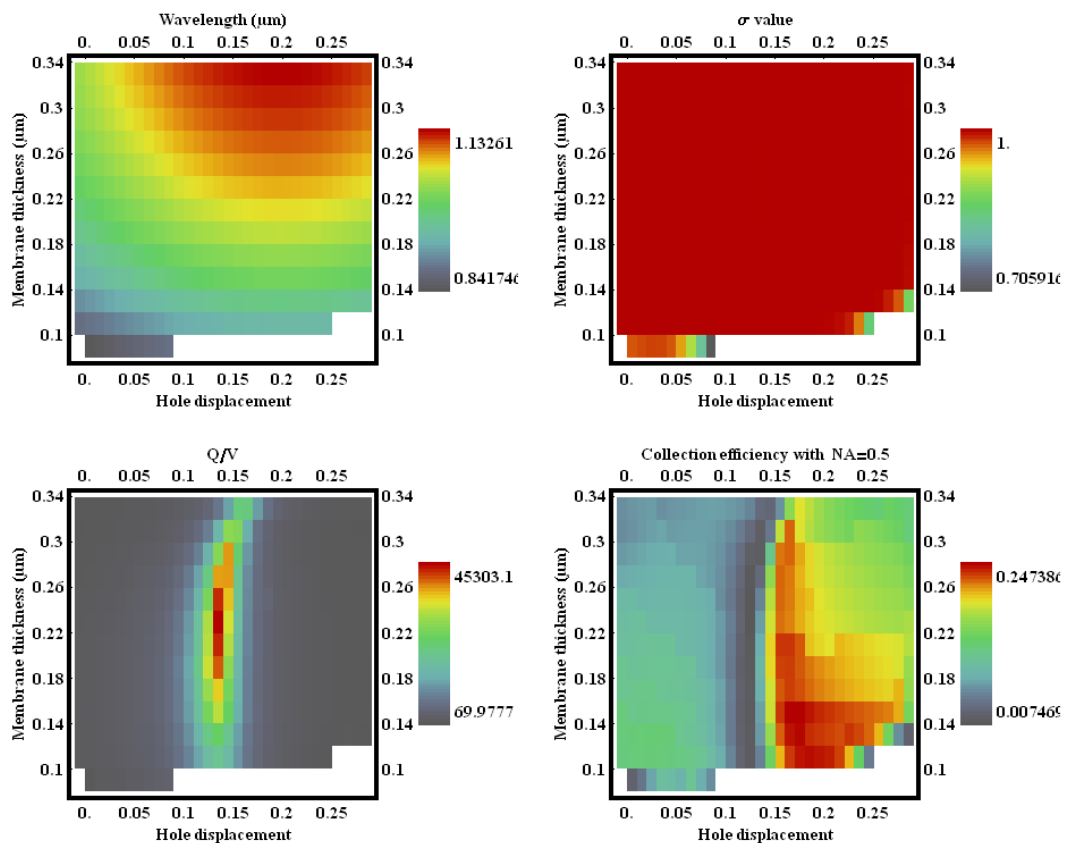


Figure 2.23: Characteristics of the H1 dipole mode as a function of the hole displacement of the six surrounding holes and of the membrane thickness <sup>19</sup>.

the obtained characteristic values strongly varies over this wide range of filling. For H1 designs made on InP the optimal filling for high  $Q_c/V_c$  values is 0.33, whereas for high collection it is 0.39. The maximal collection efficiency is locally flat, a small variation of the filling in order to spectrally match the resonance is tolerable ( $f \sim 0.39 \pm 0.02$ ). This demonstrates in particular that characteristics such as the radiative pattern are not too sensitive to the technologically induced fluctuations of the filling factor. For stronger modifications in order to obtain spectral matching, one has to be careful and check the resulting characteristics of the design.

### Distance to the substrate

Up to now, we have only considered cavities with a vertical symmetry: the membrane is suspended in air. However, as previously studied by other groups on the hexapole mode of the H1 design for instance [22], the presence of substrate below the membrane has a strong impact on the radiative pattern <sup>27</sup>. The interface between the air and the substrate acts as a mirror and reflects part of the back-emitted light. This reflected light interferes with the up-emitted one. I will illustrate this with a peculiar example: the “modified” H1 cavities optimized for the generation of polarization entangled

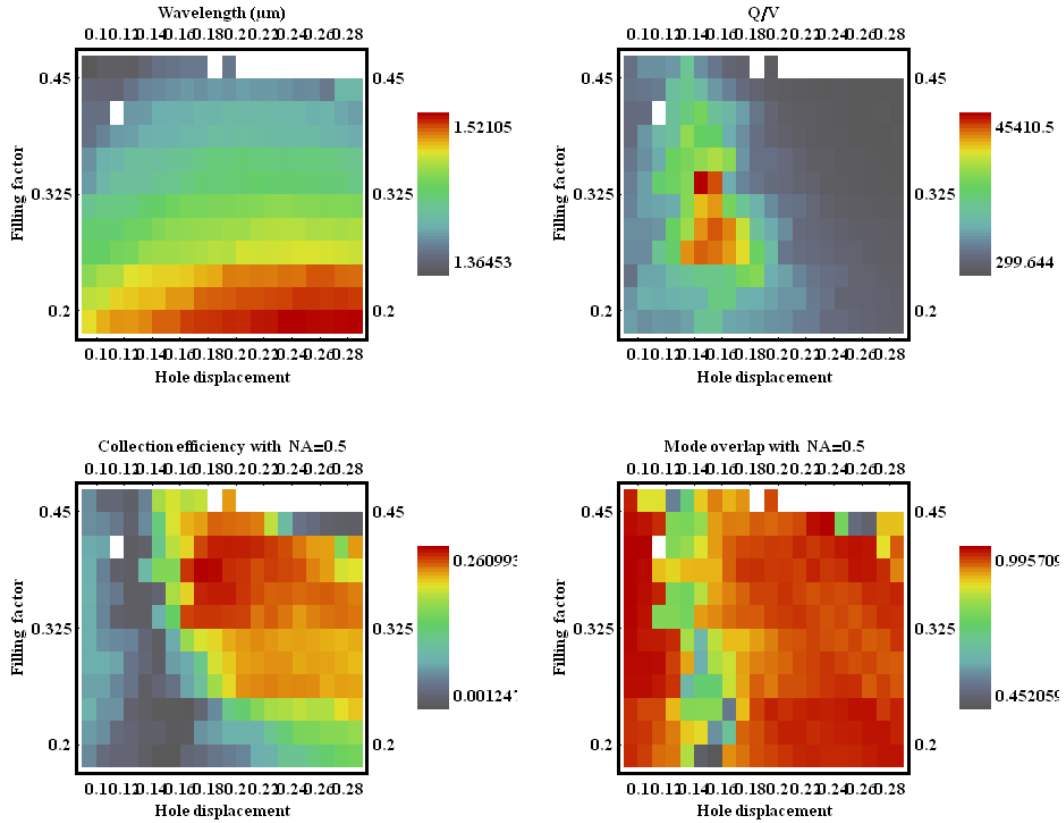


Figure 2.24: Characteristics <sup>26</sup> of the dipole mode of a H1 cavity as a function of the 6 holes' displacement and the filling factor of the photonic crystal. Values in the top right corner are to be taken cautiously considering their  $\sigma$  value.

photons <sup>28</sup>.

figure 2.25 shows the variations of the different key factors of interest (wavelength, Q/V and collection efficiency) of the cavity as a function of the distance separating the membrane from the substrate. If there is no air gap between the membrane and the substrate, all the energy stored in the cavity leaks into the substrate and we do not observe any more a 3D confinement of light in a small volume. For distance higher than  $0.4 \mu m$ , the wavelength is rather unchanged but the collection efficiency and the quality factor display large oscillations resulting from the constructive or destructive interference between the outgoing light and the reflected light on the substrate. The local maxima of the collection efficiency as a function of the air gap thickness correspond to local minima of the quality factor, and the other way round. We observe again that high collection efficiency and high quality factors are not compatible. Maxima of the collection efficiency are obtained for air thicknesses of  $\lambda_c/2$  and  $\lambda_c$ . For H1 designs that are not highly directive, such as the unmodified H1 cavity, the change of the factors of interest as function of the air gap is not as clearly observed, but phase opposition between Q/V and collection efficiency is still visible.

<sup>27</sup>For a discussion on other alternatives than a suspended membrane on a substrate, see for example [39]. At least for such directive designs, a Bragg mirror with high reflectivity at the cavity's wavelength, instead of the substrate, should give even better results.

<sup>28</sup>The geometrical parameters values are:  $a = 270nm$ ,  $r = 80nm$ ,  $h = 180nm$ ,  $d = 0.16a$  and  $v = 0.9$ .

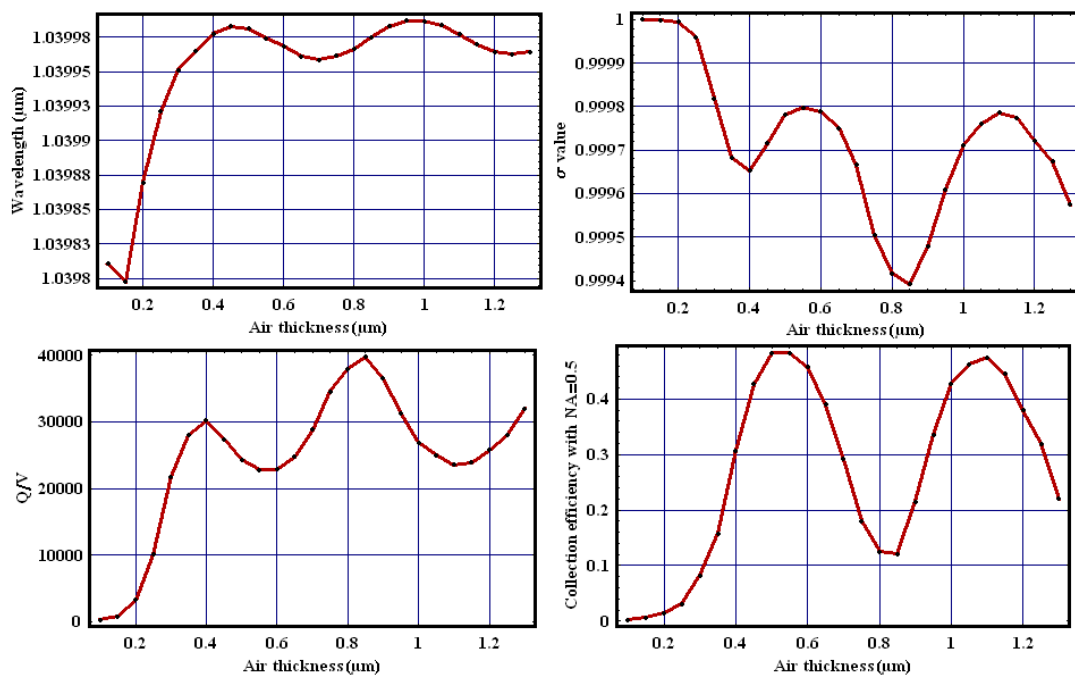


Figure 2.25: Characteristics of the “modified” H1 dipole mode as a function of the distance between the membrane and the substrate. A simulation of this same design without a substrate gives the same wavelength,  $Q/V = 28800$  and  $\eta = 26\%$  for  $NA = 0.5$ .

#### 2.4.4 Impacts of the absorption on the optical properties of the cavities

It has been observed <sup>29</sup> that the quality factor of GaAs based cavities is generally limited under  $Q = 10000$  due to absorption of the wetting layer, or free electron charges on the holes’ sidewalls. The quality factor of the cavity, taking in account the absorption ( $\alpha$ ) is given by

$$\frac{1}{Q} = \frac{1}{Q_c} + u * \alpha \quad (2.11)$$

While it is simple in general to calculate the absorption coefficient to obtain a quality factor of  $Q = 10000$ , in the case of photonic crystal cavities, such estimations are complex, since they require to integrate spatially the interaction of the optical mode with the absorbing medium and take into account the group velocity. On the other hand a FDTD simulation can estimate the absorption coefficient directly. Figure 2.26 displays the characteristics of a modified L3 cavity. the two boundary holes in the  $\Gamma - K$  direction are shifted by  $0.16a$  in order to maximize the quality factor. A  $0.5\text{nm}$  thick (between one to two monolayers) absorbing layer is added in the centre of the suspended membrane.

The cavity has an intrinsic quality factor of  $Q_c = 59000$ , and the evolution of  $1/Q$  of figure 2.26 can indeed be fitted to a simple line ( $u = 3, 3 \cdot 10^{-6} \text{cm}$  in 2.11). A quality factor of  $Q=10000$  implies an absorption coefficient of  $\alpha = 40 \text{cm}^{-1}$ . This absorption coefficient is in fact an order of magnitude greater than the absorption coefficient of the wetting layer at resonance. Out of resonance, the absorption of the wetting layer should be even lower. One can hence conclude that most of the absorption is due to either free electrons absorption, or an enhanced absorption of the wetting layer due to the strong light confinement.

Note that, as expected, the absorption does not impact the emission wavelength or the emission

<sup>29</sup>Private communication from various research groups

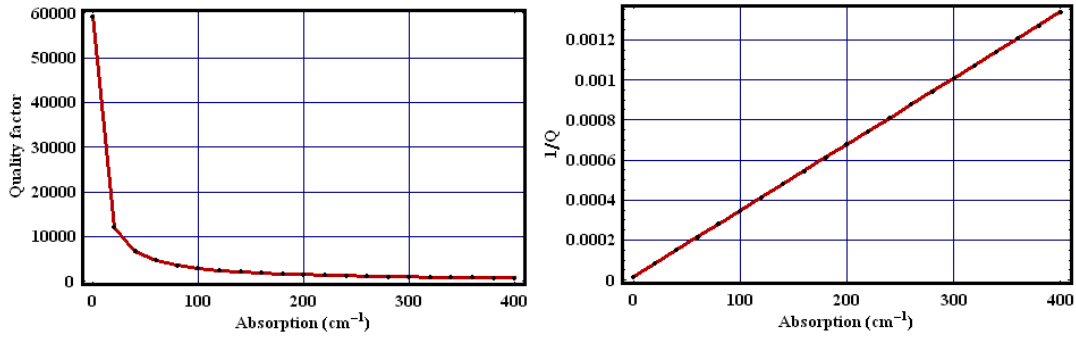


Figure 2.26: Effect of the absorption on the optical properties of a “ modified” L3 cavity displaying a high quality factor ( $s = 0.16a$ ). The monomodal condition is always verified.

## 2.5 Experimental wavelength resonance and quality factors of photonic crystal cavities

In order to validate our theoretical predictions, some of the optical predicted properties have been checked experimentally, namely the optical wavelength and the quality factor. Before describing the experimental results I obtained, I will describe the experimental set-up I used.

### 2.5.1 Experimental setup

In order to experimentally study the modes of the photonic crystal cavities, the cavities are etched on a suspended membrane embedding a dense array of quantum dots. In order to measure the quality factor, the dots are excited by a continuous wave laser. Thanks to their large inhomogeneous linewidth, the quantum dots emission can be considered an incoherent white light source inside the cavity volume. The cavity therefore plays the role of a filter and one can measure the quality factor and emission wavelength directly on a spectrometer. Discussion on the validity of this technique based on the luminescence of an array of dots embedded in the cavity is described in more details in [40].

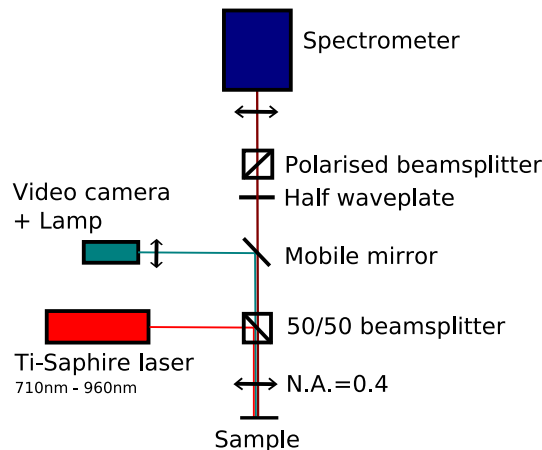


Figure 2.27: Experimental setup to spectrally study photonic crystal cavities by photoluminescence.

Figure 2.27 depicts the experimental setup. The sample is placed inside a liquid flow He

cryostat cooled down at 4K. An objective with a numerical aperture of 0.4 is placed in front of the sample and is used to both focalize the pump light and collect the luminescence. Pumping is obtained by a Ti-Sa laser operating at 800nm. The luminescence is separated from the laser by a dichroic mirror, then a set of an achromatic halfwave plate and a polarizer beamsplitter allows the selection of the linear polarization. The optical spectrum is measured by a nitrogen cooled CCD camera placed after a 250mm monochromator. The spectral resolution is estimated to be  $\sim 0.2nm$ .

### 2.5.2 Wavelength resonance of “modified” L3 cavities

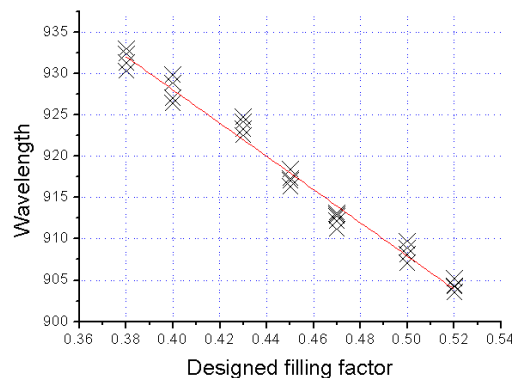


Figure 2.28: Measured wavelength of L3 cavities with various filling factors.

Figure 2.28 displays the measured wavelength  $\lambda_{exp}$  of several cavities with the same design (L3 with shifted holes) and various filling factor  $f_{GDS}$ . The wavelength varies linearly as  $\lambda_{exp} = 1008nm - 200nm \times f_{GDS}$ . The predicted wavelength  $\lambda_{th}$  as a function of the filling factor  $f_{th}$  is  $\lambda_{th} = 1051nm - 292nm \times f_{th}$ . The comparison between both wavelengths  $\lambda_{exp}$  and  $\lambda_{th}$  indicates that  $f_{GDS} = 1.46f_{th} - 0.215$ . This adjustment is however sensitive to the lattice constant of the crystal. For smaller lattice constants the deviation of the experimental filling factor from the nominal one increases due to proximity effects. Here the lattice constant value was  $a = 250nm$ . Moreover it obviously also depends on the electron beam dose during lithography. It is therefore necessary to produce several cavities with a small variation of the filling factor ( $\Delta r \sim 1nm$ ) in order to be sure to obtain the expected wavelength. For a fixed filling factor, the experimental wavelength fluctuates around its mean value by  $1nm$ . This corresponds for example to a fluctuation of less than  $0.3nm$  in the holes' radius. Such fluctuations are inherent in the design's sensitivity.

### 2.5.3 Quality factor of modified L3 and H1 cavities

Figure 2.30 represents the experimental values of the inverse of the quality factor for several “modified” L3 and H1 cavities, as a function of their resonant energy. These values have been measured under continuous non resonant pumping (800nm). The absorption of the quantum dots does not permit a direct measurement of the quality factor of the cold cavity. The cold cavity value of the quality factor can be obtained by saturating the quantum dots. Figure 2.29 depicts the evolution of the emitted power and inverse linewidth as a function of the pumping power. No lasing can be observed on the power curves, although a kink in the curve is present. The quality factor steadily rises up to  $P \approx 35\mu W$  due to the gradual saturation of the quantum dots. The decrease of the quality factor at higher excitation powers is probably due to thermal broadening of the emission line.

Figure 2.30 shows the measured quality factors as a function of the emission wavelength. Clearly the quality factor saturated at high values. This value is not the limit of the spectrometers

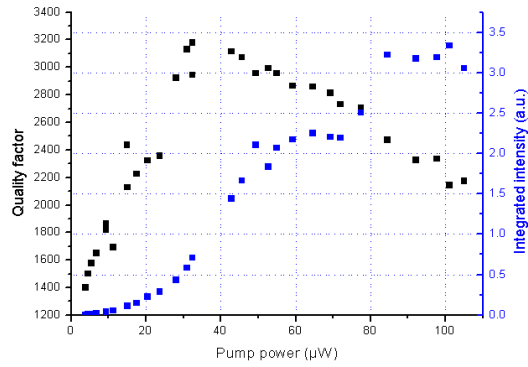


Figure 2.29: Example of the evolution of the mode’s intensity and quality factor as a function of the excitation power.

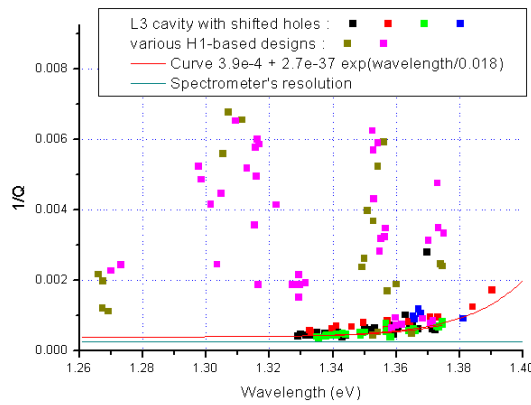


Figure 2.30: Inverse of the quality factor for several “modified” L3 and H1 cavities, as a function of their resonance energy. The various colours correspond to various electron beam doses during lithography on the same cavity designs.

resolution, nor the quantum dot’s absorption. One observes an exponential increase of the lower limit of  $1/Q$  as function of the cavity energy. This effect could arise from an Urbach tail of the wetting layer or even of the GaAs. Indeed the inverse quality factor increases linearly as a function of the absorption. Moreover the Urbach’s rule states that the absorption of a quantum well increases exponentially for increasing frequency. The combination of these two facts can explain the exponential shape of the minimal measured value of  $1/Q_c$ . The reason of the high value of this absorption’s tail remains unclear. However, the highest quality factors measured on GaAs photonic crystal slab cavities around 950 nm do not exceed 10000. Higher quality factors have been obtained [41], but at telecommunications wavelengths, far from the band gap of the surrounding material. Yet, quality factors of few thousands are sufficient to implement entangled photon sources.

## 2.6 Experimental far-field patterns of photonic crystal cavities

### 2.6.1 Choice of the material

The goal of the following section is to experimentally measure the emission diagrams of processed H1 and L3 cavities and compare the results to the theoretical simulations. As demonstrated in § 2.4.3 the major difference of the emission diagram is mostly visible at large numerical apertures, above  $NA=0.5$ . This condition is incompatible with the current setup, since InAs/GaAs based photonic crystal cavities are operated at 4K. Since large numerical aperture microscope objectives with long working distance are not available, it is necessary to operate the cavities at room temperature and replace the standard objective with a metallographic one.

However, several issues are associated with the operation of InAs/GaAs systems at room temperature. First, the emission wavelength of the quantum dots is not centred at 950 nm anymore, but mostly around  $1.3\mu m$ , outside of the detection window of the Si detector. Secondly, the quantum efficiency of the quantum dots is strongly reduced due to thermal escape of the carriers, and also, the GaAs surfaces are known to be efficient carrier traps at room temperature, implying that one must use very high pump powers in order to saturate the traps.

In order to circumvent the above limitations, two steps were undertaken.

- The device was protected by an HSQ resist and then annealed at  $700^{\circ}C$  during 1 minute and 30 seconds. This technique is known to shift the emission wavelength of the quantum dots.
- The system is operated at  $-20^{\circ}C$  using a Peltier cooling under a constant Nitrogen flow to avoid condensation

This approach did not give conclusive results and no luminescence of photonic crystals was observed even at lower temperature.

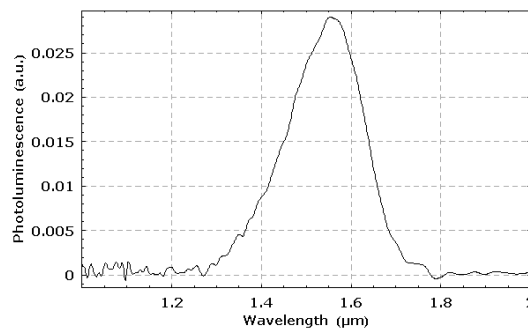


Figure 2.31: Bulk spectrum of the InP sample.

On the other hand, photonic crystal cavities based on InAs/InP material combination are known to operate at room temperature, and are routinely produced at the laboratory (figure 2.31). I therefore decided to make the emission diagram experiments using InAs/InP photonic crystals. Since their emission wavelength is around  $1.5\mu m$ , I used another setup available.

### 2.6.2 Experimental setup

A simple version of the experimental setup is described on figure 2.32.

The measurement is performed step by step by moving a pinhole perpendicularly to the photoluminescence path. The desired measurement is in fact a measurement of the intensity map of the

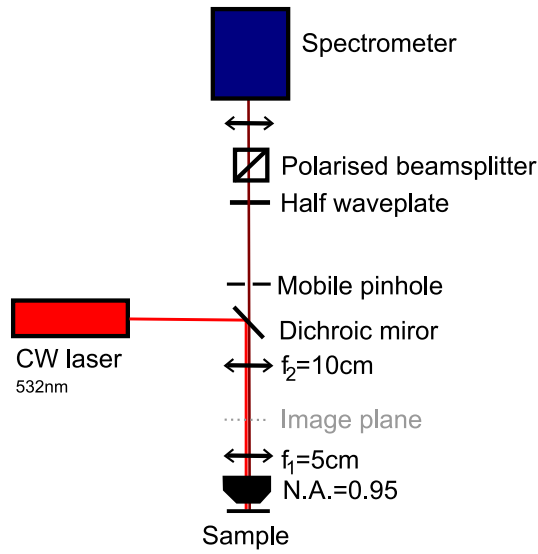


Figure 2.32: Radiative patterns measurement's setup. The objective and the lens  $f_1$  constitute an imaging system, and the sample is at the focal of the objective. The lenses  $f_1$  and  $f_2$  are mounted in a confocal setup. The mobile pinhole is at the focal of the lens  $f_2$ . A video system to localise the cavities is also present but not schematised here.

Fourier transform of the image plane of the photonic crystal cavity, thus the pinhole is placed on the focal of a lens or of the objective. This is impracticable. The output focal plane of our objective is at the level of its mounting. If the pump laser is inserted after the pinhole, much of its power will be lost, and there is not sufficient room between the objective and its output focal plane to leave room to the dichroic mirror used to inject the pump laser. Therefore the image plane must be transferred and reconstructed further away from the objective, and then another lens must perform the Fourier transform.

Our setup is as follows (see. figure 2.32): the cavity is pumped by a laser and its luminescence is collected through an objective of numerical aperture  $NA = 0.95$  and corrected for the far-infrared, with a magnification of 80 and a pupil's diameter of  $5\text{mm}$ . A first lens (with a focal  $f_1 = 5\text{cm}$ ) constitutes with the objective an imaging system, and the plane at the luminescence-output focal is the required transferred image plane of the cavity. This first lens and a second one (with focal  $f_2 = 10\text{cm}$ ) are set in a confocal configuration, such as the luminescence output focal plane of the second lens is the desired Fourier plane of the image of the cavity. The moving pinhole used to spatially select the intensity of this Fourier signal is placed on this plane. The dichroic mirror used to inject the pump laser is inserted between the pinhole and the second lens. Eventually the photoluminescence undergoes some diffraction after the pinhole due to the size of the pinhole. The photoluminescence is polarisation selected then sent through the spectrometer.

In order to avoid diffraction during the photoluminescence propagation from the objective's pupil (with a diameter  $D = 5\text{mm}$ , which is the smallest pupil in the setup) to the pinhole, the distance between these two is  $d = 27\text{cm}$ . Taking into account the magnification of the confocal system, this gives an Airy radius of the diffraction at the level of the pinhole of  $r_{\text{Airy}} = 1.22d\lambda_c/D \times f_2/f_1 = 198\mu\text{m}$ . A smaller pinhole will not lead to a better resolution. I took a diameter of  $D_{\text{pinhole}} = 400\mu\text{m} \simeq 2r_{\text{Airy}}$ . At the level of the pinhole, the diameter of the photoluminescence beam is  $D_{\text{beam}} = D \times f_2/f_1 = 10\text{mm}$ . Under the strong assumption that the photoluminescence intensity is equally distributed across the whole section of the beam, the use of such a pinhole leads to a reduction of the signal by a factor

$D_{\text{pinhole}}^2/D_{\text{beam}}^2 = 625$ . I compensated this loss by increasing the integration time from 0.5s to 5s for each pinhole's position. Because the spectral camera is a low noise one cooled at nitrogen temperature, the signal to noise (dark count) ratio remained of the order of 700.

The moving steps of the pinhole were set to the value of its diameter ( $400\mu\text{m}$ ) in order to cover the whole beam's section. About 450 acquisitions were needed to perform the measure of one far-field pattern, leading to a total acquisition time of  $\sim 50\text{min}$ . This remained an acceptable duration for such an acquisition: the pump laser's intensity is stable on time scales ten times greater than that, as well as for the mechanical stability. The scanned region is a few pixels wider than the photoluminescence beam's cross-section, but due to bad initialisations some of the patterns displayed further on are badly centred and the pattern is a few pixel cut on one side. Putting this aside, when the pinhole was outside this scanned region the spectrometer's signal went down to the dark count level as expected and confirmed all the photoluminescence's beam was scanned.

First the pinhole was opened to allow spectral localisation and to optimise the positioning of the sample, then the far-field's scanning was performed. Each spectrum is fitted with a Lorentzian to deduce the intensity of the mode corresponding to the pinhole's position, as well as the mode's spectral position, its linewidth and the photoluminescence intensity of the uncoupled dot at the mode's wavelength (further called "noise" for simplicity). The data for which the signal was too low and the fit did not converge correctly were finally removed.

### 2.6.3 Far-field measurements

We performed far-field measurements on modified H1 cavities as well as modified L3 cavities. The obtained results are described on the following paragraphs

#### H1-type cavities

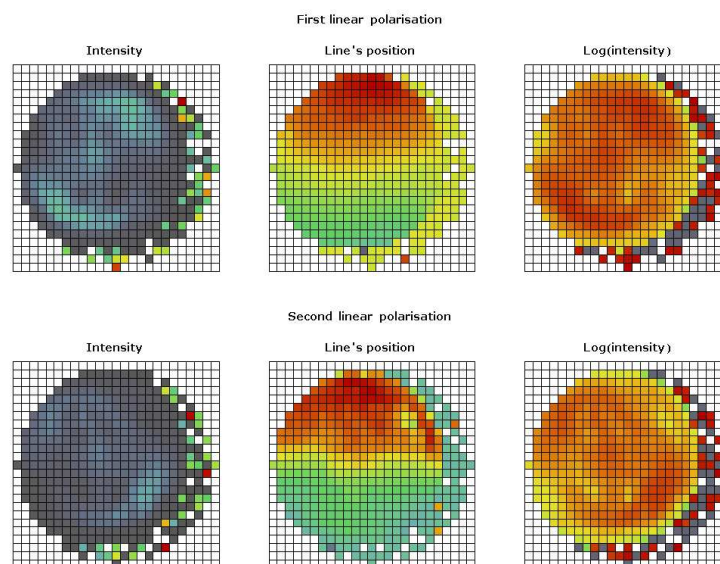


Figure 2.33: Patterns measured for a modified H1 design, for both polarizations <sup>30</sup>.

<sup>30</sup>The deviation of the measured wavelength is well explained by the variation of the angle at which the beam enters the spectrometer. This angle's variation corresponds to the displacement of the pinhole.

Figure 2.33 shows a typical measured pattern of H1 cavities. The most striking feature is that the emission diagram seems to be independent of the technological design in contrast with the theoretical simulations § 2.4.3 in spite of the wide variety of the values chosen for the displacement of the six surrounding holes and for the filling factors. Reasons remain unclear today. On the other hand, the measured emission diagram for both polarizations is clearly different as expected<sup>31</sup> from H1 structures. The two emission patterns are symmetric by a 90° rotation corresponding to the two polarizations.

Note that for most of the cavities, the two polarization emission wavelengths were not degenerate as expected from perfect H1 cavities, but present a splitting of about 4 nm. This technologically induced imperfection is already well known [5]. Another remarkable point is that the polarisation orientations (and the corresponding far-field patterns) are rotated by  $\pm 45^\circ$  from the  $\Gamma - K$  direction. This could give an indication on the technological issues behind the mode splitting.

### L3-Type cavities

Similar results as with the H1 cavities were obtained on modified L3 cavities and the emission patterns are shown on figure 2.36

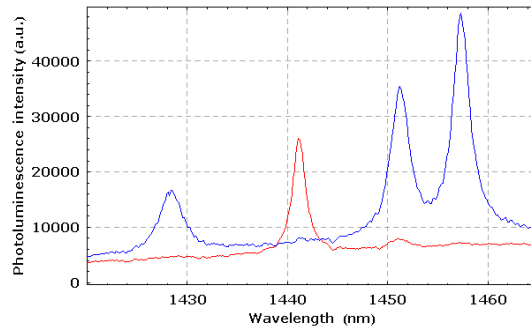


Figure 2.34: Spectrum of a modified L3 design, for both linear polarisations. The fundamental mode is most probably the one on the blue curve at 1458nm.

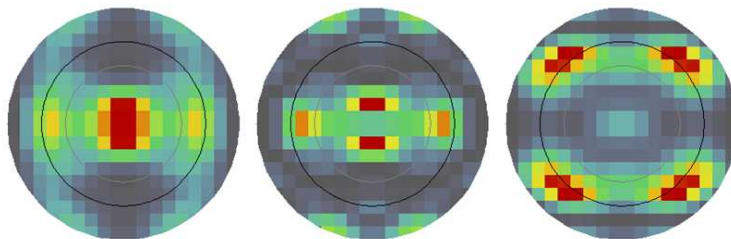


Figure 2.35: Examples of the diversity of far-field patterns which were expected to be measured.

This experiment was also performed on L3 designs modified in the way described on the next chapter (figure 3.8). For now we should only retain this design contains three modes with the same polarisation (figure 2.34): the usual L3 mode and the two modes localised on the extremities of the L3 and spectrally close to the fundamental one (see figure 2.19). These three modes were indeed experimentally witnessed at their expected wavelength and were indeed spectrally close as one can

<sup>31</sup>These expectations were obviously obtained with simulations taking into account the substrate (§ 2.4.3).

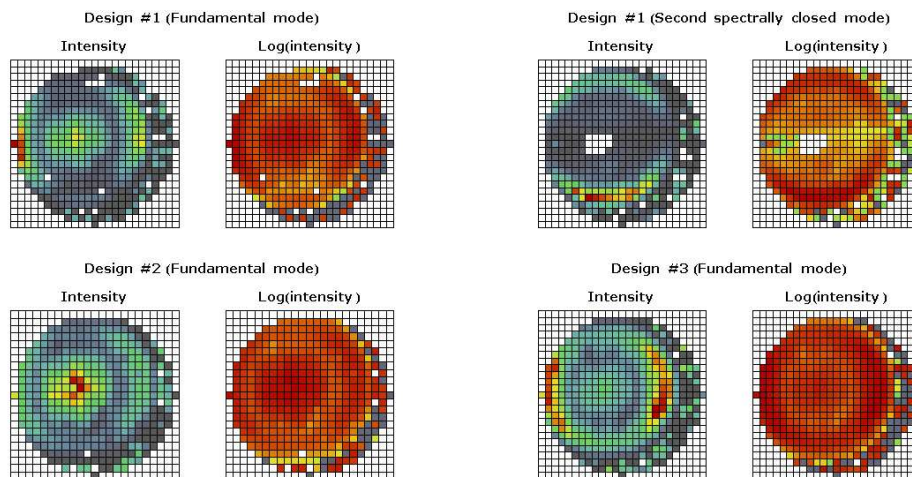


Figure 2.36: Patterns measured for some of the modes of three different modified L3 designs.

see on figure 2.34. Again many variations of the design were etched in the hope to measure different patterns (figure 2.35) but this expected diversity was not measured. All the patterns do have the same shape with a central peak surrounded by two crescents. Only the relative intensities of these three elements changes from one design to another.

### Conclusion to this experiment

Even if emission diagrams of photonic crystal cavities are of great interest in order to be able to efficiently collect the emitted light, for quantum information applications, all other far-field measurement were performed on lasing modes, which permits to be much less regarding on the noise problem and to perform such a measurement with much simpler setups.

From what we observe, our experimental and theoretical results do not coincide, the reason for this remains unknown.

Because of a lack of other means I tried to compare the measured patterns with all the other kinds I saw during my PhD. These patterns are surprisingly close to the in-plane distribution of the intra-cavity's wavevectors restricted to (less than <sup>32</sup>) the light-cone. The difference in the computations between the expected far-fields and this one is that the fields' values taken to compute them is, in the first case, in the centre of the membrane, whereas in the second case, it is just above the membrane, 100nm above the other. This distance is smaller than the resolution depth of the objective, but I expected to measure what I named far-field, and not this intra-cavity Fourier transform, because the wavevectors of these intra-cavity fields have a null vertical component and therefore could not propagate inside the setup.

On the other hand, if one accepts that this optical setup performs what I am expected, then these experimental results seem to state that the simulation's predictions are false. This calls into questions the method used to perform these far-field's simulations, which are now often used. Most of all, as I already claimed, similar results to the one we predicted for H1 designs, were obtained by another team with another simulations software and another method [16].

<sup>32</sup>In fact this cannot be the complete lightcone but only its part corresponding to the numerical aperture  $NA = 0.95$ . Considering the small difference between 0.95 and 1 I do not insist more on this aspect.

## 2.7 Conclusion

We have described how bi-dimensional photonic crystal cavities are etched on a GaAs sample, and how it is possible to simulate accurately the propagation of the light inside these sub-wavelength scaled structures. These simulations allowed us to study various designs, mostly based on the H1 (one hole removed) and the L3 (three holes removed in a row), in order to obtain the required cavity characteristics for the efficient generation of entangled photon, both in the time-bin and polarisation encoding schemes. For this aim various characteristics of these cavities were computed: the wavelength, the volume, the quality factor, the radiative pattern, the collection efficiency and the mode overlap. In order to validate these simulations some experimental measurement of these characteristics were also performed. These experiments show that the absorption inside the photonic crystal cavities can be explained as an Urbach's tail of the wetting layer if one accepts the assumption that the photonic crystal somehow degrades by at least one order of magnitude the absorption quality of the wetting layer. This absorption is a strong limit on the quality factor of GaAs photonic crystal cavities around  $950nm$  but has a smaller impact and becomes quite negligible for higher wavelengths. Measurements on room temperature InP photonic crystal cavities around  $1500nm$  (close to the C-band telecommunication wavelength) were also performed in the hope to confirm the predicted far-fields, but the differences between the expected and the measured results are not explained.

## Annex: From Scanning Electron Microscopy images to simulation

In practice, the experimental study of a photonic crystal cavity is done in two steps: (1) design of the structure and (2) processing of the structure. Yet, due to technological defects, some deviations appear in the geometrical parameters of the fabricated resonators in comparison to the nominal parameters. One may wish to explain the behaviour and characteristics of one particular experimental cavity and simulate its optical properties. This annex focuses on the methodology I developed with this aim.

I am interested here in only one particular cavity, for which the wavelength and the quality factor have been experimentally measured. We can easily make an image of this cavity by use of a Scanning Electron Microscope (SEM). This image gives the exact design of the cavity, technological fluctuations included (see figure 2.37 for example). From this image it is possible to deduce the spatial distribution of the refractive index with a very simple image analysis algorithm: black regions with a sufficiently high number of coincident pixels are holes, the rest is the membrane. The only important parameter in this process is the threshold which separates these two domains. The spatial resolution of the simulation is poorer than the original image's resolution (if the electronic microscope was adequately used as for 2.37 (a)). This implies that the exact value of the threshold value is not so important. The histogram of the pixels' values of the cavity's image contains two maxima corresponding to the mean colour value of the holes and of the semiconductor (2.37 (b)). The threshold has to be around the local minimum between these two maxima.

I performed this algorithm only on some cavities etched on InP samples. The calculated wavelength obtained this way agrees with the experimental one with a precision of more than  $5nm$ . The simulated quality factor is usually of the same order of magnitude as the experimental one. These results are a good indication of the validity of this approach and may be extended to the calculation of other values that cannot be measured experimentally but easily computed, such as the cavity volume. We used this method for the work published in [43].

## Bibliography

- [1] E. Yablanovitch. Inhibited spontaneous emission in solid-state physics and electronics. *Phys. Rev. Lett.*, 58:2059, 1987.

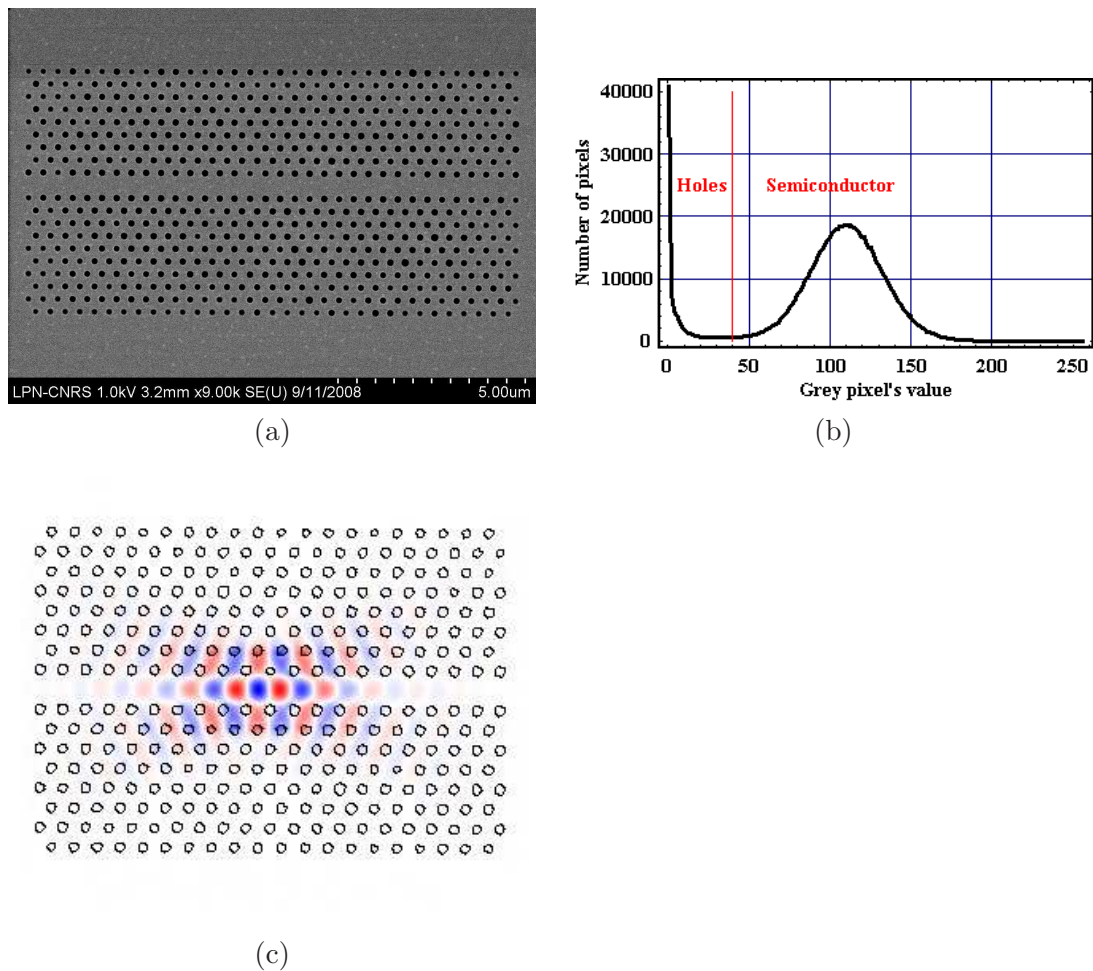


Figure 2.37: (a): SEM image of a photonic crystal cavity. The original design is a heterostructure where the lattice constant is slightly increased along the waveguide over two periods, in the middle of the structure [42, 5]. (b): statistics of the pixels values of the image (a). (c): Electric internal cavity field of the simulated structure. The roughness of the holes results from the plotting and is much enhanced compared to the exact roughness of the real and simulated structures. Our software performs some smoothing which does not appear here.

- [2] S. John. Strong localization of photons in certain disordered dielectric superlattices. *Phys. Rev. Lett.*, 58:2486, 1987.
- [3] N. Litchinitser *et al.* Review of optical simulation softwares. <http://optical-waveguides-modeling.net/>.
- [4] J. D. Joannopoulos, S. G. Johnson, J. N. Winn, and R. D. Meade. *Photonic crystals, Molding the flow of light*. Princeton University Press, 2007.
- [5] R. Braive. *Contrôle de l'émission spontanée dans les cristaux photoniques*. PhD thesis, 2008.
- [6] L. C. Andreani and D. Gerace. Photonic-crystal slabs with a triangular lattice of triangular holes investigated using a guided-mode expansion method. *Phys. Rev. B*, 73:235114, 2006.
- [7] F. Wen, S. David, X. Checoury, M.El Kurdi, and P. Boucaud. Two-dimensional photonic crystals

- with large complete photonic band gaps in both te and tm polarizations. *Opt. Expr.*, 16:12278, 2008.
- [8] L. C. Andreani *et al.*. Research team “photonic crystals” at the university and infm unit of pavia. <http://fiscavolta.unipv.it/dipartimento/ricerca/Fotonici/Index.htm>.
- [9] R. Braive, L. Le Gratiet, S. Guilet, G. Patriarche, A. Lemaître, A. Beveratos, I. Robert-Philip, and I. Sagnes. Inductively coupled plasma etching of gaas suspended photonic crystal cavities. *J. Vac. Sci. Technol. B*, 27:1909, 2009.
- [10] R. Braive, S. Barbay, I. Sagnes, A. Miard, I. Robert-Philip, and A. Beveratos. Transient chirp in high-speed photonic-crystal quantum-dot lasers with controlled spontaneous emission. *Opt. Lett.*, 34:554, 2009.
- [11] A. Taflove and S. C. Hagness. *Computation of electrodynamics: the finite difference time-domain method*. Archtec House Publishers, 2005.
- [12] S. G. Johnson *et al.*. The meep software. <http://ab-initio.mit.edu/wiki/index.php/Meep>.
- [13] A. Farjadpour, D. Roundy, A. Rodriguez, M. Ibanescu, P. Bermel, J. D. Joannopoulos, S. G. Johnson, and G. Burr. Improving accuracy by subpixel smoothing in fdtd. *Opt. Lett.*, 31:2972, 2006.
- [14] S. Mazoyer, J. P. Hugonin, and P. Lalanne. Numerical tool for analyzing light propagation in photonic-crystal waveguides in the presence of fabrication imperfections. *Proc. SPIE*, 7366:736611, 2009.
- [15] S. G. Johnson, S. Fan, A. Mekis, and J. D. Joannopoulos. Multipole-cancellation mechanism for high-q cavities in the absence of a complete photonic band gap. *Appl. Phys. Lett.*, 78:3388, 2001.
- [16] F. Romer and B. Witzigmann. Spectral and spatial properties of the spontaneous emission enhancement in photonic crystal cavities. *Journ. Opt. Soc. Am. B*, 25:31, 2008.
- [17] J. Vuckovic, M. Loncar, H. Mabuchi, and A. Scherer. Optimization of the q factor in photonic crystal microcavities. *IEEE Journ. Quant. Elec.*, 38:850, 2002.
- [18] D. Englund, I. Fushman, and J. Vuckovic. General recipe for designing photonic crystal cavities. *Opt. Expr.*, 12:5961, 2005.
- [19] M. Halder, A. Beveratos, N. Gisin, V. Scarani, C. Simon, and H. Zbinden. Entangling independent photons by time measurement. *Nat. Phys.*, 3:692, 2007.
- [20] J. Fulconis, O. Alibart, J. L. O’Brien, W. J. Wadsworth, and J. G. Rarity. Nonclassical interference and entanglement generation using a photonic crystal fiber pair photon source. *Phys. Rev. Lett.*, 99:120501, 2007.
- [21] O. Painter, J. Vuckovic, and A. Scherer. Defect modes of a two-dimensional photonic crystal in an optically thin dielectric slab. *Journ. Opt. Soc. Am. B*, 16:275, 1999.
- [22] Se-Heon Kim, Sun-Kyung Kim, and Yong-Hee Lee. Vertical beaming of wavelength-scale photonic crystal resonators. *Phys. Rev. B*, 73:235117, 2006.
- [23] C. Sauvan, P. Lalanne, , and J. P. Hugonin. Slow-wave effect and mode-profile matching in photonic crystal microcavities. *Phys. Rev. B*, 71:165118, 2005.

- [24] K. Nozaki and T. Baba. Laser characteristics with ultimate-small modal volume in photonic crystal slab point-shift nanolasers. *Appl. Phys. Lett.*, 88:211101, 2006.
- [25] Ziyang Zhang and Min Qiu. Small-volume waveguide-section high q microcavities in 2d photonic crystal slabs. *Opt. Expr.*, 12:3988, 2004.
- [26] S.-H. Kwon, T. Sunner, M. Kamp, and A. Forchel. Ultrahigh-q photonic crystal cavity created by modulating air hole radius of a waveguide. *Opt. Expr.*, 16:4605, 2008.
- [27] M. Notomi, E. Kuramochi, and H. Taniyama. Ultrahigh-q nanocavity with 1d photonic gap. *Opt. Expr.*, 16:11095, 2008.
- [28] C. Sauvan. *Etude de la propagation et du confinement de la lumière dans des nanostructures*. PhD thesis, 2005.
- [29] Y. Akahane, T. Asano, B.-S. Song, and S. Noda. High-q photonic nanocavity in a two-dimensional photonic crystal. *Nature*, 25:944, 2003.
- [30] M. Shirane, S. Kono, J. Ushida, S. Ohkouchi, N. Ikeda, Y. Sugimoto, and A. Tomita. More identification of high-quality-factor single-defect nanocavities in quantum dot-embedded photonic crystals. *Journ. Appl. Phys.*, 101:73107, 2007.
- [31] K. Hennessy, C. Hogerle, E. Hu, A. Badolato, and A. Imamoglu. Tuning photonic nanocavities by atomic force microscope nano-oxidation. *Appl. Phys. Lett.*, 89:041118, 2006.
- [32] W. R. Frei, H. T. Johnson, and K. D. Choquette. Optimization of a single defect photonic crystal laser cavity. *Journ. Appl. Phys.*, 103:033102, 2008.
- [33] D. G. Gevaux, A. J. Bennett, R. M. Stevenson, A. J. Shields, P. Atkinson, J. Griffiths, D. Anderson, G. A. C. Jones, and D. A. Ritchie. Enhancement and suppression of spontaneous emission by temperature tuning inas quantum dots to photonic crystal cavities. *Appl. Phys. Lett.*, 88:131101, 2006.
- [34] H.-Y. Ryu, M. Notomi, and Y.-H. Lee. High-quality-factor and small-mode-volume hexapole modes in photonic-crystal-slab nanocavities. *Appl. Phys. Lett.*, 83:4294, 2003.
- [35] N.-V.-Q. Tran, S. Combrie, and A. De Rossi. Directive emission from high-q photonic crystal cavities through band folding. *Phys. Rev. B*, 79:041101, 2009.
- [36] M. Larqué, T. Karle, I. Robert-Philip, and A. Beveratos. Optimizing h1 cavities for the generation of entangled photon pairs. *New. J. Phys.*, 11:033022, 2009.
- [37] A. R. A. Chalcraft, S. Lam, D. O'Brien, T. F. Krauss, M. Sahin, D. Szymanski, D. Sanvitto, R. Oulton, M. S. Skolnick, A. M. Fox, D. M. Whittaker, H.-Y. Liu, and M. Hopkinson. Mode structure of the l3 photonic crystal cavity. *Appl. Phys. Lett.*, 90:241117, 2007.
- [38] A. Tandaechanurat, S. Iwamoto, M. Nomura, N. Kumagai, and Y. Arakawa. Increase of q-factor in photonic crystal h1-defect nanocavities after closing of photonic bandgap with optimal slab thickness. *Opt. Expr.*, 16:448, 2008.
- [39] H.-Y. Ryu, J.-K. Hwang, and Y.-H. Lee. Conditions of single guided mode in two-dimensional triangular photonic crystal slab waveguides. *Journ. Appl. Phys.*, 88:4941, 2000.
- [40] B. Gayral and J. M. Gérard. Photoluminescence experiment on quantum dots embedded in a large purcell-factor microcavity. *Phys. Rev. B*, 78:235306, 2008.

- [41] E. Weidner, S. Combrie, N.-V.-Q. Tran, A. De Rossi, J. Nagle, S. Cassette, A. Talneau, and H. Benisty. Achievement of ultrahigh quality factors in gas photonic crystal membrane nanocavity. *Appl. Phys. Lett.*, 89:221104, 2006.
- [42] B.-S. Song, S. Noda, T. Asano, and Y. Akahane. Ultra-high-q photonic double-heterostructure nanocavity. *Nature Materials*, 4:207, 2005.
- [43] R. Hostein, R. Braive, M. Larqué, K.-H. Lee, A. Talneau, L. Le Gratiet, I. Robert-Philip, I. Sagnes, and A. Beveratos. Room temperature spontaneous emission enhancement from quantum dots in photonic crystal slab cavities in the telecommunications c band. *Appl. Phys. Lett.*, 94:123101, 2009.

## Chapter 3

# Time-bin entanglement

Quantum entanglement expresses the nonlocal correlations allowed by quantum mechanics between distinct systems. It is one of the fundamental concepts embodied in quantum mechanics and challenged the deepest thinkers of the 20th century. Entanglement was first demonstrated in an experiment based on Bell's inequality in 1982 [1]. Since then, it has become an important element in the arsenal of quantum optics experimental techniques and was subsequently used in many studies of fundamental aspects of quantum mechanics. More recently, it has become a key resource of potentially disruptive Quantum Information Processing and Communications (QIPC) technologies. As indicated in the first chapter, these include, for example, quantum cryptography systems that offer unconditionally secure information transport guaranteed by quantum-mechanical laws. In this context, entangled photons are particularly attractive for applications such as quantum cryptography and essential for quantum relays based on quantum teleportation.

In quantum optics, entanglement based on discrete variables is usually created by the spontaneous parametric down conversion process in a nonlinear optical crystal under excitation of a laser beam, either in continuous wave or pulse operation. By this process highly pure entangled states are produced by encoding qubits in a particular degree of freedom of the photons, such as polarization as we will see in the next chapter, linear and angular momentum [2], and energy-time [3]. Energy-time entanglement, or its discrete version, time-bin entanglement [4], is based on the interferometric scheme proposed by Franson [3] which allows the creation of a superposition state of emission times.

One of the criteria for Bell State measurements with time-bin entangled photons is the indistinguishability between the two photons: the photons must be described by identical spatial, spectral, polarization and temporal modes. Such photons have already been produced by parametric down conversion [3, 5, 6, 7, 8, 9, 10]. However, such sources are based on parametric down-conversion, which follows a Poissonian emission statistics. On the other hand, deterministic sources of entangled photons can be obtained from cascade emission in single emitters such as a single quantum dot. A scheme producing deterministic time-bin entangled photons using the cascade emission of a single quantum dot excited from a still unknown metastable state has also been recently proposed [11]. In such two photon emitters, photons emerge from a common source and are produced in an entangled state by the emission processes itself. Alternatively, deterministic polarization entangled photons can be obtained with two indistinguishable single photons emitted sequentially and linear optic components [12]. More recently, two sequential indistinguishable single photons emitted by a single quantum dot have been used to engineer a source of time-bin entangled photons [13]. By use of this source, quantum interferences have been observed but with a visibility that was not high enough to prove their non-local character.

In order to determine the conditions to produce time-bin entangled photons from a single dot, I derived a full quantum mechanical analysis of such time-bin entanglement for emitters subject to

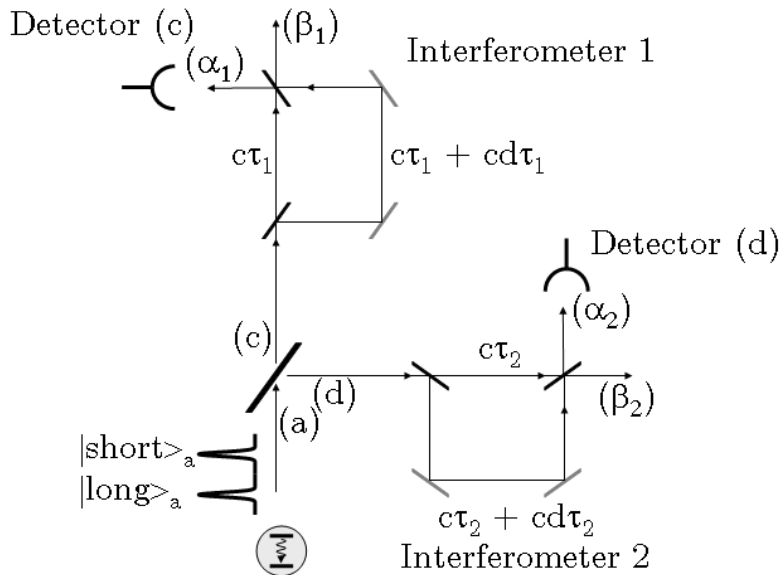


Figure 3.1: Schematic of entanglement generation and analysis. Two sequential indistinguishable single photons, with a relative time delay of  $T$ , are split by a beamsplitter and sent to unbalanced Mach-Zender interferometers.

uncorrelated dephasing processes and applied this model to sequential single photons emerging from a single semiconductor quantum dot. The scheme I used for the creation of time-bin entangled states out of two subsequent single photons, is the following. Two sequential indistinguishable single photons (figure 3.1), separated by a time delay  $T$  large compared with the single photon pulse duration, are incident on the same input port of a beamsplitter. Let us denote them  $|short\rangle_a$  and  $|long\rangle_a$ . The two output ports of the beamsplitter are denoted  $c$  and  $d$ . If we discard the events when both photons follow the same output port (states  $|short\rangle_c|long\rangle_c$  and  $|short\rangle_d|long\rangle_d$ ), the post-selected state, obtained with a probability  $1/2$  at the output of the beamsplitter, reads:

$$|\Psi^+\rangle = \frac{1}{\sqrt{2}}(|short\rangle_c|long\rangle_d + |short\rangle_d|long\rangle_c) \quad (3.1)$$

This state is a time-bin entangled state, that can be further analyzed in a Franson-type photon correlation set-up [3, 8], composed of two interferometers 1 and 2 respectively placed along the output ports  $c$  and  $d$  of the beamsplitter. Post selection of state  $|\Psi^+\rangle$  is achieved by recording only coincidence events between the output ports of interferometer 1 and the output ports of interferometer 2. In such an experiment, we perform an analysis of the entangled state created on the beamsplitter by which-path interferometry. Such a scheme relies on two crucial features, namely the efficient generation of deterministic single photon states and the indistinguishability of these states.

In this chapter, we will focus more on the second criteria which is the photon indistinguishability and we will present the theory of time-bin entanglement generation from a single photon emitter by considering explicitly the effect of dephasing processes. I will first describe the main ingredient in my model, namely, the single photon emitter subject to random phase fluctuations during emission. I will then calculate the probability of simultaneous detection between the output ports of two Mach-Zender interferometers placed on each output port of the beamsplitter and derive the visibility

of the two-photon interference. These calculations will serve as a guide for identifying experimental situations in which time-bin entanglement can be realized efficiently.

### 3.1 The model

We consider the situation in which two photons are emitted sequentially by a single-photon emitter. In this section, the theoretical description of such an experiment is done in two steps: first we present the model for the material emitters and the radiative interaction subject to phase diffusion and then we deal with photon propagation in the experimental setup.

#### 3.1.1 Single photons with phase diffusion

The single photon emitter is modelled as a two-level system that interacts with the electromagnetic field by absorbing or emitting photons whenever it undergoes a transition between its two states. The emission of a photon at time  $t_0$  and its propagation during a time  $\tau$  can be described by a creation operator  $\hat{\gamma}_{t_0}^{(+)}$ :

$$\hat{\gamma}_{t_0}^{(+)} = \int_{\mathbf{R}} \mu(t' - t_0) \hat{a}^{(+)}(t' + \tau) dt' \quad (3.2)$$

where  $\hat{a}^{(+)}(t)$  is the photon creation operator at time  $t$  and  $\mu(t)$  represents the temporal shape of the single photon emitted by the two-level system. For a perfect two-level system isolated from the environment, the function  $\mu(t)$  would be an exponential decay with a characteristic time constant related to the radiative lifetime  $T_1 = 1/\Gamma'$  of the two-level system placed in its excited state. However, most single emitting dipoles are subject to sudden, brief, and random fluctuations of their energy (arising, for example, from collisions with phonons and electrostatic interactions with fluctuating charges located in the dipole vicinity [14]). These fluctuations of the two-level system are assumed to be completely uncorrelated between them. In this context, the wavefunction  $\mu(t)$  reads [15]:

$$\mu(t) = K e^{-i\Omega_0 t - i\phi(t) - \frac{\Gamma'}{2} t - i\Delta t} H(t) \quad (3.3)$$

where  $K$  is a normalization constant,  $H(t)$  is the Heaviside function,  $\hbar\Omega_0$  is the energy of the transition energy of the two-level system isolated from its environment and  $\Delta$  is the radiative frequency shift due to the interaction with the surrounding. In the following, we shall denote  $\Omega = \Omega_0 + \Delta$ . The phase  $\Phi(t)$  is the fluctuating phase of the two-level system subject to phase diffusion, which, in the interaction picture, is transferred to the emitted photon. It satisfies the following relations:

$$\overline{e^{i\Phi(t)}} = 1 \quad (3.4)$$

$$\overline{e^{i\Phi(t) - i\Phi(t')}} = e^{-\Gamma|t-t'|} \quad (3.5)$$

where the overline denote statistical averaging.  $\Gamma$  is the dephasing rate of the two-level system and can be expressed as a function of the characteristic time for pure dephasing according to  $T_2^* = 1/\Gamma$ . The dephasing rate  $\Gamma$  and the decay rate  $\Gamma'$  are related to the coherence time  $T_2$  as follows:

$$\frac{1}{T_2} = \Gamma + \frac{\Gamma'}{2} = \frac{1}{T_2^*} + \frac{1}{2T_1} \quad (3.6)$$

Let us suppose that after a propagation time  $\tau$ , the photon emitted at time  $t_0$  is detected by a detector that converts the single photon received into an electric pulse that can subsequently be processed. The

probability  $p(t)$  of photodetection of the single photon at time  $t$  can then be expressed by use of the  $\hat{E}^{(-)}(t)$  photodetection annihilation operator at time  $t$  as:

$$p(t) = \overline{\langle 0 | \hat{\gamma}_{t_0}^{(-)} \hat{E}^{(+)}(t) \hat{E}^{(-)}(t) \hat{\gamma}_{t_0}^{(+)} | 0 \rangle} \quad (3.7)$$

where the angular brackets denote quantum mechanical averaging with respect to the state of the electromagnetic field and the overline the statistical averaging with respect to the fluctuations. By use of eq. (3.2) and (3.3), this probability reads:

$$p(t) = \overline{|\mu(t - \tau - t_0)|^2} \quad (3.8)$$

$$= |K|^2 e^{-\Gamma'(t - \tau - t_0)} H(t - \tau - t_0) \quad (3.9)$$

The normalization condition  $\int_{\mathbf{R}} p(t) dt = 1$  (no transmission losses and perfect detector) implies  $|K|^2 = \Gamma'$ .

### 3.1.2 Propagation

The experimental set up we will consider here is described on figure 3.1. Two single photons are produced sequentially by the same two-level system, with a time delay  $T \gg T_1$ . Both photons impinge the beamsplitter on the same input port  $a$ . In the following, we shall only consider the situation in which the two photons are separated by the beamsplitter along two different output ports, noted  $c$  and  $d$ . The creation operator of the photon pair can then be expressed as:

$$\hat{\gamma}_{t=0}^{a,(+)} + \hat{\gamma}_{t=T}^{a,(+)} \rightarrow \sqrt{R_{BS}T_{BS}} (\hat{\gamma}_0^{c,(+)} \hat{\gamma}_T^{d,(+)} + \hat{\gamma}_0^{d,(+)} \hat{\gamma}_T^{c,(+)}) \quad (3.10)$$

where  $\hat{\gamma}_{t_0}^{x,(+)}$  is the creation operator of a photon emitted at time  $t_0$  on port  $x$  of the beamsplitter.  $R_{BS}$  and  $T_{BS}$  are the intensity reflection and transmission coefficients of the beamsplitter. These photons propagate respectively through two unbalanced interferometers 1 and 2 and are further detected on two detectors placed on the outputs  $\alpha_i$  ( $i = 1, 2$ ) of these interferometers. This setup post selects the configuration in which the photons exit different output ports of the beamsplitter. In addition, joint photodetections are registered only for delays between detection events lower than the delay  $T$  between photon emission occurrences. The results of such an experiment give the probability  $p_{12}$  of joint photodetection of one photon on output port  $\alpha_1$  and of one photon on output port  $\alpha_2$ , provided the first (resp. second) photon passed through the long (resp. short) arm of the interferometer. This probability is related to the interference between two possible paths leading to photons on outputs  $\alpha_1$  and  $\alpha_2$ , with no information (in ideal case) on which photon was the first or the second emitted by the source. The other joint photodetection events with delay greater than  $T$  are not resulting from this interference but can be used experimentally to normalize the probability  $p_{12}$ .

In order to express  $p_{12}$ , let us first consider the situation in which one single photon emitted at time  $t_0$  travels through an unbalanced interferometer with arm lengths equal to  $c\tau_i$  and  $c(\tau_i + d\tau_i)$  as described on figure 3.2. We suppose that one input state of the interferometer is vacuum ( $\hat{y}^{i,(+)}(t) = 0$ ) and that the other input state  $\hat{x}^{i,(+)}(t)$  is the single photon state arriving at time  $t$  on the input port. The creation operator  $\hat{x}^{i,(+)}(t)$  and the operator  $\hat{\xi}^{i,(+)}(t')$  of creation at time  $t'$  of one photon along the output  $\alpha_i$  of the interferometer are related by:

$$\hat{x}^{i,(+)}(t) = \sqrt{R_i T_i} \hat{\xi}^{i,(+)}(t + \tau_i + d\tau_i) - \sqrt{R_i T_i} \hat{\xi}^{i,(+)}(t + \tau_i) \quad (3.11)$$

The first term in the previous equation corresponds to the situation in which the photon has followed the long arm of the interferometer, while the second term corresponds to propagation along the short arm.  $R_i$  and  $T_i$  are the intensity reflection and transmission coefficients of the interferometer. In this

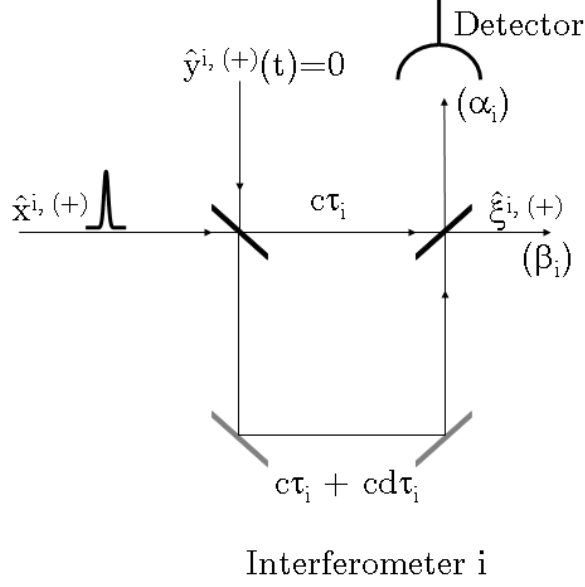


Figure 3.2: Schematic of an unbalanced interferometer.

context, the detection probability  $p_i$  of a single photon along the  $\alpha_i$  output of the interferometer at time  $t$  reads:

$$p_i(t) = \overline{\langle 0 | (\hat{\alpha}_{t_0}^{li,-} + \hat{\alpha}_{t_0}^{si,-}) \hat{E}_i^{(+)}(t) \hat{E}_i^{(-)}(t) (\hat{\alpha}_{t_0}^{li,+} + \hat{\alpha}_{t_0}^{si,+}) | 0 \rangle} = \left\| \hat{E}_i^{(-)}(t) (\hat{\alpha}_{t_0}^{li,+} + \hat{\alpha}_{t_0}^{si,+}) | 0 \right\|^2 \quad (3.12)$$

where  $\hat{E}_i^{(-)}(t)$  is the photodetection annihilation operator at time  $t$  on the detector placed on the  $\alpha_i$  output. The creation operators  $\hat{\alpha}_{t_0}^{li,+}$  and  $\hat{\alpha}_{t_0}^{si,+}$  can be expressed as follows by use of equations (3.2) and (3.11):

$$\hat{\alpha}_{t_0}^{li,+} = \sqrt{R_i T_i} \int_R \mu(t' - t_0) \hat{\xi}^{i,+}(t + \tau_i + d\tau_i) dt' \quad (3.13)$$

$$\hat{\alpha}_{t_0}^{si,+} = -\sqrt{R_i T_i} \int_R \mu(t' - t_0) \hat{\xi}^{i,+}(t + \tau_i) dt' \quad (3.14)$$

In these expressions, only propagation times through the interferometers are taken into account.

### 3.2 Entanglement on a beamsplitter

In the scheme we proposed to produce time-bin entangled photons, two sequential photons separated by a time delay  $T$  are sent to two different interferometers. Quantum interference between two propagation configurations will occur : (1) the first photon follows the long arm of one interferometer and the second delayed photon follows the short arm of the other interferometer and (2) vice versa. This interference is observed through photon correlation measurements between two output ports of the two interferometers.

### 3.2.1 Two photons travelling through two different interferometers

In the experiment involving two photons separated by a time delay  $T$ , joint photodetection can only occur if the single photon state created at time  $t = 0$  follows the long arm of one interferometer, and the single photon state created at time  $t = T$  follows the short arm of the other interferometer. In this context, the probability  $p_{12}(t_1, t_2)$  of photodetection of one single photon on  $\alpha_1$  port at time  $t_1$  and of one single photon on  $\alpha_2$  port at time  $t_2$  reduces, by use of (3.10), to:

$$p_{12}(t_1, t_2) = R_{BS}T_{BS} \overline{\left| \hat{E}_2^{(-)}(t_2) \hat{E}_1^{(-)}(t_1) (\hat{\alpha}_0^{l1,+} \hat{\alpha}_T^{s2,+} + \hat{\alpha}_0^{l2,+} \hat{\alpha}_T^{s1,+}) |0\rangle \right|^2} \quad (3.15)$$

Using relations (3.13) and (3.14), the joint photodetection probability  $p_{12}$  can be evaluated as:

$$\begin{aligned} p_{12} &= \int_{\mathbf{R}^2} dt_1 dt_2 p_{12}(t_1, t_2) \\ &= R_{BS}T_{BS}R_1T_1R_2T_2 \int_{\mathbf{R}^6} \prod_{i=1}^6 dt_i \overline{\mu(t_3)^* \mu(t_4 - T)^* \mu(t_5 - T) \mu(t_6)} \\ &\quad \langle 0 | [\hat{\xi}^{1,-}(t_3 + \tau_1 + d\tau_1) \hat{\xi}^{2,-}(t_4 + \tau_2) + \hat{\xi}^{2,-}(t_3 + \tau_2 + d\tau_2) \hat{\xi}^{1,-}(t_4 + \tau_1)] \hat{E}_1^{(+)}(t_1) \hat{E}_2^{(+)}(t_2) \\ &\quad \hat{E}_2^{(-)}(t_2) \hat{E}_1^{(-)}(t_1) [\hat{\xi}^{1,+}(t_6 + \tau_1 + d\tau_1) \hat{\xi}^{2,+}(t_5 + \tau_2) + \hat{\xi}^{2,+}(t_6 + \tau_2 + d\tau_2) \hat{\xi}^{1,+}(t_5 + \tau_1)] |0\rangle \end{aligned} \quad (3.16)$$

In this expression, integration over all detection times  $t_1$  and  $t_2$  and not only for  $|t_2 - t_1| < T$  is allowed, since only the paths leading to joint photodetection are selected in equation (3.15). This integral can be readily evaluated by commuting the two annihilation (resp. creation) electric field operators through the photon creation (resp. annihilation) operators. Operating these commutations, the joint photodetection probability can be written as:

$$\begin{aligned} p_{12} &= R_{BS}T_{BS}R_1T_1R_2T_2 \int_{\mathbf{R}^6} \prod_{i=1}^6 dt_i \overline{\mu(t_3)^* \mu(t_4 - T)^* \mu(t_5 - T) \mu(t_6)} \\ &\quad [\delta(t_3 + \tau_1 + d\tau_1 - t_1) \delta(t_4 + \tau_2 - t_2) + \delta(t_3 + \tau_2 + d\tau_2 - t_2) \delta(t_4 + \tau_1 - t_1)] \\ &\quad [\delta(t_6 + \tau_1 + d\tau_1 - t_1) \delta(t_5 + \tau_2 - t_2) + \delta(t_6 + \tau_2 + d\tau_2 - t_2) \delta(t_5 + \tau_1 - t_1)] \quad (3.18) \\ &= R_{BS}T_{BS}R_1T_1R_2T_2 \int_{\mathbf{R}^2} dt_1 dt_2 \\ &\quad \overline{\mu(t_1 - \tau_1 - d\tau_1)^2 \mu(t_2 - \tau_2 - T)^2 + \mu(t_2 - \tau_2 - d\tau_2)^2 \mu(t_1 - \tau_1 - T)^2} \\ &\quad + (\overline{\mu(t_1 - \tau_1 - d\tau_1)^* \mu(t_2 - \tau_2 - d\tau_2)} \overline{\mu(t_2 - \tau_2 - T)^* \mu(t_1 - \tau_1 - T)} + c.c.) \quad (3.19) \end{aligned}$$

where "c.c." denotes the complex conjugate. The emission process by the source is supposed to be much faster than the delay  $T$  between the two emission events, so that the emission of the first photon does not affect the emission of the second one, and statistical averaging can be made independently on each photon. Thus, using the expression of  $\mu(t)$  given by equation (3.3) and upon integration<sup>33</sup>, we obtain the probability of joint photodetection of single photons on both outputs  $\alpha_1$  and  $\alpha_2$  as:

$$p_{12} = 2R_{BS}T_{BS}R_1T_1R_2T_2 [1 + V \times \cos(\Omega(d\tau_1 - d\tau_2))] \quad (3.20)$$

<sup>33</sup>The integration of the third term in 3.19 is not straightforward. See the annex of this chapter for more details.

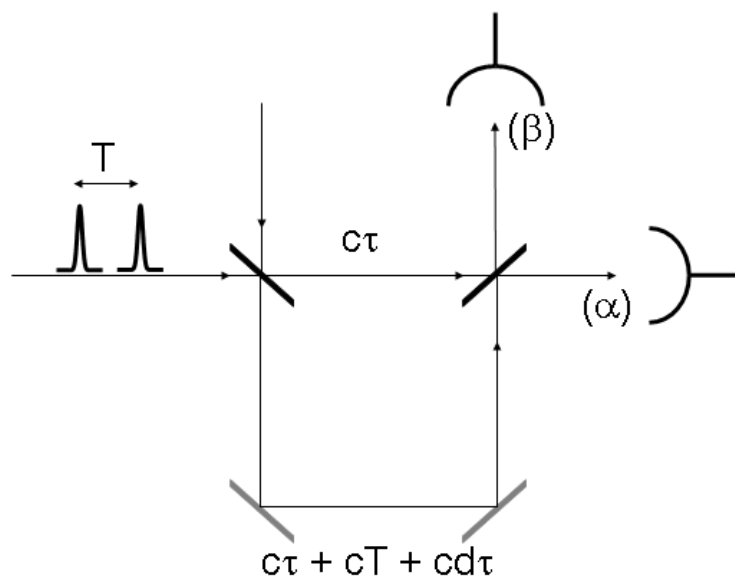


Figure 3.3: Schematic of a Hong-Ou-Mandel setup.

where:

$$V = e^{-\frac{\Gamma'}{2}(|T-d\tau_1|+|T-d\tau_2|)-\Gamma|d\tau_1-d\tau_2|} [1 + e^{-\frac{\Gamma'}{2}|d\tau_1-d\tau_2|} \cosh(\Gamma' \frac{|T-d\tau_1| - |T-d\tau_2|}{2}) (\frac{T_2}{2T_1} - 1)] \quad (3.21)$$

The coincidence rate between the two detectors displays an oscillatory behaviour as a function of the phase difference  $\Omega(d\tau_1 - d\tau_2)$  between the two interferometers.  $V$  is the visibility of the interference fringes. This interference is a two-photon interference and results from equal probability amplitudes of two indistinguishable paths: (1) first and second photons respectively in the long arm of interferometer 1 and short arm of interferometer 2 and (2) first and second photons respectively in the long arm of interferometer 2 and short arm of interferometer 1. As expected, the interference pattern only depends on the phase difference of the two analyzing interferometers. Contrary to experiments with time-bin entangled parametric down converted photons [8], it does not depend on the phase of the pump interferometer, since the photon emission is an incoherent effect. In equation (3.20) all the reflection and transmission coefficients are factorized. This corresponds to the simplest setup with a folded interferometer.

### 3.2.2 Entanglement and indistinguishability

The maximum visibility  $V$  of the interference is equal to the ratio  $T_2/2T_1$ , where  $T_2$  and  $T_1$  are respectively the coherence time and the spontaneous emission lifetime of the two-level system. This ratio is also the visibility of the interference in a Hong-Ou-Mandel experiment causing the coalescence of two single photons impinging simultaneously the two input ports of a beamsplitter [16]. In this experiment, the two sequential photons emitted by the same source at times separated by  $T \gg T_1$ , enter an interferometer with a path difference  $cd\tau_i \simeq cT$  (figure 3.3). We will only consider the situations in which the two photons impinge simultaneously the output beamsplitter of the interferometer. In that cases, which occur with a probability  $R_{BS}T_{BS}$ , the first photon travelled through the long arm of the interferometer and the second one travelled through the short arm of the interferometer.  $R_{BS}$  and  $T_{BS}$  are the intensity reflection and transmission coefficients of the beamsplitter in the folded

interferometer. Let us denote  $p_{HOM}$  the probability to detect one photon on one output port of the interferometer and to detect the other photon on the other output port. Because the time delay  $T$  is greater than the lifetime of the photons  $T_1$ , there are no single photon interference. This post selected probability to detect one photon at time  $t_\alpha$  on output  $\alpha$  and one at time  $t_\beta$  at time  $\beta$  is

$$p(t_\alpha, t_\beta) = R_{BS}T_{BS} \left\| \overline{\hat{E}_\alpha^{(-)}(t_\alpha) \hat{E}_\beta^{(-)}(t_\beta) \hat{\alpha}_0^{l,(+)} \hat{\alpha}_T^{s,(+)}} |0\rangle \right\|^2 \quad (3.22)$$

After replacing  $t_i - \tau - T$  ( $i = \alpha, \beta$ ) by  $t_i$ , the integration of this expression over the detection times leads to

$$\begin{aligned} p_{HOM}(d\tau) &= R_{BS}T_{BS}(R_{BS}^2 + T_{BS}^2 - R_{BS}T_{BS} \int dt_\alpha dt_\beta \overline{\mu(t_\alpha - d\tau)^* \mu(t_\beta - d\tau)} \overline{\mu(t_\beta)^* \mu(t_\alpha)}) + (3.23) \\ &= R_{BS}T_{BS}(R_{BS}^2 + T_{BS}^2 - 2R_{BS}T_{BS} \frac{T_2}{2T_1} e^{-\Gamma'|d\tau|}) \end{aligned} \quad (3.24)$$

which simplifies, when the reflection and transmission coefficient of the interferometer's beamsplitter are ideal ( $R_{BS} = T_{BS} = \frac{1}{2}$ ):

$$p_{HOM}(d\tau) = \frac{1}{8} \left( 1 - \frac{T_2}{2T_1} e^{-\Gamma'|d\tau|} \right) \quad (3.25)$$

That is, the probability of joint photodetection in the Hong-Ou-Mandel experiment displays at zero time delay a dip, the depth of which varies like  $(1 - T_2/2T_1)$  and the width of which is of the order of  $T_1$ . In the absence of pure dephasing processes in the two-level systems, when the emitted photons are "Fourier transform limited", (that is their temporal profile corresponds to the Fourier transform of their spectrum), we have  $T_2 = 2T_1$  and the central dip goes all the way down to zero. This means that, in the absence of dephasing, every time the photons arrive simultaneously on the beamsplitter they coalesce into a two-photon state and both leave by the same output port. However, in the presence of dephasing, the depth of the coalescence dip is reduced and in that case the efficiency of photon coalescence is reduced to  $T_2/2T_1$ . This ratio is also the maximum visibility of the two-photons interference in the Franson-type experiment.

### 3.2.3 Conditions for creating and observing entanglement

The visibility  $V$  of the Franson-type experiment (eq. 3.21) given by :

$$V = e^{-\frac{\Gamma'}{2}(|T-d\tau_1|+|T-d\tau_2|)-\Gamma|d\tau_1-d\tau_2|} \left[ 1 + e^{-\frac{\Gamma'}{2}|d\tau_1-d\tau_2|} \cosh\left(\Gamma' \frac{|T-d\tau_1| - |T-d\tau_2|}{2}\right) \left(\frac{T_2}{2T_1} - 1\right) \right] \quad (3.26)$$

is experimentally measured as a function of the optical path difference  $c(d\tau_1 - d\tau_2)$  between the two interferometers. It decreases with increasing time delay ( $d\tau_1 - d\tau_2$ ): this decrease is related to the timing information one could extract from the detection events and give rise to which-path information. However,  $V$  is a slow-varying function of  $(d\tau_1 - d\tau_2)$  compared with the cosine term. Therefore, its maximum amplitude can be inferred from experiments in which  $d\tau_1 \approx d\tau_2 \approx T$  within small variations of  $(d\tau_1 - d\tau_2)$  compared with  $1/\Gamma$  and  $1/\Gamma'$ .

### Impact of the degree of indistinguishability between the two photons

Perfect visibility ( $V = 1$ ) is obtained for perfectly indistinguishable single photons ( $T_2 = 2T_1$ ). In the absence of pure dephasing, the produced entangled state is maximally entangled, hence giving rise to perfect correlations. On the other hand, the maximal visibility drops to  $T_2/(2T_1)$  for single photons which are not Fourier-transform limited ( $T_2 < 2T_1$ ). This value of  $T_2/(2T_1)$  is the "degree of indistinguishability" of the single photons, i.e. the amplitude of the coincidence dip observed

in a Hong-Ou-Mandel two photon interferometer (see equation (3.25)) [16]. Yet, a visibility lower than one does not imply that the state is not entangled. Among the different criteria demonstrating entanglement, one of them is the violation of the Clauser-Horne-Shimony-Holt (CHSH) inequality. The violation of such inequality involves a visibility  $V$  higher than  $1/\sqrt{2}$  [17].

In order to illustrate our results with a concrete example, we shall consider the case of a semiconductor quantum dot as the single emitting dipole. Their lifetime is generally equal to  $T_1 = 1ns$ , and the pure dephasing time varies from  $T_2^* = 30ps$  to  $T_2^* = 300ps$  and  $T_2^* = 1ns$  for quantum dots under non-resonant pumping in the wetting layer, quasi-resonant pumping on a confined excited state and under resonant pumping respectively [18, 19] (see § 3.3). Under these conditions, the visibility given from equation (3.21) is equal to  $V_{30ps} = 0.014$ ,  $V_{300ps} = 0.130$  and  $V_{1ns} = 0.33$  respectively. All these visibilities indicate that Bell inequalities cannot be violated. Improvement of this visibility can be achieved by combining operating conditions allowing for long dephasing times<sup>34</sup> and a reduction the radiative lifetime of the quantum dot through its introduction in a resonant microcavity and the exploitation of the Purcell effect. In these conditions, the photon is emitted faster than any dephasing mechanism. This is obtained by use of cavity quantum electrodynamics: the density of optical states is increased by use of an appropriate microcavity, leading to a decrease in the dipole's lifetime as predicted by Purcell. First observation of cavity quantum electrodynamics effects in semiconductor dots was obtained by Gerard *et al* [20] and since then Purcell factors (i.e. spontaneous emission enhancement) as high as 10 have been observed by several groups on single dots. Such values of the Purcell effect leads to a ratio of  $T_2/(2T_1)$  as high as 0.8 as experimentally demonstrated [21, 22, 23].

Figure 3.4 depicts the maximum visibility  $V$  of the interference pattern for such emitters, as a function of the spontaneous emission enhancement  $F$  for different pure dephasing time  $T_2^*$  and  $d\tau_1 \approx d\tau_2 \approx T$ . It confirms that improvement of the visibility is achieved with the exploitation of the Purcell effect. For quantum dots with an excitation above the wetting layer band edge however, a Purcell factor higher than 160 would be necessary (figure 3.4 - dotted line). Conversely, for dots with a quasi-resonant excitation, a Purcell factor of the order of 16 would be enough to violate Bell's inequality (figure 3.4 - dashed line). Such Purcell factors have already been achieved, indicating that the possibility of realizing time-bin entangled photons with semiconductor quantum dots embedded in microcavities is totally accessible with available technology.

### Impact of the phase drifts

The main advantage of this scheme compared with parametric down-conversion time-bin entangled schemes resides in the fact that it is not necessary to compensate for any phase drifts of the time delay  $T$  between two emission events. As long as the phase drifts  $\pm dT$  are small compared with the photon pulse duration  $T_1$ , the interference visibility remains almost constant. Indeed,  $T$  may fluctuate from one experimental realization to another, for instance if the duration of the excitation pulse is not negligible compared to the duration  $T_1$  of the emitted photon [25]. For  $d\tau_1 = d\tau_2$ , derivation of equation (3.21) indicates that:

$$\text{for } d\tau_1 = d\tau_2: \frac{dV}{V} = -\Gamma'|dT| = -\frac{|dT|F}{T_1^{vac}} \quad (3.27)$$

$T_1^{vac}$  corresponds to the quantum dot radiative lifetime with no spontaneous emission enhancement. This equation indicates that any variations of  $T$  within the pulses duration  $T_1$  will reduce the mean overlap between the wave packets of the two photons and thus reduce the visibility of the two-photon

<sup>34</sup>This can be done by cooling the samples and operating under quasi-resonant pumping [21, 22, 23]. However, even in these conditions, the maximal amplitude of  $T_2/2T_1$  is of the order of 30 %. F. Patell *et al* [24] also used a diode structure to evacuate the charges around the dot responsible for at least part of the decoherence [14].

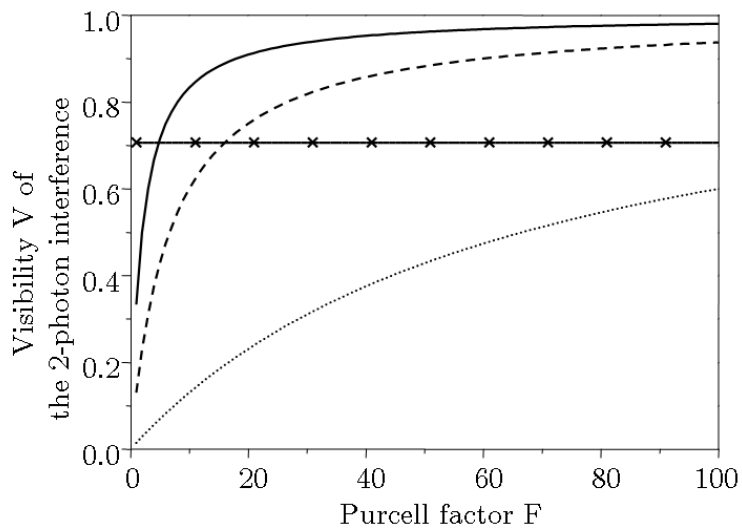


Figure 3.4: Maximum visibility of the two-photon interference as a function of the Purcell factor for a two-level system displaying a spontaneous emission lifetime  $T_1 = 1$  ns. (a) dotted line:  $T_2^* = 30ps$ , of the order of magnitude of the pure dephasing time of quantum dots under non-resonant pumping in the wetting layer. (b) dash line:  $T_2^* = 300ps$ , of the order of magnitude of the pure dephasing time of quantum dots under quasi-resonant pumping on a confined excited state. (c) solid line:  $T_2^* = 1$  ns, of the order of magnitude of the pure dephasing time of quantum dots under resonant pumping. (d) Solid line with crosses: value of  $1/\sqrt{2}$

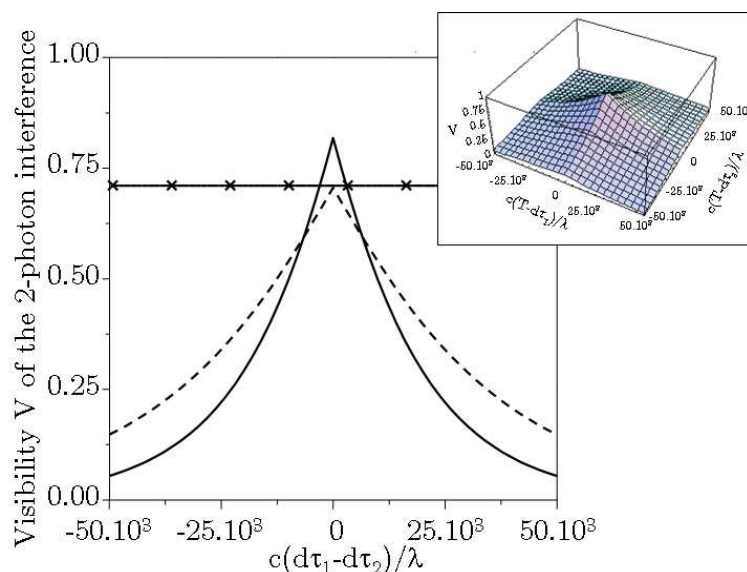


Figure 3.5: Visibility  $V$  of the two-photon interference as a function of the delay  $d\tau_1 - d\tau_2$  for  $T = d\tau_1$  and for photons emerging from a single emitter with  $T_1 = 1$  ns,  $T_2^* = 300$  ps and subject to the Purcell effect with: (a) dashed line:  $F = 16$  and (b) solid line:  $F = 30$ . Solid line with crosses corresponds to a value of the visibility of  $1/\sqrt{2}$ . Insert: visibility  $V$  of the two-photon interference as a function of the delay  $T - d\tau_1$  and  $T - d\tau_2$  for photons emerging from a single emitter with  $T_1 = 1$  ns,  $T_2^* = 300$  ps and subject to the Purcell effect with  $F = 16$ .

interference. As an example, variations of an amplitude of  $2dT$  of the order of  $1$  ps corresponds to a maximum visibility of 79.8% instead of 81% for dots with  $T_1 = 1$  ns,  $T_2^* = 300$  ps and subjected to a Purcell effect with  $F = 30$ .

### Impact of the balancing between the interferometers

In previous paragraphs, we have assumed that  $d\tau_1 \approx d\tau_2 \approx T$ . This can be achieved only with a certain precision. Figure 3.5 shows the visibility  $V$  of the two-photon interference as a function of  $d\tau_1 - d\tau_2$  in two situations. For two-photon interferences, the maximum visibility of which is equal to  $1/\sqrt{2}$  (dashed line), observation of entanglement requires that the arm length differences  $cd\tau_i$  of both interferometers be equal to  $cT$  with wavelength-scale precision. This situation occurs for quantum dots with  $T_1 = 1$  ns,  $T_2^* = 300$  ps and subject to a Purcell effect with  $F = 16$ . Such balancing of the interferometers is not easily obtained experimentally, and interference fringes will rapidly lose visibility when scanning the interferometers. Consequently, violation of Bell inequalities requires the use of dots with a higher Purcell factor  $F$ . For Purcell factors as high as 30, the violation of Bell inequalities is achieved if the arms length difference  $c(d\tau_1 - d\tau_2)$  of the two interferometers is positioned within  $\pm 3144 \lambda$  where  $\lambda$  is the wavelength of the photon involved in the interference (see solid line on figure 3.5). For quantum dots emitting around 900 nm, this corresponds to a precision of  $c(d\tau_1 - d\tau_2)$  of the order of  $\pm 2.8$  mm achievable with usual Mach-Zender interferometer balancing techniques.

### 3.3 Cavity design for restoring entanglement

#### 3.3.1 The need of quasi-resonant pumping

We have shown previously that the criteria of indistinguishability impose high Purcell factors and a quasi-resonant pumping. The high Purcell factor allows for a reduction of the spontaneous emission lifetime and the quasi-resonant pumping allows for a lengthening of the pure dephasing time. This results in an increase of the “degree of indistinguishability” between the single photons emerging from the excitonic transition in a single quantum dot and thus an increase of the entanglement visibility  $V$ .

By quasi-resonant pumping, we mean excitation on a trapped excited state of the exciton. This state can be for instance a virtual state, which is separated from the quantum dot ground state by a multiple of longitudinal optical (LO) phonon transition. The energy of one optical phonon is  $E_{\text{phonon}} = 8.6\text{meV}/K$  and at 4K it is  $E_{\text{phonon}} = 34\text{meV}$ . This involves, for dots emitting around 950 nm, the excitation the dot with a pump laser tuned  $24\text{nm}$ . Such an excitation scheme prevents of random captures and the escapes of carriers in traps located in the quantum dot vicinity. Indeed, the existence of a fluctuating environment around the quantum dot leading to dephasing processes originates partly from the presence of impurities or of defects in the barrier material or in the wetting layer. Furthermore, this latter heterostructure is far from being an ideal two-dimensional quantum well, so the unavoidable interface roughness also gives rise to localized states in the quantum-dot surroundings. By exciting directly inside the dot on an excited state, it becomes possible to reduce the impact of such dephasing mechanisms and to lengthen the pure dephasing time. Moreover, under high Purcell effects, the exciton lifetime may become shorter than the carrier lifetime in the surrounding reservoir, such as the wetting layer (in which the spontaneous emission lifetime is of the order of  $100\text{ps}$ ). In this context and under resonant pumping, more than one excitation-emission cycles on the dot ground state may occur during each excitation pulse. Since the exciton lifetime is of the order of few tens picoseconds, the quantum dot may capture a second electron-hole pair after emitting its first excitonic photon, since the carriers trapped in the wetting layer have not all relaxed already. Quasi-resonant pumping conversely insures that one and only one photon is emitted during each excitation cycle.

However a major difficulty then is to design a cavity allow for high Purcell factors while allowing for a quasi-resonant pumping. In order to check the possibility to pump quasi-resonantly a single quantum dot embedded inside a cavity, we performed excitonic photoluminescence excitation on dots embedded in photonic crystal cavities. When the pump is about  $30\text{nm}$  below the cavity’s wavelength, if the pumping laser is injected in the cavity, it may excite parts of the dots in resonance with the cavity mode and a signal will emerge from the cavity at its resonant wavelength. Conversely, if the pump laser is rejected by the cavity, no signal is expected at the cavity wavelength. Such a setup makes possible to test easily the compatibility of quasi-resonant pumping with the use of cavities with high quality factors and small mode volumes. This compatibility has already been encountered on several systems. For example, in micropillar cavities, quasi-resonant pumping is possible only if the laser impinge the cavity at oblique angles on the side of micropillars, since the top Bragg mirror reflects the light at normal incidence at such wavelength. In other terms, under quasi-resonant pumping, the laser wavelength is in the stop-band of the Bragg mirror. Quasi-resonant pumping has also been performed on a single quantum dot inside a H1 cavity [23]. However, the Purcell factors allowed by such cavities are not sufficient for time-bin entanglement restoration. Modified H1 design (as in § 2.4.3) leading to enhanced Purcell factors were tested but did not allow for quasi-resonant pumping [26]. This effect has been confirmed by testing different modified L3 cavities: no signal emerges from the cavity when the excitation laser is tuned 30 nm below the mode wavelength, since the laser wavelength is situated in the photonic crystal stop-band.

### 3.3.2 Excitation schemes

#### Excitation at 45° incidence

One way to avoid this problem may be inspired by the excitation configuration used in the micropillar case. The main idea is that the bi-dimensional photonic crystal has a stop band only for the TE modes. Consequently, a laser at oblique incidence may couple to the TM modes in the membrane and thus excite the quantum dots inside the cavity. This configuration was tested for angles of incidence of 45 deg; the photoluminescence was still collected by the objective at normal incidence. In our experiment, the laser spot shown on Figure 3.6 may display interference patterns or speckle depending on the laser wavelength. Interference fringes also appear on the signal emerging from the photonic crystal. These interferences are likely to arise from reflections of the laser on the successive interfaces of the sample (air/membrane, membrane/air, and air/substrate) or along the arrangement of holes. These reflections interfere constructively or destructively leading to interference pattern as shown on Figure 3.6 (right). We did not perform precise calculations to check if the interfringe's distance matched this interpretation, but the orders of magnitude agree. Moreover, for other wavelengths, the laser spot displays an ellipsoid shape spreading out of the crystal (see Figure 3.6 (left)), which would pump the quantum dots around the crystal. The uncoupled quantum dots would then contribute to a significant signal noise. In the case of micropillars such a problem does not appear because the material around the micropillar has been removed. In the case of bi-dimensional photonic crystal cavities, the surrounding material cannot be removed, obviously to bind the suspended membrane to the sample. Consequently, an excitation scheme at oblique incidence is not suitable with bi-dimensional photonic crystal cavities on a suspended membrane.

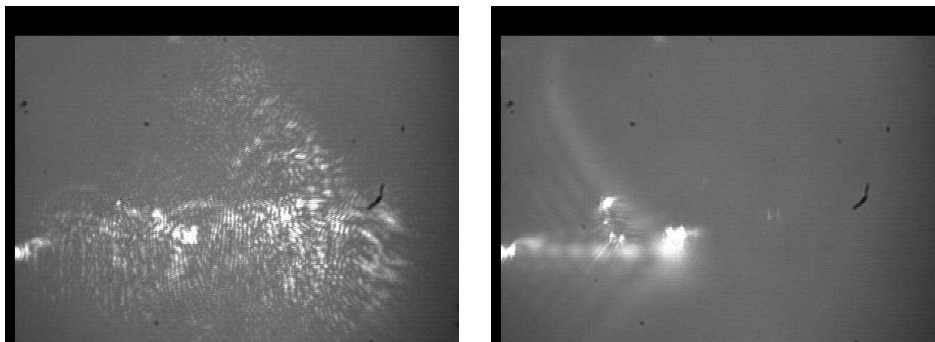


Figure 3.6: Images of the laser spot focused with a 45deg angle on a bi-dimensional photonic crystal cavity, for two laser wavelengths.

#### Excitation at normal incidence

Another strategy would be to excite at normal incidence a cavity sustaining two modes: one tuned at the dot wavelength and one tuned at the pumping laser wavelength. Two designs were investigated: the H1 cavity and the L3 cavity.

The H1 cavity sustains two modes, with perpendicular polarizations. One solution may be to break the degeneracy of these two modes, one (denoted X) tuned at the exciton wavelength and the other one (denoted Y) at the excitation laser wavelength. Two techniques can be used to lift the degeneracy between these modes : shrinking the whole crystal in the Y direction by a factor  $c$  of compression (i.e. the distance between two lines of holes becomes  $c \times a\sqrt{3}/2$ ), and moving in the Y direction four of the six holes surrounding the H1 cavity (see 3.7). The compression to apply to lift the



cavity mode (3.8), a very small fraction of the energy of the fundamental mode spreads at the location of the two removed holes. This explains why the wavelength of the L3 cavity mode is not changed, and its quality factor reduced by only about 10%. Nevertheless the light emerging from of the L3 fundamental mode is diffracted by the two newly removed holes and creating a new path of emission in the Y direction (these supplementary removed holes are at the  $k_X = 0$ ). Again, high directivity of the cavity mode and excitation at normal incidence do not seem compatible.

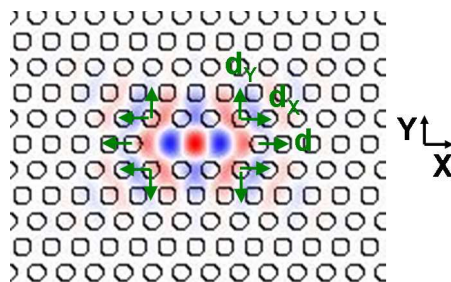


Figure 3.8: Modifications of the L3 design to obtain directive emission from the fundamental L3 mode <sup>18</sup>.

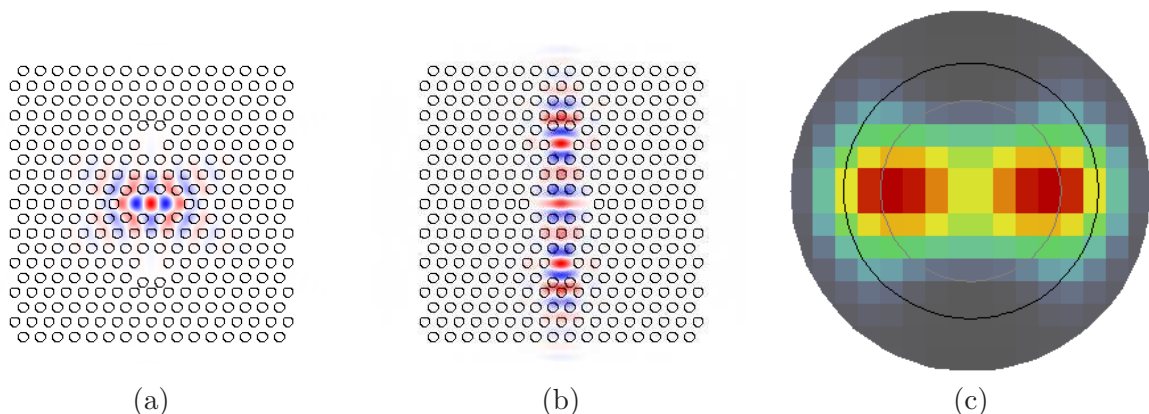


Figure 3.9: The L3 cavity with two more holes removed to create a mode for the pump laser <sup>37</sup>: (a) fundamental mode (Y component of the electric field of this mode), (b) mode for the pump (X component of the electric field of this mode), (c) best farfield obtained for the fundamental mode while moving the holes around the two supplementary removed ones.

<sup>36</sup>For reference:  $a = 270nm$ ,  $r = 80nm$ ,  $h = 260nm$ , X displacement of the two holes in alignment with the L3  $d = 0.2a$ , X (resp. Y) displacement of the four other holes  $d_X = 0.08a$  ( $d_Y = -0.06a$ ) <sup>18</sup>. Expected characteristics are  $\lambda_c = 1.1\mu m$ ,  $Q_c = 64000$  and  $\eta = 23\%$  for  $NA = 0.5$  (about half of the maximum). Obviously some shrinking must be performed for spectral matching § 2.4.3, and the quality factor was a bit too high.

<sup>37</sup>For reference:  $a = 233nm$ ,  $r = 67nm$ ,  $h = 180nm$ ,  $d = 0.2a$ ,  $d_X = 0.08a$ ,  $d_Y = -0.08a$ , displacement along Y of the two holes close to the H1-like holes but on the L3 side  $d_1 = -0.075$ , displacement along Y of the two holes close to the H1-like holes and the farthest from the L3  $d_2 = 0.225a$ . Expected characteristics are:  $\lambda_c = 936nm$ ,  $Q_c = 59000$ ,  $\eta = 19\%$  for  $NA = 0.5$  and  $\lambda_c - \lambda_{Pump} = 28nm$  (38meV)

### 3.4 Conclusion

We have studied the generation of time-bin entanglement by use of two single photons incident on a beamsplitter. These photons are emitted sequentially with a time delay  $T$  by a two-level system that undergoes dephasing in the course of the emission process. This emission process generates a state  $|short\rangle + |long\rangle$  sent on a fifty-fifty beamsplitter. If we post-select the situation in which the two photons leave on two different output ports  $c$  and  $d$  of the beamsplitter, the obtained state after the beamsplitter is the time-bin entangled state  $|\Psi^+\rangle = (|short\rangle_c|long\rangle_d + |short\rangle_d|long\rangle_c)/\sqrt{2}$ .

The fidelity of entanglement is related to the visibility of the two-photon interference obtained in a Franson-type set-up composed of two interferometers. This visibility  $V$  can be inferred from joint photodetection measurements between the respective outputs of the two interferometers. We have calculated the visibility  $V$  for two photons originating in a single emitter characterized by an excited state lifetime  $T_1$  and a coherence time  $T_2$ , by modelling the dephasing process as resulting from stochastic fluctuations of the excited state energy of the emitter corresponding, for example, to fluctuations due to collisions or interactions with fluctuating carriers. Our results indicate that the maximum visibility of the interference is equal to  $T_2/(2T_1)$ . Calculations using the physical parameters of semiconductor quantum dots highlight that, because of the relatively rapid dephasing, the visibility of the two-photon interference produced by bare quantum dots is very low (of the order of 10-30%) and does not allow the violation of Bell's inequality. By enhancing the spontaneous emission lifetime of the quantum dots by a factor of 30 by use of Cavity Quantum Electrodynamics effects, it is possible to raise this visibility to levels that could become interesting for quantum information processing schemes. Experiments are in progress in our laboratory to implement these ideas.

However, a major difficulty resides in the necessity to pump quasi-resonantly the quantum dot (in order to warrantee both anti-bunching and reduce the impact of dephasing mechanisms) while submitting the dot to high Purcell cavity. Different cavity designs based on modified H1 or L3 have been investigated but none of them seem to allow a good collection of the emitted single photons and a quasi-resonant pumping of the dots. Further investigations have still to be done in order to design the appropriate photonic crystal cavity. Another strategy could be to use other types of cavities, such as micropillars.

### Annex: Calculation details of the visibility

From 3.19 we consider only the cross-term

$$I = \int_{\mathbf{R}^2} dt_1 dt_2 \overline{\mu(t_1 - \tau_1 - d\tau_1)^* \mu(t_2 - \tau_2 - d\tau_2)} \overline{\mu(t_2 - \tau_2 - T)^* \mu(t_1 - \tau_1 - T)} \quad (3.28)$$

Let us be  $x_i = T - d\tau_i$  and  $u_i = t_i - \tau_i - d\tau_i - \frac{x_i}{2}$ . With the use of the definition of the time envelop (eq. 3.3) and upon the statistical averaging (eq. 3.5) we have:

$$I + c.c. = 2|K|^4 \cos(\Omega(d\tau_2 - d\tau_1)) \int_{u_i > \left| \frac{x_i}{2} \right|} du_1 du_2 e^{-\Gamma'(u_1+u_2) - \Gamma\left(\left|u_1-u_2 + \frac{x_2-x_1}{2}\right| + \left|u_1-u_2 - \frac{x_2-x_1}{2}\right|\right)} \quad (3.29)$$

which simplifies into the sum of two integrals  $I + c.c. = 2|K|^4 \cos(\Omega(d\tau_2 - d\tau_1)) \times (I_1 + I_2)$ :

$$I_1 = \int_{u_i > \left| \frac{x_i}{2} \right|, |u_1-u_2| < \left| \frac{x_2-x_1}{2} \right|} du_1 du_2 e^{-\Gamma'(u_1+u_2) - \Gamma|x_1-x_2|} \quad (3.30)$$

$$I_2 = \int_{u_i > \left| \frac{x_i}{2} \right|, |u_1-u_2| < \left| \frac{x_2-x_1}{2} \right|} du_1 du_2 e^{-\Gamma'(u_1+u_2) - 2\Gamma|u_1-u_2|} \quad (3.31)$$

Let us be  $z = \frac{|x_2| - |x_1|}{2}$ ,  $w = \frac{|x_2 + x_1|}{2}$ ,  $a = u_1 + u_2 - |x_1|/2 - |x_2|/2$  and  $b = u_1 - u_2$ , then

$$I_1 = \int_{a > |b+z|, |b| < w} \frac{dad b}{2} e^{-\Gamma' a - 2\Gamma w} \quad (3.32)$$

$$= \frac{e^{-2\Gamma w}}{\Gamma'} (1 - e^{-\Gamma' w} \cosh(\Gamma' z)) \quad (3.33)$$

$$I_2 = \int_{a > |b+z|, |b| > w} \frac{dad b}{2} e^{-\Gamma' a - 2\Gamma |b|} \quad (3.34)$$

$$= \frac{e^{-(2\Gamma + \Gamma') w}}{\Gamma'(\Gamma' + 2\Gamma)} \cosh(\Gamma' z) \quad (3.35)$$

The calculation of the visibility is then straightforward.

## Annex: Preparation of the time-bin experimental setup

In order to perform the measure of the interference in the time-bin entanglement scheme as shown on figure 3.1, I built two actively stabilized interferometers with a 40cm path difference. The path difference of 40cm corresponds to a time delay  $T = 1300ps \gg T_1$  as required. Since the probability of joint photodetection evolves like  $\cos(\Omega(d\tau_1 - d\tau_2))$  (eq. 3.20), the balancing between the two interferometers has to be stabilized with a precision of more than  $\lambda/10 \sim 90nm$  during several hours to register enough time correlations to reconstruct the sinusoidal shape of the expected curve (based on an experiment with about at least 10 points and 1 hour per point).

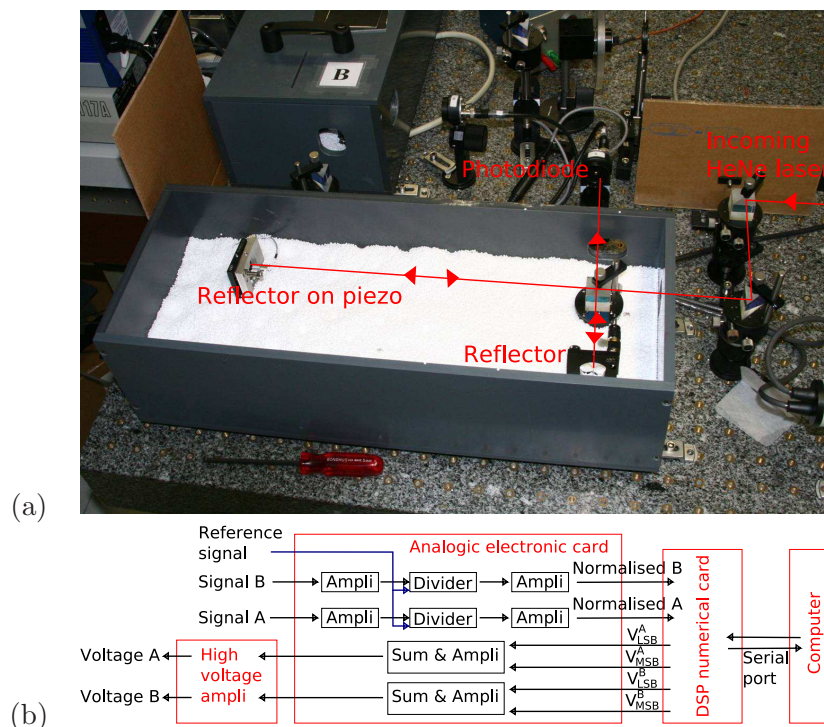


Figure 3.10: (a) Picture of the stabilized interferometers. The two interferometers are enclosed in a box (one of them is open for the sake of the picture). (b) Schematic of the electronic setup.

The figure 3.10 displays one of the two folded interferometers I built. The optical elements are a beamsplitter and two reflectors, one of them is mounted on a piezoelectric stack. They are mounted

on a metallic plate with low thermal expansion. Below this plate are mounted high current heating resistances and a thermal sensor. The whole system (plate + heaters + optics) is placed inside a hermetic box. The box is filled with polymer spheres up to the level of the beam path, and a block of foam rubber is glued on the lid, in order to fill the maximum of empty space without cutting the path of the optical beams. The box is thermally stabilized a few degrees above room temperature in order to avoid thermal fluctuations. The polymer spheres and the foam rubber are used to avoid cavitations effects in the box which may change the optical path length of the two arms due to air displacements at different temperatures. These precautions proved to be useful as they increased the stabilization resolution by a factor  $\sim 4$  and allowed to avoid sensitivity to air movements in the vicinity of the apparatus.

Different elements in the setup induce fluctuations of the interferometers. Among those we have identified, we can mention:

- laser intensity fluctuations of 0.5% with peaks reaching 10%, compensated by signal normalization,
- external thermal fluctuations (0.1 deg  $C$  corresponds to one fringe), compensated by thermal locking and insulation,
- noise at frequencies up to 1MHz, compensated by mechanical locking (see further) for low frequencies, hopefully of small amplitude for the highest frequencies,
- some mechanical and acoustic resonances (speaking in the room must be avoided),
- other slow fluctuations of high amplitude of unknown origin <sup>38</sup>. Their characteristic time is more than the hour, their amplitude more than a few  $\mu m$  (or equivalent), and they are highly correlated on both interferometers (in direction of path elongation and amplitude).

A frequency stabilized HeNe laser, protected by an optical isolator, is sent in each interferometer (figure 3.10), and the outgoing laser signal is analogically normalized (by a homemade electronic card) by the intensity of the laser measured at the entrance on the interferometer. An independent Digital Signal Processor (DSP) electronic card which I programmed, controls the voltage applied to the piezoelectric stacks in order to maintain a constant signal on the HeNe interferences. Through a serial port and a simple communication protocol, the DSP card communicates its status to the computer and is controlled by it. We chose not to perform the locking with the computer but with an independent card in order to avoid any problems of slowdown which may be created by other programs in the computer. In order to increase the signal to noise ratio, the DSP card performs four successive measures of its entries and takes the mean value. The locking algorithm is a proportional integral derivative (PID). The applied voltages are updated every 250 $\mu s$  (4kHz). A higher updating rate gave a poorer stabilization because it implied to use only one DSP measure per computation (i.e. more noisy measures) and the mechanical parts were not able to operate at such high frequency. The cutting frequency of the reflector mounted on the piezoelectric stack was around 100kHz. A lower updating rate proved to be too slow. The analogue card also adjusts the range of the input and output signals to the range of the DSP analog convertors in order to minimize the effect of numerical quantifications. In order to avoid this quantification effects, the voltage controlled by the DSP was encoded on a 16 bits value.

In order to check the stabilization of our set-up, we recorded during several hours the difference  $D(t)$  between the paths difference of the two interferometers, measured in distance units and stabilized around a value  $D_{PID}$ . The exact value of the unbalance of each interferometers is not important in the Franson-type experiment (as soon as they are sufficiently closed to the time delay  $T$  of the photons), but it has to vary over a continuous range of values of  $D_{PID}$  spreading over several fringes (at the

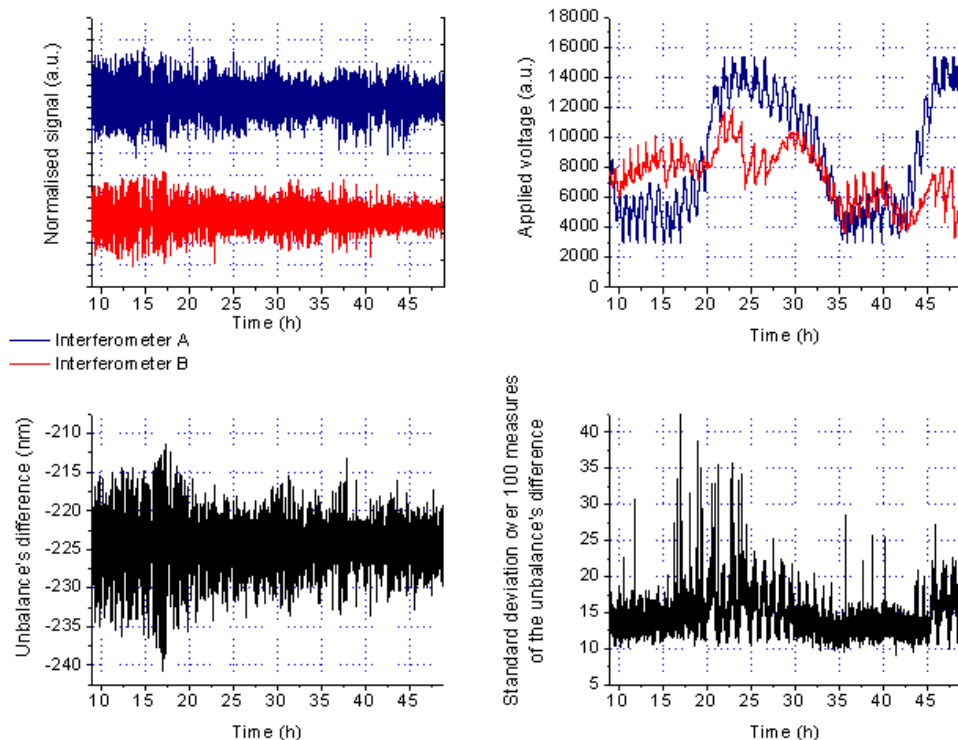


Figure 3.11: Difference of the unbalance locked during 25 hours with a precision below  $20nm$  most of the time.

quantum dot's wavelength  $\sim 950nm$ ). It proved possible to vary the value of  $D_{PID}$  by  $8\lambda_{HeNe}$ , which is good enough. Using this setup, I managed to maintain continuously lock on a fixed value of  $D_{PID}$  during 40h with a mean deviation of  $25nm$  ( $\sim \lambda_{QD}/40$ ). Figure 3.11 displays various parameters of the system (signal out of each interferometer, applied voltage, difference  $D(t)$  and standard deviation) as a function of time. Despite all the techniques we used to passively stabilize the interferometers, a slow variation still appears on a timescale of hour. These variations induce progressively strong variations of the applied voltages, which can reach their maximum possible value (equal to 10 V). I did not find the origin of these variations<sup>38</sup> and in order to avoid this problem, we added an active lock consisting in shifting simultaneously both interferometers over one fringe of the HeNe interferences, when the applied voltage reaches its upper limit on one of the two interferometers. These jumps are clearly visible on the curve of the applied voltage. Sometimes the deviation of  $D(t)$  increases. This is due to the turning on of the air condition system, or some local human activity<sup>39</sup>.

<sup>38</sup>I suspected the thermal stabilization, fluctuations in the current source of the analog card or the photodiodes measuring the laser's intensity, and the wavelength stability of the laser itself. For the two first hypothesis, registering their value over long times proved that they did not fluctuate sufficiently to be responsible for fluctuations of this amplitude. I also performed Fourier transform spectroscopy of the HeNe laser to check its stability.

<sup>39</sup>The set up is sensitive for instance to a slammed door everywhere in about half of the building.

## Bibliography

- [1] A. Aspect, P. Grangier, and G. Roger. Experimental realization of einstein-podolsky-rosen-bohm gedankenexperiment: A new violation of bell's inequalities. *Phys. Rev. Lett.*, 49:91, 1982.
- [2] J. G. Rarity and P.R. Tapster. Experimental violation of bell's inequality based on phase and momentum. *Phys. Rev. Lett.*, 64:2495, 1990.
- [3] J. D. Franson. Bell inequality for position and time. *Phys. Rev. Lett.*, 62:2205, 1989.
- [4] J. Brendel, N. Gisin, W. Tittel, and H. Zbinden. Pulsed energy-time entangled twin-photon source for quantum communication. *Phys. Rev. Lett.*, 82:2594, 1999.
- [5] W. Tittel, J. Brendel, H. Zbinden, and N. Gisin. Violation of bell inequalities by photons more than 10 km apart. *Phys. Rev. Lett.*, 81:3563, 1998.
- [6] W. Tittel, J. Brendel, B. Gisin, T. Herzog, H. Zbinden, and N. Gisin. Experimental demonstration of quantum correlations over more than 10 km. *Phys. Rev. A*, 57:3229, 1998.
- [7] S. Tanzilli, W. Tittel, H. de Riedmatten, H. Zbinden, P. Baldi, M.P. De Micheli, D.B. Ostrowsky, and N. Gisin. Ppln waveguide for quantum communication. *Eur. Phys. Journ. D*, 18:155, 2002.
- [8] I. Marcikic, H. de Riedmatten, W. Tittel, V. Scarani, H. Zbinden, and N. Gisin. Time-bin entangled qubits for quantum communication created by femtosecond pulses. *Phys. Rev. A*, 66:062308, 2002.
- [9] I. Marcikic, H. de Riedmatten, W. Tittel, H. Zbinden, M. Legré, and N. Gisin. Distribution of time-bin entangled qubits over 50 km of optical fiber. *Phys. Rev. Lett.*, 93:180502, 2004.
- [10] S. Fasel, N. Gisin, G. Ribordy, and H. Zbinden. Quantum key distribution over 30 km of standard fiber using energy-time entangled photon pairs: a comparison of two chromatic dispersion reduction methods. *Eur. Phys. Journ. D*, 30:143, 2004.
- [11] C. Simon and J.P. Poizat. Creating single time-bin-entangled photon pairs. *Phys. Rev. Lett.*, 94:030502, 2005.
- [12] D. Fattal, K. Inoue, J. Vuckovic, C. Santori, G. S. Solomon, and Y. Yamamoto. Entanglement formation and violation of bell's inequality with a semiconductor single photon source. *Phys. Rev. Lett.*, 92:037903, 2004.
- [13] A. J. Bennett, D. G. Gevaux, Z. L. Yuan, A. J. Shields, P. Atkinson, and D. A. Ritchie. Experimental position-time entanglement with degenerate single photons. *Phys. Rev. Lett.*, 77:023803, 2008.
- [14] A. Berthelot, I. Favero, G. Cassabois, C. Voisin, C. Delalande, Ph. Roussignol, R. Ferreira, and J. M. Gerard. Unconventional motional narrowing in the optical spectrum of a semiconductor quantum dot. *Nat. Phys.*, 2:759, 2006.
- [15] J. Bylander, I. Robert-Philip, and I. Abram. Interference and correlation of two independent photon. *Eur. Phys. Journ. D*, 22:295, 2003.
- [16] C.K. Hong, Z.Y. Ou, and L. Mandel. Measurement of subpicosecond time intervals between two photons by interference. *Phys. Rev. Lett.*, 59:2044, 1987.

- [17] W. Tittel, J. Brendel, N. Gisin, and H. Zbinden. Long-distance bell-type tests using energy-time entangled photons. *Phys. Rev. A*, 59:4150, 1999.
- [18] C. Kammerer, C. Voisin, G. Cassabois, C. Delalande, Ph. Roussignol, F. Klopff, J. P. Reithmaier, A. Forchel, and J. M. Gerard. Line narrowing in single semiconductor quantum dots: Toward the control of environment effects. *Phys. Rev. B*, 66:041306(R), 2002.
- [19] P. Borri, W. Langbein, S. Schneider, U. Woggon, R. L. Sellin, D. Ouyang, and D. Bimberg. Ultralong dephasing time in ingaas quantum dots. *Phys. Rev. Lett.*, 87:157401, 2001.
- [20] J. M. Gerard, B. Sermage, B. Gayral, B. Legrand, E. Costard, and V. Thierry-Mieg. Enhanced spontaneous emission by quantum boxes in a monolithic optical microcavity. *Phys. Rev. Lett.*, 81:1110, 1998.
- [21] C. Santori, D. Fattal, J. Vuckovic, G.S. Solomon, and Y. Yamamoto. Indistinguishable photons from a single-photon device. *Nature*, 419:594, 2002.
- [22] S. Varoutsis, S. Laurent, P. Kramper, A. Lemaitre, I. Sagnes, I. Robert-Philip, and I. Abram. Restoration of photon indistinguishability in the emission of a semiconductor quantum dot. *Phys. Rev. B*, 72:041303(R), 2005.
- [23] S. Laurent, S. Varoutsis, L. Le Gratiet, A. Lemaitre, I. Sagnes, F. Raineri, A. Levenson, I. Robert-Philip, and I. Abram. Indistinguishable single photons from a single-quantum dot in a two-dimensional photonic crystal cavity. *Appl. Phys. Lett.*, 87:163107, 2005.
- [24] F. Patell, F. Arciprete, E. Placidi, M. Fanfoni, A. Balzarotti, A. Vinattieri, L. Cavigli, M. Abbarchi, M. Gurioli, L. Lunghi, and A. Gerardino. Single quantum dot emission by nanoscale selective growth of inas on gaas: A bottom-up approach. *Appl. Phys. Lett.*, 93:231904, 2008.
- [25] H. de Riedmatten, I. Marcikic, W. Tittel, H. Zbinden, and N. Gisin. Quantum interference with photon pairs created in spatially separated sources. *Phys. Rev. A*, 67:022301, 2003.
- [26] Private communications.



## Chapter 4

# Polarization entanglement

In the previous chapter, we studied one type of photon entanglement: the time-bin entanglement. However, other types of photon entanglement can be implemented, among which polarization entanglement, which has attracted much interest. Early experiments with polarization entangled photons, such as Aspect's landmark EPR experiment [1], used the correlated spontaneous emission of photons in an atomic cascade to generate polarization entanglement. However, single atoms are not a viable solution for the engineering of practical sources of entangled photons, since their production, manipulation and storage involve extremely complex experimental set-ups and short use periods. The most common way at present to generate pairs of polarization entangled photons involves non-linear optical processes such as parametric down conversion [2, 3]. Different material systems have been explored: type I or type II non-linear crystals, semiconductor materials... Unfortunately, these techniques do not provide unique pairs of entangled photons on demand, since the number of pairs emerging in these non-linear processes is probabilistic. An alternative approach providing deterministic event-ready entangled photons uses a triggered source of indistinguishable single photons and linear-optics [4]. However, it requires post-selection techniques that considerably reduce the generation rate of entangled photons. Therefore, bright and compact sources that deliver one single pair of entangled photons deterministically, are still the subject of investigation.

In this context, previous studies have revealed the potential of self-assembled semiconductor quantum dots. These nano-emitters can emit deterministically pairs of correlated photons [5]. These correlated photons can even be entangled [6]: a quantum dot containing two electron-hole pairs (a biexciton) decays radiatively through two intermediate excitonic states; if these two decay paths with different polarizations are indistinguishable, the cascade of two photons provides entanglement. Indeed, when two electron-hole pairs (abusively called biexciton) are confined in the dot and trapped on the ground state of the dot, Pauli's principle states they should be at the same energy with opposite spin. The electromagnetic interactions between the different carriers induce a separation in energy between the state corresponding to two electron-hole pairs in the dot and the state corresponding to one electron hole pair in the dot. This energy separation is of the order of few meV in InAs/GaAs quantum dots, much greater than their spectral width (of the order of few tens  $\mu eV$  at 4 K). This difference allows the spectral separation of the emission line of the biexciton from the excitonic one. Moreover the total momentum of the two pairs is null, which implies that the total momentum of the two photons emitted by the successive recombination of the biexciton and the exciton, is also null. The polarizations of the photons are thus entangled, at least if the two paths are indistinguishable even in principle.

However, in typical InAs/GaAs quantum dots, different mechanisms, such as the splitting of the excitonic relay level, can degrade or even destroy entanglement. In order to assess the most appropriate techniques to restore polarization entanglement from the biexciton cascade, we theoretically

investigated the joint photodetection probabilities in the biexciton cascade and analytically derived the density matrix as well as an entanglement witness based on the Clauser-Horne-Shimony-Holt (CHSH) inequalities. This chapter begins by defining the model used to describe the four-level system interacting with a solid-state environment and subject to incoherent population exchange between the two relay levels. We then quantify the entanglement of the photons produced by deriving an analytical expression of the CHSH inequality as a function of the different dynamical parameters of the four-level system, as well as the density matrix corresponding to the biexciton cascade. We then stress the necessity to combine the use of techniques controlling the fine structure splitting of the exciton and the use of the Purcell effect, in order to violate Bell's inequalities from the cascade emission in self-assembled quantum dots. Constraints on the cavity design are then described, as well as possible solutions.

## 4.1 The model

The point emitter is here a quantum dot modelled as a four level system: the fundamental level, the excitonic level divided into two levels with opposite angular momentum, and the biexcitonic level. Two levels, called "dark exciton", are not taken into account. In these one electron-hole pair states, both spins of the electron and the hole are simultaneously up or down, therefore they are not optically coupled to the others considered levels. Only the two others levels of the exciton, called "bright excitons" are considered. In ideal quantum dots, the bright exciton states are degenerate. However, in usual dots, the excitonic relay level is split by the anisotropic exchange interaction, caused by in-plane anisotropy of the exciton wave function [7, 8]. This splitting will be addressed more specifically in § 5.2. In this section, we will present the model used to describe this four-level system and its interaction with its surroundings. We will then derive from its Hamiltonian a time evolution equation of the system excited on its upper state.

No spectral filtering of the emitted photons is performed such as in ref. [9]. This filter cancels the energy dependency of the polarization at the expense of losses in the luminosity [9, 10]. No temporal filtering is applied, such as in ref. [11]. Such filtering is the time-equivalent of the spectral one, and post-selects only the pair of photons for which the dot lasted a very short time at the intermediary level (i.e. the excitonic level). As we will see all degrading processes of the entanglement occur at this step, thus this filter selects the pairs of photons minimally marked by these processes. As for the spectral filter, this reduces significantly the efficiency of entangled photon pairs generation.

### 4.1.1 The four-level system

In the cascade emission from a four-level system, the decay paths involve two radiative transitions, one from the upper level  $|2\rangle$  (i.e. the biexciton) to an intermediate state  $|1_H\rangle$  or  $|1_V\rangle$  (i.e. the two excitonic relay levels) and the other from these relay states to the ground state  $|0\rangle$  (corresponding to an "empty" dot) (figure 4.1). The energies of these levels  $|2\rangle$ ,  $|1_H\rangle$  and  $|1_V\rangle$  are respectively denoted  $\hbar(\omega_1 + \omega_2)$ ,  $\hbar(\omega_1 + \delta\omega)$  and  $\hbar(\omega_1 - \delta\omega)$ . We will further assume that this  $\mathcal{B} = \{|2\rangle, |1_H\rangle, |1_V\rangle, |0\rangle\}$  basis corresponds to the eigenbasis of the quantum dot, with therefore an excitonic energy splitting  $2\delta\omega$  but no coherent coupling between the two excitonic eigenstates [12]. Radiative transitions from the biexciton in such basis emit collinearly polarized photons with linear polarization denoted  $H$  and  $V$  (see figure 4.1)<sup>40</sup>. The state of a photon is denoted by  $|u, \omega\rangle$  where  $u$  is its polarisation, and  $\hbar\omega$  its energy.

<sup>40</sup>This description in a linear polarization eigenbasis is a good approximation. If it was not, that is, if the eigenbasis of the excitonic level were not corresponding to the emission of linearly polarized photons, then the two excitonic levels would be coupled in whichever dot basis corresponds to a linearly polarized basis of the emitted photons. This coupling would appear as a beat between the populations of the emitted excitonic photons observed in any polarisation basis.

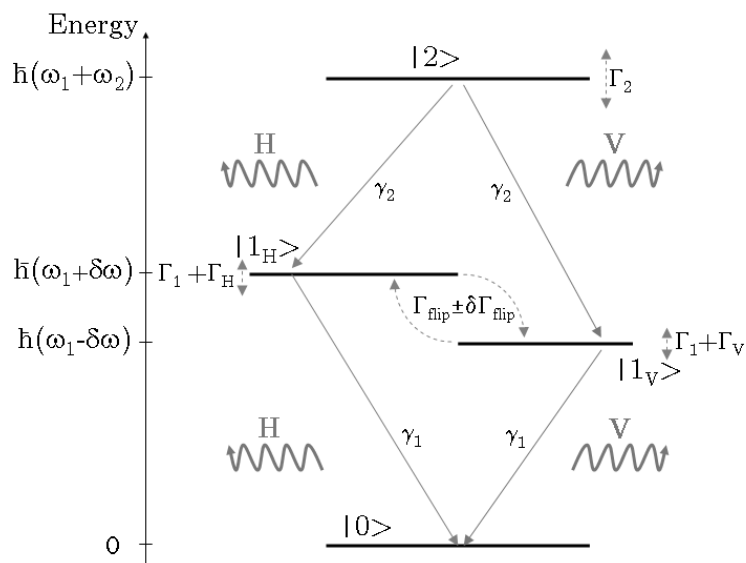


Figure 4.1: Schematic description of the two-photon cascade in a typical four-level system with an energy splitting  $2\hbar\delta\omega$  of the relay level, yielding two collinearly polarized photons (either  $H$  or  $V$ ).

In the ideal case ( $\delta\omega = 0$ ), the four-level system relaxes, generating the maximally entangled two-photon state by cascade emission [1, 6]:

$$|\Phi^+\rangle = \frac{1}{\sqrt{2}}(|H, \omega_1\rangle |H, \omega_2\rangle + |V, \omega_1\rangle |V, \omega_2\rangle) \quad (4.1)$$

The phase difference between the two component states  $|H, \omega_1\rangle |H, \omega_2\rangle$  and  $|V, \omega_1\rangle |V, \omega_2\rangle$  is null, as determined by the angular momentum of the different involved levels and the Clebsch-Gordan coefficients [15] and as confirmed experimentally [16]. In a first approximation, the total energy of the  $|HH\rangle$  pair (resp.  $VV$ ) is  $E_{HH}/\hbar = (\omega_2 - \delta\omega) + (\omega_2 + \delta\omega)$  including the contribution of each photon forming the pair (first brackets: biexciton, second brackets: exciton). For the  $|VV\rangle$  pair  $E_{VV}/\hbar = (\omega_2 + \delta\omega) + (\omega_2 - \delta\omega) = E_{HH}/\hbar$ . Consequently, no obvious time-dependent phase-energy term appears between the two components states.

Unfortunately, in realistic two-level systems (such as single quantum dots for example), the relay levels are split ( $\delta\omega \neq 0$ ). Furthermore, relaxation mechanisms between the two relay states  $|1_H\rangle$  and  $|1_V\rangle$  can occur (for example from spin flip processes). They will be accounted for by two phenomenological decay rates  $\Gamma_{flip} \pm \delta\Gamma_{flip}$ . In addition, the relay levels and the upper level may be subject to sudden, brief and random fluctuations of their energies without population exchange (arising, for example, from collisions with thermal phonons). In this model, the ground level  $|0\rangle$  is chosen as the reference in energy and phase. Dephasing of the upper level  $|2\rangle$  is described by the dephasing rate  $\Gamma_2$ . On the two relay levels  $|1_H\rangle$  and  $|1_V\rangle$ , we distinguish two dephasing processes without population exchange between these relay levels: (1) dephasing processes that occur simultaneously and attach the same information on the phase and energy of these two levels with a dephasing rate denoted  $\Gamma_1$  and (2) dephasing processes that do not affect identically the two relay levels, the impact of which depends on the polarization of the excitonic states [17]. These last processes will

---

Conversely, if no beat was occurring in the populations of the excitonic photon in one linear polarization basis, then this particular basis would correspond to the eigenbasis of the dot. The presence or absence of such beating, at least within the experimental resolution, has been observed in time resolved experiments depending on the polarization basis used [13, 11, 12, 14].

be described by polarization-dependent dephasing rates  $\Gamma_H$  and  $\Gamma_V$ . The cross-dephasing between the two relay states is therefore  $\Gamma = \Gamma_H + \Gamma_V$ . This model includes all possible dephasing processes without the possibility of population modifications.

#### 4.1.2 Dynamics of the four levels system

In order to account for the open nature of the four-level system (resulting from its coupling with the phonon and the photon reservoirs for example), the time evolution of the density operator  $\rho$  is described by means of the following master equation in the Lindblad form [18]:

$$\frac{d\rho}{dt} = -[iH, \rho] + (\mathcal{L}_r + \mathcal{L}_d + \mathcal{L}_{flip})\rho \quad (4.2)$$

In the previously described eigenbasis  $\mathcal{B}$  of the four-level system, the Hamiltonian  $H$  has the form:

$$H = (\omega_1 - \delta\omega)|1_V\rangle\langle 1_V| + (\omega_1 + \delta\omega)|1_H\rangle\langle 1_H| + (\omega_1 + \omega_2)|2\rangle\langle 2| \quad (4.3)$$

The Lindblad operators include three contributions. The first one describes the interaction of the emitter with the electromagnetic field by emitting photons, whenever it undergoes a transition from its upper state to the relay levels or from the relay levels to the ground state. This radiative relaxation is accounted for by the following Lindblad operator:

$$\mathcal{L}_r = \sum_{p=H,V} \left( \frac{\gamma_1}{2} \mathcal{L}(|0\rangle\langle 1_p|) + \frac{\gamma_2}{2} \mathcal{L}(|1_p\rangle\langle 2|) \right) \quad (4.4)$$

where  $\gamma_1$  and  $\gamma_2$  are respectively the radiative decay rates between the relay states and the ground state and between the upper level and the relay levels. These decay rates are assumed to not depend on the decay path the photons were released along. I will come back on this point later on.  $\mathcal{L}(D)\rho = 2D\rho D^\dagger - D^\dagger D\rho - \rho D^\dagger D$  is the Lindblad operator. The second contribution  $\mathcal{L}_d$  is related to dephasing processes and reads:

$$\mathcal{L}_d = \Gamma_2 \mathcal{L}(|2\rangle\langle 2|) + \sum_{p=H,V} \Gamma_p \mathcal{L}(|1_p\rangle\langle 1_p|) + \Gamma_1 \mathcal{L}(|1_H\rangle\langle 1_H| + |1_V\rangle\langle 1_V|) \quad (4.5)$$

This Liouvillian includes any phenomenological dephasing effect (e.g. phonons) occurring on the levels of the dot without population transfers as described previously. The last contribution  $\mathcal{L}_{flip}$  accounts for the incoherent coupling between the two relay states:

$$\begin{aligned} \mathcal{L}_{flip} = & \alpha_P \mathcal{L}(|1_H\rangle\langle 1_V| + |1_V\rangle\langle 1_H|) + \beta_P \mathcal{L}(i(|1_H\rangle\langle 1_V| + |1_V\rangle\langle 1_H|)) \\ & + \beta_Q \mathcal{L}(|1_V\rangle\langle 1_H| - |1_H\rangle\langle 1_V|) + \alpha_Q \mathcal{L}(i(|1_V\rangle\langle 1_H| - |1_H\rangle\langle 1_V|)) \end{aligned} \quad (4.6)$$

The phenomenological rate  $\Gamma_{flip}$  between the two relay states  $|1_H\rangle$  and  $|1_V\rangle$  appears to be twice the sum of the different rates  $\alpha_i$  and  $\beta_i$  ( $i = P, Q$ ) involved in this equation. The rate  $\delta\Gamma_{flip}$  expresses likewise as :  $2(\alpha_Q - \alpha_P + \beta_Q - \beta_P)$ . These rates simulate any unspecified process inducing an incoherent interaction between the two relay levels with population exchange before radiative relaxation.  $\delta\Gamma_{flip}$  accounts for asymmetry of these processes. These non-radiative processes may include spin-flip processes and transitions through dark states (assuming that the probability for the source to be in these dark-states is small compared to the probabilities related to the optically active states).

In accordance with all these assumptions, the time evolution of the four-level system can be decomposed by use of master equation (4.2) in a set of differential equations, which reduces to <sup>41</sup>:

$$\frac{dV}{dt} = AV \quad (4.7)$$

In this equation,  $V$  is a vector composed of the following mean values:

$$V = \begin{pmatrix} \text{Tr}[S_{\Delta}\rho] \\ \text{Tr}[S_Q\rho] \\ \text{Tr}[S_P\rho] \end{pmatrix} \quad (4.8)$$

The operator  $S_{\Delta} = |1_H\rangle\langle 1_H| - |1_V\rangle\langle 1_V|$  is related to population difference between the two excitonic relay states. The two other Pauli matrices  $S_Q = i|1_V\rangle\langle 1_H| - i|1_H\rangle\langle 1_V|$  and  $S_P = |1_H\rangle\langle 1_V| + |1_V\rangle\langle 1_H|$  correspond to the quadratures of the dipole between these two relay states. The  $A$  matrix is given by:

$$A = \begin{pmatrix} -\gamma_1 - 2\Gamma_{flip} & 0 & 0 \\ 0 & -\mu_Q & 2\delta\omega \\ 0 & -2\delta\omega & -\mu_P \end{pmatrix} \quad (4.9)$$

The decay constants  $\mu_{P/Q}$  are equal to  $\gamma_1 + \Gamma_{flip} \pm \delta\Gamma_{flip} + \Gamma$ . The positions of the zeros in the matrix  $A$  state the independency in the evolution of the quadratures of the excitonic spin, and its population. The quadratures are coupled via the excitonic splitting (off-diagonal terms) and have the same decay rate if we consider  $\delta\Gamma_{flip} = 0$ .

In the following, we shall denote  $M(U)$  the matrix transformation of  $V$ , where  $U$  is an arbitrary unitary transformation of the excitonic levels of the source (letting the upper and fundamental states unchanged), by

$$M(U)V(t) = \begin{pmatrix} \text{Tr}[US_{\Delta}U^{\dagger}\rho(t)] \\ \text{Tr}[US_QU^{\dagger}\rho(t)] \\ \text{Tr}[US_PU^{\dagger}\rho(t)] \end{pmatrix} \quad (4.10)$$

$M(U)V(t)$  are the mean values (4.8) measured at time  $t$  under the transformed basis  $\mathcal{B}$ .

## 4.2 Polarization entanglement from the biexciton cascade

From such a model, we quantify the entanglement of the photons produced by deriving an analytical expression of the CHSH inequality as a function of the different dynamical parameters of the four-level system, as well as the density matrix corresponding to the biexciton cascade. But let us first describe the experimental setup to demonstrate the violation of Bell's inequalities.

### 4.2.1 Experimental setup

The experimental setup we consider is described in figure 4.2. It comprises two polarization analyzers with an orientation  $\vec{\theta}_2$  and  $\vec{\theta}_1$  relatively to polarization eigenvectors of the quantum dot  $|H\rangle$ , measuring respectively the polarization of the first photon at energy  $\hbar\omega_2$  and the second photon at energy  $\hbar\omega_1$ . The exciton and biexciton photon are spectrally separated by means of optical filters and send through the optical path denoted  $i$  ( $i=1$  or  $2$  for the exciton and biexciton respectively). The analyzers are followed by two detectors, giving results  $+1$  or  $-1$ , corresponding to a linear polarization found parallel or perpendicular to the analyzers orientation [1]. In practice, since several points of the Bloch sphere have to be measured [1], a quarter-wave plate followed by a half-wave plate is inserted in the photons path (see figure 4.3).

The fast axis of the quarter-(resp. half-)wave plate is rotated by an angle  $\chi_i$  (resp.  $\theta_i$ ) with respect to the so-called horizontal polarization direction defined by the orientation of the dot (see figure 4.3). By applying the projection theorem, measuring  $+1$  in the optical setup  $i$  corresponds to the detection of a photon  $i$  emitted by the source with the polarization  $\Lambda(\theta_i, \chi_i)^{\dagger}|H\rangle$  where  $\Lambda(\theta, \chi)$

<sup>41</sup>The whole equations system was solved by use of the Mathematica software.

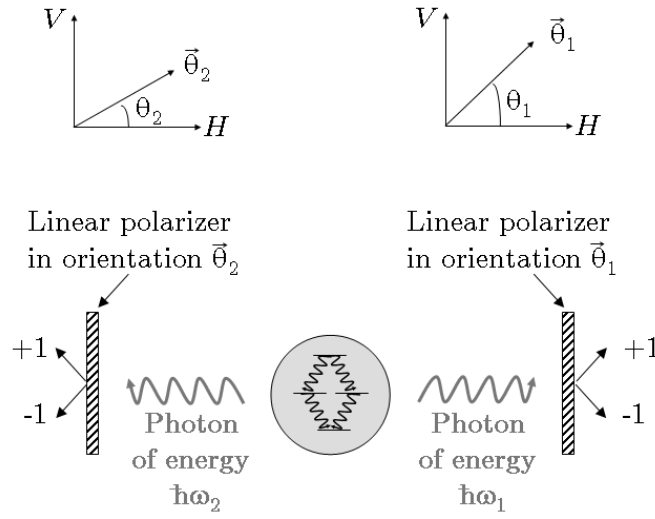


Figure 4.2: Scheme for the measure of the CHSH inequality. The two photons are analyzed by linear polarisers in orientation  $\theta_2$  and  $\theta_1$ . One measure the probabilities of joint detections in the output channels of the polarisers

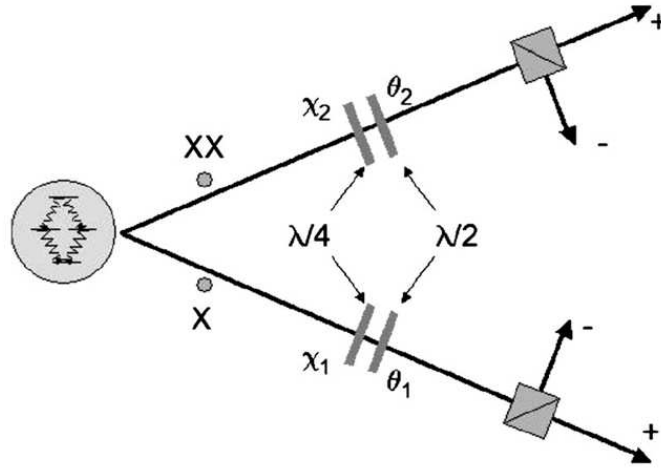


Figure 4.3: Experimental setup for measuring CHSH or reconstructing the density matrix

describes the transformation of the polarization basis  $\{H, V\}$  when a photon successively propagates through a quarter- and a half-wave plates rotated by the angles  $\theta$  and  $\chi$ .

$$\Lambda(\theta, \chi) = R(\theta)T(\pi)R(\chi - \theta)T(\pi/2)R(-\chi) \tag{4.11}$$

where  $R(x)$  is the rotation matrix and  $T(r)$  is the Jones matrix of a retarder plate.

$$R(x) = \begin{pmatrix} \cos(x) & \sin(x) \\ -\sin(x) & \cos(x) \end{pmatrix}, \quad T(r) = \begin{pmatrix} 1 & 0 \\ 0 & e^{-ir} \end{pmatrix} \tag{4.12}$$

In the following, for the sake of clarity we will denote  $\Lambda(\theta, \chi)^\dagger |1_H\rangle$  the superposition of the source's states  $|1_H\rangle$  and  $|1_V\rangle$  which analytically corresponds to the same transformation  $\Lambda(\theta, \chi)^\dagger |H\rangle$  of the photonic state  $|H\rangle$ .

Experimentally one measures the joint photodetection probabilities  $P_{\pm, \pm}^{det}(\theta_2, \chi_2, \theta_1, \chi_1)$  of the first photon and second photon in channels  $\pm$  of their respective optical setups with each retarder plate rotated by  $\theta_i$  and  $\chi_i$ . The source is pumped at time  $t = 0$  from its ground state to the biexcitonic state with a laser pulse shorter than the lifetime  $1/(2\gamma_2)$  of the upper state. We will further post select joint photodetection events corresponding to a sequential detection of the biexcitonic photon and then of the excitonic photon during one excitation cycle. In practice, if the pump is non resonant and creates electrons and holes in the wetting layer, one must avoid refilling the dot with carriers trapped in the wetting layer reservoir during the cascade. In that case, the dot can capture new pairs of electrons and holes and reemit photons. This may for example lead to the emission sequence of three photons such as biexciton - exciton - exciton. In this example only the two first photons are correlated, and if the second exciton is detected instead of the first one (due to the finite quantum efficiency of the detectors, or any kind of losses during the propagation), the pair of detected photons is not entangled. This kind of process degrades strongly the quality of the measured entanglement, as the Poissonian statistical aspect of the laser-based sources of entangled photons pairs does [19, 20]. Here, this problem is usually called repumping by the wetting layer. How to avoid this problem will be addressed in the following (§ 4.3.3).

#### 4.2.2 Joint photodetection probability

In this context, the probability of joint photodetection  $P_{+,+}^{det}(\theta_2, \chi_2, \theta_1, \chi_1, t_2, t_1)$  is proportional to the emission probability  $P_{+,+}(\theta_2, \chi_2, \theta_1, \chi_1, t_2, t_1)$  of a pair of photons with respective polarization orientation  $\Lambda(\theta_i, \chi_i)^\dagger |H\rangle$ , at respective energies  $\hbar\omega_2$  and  $\hbar\omega_1$  emitted respectively at the times  $t_2$  and  $t_2 + t_1$ , assuming that the source is in state  $|2\rangle$  at time  $t = 0$ . This radiative transition probability can be regarded as the product of two probabilities: the probability of emission of the first photon with polarization  $\Lambda(\theta_2, \chi_2)^\dagger |H\rangle$ , multiplied by the conditional probability of radiative transition from the relay levels to the ground state with emission of a photon polarized along  $\Lambda(\theta_1, \chi_1)^\dagger |H\rangle$ . This amounts in considering the photon cascade as a two-step process and applying the quantum-measurement projection postulate. First the photon at energy  $\hbar\omega_2$  and polarized along  $\Lambda(\theta_2, \chi_2)^\dagger |H\rangle$  is detected at time  $t_2$ , which projects the emitter on the superposition  $\Lambda(\theta_2, \chi_2)^{* \dagger} |1_H\rangle$  of the exciton states  $|1_H\rangle$  and  $|1_V\rangle$ . Secondly, the superposition state evolves in time until the detection of the second photon at energy  $\hbar\omega_1$  at time  $t_1 + t_2$ . Consequently, this conditional probability will be related to the population in the superposition  $\Lambda(\theta_1, \chi_1)^\dagger |1_H\rangle$  at time  $t_2 + t_1$ , knowing that the intermediate levels were in the superposition  $\Lambda(\theta_2, \chi_2)^{* \dagger} |1_H\rangle$  at time  $t_2$ . All these probabilities are integrated over the photodetection time window.

The population at time  $t_1 + t_2$  in the superposition  $|1_H(\theta_1)\rangle$  can be expressed as  $[e^{-\gamma_1 t_1} + \langle S_\Delta \rangle(t_2 + t_1 | t_2)]/2$ . In this expression,  $\langle S_\Delta \rangle(t_2 + t_1 | t_2)$  is the first value of the vector  $V$  of Eq. (4.8) measured under the transformation of Eq. 4.10 with  $U = \Lambda(\theta_1, \chi_1)^\dagger$ , after a free evolution during the time  $t_1$  (Eq. 4.7). We have assumed here that the initial state  $V^{init}$  corresponds to the excitonic state  $\Lambda(\theta_2, \chi_2)^{* \dagger} |H\rangle$  at time  $t_2$ . Thus by defining the vector  $V_0 = \{1, 0, 0\}$  which corresponds to the values of  $V$  measured in the eigenbasis with the source in the state  $|1_H\rangle$ , it follows that:

$$V^{init} = M(\Lambda(\theta_2, \chi_2)^{* \dagger})^{-1} V_0 \quad (4.13)$$

$$V^{measured} = M(\Lambda(\theta_1, \chi_1)^\dagger) e^{At} V^{init} \quad (4.14)$$

$$\langle S_\Delta \rangle(t_1 | 0) = \langle S_\Delta \rangle(t_2 + t_1 | t_2) \quad (4.15)$$

$$= [M(\Lambda(\theta_1, \chi_1)^\dagger) e^{At} M(\Lambda(\theta_2, \chi_2)^{* \dagger})^{-1}]_{11} \quad (4.16)$$

where  $[\dots]_{ij}$  denotes the matrix element on row  $i$  and column  $j$ . The probability  $P_{+,+}(\theta_2, \chi_2, \theta_1, \chi_1, t_2, t_1)$  can therefore be written as follows:

$$P_{+,+}(\theta_2, \chi_2, \theta_1, \chi_1, t_2, t_1) = \gamma_2 e^{-2\gamma_2 t_2} \times \frac{\gamma_1}{2} (e^{-\gamma_1 t_1} + \langle S_\Delta \rangle(t_1|0)) \quad (4.17)$$

and the probability integrated over the detection times is

$$P_{+,+}(\theta_2, \chi_2, \theta_1, \chi_1) = \int_0^\infty dt_2 \int_0^\infty dt_1 P_{+,+}(\theta_2, \chi_2, \theta_1, \chi_1, t_2, t_1) \quad (4.18)$$

Upon integration, this probability reads in the particular case  $\chi_1 = \chi_2 = 0$ :

$$P_{+,+}(\theta_2, \theta_1) = \frac{1}{4} \left[ 1 + \frac{\gamma_1}{\gamma_1 + 2\Gamma_{flip}} \cos(4\theta_1) \cos(4\theta_2) + \frac{\gamma_1(\gamma_1 + \Gamma_{flip} + \Gamma - \delta\Gamma_{flip})}{(2\delta\omega)^2 + (\gamma_1 + \Gamma_{flip} + \Gamma)^2 - (\delta\Gamma_{flip})^2} \sin(4\theta_1) \sin(4\theta_2) \right] \quad (4.19)$$

For a perfect quantum dot,  $P_{+,+}(0, 0)$  tends toward  $1/2$  as expected.

### 4.2.3 Quantifying two-photon entanglement and density matrix

Entanglement can be quantified by several means like measurement of the concurrence [21], separation of the density matrix [22, 23] or more generally entanglement witness operators [24, 25, 26, 27, 21]. A non optimal entanglement witness, but nevertheless experimentally simple to measure, is the Bell inequality under the CHSH form which discriminate between states that can be explained by a Local Hidden Variable Model (LHVM) or not. The possible violation of Bell inequalities is experimentally easy to verify by measuring the fringes visibility [28] of two-photon coincidences as a function of  $(\theta_1 - \theta_2)$  whereas other measurements need the experimental knowledge of the density matrix. Hence we shall first derive the analytical form of the CHSH inequality, then generalize the result to the derivation of the density matrix and one possible entanglement witness [24] by use of the Peres criterion [22].

#### Violation of Bell's inequalities

The CHSH inequality is calculated by measuring the correlation coefficient for four sets of properly chosen angles of a half-wave plate, and therefore the angles  $\chi_i$  referring to the quarter wave plate are set to zero and discarded in the rest of this subsection. From the expression of Eq. (4.19), one deduces all the probabilities  $P_{\pm,\pm}(\theta_2, \theta_1)$  and computes analytically in a straightforward manner the correlation coefficient of the form:

$$E(\vec{\theta}_2, \vec{\theta}_1) = P_{+,+}(\vec{\theta}_2, \vec{\theta}_1) + P_{-,-}(\vec{\theta}_2, \vec{\theta}_1) - P_{-,+}(\vec{\theta}_2, \vec{\theta}_1) - P_{+,-}(\vec{\theta}_2, \vec{\theta}_1) \quad (4.20)$$

The generalized Bell's inequality in the Clauser-Horne-Shimony-Holt (CHSH) formulation [29] is expressed as a combination of such correlations functions as:

$$S(\theta_2, \theta'_2, \theta_1, \theta'_1) = E(\vec{\theta}_2, \vec{\theta}_1) - E(\vec{\theta}'_2, \vec{\theta}_1) + E(\vec{\theta}_2, \vec{\theta}'_1) + E(\vec{\theta}'_2, \vec{\theta}'_1) \quad (4.21)$$

which, for classically correlated states, is bounded by  $|S| \leq 2$ . In the case of an ideal entangled source, the maximum value of the CHSH coefficient  $S$  is obtained for every set of polarization directions of each analyzer verifying  $\theta_2 = x + \pi/16$  and  $\theta'_2 = x + 3\pi/16$ ;  $\theta_1 = x$  and  $\theta'_1 = x + \pi/8$ , where  $x$  is an arbitrary rotation of both half-wave plates. In this context and under the assumption of  $\delta\Gamma_{flip} = 0$ , the CHSH parameter  $S$  is given by the formula:

$$S = \sqrt{2} \left( \frac{\gamma_1}{\gamma_1 + 2\Gamma_{flip}} + \frac{\gamma_1(\gamma_1 + \Gamma_{flip} + \Gamma)}{(\gamma_1 + \Gamma_{flip} + \Gamma)^2 + (2\delta\omega)^2} \right) \quad (4.22)$$

which is, as expected, independent of the arbitrary rotation  $x$ . Violation of Bell's inequalities implies  $S > 2$ .

### Density Matrix

In the above section, the Bell inequalities have been derived from the coincidence probabilities when the exciton and biexciton are detected in a linear basis. We will now exploit the more general expression of the joint photodetection probability  $P_{+,+}(\theta_2, \chi_2, \theta_1, \chi_1)$  obtained upon integration of Eq. 4.18. By definition of the density matrix, this probability can also be expressed as

$$P_{+,+}^{\rho}(\theta_2, \chi_2, \theta_1, \chi_1) = \langle H_{XX}H_X | (\Lambda(\theta_2, \chi_2) \otimes \Lambda(\theta_1, \chi_1)) \cdot \underline{\rho} \cdot (\Lambda(\theta_2, \chi_2) \otimes \Lambda(\theta_1, \chi_1))^{\dagger} | H_{XX}H_X \rangle$$

where  $\underline{\rho}$  is the density matrix of the pair of photon in the basis  $\{H_{XX}H_X, H_{XX}V_X, V_{XX}H_X, V_{XX}V_X\}$ . By identifying  $P_{+,+}^{\rho}(\theta_2, \chi_2, \theta_1, \chi_1) = P_{+,+}(\theta_2, \chi_2, \theta_1, \chi_1)$  for 16 well chosen set of four angles  $(\theta_2, \chi_2, \theta_1, \chi_1)$  we construct a linear system of 16 independent equations for which the unknown variables are the 16 real values of  $\underline{\rho}$ <sup>42</sup>. In this way, we simply reconstruct the density matrix from the joint photodetection probabilities [30] and obtain a theoretical value of  $\underline{\rho}$ . Table 4.4 gives an example of the positions set of the waveplates to obtain these 16 measures. The same holds for an experimental approach. The calculated density matrix is hence :

$$\underline{\rho} = \begin{pmatrix} \alpha & 0 & 0 & d - ic_1 \\ 0 & \beta & c_2 & 0 \\ 0 & c_2 & \beta & 0 \\ d + ic_1 & 0 & 0 & \alpha \end{pmatrix} \quad (4.23)$$

where

$$\begin{aligned} \alpha &= \frac{1}{2} \frac{\gamma_1 + \Gamma_{flip}}{\gamma_1 + 2\Gamma_{flip}} \\ \beta &= \frac{1}{2} \frac{\Gamma_{flip}}{\gamma_1 + 2\Gamma_{flip}} \\ d &= \frac{1}{2} \frac{\gamma_1(\gamma_1 + 2\Gamma + \Gamma_{flip})}{(2\delta\omega)^2 + (\gamma_1 + \Gamma_{flip} + \Gamma)^2 - (\delta\Gamma_{flip})^2} \\ c_1 &= \frac{1}{2} \frac{\gamma_1\delta\omega}{(2\delta\omega)^2 + (\gamma_1 + \Gamma_{flip} + \Gamma)^2 - (\delta\Gamma_{flip})^2} \\ c_2 &= \frac{1}{2} \frac{\gamma_1\delta\Gamma_{flip}}{(2\delta\omega)^2 + (\gamma_1 + \Gamma_{flip} + \Gamma)^2 - (\delta\Gamma_{flip})^2} \end{aligned} \quad (4.24)$$

Note that for a perfect quantum dot<sup>43</sup>,  $\rho$  tends, as expected, toward the  $|\Phi^+\rangle$  Bell state:  $\underline{\rho} \rightarrow |\phi^+\rangle\langle\phi^+|$ . The two off-diagonal terms  $c_1$  and  $c_2$  which should be null are respectively proportional to the splitting and the asymmetric rate in the spin flip process. Compared to published experimental tomography, this asymmetry is of importance as it allows to explain the fact the  $HVVH$  term in the density matrix is non zero, as measured by other teams.

<sup>42</sup>The  $4 \times 4$  density matrix has 4 diagonal real values, and 6 off-diagonal imaginary values, for a total of  $4 + 6 * 2 = 16$  real values. With the use of the normalization of the matrix (the diagonal sum equals to 1), it is possible to perform only 15 of the measures. Any other protocol to experimentally constitute the density matrix which needs fewer measures than that, makes necessarily some hypothesis.

<sup>43</sup>That is:  $\delta\omega \rightarrow 0$ ,  $\Gamma_{flip} \rightarrow 0$ ,  $\Gamma \rightarrow 0$ , which is equivalent to:  $\alpha, d \rightarrow 1$  and  $\beta, c_1, c_2 \rightarrow 0$ .

Analyzer 1		Analyzer 2	
Halfwave plate	Quarter wave plate	Halfwave plate	Quarter wave plate
$\pi/4$	0	$\pi/4$	0
$\pi/4$	0	0	0
0	0	0	0
0	0	$\pi/4$	0
$\pi/8$	0	$\pi/4$	0
$\pi/8$	0	0	0
$\pi/8$	$\pi/4$	0	0
$\pi/8$	$\pi/4$	$\pi/4$	0
$\pi/8$	$\pi/4$	$\pi/8$	0
$\pi/8$	$\pi/4$	$\pi/8$	$\pi/4$
$\pi/8$	0	$\pi/8$	$\pi/4$
$\pi/4$	0	$\pi/8$	$\pi/4$
0	0	$\pi/8$	$\pi/4$
0	0	$\pi/8$	0
$\pi/4$	0	$\pi/8$	0
$\pi/8$	0	$\pi/8$	0

Figure 4.4: Example of the set of angle of rotations of the waveplates for the 16 measures to perform the tomography of the photon pair.

#### 4.2.4 Quantum dot spectroscopy from quantum tomography

An interesting feature of the analytical form of the density matrix arises from the fact that once it is computed experimentally, one can deduce all the quantum dot parameters provided  $\gamma_1$  is measured independently. They are expressed as a function of the density matrix elements <sup>44</sup>:

$$\begin{aligned}
\delta\omega &= \gamma_1 \frac{c_1}{4(d^2 + c_1^2 - c_2^2)} \\
\delta\Gamma_{flip} &= \gamma_1 \frac{c_2}{2(d^2 + c_1^2 - c_2^2)} \\
\Gamma_{flip} &= \gamma_1 \frac{2\beta}{1 - 4\beta} \\
\Gamma &= \gamma_1 \frac{d(1 - 2d - 4\beta + 4d\beta) + 2(c_1^2 - c_2^2)(2\beta - 1)}{4(d^2 + c_1^2 - c_2^2)(4\beta - 1)}
\end{aligned} \tag{4.25}$$

Obviously one can perform the tomography and express the density matrix in any basis. To deduce experimentally the phenomenological constants, one has to make the measure in the linear eigenbasis of the dot. This basis corresponds to the basis in which the amplitude of the beating is minimal (it is even null if the eigenbasis is linear). Therefore one can perform a common rotation by an angle  $\theta$  of the linear axis of both exciton and biexciton polarization, such as the  $HH$  and  $VV$  terms reach their maximum.

<sup>44</sup>An error appeared in my article [31] on the sign of  $\Gamma_{flip}$ . Here the expression is right.

### 4.2.5 Other entanglement criteria

#### Peres criterion

Apart from the CHSH inequality other entanglement witnesses can be constructed and following [24] we define an entanglement witness as  $Tr[W\rho]$  where  $W$  is an operator. In the case where  $W$  is an optimal witness, the above mentioned quantity is negative if  $\rho$  is an entangled state. As proposed in [22] we define the partial transpose  $\rho_0^{T_2}$  of an arbitrary density matrix  $\rho_0$  as follows :

$$\begin{aligned}\rho_0 &= \sum_{i,j,k,l=H,V} \rho_{0\ i,j,k,l} |ij\rangle\langle kl| \\ \rho_0^{T_2} &= \sum_{i,j,k,l=H,V} \rho_{0\ k,j,i,l} |ij\rangle\langle kl|\end{aligned}\quad (4.26)$$

As demonstrated in [22], if  $\rho_0^{T_2}$  has a negative eigenvalue  $\lambda$  associated to the eigenvector  $|\nu\rangle$  then the density matrix  $\rho$  represents an entangled state. Thus defining  $W = |\nu\rangle\langle\nu|^{T_2}$  we have

$$Tr[W\rho_0] = Tr[|\nu\rangle\langle\nu|\rho_0^{T_2}] = \lambda < 0 \quad (4.27)$$

In our case we choose for  $\rho_0$  the density matrix  $|\phi^+\rangle\langle\phi^+|$  toward which the biexciton density matrix  $\rho$  of our model tends to. This gives a non optimal witness but already less demanding than Bell inequalities and with a simple analytical form:

$$W = \begin{pmatrix} 0 & 0 & 0 & -1/2 \\ 0 & 1/2 & 0 & 0 \\ 0 & 0 & 1/2 & 0 \\ -1/2 & 0 & 0 & 0 \end{pmatrix} \quad (4.28)$$

$$\begin{aligned}Tr[W\rho] &= \beta - d \\ &= \frac{1}{2} \frac{\Gamma_{flip}}{\gamma_1 + 2\Gamma_{flip}} \\ &= \frac{1}{2} \frac{\gamma_1(\gamma_1 + 2\Gamma + \Gamma_{flip})}{(2\delta\omega)^2 + (\gamma_1 + \Gamma_{flip} + \Gamma)^2 - (\delta\Gamma_{flip})^2}\end{aligned}\quad (4.29)$$

#### Time-dependent fidelity

Following [11], another criterion that can be used is the time-dependent fidelity  $f$  to the expected photonic state, of the emitted states as a function of the time spent in the excitonic level, between  $t_1$  and  $t_1 + dt_1$ . From the probability  $P_{+,+}(\theta_2, \chi_2, \theta_1, \chi_1, t_2, t_1)$  given by equation (4.17) integrated over the biexcitonic emission time  $t_2$ , it is possible to deduce the density matrix  $\rho(t_1)dt_1$  as a function of  $t_1$  by the same tomographic method as previously (§ 4.2.3). The composition of this matrix is the same as before (same zeros ...). The fidelity  $f(t_1)dt_1$  to the expected state  $|\Phi^+\rangle$  given by equation (4.1) reads:

$$f(t_1) = \langle\Phi^+|\rho(t_1)|\Phi^+\rangle \quad (4.30)$$

$$= \frac{\gamma_1}{2} \left( e^{-\gamma_1 t_1} + e^{-(\gamma_1 + 2\Gamma_{flip})t_1} + 2 \cos(2\delta\omega t_1) e^{-(\gamma_1 + 2\Gamma + \Gamma_{flip})t_1} \right) \quad (4.31)$$

The fidelity oscillates at the frequency's splitting  $2\delta\omega$  as reported by [11]. If we only consider the photon pairs emitted with a time spent in the intermediary level, small compared to the oscillation period of the fidelity, then the fidelity tends to 1. This clearly models the time filter used by Stevenson et al [11].

### 4.2.6 Further developments of the model

This model has the advantage to give analytical formulae and to be quite complete. The strongest assumption is that the biexcitonic and excitonic decay rates do not depend on the polarization of the emitted photons. I have tried to obtain a complete model by getting rid of this symmetry between the H and V exciton levels while keeping the other aspects of the model. Such asymmetry arises naturally for high splitting because the decay rates depend in fact on the energy of the transition. This difference in decay rates can also arise from a cavity Purcell effect depending on the polarization (see § 4.4.3 and ref. [32] for an experimental example).

When we distinguish the decay rates for the H and V polarizations, the evolution matrix  $A$  (eq. (4.9)) is transformed into a four by four matrix which is still be diagonalized analytically, even if the obtained formulae are no more easily understandable. The evolution of the system is not the problem. The main problem resides in writing the equivalent equation given by (4.16), which represents the measure projection. For example, with  $\gamma_{H2}$  (resp.  $\gamma_{V2}$ ) the decay rate of the biexciton with the emission of a horizontally (resp. vertically) polarized photon, it is unclear how to evaluate the probability to measure the biexcitonic photon emitted at the time  $t_2$ , measured in the polarisation  $\vec{\theta}_2$ . This is not

$$\left| \left\langle \vec{\theta}_2 \left| (e^{-\gamma_{H2}t_2} |1_H\rangle + e^{-\gamma_{V2}t_2} |1_V\rangle) \right. \right\rangle \right|^2 \quad (4.32)$$

because if the splitting is strong and the two excitonic levels are clearly separated in energy, the probability to measure a biexcitonic photon with this polarization is the sum of the probability to measure the horizontal biexcitonic photon projected on  $\vec{\theta}_2$  plus the probability on the vertical photon, that is:

$$\left| \left\langle \vec{\theta}_2 \left| e^{-\gamma_{H2}t_2} |1_H\rangle \right. \right\rangle \right|^2 + \left| \left\langle \vec{\theta}_2 \left| e^{-\gamma_{V2}t_2} |1_V\rangle \right. \right\rangle \right|^2 \quad (4.33)$$

It can be this formula either because this one erases all phase information between the  $|1_H\rangle$  and  $|1_V\rangle$  which should be projected on the excitonic level by the measure process. In the previous symmetric case, this probability was obviously  $e^{-\gamma_2 t_2}$ .

Let us mention that the biexcitonic cascade has also been studied theoretically, in a general point of view [33, 34, 35, 36, 37], or addressed more specifically on a few aspects of the problem [38, 39], or more recently with models specific to a peculiar experiment [40, 11, 10]. Except for the most recent articles, these theoretical studies suffer from being exclusively numerical, and/or from making strong hypothesis on the entanglement degrading processes, by exploring for instance a reduced number of causes (usually only the exciton fine structure splitting).

## 4.3 Restoration of entanglement

Since the pioneering paper by O. Benson *et al* [6], many research groups have investigated the possibility to produce such polarization entangled photons from quantum dots. The most important experimental realizations are:

- the experimental demonstration of the deterministic behaviour of the source [41, 42]
- the observation of the cascade behaviour from the biexcitonic state and the associated sequential emission of the photons [5, 43]
- the beating introduced by the polarization-degeneracy breaking of the excitonic level (called excitonic splitting) widely observed [13, 11], as also the spin memory of the excitonic level [44, 14],

- the measurement of the phase between the two decay paths [16],
- the experimental degree of entanglement of the photon pair has slowly progressed, from only correlated photon pairs [45, 12] to controversially entangled ones [46, 47]<sup>45</sup>, then to entangled ones by use of spectral [9] or more recently temporal [11, 48] filtering, at the expense of a very poor generation of entangled photon pairs. This last technique has been combined to techniques bringing the fine structure splitting close to zero [48].

The results obtained by our model can be used to determine the main ingredients degrading polarization entanglement in the biexciton cascade from a quantum dot. This can be done by use of the CHSH inequality as well as the density matrix. However, the density matrix as a function of the internal parameters of the QD is less interesting than the CHSH inequality since the latter is an intuitive entanglement witness with a simple experimental realization. In the first part of this section, we will identify the main parameters contributing to a decrease of the degree of entanglement. We will then list different approaches that have been proposed or even implemented to restore entanglement.

### 4.3.1 Ingredients degrading entanglement

Equation (4.22) indicates that polarization entanglement in the cascade emission from a biexciton in a self-assembled quantum dot may be affected by the relative contribution of three processes with respect to the exciton radiative lifetime  $1/\gamma_1$ : the mutual coherence between the two non-degenerate excitonic levels described by a cross-dephasing time  $1/\Gamma$ , the excitonic energy splitting giving rise to quantum beats with a time period  $2\pi/2\delta\omega$  and the incoherent population exchange between the two bright excitons with a decay time  $1/\Gamma_{flip}$ . Entanglement does not depend on the biexciton radiative rate ( $\gamma_2$ ) and among all the dephasing processes taken into account in our model, only the cross-dephasing between the excitonic levels affects the visibility of entanglement. The analytical expression of  $S$  given by (4.22) also confirms that polarization entanglement from the biexciton cascade in self-assembled quantum dots is exclusively affected by the dynamics and mutual coherence of the excitonic states.

For quantum dots with no excitonic energy splitting ( $\delta\omega = 0$ ) and in absence of cross-dephasing ( $\Gamma = 0$ ) and incoherent population exchange ( $\Gamma_{flip}=0$ ), the  $S$  quantity reaches its maximum value of  $2\sqrt{2}$  and the photons emerging from the biexcitonic cascade are maximally entangled [6]. Conversely, for quantum dots with split excitonic states and which are affected by spin-dependent dephasing mechanisms and incoherent population exchange between the exciton bright states, the  $S$  parameter rapidly decreases so that the two photons emitted are only partially entangled or even only correlated in one preferred polarization basis corresponding to the polarization eigenbasis of the dot [12].

As an example, the characteristic excitonic lifetimes  $1/\gamma_1$  of InAs quantum dots embedded in GaAs are typically of the order of 1 ns [50] and the excitonic energy splitting  $2\hbar\delta\omega$  is of the order of few  $\mu\text{eV}$  [51] corresponding to quantum beat periods lower than few hundred picoseconds. Numerous observations also indicate that the exciton spin relaxation is quite negligible on the timescale of the exciton lifetime and may reach values of about 10 ns or even higher [44, 14]. The mutual coherence time  $1/\Gamma$  is likely to be longer than few ns [40], since it involves hypothetical spin-dependent dephasing processes. These typical values indicate that the main ingredient affecting entanglement is the excitonic energy splitting; they imply that in an experimental setup involving bare InAs quantum dots, the  $S$  quantity is lower than 2 and tests of the Bell's inequalities on the two photons emerging from the biexciton cascade will not lead to any violation of the CHSH inequality (see dashed line on figure 4.5). Even for relatively small exciton energy splitting ( $2\hbar\delta\omega$  of the order of few  $\mu\text{eV}$ ),

<sup>45</sup>I say controversially due to the debate following the first experimental realization on the criteria to be used to prove entanglement [24]. Since the quantity of entangled information which can be shared by two distant people via an entangled photon source, is in fact measured by the CHSH witness [49], I base my work on the Bell's test inequality. These articles do not say they violate this inequality but usually use other criteria.

the  $S$  value tends to 1.2, a value significantly lower than the  $S = \sqrt{2} \sim 1.41$  limit of perfectly correlated photons without any hidden variables. The incoherent population exchange between the excitonic relay levels destroys entanglement and the emitted photons are a statistical mixture of  $\{|HH\rangle, |VV\rangle, |HV\rangle, |VH\rangle\}$  states. Even for bare quantum dots with no exciton energy splitting, entanglement is spoiled by cross-dephasing and incoherent population exchange between the two bright excitonic states: the maximum value of  $S$  on figure 4.5 for such quantum dots reaches only 2.06, a value very close to the classical limit of 2.

### 4.3.2 Controlling the fine structure splitting

In order to erase the "which path" information and restore entanglement with a high fidelity, it is crucial to reduce the excitonic energy splitting within the radiative linewidth of the relay levels. One strategy relies on strong spectral filtering [9], discarding the non entangled photon pairs; however, this strongly decreases the photon pairs collection rate and hence the quantum efficiency of the source. Different other techniques are currently explored to monitor finely this energy splitting: control via growth conditions (inducing structural modification [52, 53] or affecting the dot size [38] for example), control via magnetic [40] or electric [54, 55, 56, 14, 57, 58] fields, control via uniaxial stress [59]... We shall detail briefly some of these techniques.

As the splitting of the exciton state derives from anisotropy in the shape and strain in the vicinity of the dot, it varies considerably from sample to sample. It has been demonstrated that the proportion of dots with close to zero exciton splitting may be increased by annealing the sample, so as to intermix the dot and barrier material [52]. An outstanding problem is that these annealed dots emit at a wavelength close to the wetting layer, resulting in a large amount of background emission which dilutes the entangled photon pairs. It has however possible to reduce slightly the amplitude of the background by blue shifting the wetting layer emission away from the quantum dot peaks [47].

An alternative solution to achieve the fine tuning of this splitting relies on the application of an electric field. An in-plane electric field applied with lateral electrodes, along one of the quantum dot eigenaxis, has been proven to significantly influence the excitonic splitting in the case of strong anisotropy [60]. This results from a subtle interplay between the rigid quantum dot confinement potential and the field-induced displacement of the single particle wavefunctions. The electric field leads thus to an indirect control of the exciton wavefunction symmetry and thus of the splitting caused by the long range part of the electron-hole exchange. However, all these investigations have been done on dots displaying a large fine structure splitting and it is still not obvious if this technique may be efficient in the case of initially small excitonic splitting (i.e. less than  $10 \mu eV$ ) and if applying an electric field in a fixed direction is sufficient to compensate for all the small contributions to the splitting. The vertical configuration consisting in applying a field parallel to the quantum dot growth axis may be another approach since it produces also a perturbation of low symmetry ( $C_{2v}$ ) able to compensate the quantum dot anisotropy. This strategy has also been explored during my PhD and our results will be detailed in the next chapter.

Last but not least, depending on barrier materials and confinement energies, the energy splitting of the excitonic level can be decreased to zero by applying an in-plane magnetic field [61]. In a magnetic field, the Zeeman interaction causes the relay level to be a hybrid of bright and dark excitonic states. The impact of this hybridization of the excitonic states on entangled photons emitted by a quantum dot under a magnetic field has however still to be investigated.

### 4.3.3 Exploiting the Purcell effect

The previous approaches consisted in reducing the excitonic energy splitting within the radiative linewidth of the relay levels. Another approach could be to increase the radiative linewidth of the

relay levels well above the excitonic splitting so that the two relay levels become indistinguishable. In that case, the polarizations of the photons are not predictable due to a correlation between their polarization and their energy. In order to measure the energetic separability of the excitonic line, we define the spectral overlap of two lines as:

$$R_X = \frac{\int d\omega S_H(\omega) S_V(\omega)}{\sqrt{\int d\omega S_H(\omega)^2} \sqrt{\int d\omega S_V(\omega)^2}} \quad (4.34)$$

with  $S_H(\omega)$  the spectrum of the horizontally polarized line of the exciton (resp. for the vertically polarized one).  $R_X$  has maximal value of 1 when both lines are identical, and is null when they are totally separated. For lines with a Lorentzian shape of width  $1/\gamma_1$  and separated by  $2\delta\omega$ , the overlap equals to

$$R_X = \frac{1}{1 + \left(\frac{2\delta\omega}{\gamma_1}\right)^2} \quad (4.35)$$

A way to increase the exciton linewidths consists in reducing the excitonic radiative lifetime of the quantum dot by a factor of  $F$  through its introduction in a resonant microcavity and the exploitation of the Purcell effect [35]. Moreover, all previous strategies impacted only one ingredient degrading entanglement that is the fine structure splitting. However, other mechanisms that may be responsible for destroying or reducing the visibility of any entanglement, stems from relative dephasing between the two relay excitonic states, due to the interaction of the electrons and holes trapped in the quantum dot with the environment and the incoherent population exchange between the two relay levels. This relative dephasing and this incoherent population exchange break the indistinguishability of the two recombination paths. In order to restore quantum correlations, the impact of dephasing mechanisms and spin-flip processes can be alleviated by engineering of photon emission through the exploitation of the Purcell effect. The Purcell effect increases the linewidth of the intermediate levels, hides the random energy splitting induced by decoherence mechanisms and prevents from slow incoherent population exchanges. Indeed, by making the excitonic spontaneous emission faster than the quantum beats period ( $F\gamma_1 \gg 2\delta\omega$ ), the cross-dephasing time ( $F\gamma_1 \gg \Gamma$ ) and the decay time of incoherent excitonic population exchange ( $F\gamma_1 \gg \Gamma_{flip}$ ), it should be possible to preserve the quantum correlations between the two recombination paths. Let us determine the required amplitude of the Purcell effect allowing for violation of Bell's inequality in usual quantum dots.

We consider here that both excitonic transitions releasing either  $H$  or  $V$ -polarized photons are accelerated by cavity effects with the same spontaneous emission enhancement factor  $F$ . For dots subject to a spontaneous emission enhancement of its excitonic transition by a factor  $F = 10$  (see solid line on figure 4.5),  $S$  values higher than 2.6 should be achievable for null exciton energy splitting ( $2\hbar\delta\omega = 0$ ). In such microcavity sources however, the violation of Bell's inequalities ( $S > 2$ ) requires the use of quantum dots with an excitonic energy splitting smaller than  $7\mu eV$ . This corresponds to a spectral overlap of the excitonic lines  $R_X = 47\%$ . Entanglement is possible even with partially energetically distinguishable lines. With a Purcell effect of  $F = 30$ ,  $S$  reaches the value of 2.76 close to its maximum value of  $2\sqrt{2}$  for dots with no exciton energy splitting, and Bell's inequalities are violated for quantum dots displaying an energy splitting up to  $20\mu eV$  (figure 4.6).

However, a high Purcell effect on both the excitonic and the biexcitonic line can become detrimental regarding the repumping effect from the wetting layer. Indeed one possible way to avoid multiphoton (at least more than two) emission per excitation cycle, consists in creating a bottleneck on the biexciton transition: if the biexciton decay time is much longer than the excitation pulse duration and the carrier reservoir decay time, then the probability to refill the dot after emission of one or two photons during each excitation cycle gets close to zero. Consequently, in order to restore entanglement

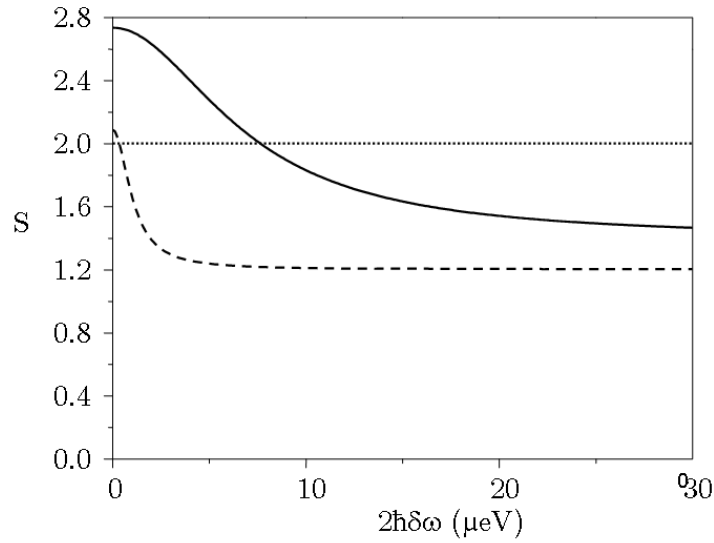


Figure 4.5: CHSH inequality as a function of the energy splitting of the exciton line, for a single quantum dot in bulk material (dashed line) and subject to a Purcell effect with  $F = 10$  (continuous line). Dotted line corresponds to the classical limit of 2. For these two curves,  $T_1 = 1/\gamma_1 = 1$  ns,  $1/\Gamma_{flip} = 10$  ns and  $1/\Gamma = 2$  ns.

by cavity effect, one has to be cautious to accelerate significantly the exciton transition only and not the biexciton transition. These conditions, combined with the selection of joint photodetections which only correspond to the emission of the two photons in the right sequence (§ 4.2.1), warrant that only the photon pairs corresponding to the same radiative cascade are detected. Such a cascade has already been clearly observed [5] which demonstrates the feasibility of these experimental conditions. Typical lifetimes of the biexcitonic level, the excitonic level, and the wetting layer are respectively  $1.2\text{ns}$ ,  $700\text{ps}$  and  $100\text{ps}$ , therefore if we want to maintain the excitonic lifetime longer than the wetting layer's lifetime to avoid repumping while reducing as possible the excitonic lifetime, a Purcell factor of 7 is a maximum for the biexcitonic level. This is adequate, as I previously demonstrated, with a Purcell factor of 5 allowing for a good collection of the photons. The issue of the cavity design will be addressed in the following (§ 4.4).

Nevertheless the use of cavity effects only is not sufficient to restore entanglement. Figure 4.6 shows the value of  $S$  as a function of  $2\hbar\delta\omega$  and as a function of  $F$  for values of  $\gamma_1$ ,  $\Gamma$  and  $\Gamma_{flip}$  considered above as typical of currently available quantum dots. The results confirm that the main ingredient degrading entanglement is the exciton fine structure splitting. Yet, reducing the exciton energy splitting within the exciton linewidth is not experimentally sufficient and hardly allows for violation of Bell's inequalities. Violation of the CHSH inequalities requires a combination of cavity effects enhancing the excitons spontaneous emission rate and techniques leading to a reduction of the exciton energy splitting, such as growth optimization [38] or use of external magnetic [61] or electric [55] field). For typically available quantum dots, a Purcell factor of the order of 10 exalting equally both excitons transitions, would be sufficient for reaching values of  $S$  higher than the classical limit of 2. Yet, the generation of maximally-entangled photons ( $S = 2\sqrt{2}$ ) with a single quantum dot is precluded by all decoherence mechanisms such as cross-dephasing between the exciton states and incoherent population exchange between the two bright excitons.

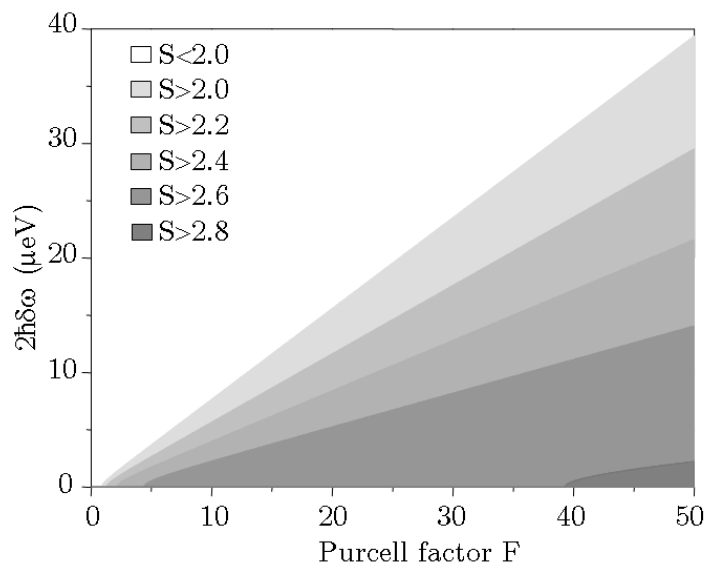


Figure 4.6: CHSH inequality as a function of the energy splitting of the exciton line and its spontaneous emission exaltation  $F$ , for a single quantum dot with  $T_1 = 1/\gamma_1 = 1$  ns in bulk material,  $1/\Gamma_{flip} = 10$  ns and  $1/\Gamma = 2$  ns.

## 4.4 Cavity design for restoring entanglement

We have seen previously that one has to combine cavity effects and techniques to control the energy fine structure splitting to restore entanglement. I will here focus on the design of the cavity to be used. Different parameters will be taken into account. In a first step, the design of the cavity will aim at obtaining the required Purcell effect and bright sources. I will demonstrate that a cavity with only one polarization degenerate mode with a poor quality factor can be sufficient. Another alternative would be the use of cavities sustaining two polarization degenerate modes, one resonant with the excitonic line and another with the biexcitonic one. In a second step, I will focus on the issue of farfield discernability and the impact of the dot's position respective to the field distribution.

### 4.4.1 Optimization of the Purcell effect and the collection efficiency

The brightness of the source is related to the collection efficiency of both photons  $\eta_{EPR}$ , defined by  $\eta_{EPR} = \eta_X * \eta_{XX}$ , where  $\eta_X$  and  $\eta_{XX}$  are the collection efficiencies of the exciton and biexciton photons respectively. Hence, if only one of the photons is efficiently collected, the overall collection efficiency will be lowered. If the two emission lines are coupled with the same cavity mode, the two individual collection efficiencies depend on the coupling efficiency of both photons in the cavity mode ( $\beta_X$  and  $\beta_{XX}$  resp.) and the collection efficiency  $\eta_i, i \in [X, XX]$  of the mode itself. The fraction  $(1 - \beta_i)$  of photons not coupled to the cavity mode will most probably not be collected by the microscope objective as demonstrated in chapter 2 [62]. Therefore the collection efficiency reads :

$$\eta_{EPR} = \beta_X * \beta_{XX} * \eta^2 \quad (4.36)$$

As demonstrated in § 1.4.2, a Purcell factor  $F_{XX}$  of 5 is sufficient to emit more than 80% (i.e.  $\beta_{XX} > 0.8$ ) of the biexcitonic photons in the cavity mode (The same stands for the excitonic transition).

For standard InAs/GaAs quantum dots emitting around  $\lambda_{QD} = 900$  nm, the energy splitting between the two photon lines is around  $\lambda_X - \lambda_{XX} = \delta\lambda_{X-XX} = 2$  nm [5]. Let us define  $\delta = \delta\lambda_{X-XX}/\lambda_X$

and Let us consider that the exciton is perfectly in resonance with the cavity mode. The Purcell factor of the biexciton can be written as  $F_{XX} = F_X/(1 + 4Q^2\delta^2)$ . Considering that  $Q = (4\pi^2/3)V_{cav}F_X$  where  $V_{cav}$  is the cavity volume expressed in  $(\lambda/n)^3$  units, we can rewrite the above equation as :

$$F_{XX} = \frac{F_X}{1 + \left(\frac{8\pi^2}{3}V_{cav}F_X\delta\right)^2} \quad (4.37)$$

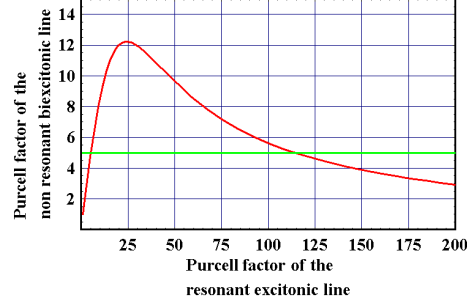


Figure 4.7: Red curve: The Purcell factor of the non resonant biexcitonic line as a function of the Purcell factor on the resonant excitonic line, with  $V_{cav} = 0.7$  and  $\delta = 2/900$ . Green curve: Minimal bi-excitonic Purcell factor acceptable for our chosen minimal mode coupling efficiency  $\beta_{XX} > 0.8$ .

Hence the Purcell factor of the biexciton rises almost linearly with respect to the Purcell factor of the exciton until  $F_{XX} = 12$  equivalent to a quality factor of  $Q = 225$ . Above this value, increasing the excitonic Purcell factor decreases the biexcitonic Purcell factor due to a too thin mode line (see fig. 4.7). Constraining the biexcitonic mode coupling efficiency  $\beta_{XX}$  to be higher than 80% limits the excitonic Purcell factor between 5 and 120 (for typical values of  $V_{cav} = 0.7$  in case of H1 cavities). Moreover as demonstrated earlier, a Purcell factor of 10 is sufficient to restore entanglement for a quantum dot with  $T_1 = 1/\gamma_1 = 1$  ns,  $1/\Gamma_{flip} = 10$  ns and  $1/\Gamma = 2$  ns and an energy splitting of less than  $5 \mu$  eV. This corresponds to a quality factor of  $130 < Q < 1500$ . The maximal allowable quality factor corresponds to a linewidth of 0.6nm for the cavity mode. The maximum of  $F_{XX} = 12$  is still acceptable to avoid the repumping by the wetting layer (§ 4.2.1, § 4.3.3). It is therefore possible :

- to couple both excitonic and biexcitonic lines to the same cavity modes,
- to obtain a good collection efficiency for both photons,
- to obtain a Purcell factor above the minimal requirements of 10 on the excitonic line in order to restore entanglement,
- not to accelerate the biexciton significantly in order to avoid emission cascade cycles shorter than the lifetime of the charges in the wetting layer.

In the following, we shall consider that the exciton and biexciton photons are emitted in the same cavity mode: the cavity mode is resonant with the excitonic transitions, quasi-resonant with the biexcitonic one and degenerated in polarization.

Among all the photonic crystal cavity designs, the H1 cavity is a very good candidate for the generation of entangled photon pairs since it sustains two energy degenerate dipole modes with a field maximum at the center of the cavity <sup>46</sup>. This cavity offers both a low mode volume and theoretically high quality factors by fine tuning the inner holes [63]. We are interested in the dipole mode of such cavity for the following reason. For the generation of entangled photon pairs, both polarizations shall

undergo the same effects, same emission diagram, and same Purcell factor. While the hexapole mode has been studied for its highly directive emission diagram [64], all other modes than the dipole mode present a node in the center of the cavity. The quantum dot should hence be placed out of the center of the cavity, breaking the C6 symmetry as discussed in the following. Moreover, in chapter 2, I already demonstrated that this design, when properly modified, can sustain the expected modes with a sufficient Purcell factor on the excitonic level, good modal collection efficiency and good overlap between the two degenerate modes.

#### 4.4.2 Farfield discernability

However, up to now, I have considered that the only possible effect of the cavity impacting entanglement is the Purcell effect. The reintroduction of the spatial distribution of the photon taking into account a polarization dependency rises a new important characteristic of the system which I already introduced in § 2.4.1 and called "mode overlap". It measures the amount of information on the polarization of the emitted light which is contained by the direction of the emission. Indeed, let us consider that the cavity coupled to the quantum dot sustains two modes with different polarizations but same energy. Figure 4.8 is a schematic example of what must be avoided: the photons are emitted in directions that totally dependent on their polarisation; it is then possible to know their polarization simply by filtering the emission's directions, and entanglement is destroyed. This implies that the field distribution of these two modes has to be identical.

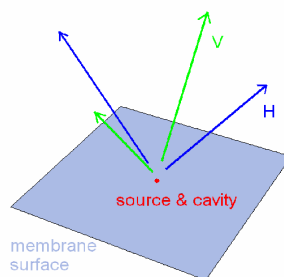


Figure 4.8: Worst case: H and V polarized photons emitted in distinctive directions (i.e. null overlap K)

In order to quantify the impact of such an effect, we can describe the photons polarization in the  $(H, V)$  basis defined by the excitonic splitting of the dot, independently of its orientation with regards to the orientation of the photonic crystal. We define  $\Phi_H(\vec{r})$  (resp.  $\Phi_V(\vec{r})$ ) the complex spatial far field distribution of the horizontal ( $H$ ) (resp. vertical ( $V$ )) polarization modes. As explained in chapter 2, these farfields correspond to the intensity profile of the beam collected by an objective focused on the cavity.  $\vec{r}$  denotes the radial vector perpendicular to the propagation axis. In the first order approximation,  $\Phi_H$  and  $\Phi_V$  are real and positive, corresponding to the case where the transverse phase is constant in the propagating modes (plane wave approximation). Let  $t(r)$  be the function describing the active areas of the detectors placed along the propagation axis (including any pupil effects along the propagation of the beams). There are in fact two distinctive detectors (one for each photon of the pair) but we suppose that they have the same sensitive area for the sake of simplicity.

<sup>46</sup>Let us stress that obtaining experimentally the polarization degeneracy of the cavity mode is not straightforward. Defects induced during the technological steps usually lift the degeneracy between the two dipole modes, leading to two linearly polarized modes with distinct wavelengths. Post-processing techniques of the sample has been developed by K. Hennessy *et al* on photonic crystal cavities [65, 66] to compensate for these effects.

The density matrix of the photon pair obtained in the previous section must now take into account the transversal distribution of the farfield wave functions  $\Phi_H$  and  $\Phi_V$  of the two polarized mode  $H$  and  $V$  of the cavity. The density matrix expressed (eq. 4.23) must then be rewritten under the form:

$$\rho(\vec{r}_1, \vec{r}_2)_{xy,uv} = \Phi_x(\vec{r}_1)^\dagger * \Phi_y(\vec{r}_2)^\dagger * \underline{\rho}_{xy,uv} * \Phi_u(\vec{r}_1) * \Phi_v(\vec{r}_2) \quad (4.38)$$

with  $xy$  and  $uv \in \mathcal{B}$  and  $\underline{\rho}_{xy,uv}$  the density matrix element on line  $xy$  and column  $uv$ .  $\rho(\vec{r}_1, \vec{r}_2)_{xy,uv}$  is the density matrix element on line  $xy$  and column  $uv$  of the new density matrix  $\rho(\vec{r}_1, \vec{r}_2)$ .  $\vec{r}_1$  and  $\vec{r}_2$  are the transversal position of the excitonic and biexcitonic photons. With  $t(\vec{r})$  the detector sensitivity, the density matrix can be reduced for the detected photon pairs as:

$$\rho = \frac{\int d^2r_1 d^2r_2 t(\vec{r}_1)t(\vec{r}_2)\rho(\vec{r}_1, \vec{r}_2)}{\text{Tr}(\int d^2r_1 d^2r_2 t(\vec{r}_1)t(\vec{r}_2)\rho(\vec{r}_1, \vec{r}_2))} \quad (4.39)$$

Finally let  $k$  and  $e$  be:

$$k = \int d^2r t(\vec{r})\sqrt{\Phi_H(\vec{r})\Phi_V(\vec{r})} \quad (4.40)$$

$$e = \int d^2r t(\vec{r})\Phi_H^2(\vec{r}) = \int d^2r t(\vec{r})\Phi_V^2(\vec{r}) \quad (4.41)$$

The overlap factor  $K$  can be expressed as  $K = k^2/e^2$ . And the final expression of the detected photon pair density matrix in the case of non-maximal overlap between the two emission modes is:

$$\rho = \begin{pmatrix} \alpha & 0 & 0 & (d - ic_1)K \\ 0 & \frac{1}{2} - \alpha & c_2K & 0 \\ 0 & c_2K & \frac{1}{2} - \alpha & 0 \\ (d + ic_1)K & 0 & 0 & \alpha \end{pmatrix} \quad (4.42)$$

Note that only the coherence terms are modified by the overlap factor  $K$ . When both modes do not overlap ( $K = 0$ ), the mutual coherence is erased and entanglement vanishes. On the contrary, maximally entangled states can only be obtained for  $K = 1$ . Following previous calculations, Bell inequalities can be rewritten as  $S = 2\sqrt{2}(\alpha + K * (d - c_2)) > 2$ . Note that even in the case of a single dot emitting maximally entangled photons, a minimum overlap of  $K > 2/\sqrt{2} - 1 = 41\%$  is required in order to violate Bell inequalities. For a typical quantum dot with an excitonic Purcell  $F_X = 10$  (a splitting  $2\bar{\delta}\omega = 5\mu eV$ , bulk excitonic life-time  $1/\gamma_1 = 1ns$ , spin exchange characteristic time  $1/\Gamma_{flip} = 10ns$  and sensitive-to-polarisation decoherence  $1/\Gamma = 2ns$ ), the CHSH reads  $S = 1.40 + 0.92K$  (maximal value  $S = 2.22 > 2.0$ ). A minimal overlap of 65% is needed. For example, the modified H1 cavity studied previously with strong astigmatism (figure 2.17  $d = 0.13a$ ) has a smaller overlap value with large numerical aperture objectives.

#### 4.4.3 Impact of the dot's position

Until now the quantum dot has been considered to be perfectly placed in the center of the cavity, implying that both polarizations undergo the same Purcell effect and that the cavity mode is equally fed for both polarizations. However, in usual self-assembled quantum dots, the nucleation site of the dots is not controlled. Deterministically aligning a photonic crystal around a single quantum dot so that the dot is positioned in the center of the cavity is technologically challenging but mandatory. Several techniques are being developed by use of an AFM techniques to identify the nucleation site of the dot creating a small bump at the surface [67, 68] or by use of optical techniques [69, 70]. After identifying the dot position, the cavity is processed around at the right position. This technique however suffers from experimental uncertainties and the mismatch of the quantum dot position with

respect to the center of the H1 cavity can be up to 10 nm [67]. Another strategy is to grow the quantum dot at predefined locations [71, 68, 72, 73, 74] then to etch the cavity by relying on alignment marks done at the same time as the dot's growth locations were defined. This second approach is however not mature and leads to the formation of quantum dots with poor optical quality comparable to the randomly grown usual ones (small decay time dominated by non-radiative processes, large linewidth even at low temperature...). We shall restrain the rest of the discussion in the case of spatial misplaced quantum dots, since our analysis places a new benchmark on the quantum dot positioning.

The position mismatch implies a breaking of the  $C_6$  symmetry. The position of the dot will be identified by a direction  $X$ , as shown on figure 4.9(a), the  $Y$  direction being orthogonal to the  $X$  direction. The two polarization modes of the cavity remain unchanged. Therefore the sustained modes of the cavity will be described in the basis  $(X, Y)$  rather than is in the  $(H, V)$  basis. Due to the mismatch with the cavity modes, the dipole will preferentially excite one of the modes ( $X$  or  $Y$  polarized) leading to an unbalance of the fraction  $\beta^i$  ( $i \in [X, Y]$ ) of spontaneous emission in the cavity mode. This will in turn impact the entanglement visibility. Note that this only affects the unbalance of the spontaneous emission and not the emission diagram of the cavity mode, which remains completely unaffected. Independently of the previous work the asymmetric branching ratio induced by a polarisation dependent Purcell factor can be modelled as follows. Let the state of the system (dot and optical fields) be

$$\begin{aligned}
|\Psi(t)\rangle &= p_2(t) |2; \emptyset; \emptyset\rangle + \sum_{u=H,V} \int d\omega_2 p_u(\omega_2, t) |1_u; \vec{u}, \omega_2; \emptyset\rangle \\
&+ \sum_{u=H,V} \int d\omega_2 d\omega_1 p_{uu}(\omega_1, \omega_2, t) |0; \vec{u}, \omega_2; \vec{u}, \omega_1\rangle
\end{aligned} \tag{4.43}$$

where the first of the three entries within the ket refers to the quantum dot's level, the two other entries refer to the first and second emitted photons of polarisation  $\vec{u}$  and pulsation  $\omega_i$  ( $i=1, 2$  respectively) (see figure 4.1). We distinguish here the emission rates  $\gamma_1$  and  $\gamma_2$  with respect to both polarizations  $H$  and  $V$ . We assume that incoherent processes are negligible, so that crossed terms combining horizontal and vertical orientations disappear.

The expressions of the  $p_2$ ,  $p_u$  and  $p_{uu}$  coefficients are determined using the Wigner-Weisskopf approximation. Considering the system at long times ( $t \gg 1/\gamma_1$  and  $\gamma_2$ ) the terms  $p_2(t)$  and  $p_u(\omega_2, t)$  tend to zero, which gives a state that can be factorized into a radiative part  $|\Psi_R\rangle$  and the fundamental source state  $|0\rangle$ . Without spectral filtering, the density matrix of the photon pair in the polarization basis is:

$$\rho = \int d\omega_1 d\omega_2 \langle \omega_2, \omega_1 | |\Psi_R\rangle \langle \Psi_R| | \omega_2, \omega_1 \rangle \tag{4.44}$$

$$= \sum_{u,v=H,V} |\vec{u} \vec{u}\rangle \langle \vec{v} \vec{v}| \int d\omega_2 d\omega_1 p_{uu}(\omega_1, \omega_2, \infty) p_{vv}(\omega_1, \omega_2, \infty)^* \tag{4.45}$$

$$= \frac{1}{2(1 + 2\delta F^2)} \begin{pmatrix} (\delta F + 1)^3 & 0 & 0 & \frac{(1-\delta F^2)^2}{1-ig} \\ 0 & 0 & 0 & 0 \\ 0 & 0 & 0 & 0 \\ \frac{(1-\delta F^2)^2}{1+ig} & 0 & 0 & (\delta F - 1)^3 \end{pmatrix} \tag{4.46}$$

where we defined the relative difference of Purcell factors  $\delta F = (F_H - F_V)/(F_H + F_V)$  and the normalized splitting  $g = 2\delta\omega/(\gamma_1^{bulk}(F_H + F_V))$ .  $\delta F$  is approximated from the ratio between the modal coupling factors as:  $(\beta_H - \beta_V)/(\beta_H + \beta_V)$ . In the same way as previously, we deduce the expression  $S$  of the Bell test, from which we deduce data presented on figure 4.9(c).

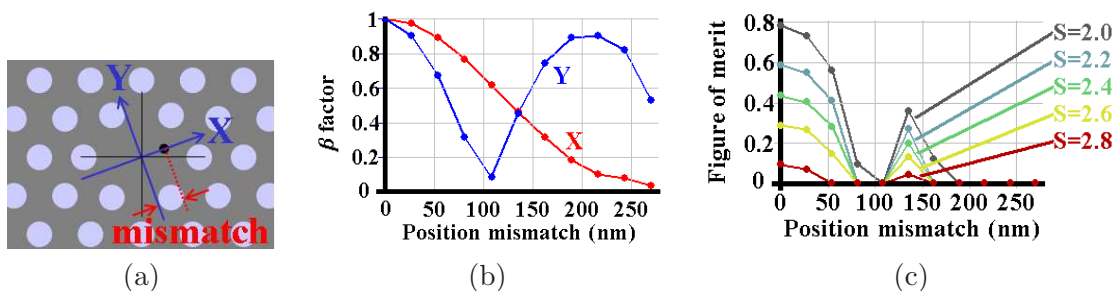


Figure 4.9: (a): Schematic of the different basis used. (b): Normalized  $\beta$  factor as a function of the position mismatch of the dot. The red (blue) curve corresponds to the X (Y) polarization. (c): Figure of merit ( $r = T_1^{bulk}\delta\omega/(\hbar F_p^{max})$ ) as a function of the position mismatch for various values of the CHSH function:  $S=2$ ,  $S=2.2$ ,  $S=2.4$ ,  $S=2.6$  and  $S=2.8$ .  $F_p^{max}$  is the Purcell factor obtained when the dot is perfectly centred.

Figure 4.9(b) depicts the normalized  $\beta^i$  factor as a function of the position mismatch along the X direction for both polarizations. The curves are normalized with respect to the case with null mismatch. The  $\beta^i$  factor is then deduced from the amplitude ratio between the electrical field at the position X,Y with respect to the maximum of the field. We also define the dimensionless ratio  $r = T_1^{bulk}\delta\omega/(\hbar F_p^{max})$  where  $T_1^{bulk}$  is the bulk lifetime of the dot,  $2\hbar\delta\omega$  the excitonic energy splitting and  $F_p^{max}$  the maximal Purcell effect of the cavity (at zero spatial mismatch). For any experimental values of  $T_1^{bulk}$ ,  $2\hbar\delta\omega$  and  $F_p^{exp}$ , we estimate an  $r$  value and plot it in on the y-axis of figure 4.9(c). On the same figure is plotted the maximum tolerable figure of merit  $r$  to obtain at least a CHSH inequality  $S$ , as a function of the quantum dot displacement (calculated using the formalism introduced in Annexe C). Entanglement fidelity increases when  $r$  tends to zero. For example, in the case of a centred dot with an excitonic bulk lifetime of 1ns, an excitonic energy splitting of about  $2\mu\text{eV}$ , submitted to a maximal Purcell factor of 10 and not subjected to incoherent processes, the figure of merit  $r = 0.3$  allows  $S$  to reach a value above 2.6. Conversely, the Bell inequality is hardly violated ( $S = 2$ ) if the same dot is about 70 nm away from the center of the cavity. For a more usual value of the excitonic splitting ( $5\mu\text{eV}$ ), the maximal spatial mismatch enabling the violation of the Bell inequality drops to  $10\text{nm}$ . One can hence establish a real world technological benchmark on the spatial mismatch between the quantum dot and the cavity mode as function of the excitonic fine structure splitting. High spatial mismatch (of the order of  $50\text{nm}$ ) can be tolerated in the case of an excitonic splitting of less than  $\delta\omega \ll 5\mu\text{eV}$ , but becomes critical if the fine structure splitting is not reduced to the smallest possible value.

## 4.5 Conclusion

We have shown analytically that in the two-photon cascade from the biexciton in a single semiconductor quantum dot, solely the dynamics and coherence of the excitonic dipole governs the visibility of polarization entanglement. We have derived Bell inequalities under the CHSH form, as well as the density matrix of such a state. In bare quantum dots, polarization entanglement is spoiled not only by the energy splitting of the relay level but also by the incoherent population exchange and cross dephasing between the two bright relay states. The use of a microcavity can restore the generation of polarization-entangled photons from the quantum dot: The presence of the microcavity enhances the spontaneous emission rate of the excitonic transition, so that emission of the second photon arises before any quantum beat, cross dephasing, or incoherent population transfer between the excitonic radiative states. For the experimentally accessible regimes, the violation of the Bell inequality can be

achieved with real quantum dots, provided they exhibit small excitonic energy splitting (lower than a few  $\mu\text{eV}$ ) and a Purcell factor of the order of 10. Such Purcell factors and excitonic energy splitting have already been achieved, indicating that the possibility of realizing polarization-entangled photons with semiconductor quantum dots embedded in microcavities is accessible with available technology.

However, two issues for the realization of an efficient source of entangled photons based on single quantum dots embedded in a photonic crystal cavity must still be addressed. On the one hand, the non overlapping emission diagram of H1 cavities adds photon path distinguishability, leading to a reduced fidelity of the entangled state. We demonstrate that by properly adjusting the membrane thickness and hole displacement in a modified H1 cavity, it is possible to obtain almost perfect mode overlap while keeping adequate quality factors and maximizing the collection efficiency. On the other hand, spatial mismatch between the quantum dot and the cavity mode rapidly degrades the quantum state. We introduce a benchmark figure of merit giving the required precision on the technological steps in order to obtain high-quality sources. Let us mention that the strategy to embed the dot inside a bi-dimensional photonic crystal cavity is not the only one. Works are done using micropillar cavities [69], the problem being to obtain simultaneously a sufficient Purcell effect on the excitonic level without a reduction of the biexcitonic luminescence by an out-of-resonance situation. This excitonic splitting appears in all kind of quantum dots, but it can vary depending on the materials used. The InP quantum dots should display a smaller splitting according to [75]. The excitonic splitting on CdSe quantum dots has also been observed and is also too high to implement polarization entanglement [76].

We have also indicated that restoring entanglement can only be achieved by a combination between cavity effects and techniques to reduce the fine structure splitting. We will address one of these techniques in the next chapter.

## Bibliography

- [1] A. Aspect, P. Grangier, and G. Roger. Experimental realization of einstein-podolsky-rosen-bohm gedankenexperiment: A new violation of bell's inequalities. *Phys. Rev. Lett.*, 49:91, 1982.
- [2] Z. Y. Ou and L. Mandel. Violation of bell's inequality and classical probability in a two-photon correlation experiment. *Phys. Rev. Lett.*, 61:50, 1988.
- [3] Y. H. Shih and C.O. Alley. New type of einstein-podolsky-rosen-bohm experiment using pairs of light quanta produced by optical parametric down conversion. *Phys. Rev. Lett.*, 61:2921, 1988.
- [4] D. Fattal, K. Inoue, J. Vuckovic, C. Santori, G. S. Solomon, and Y. Yamamoto. Entanglement formation and violation of bell's inequality with a semiconductor single photon source. *Phys. Rev. Lett.*, 92:037903, 2004.
- [5] E. Moreau, I. Robert, L. Manin, V. Thierry-Mieg, J. M. Gérard, and I. Abram. Quantum cascade of photons in semiconductor quantum dots. *Phys. Rev. Lett.*, 87:183601, 2001.
- [6] O. Benson, C. Santori, M. Pelton, and Y. Yamamoto. Regulated and entangled photons from a single quantum dot. *Phys. Rev. Lett.*, 84:2513, 2000.
- [7] D. Gammon, E. S. Snow, B. V. Shanabrook, D. S. Katzer, and D. Park. Fine structure splitting in the optical spectra of single gas quantum dots. *Phys. Rev. Lett.*, 76:3005, 1996.
- [8] M. Bayer, G. Ortner, O. Stern, A. Kuther, A. A. Gorbunov, A. Forchel, P. Hawrylak, S. Fafard, K. Hinzer, T. L. Reinecke, S. N. Walck, J. P. Reithmaier, F. Klopff, and F. Schafer. Fine structure

- of neutral and charged excitons in self-assembled in(ga)as/(al)gaas quantum dots. *Phys. Rev. B*, 65:195315, 2002.
- [9] N. Akopian, N. H. Lindner, E. Poem, Y. Berlatzky, J. Avron, D. Gershoni, D. Gerardot, and P. M. Petroff. Entangled photon pairs from semiconductor quantum dots. *Phys. Rev. Lett.*, 96:130501, 2006.
- [10] E. A. Meirom, N. H. Lindner, Y. Berlatzky, E. Poem, N. Akopian, J. E. Avron, and D. Gershoni. Distilling entanglement from random cascades with partial 'which path' ambiguity. *Phys. Rev. A*, 77:062310, 2008.
- [11] R. M. Stevenson, A. J. Hudson, A. J. Bennett, R. J. Young, C. A. Nicoll, D. A. Ritchie, and A. J. Shields. Evolution of entanglement between distinguishable light states. *Phys. Rev. Lett.*, 101:170501, 2008.
- [12] C. Santori, D. Fattal, M. Pelton, G. S. Solomon, and Y. Yamamoto. Polarization-correlated photon pairs from a single quantum dot. *Phys. Rev. B*, 66:045308, 2002.
- [13] T. Flissikowski, A. Hundt, M. Lowisch, M. Rabe, and F. Henneberger. Photon beats from a single semiconductor quantum dot. *Phys. Rev. Lett.*, 86:3172, 2001.
- [14] K. Kowalik, O. Krebs, A. Lemaître, J. A. Gaj, and P. Voisin. Optical alignment and polarization conversion of the neutral-exciton spin in individual inas/gaas quantum dots. *Phys. Rev. B*, 77:161305(R), 2008.
- [15] E. S. Fry. Two-photon correlations in atomic transitions. *Phys. Rev. A*, 8:1219, 1973.
- [16] R. M. Stevenson, A. J. Hudson, R. J. Young, P. Atkinson, K. Cooper, D. A. Ritchie, and A. J. Shields. Biphoton interference with a quantum dot entangled light source. *Opt. Expr.*, 15:6507, 2007.
- [17] A. Jankovic. *Etats électroniques des boîtes quantiques de semiconducteur : rôle de l'environnement et couplage dépendant du spin*. PhD thesis, 2006.
- [18] G. Lindblad. On the generators of quantum dynamical semigroups. *Commun. Math. Phys.*, 48:119, 1976.
- [19] JW. Pan, S. Gasparoni, R. Ursin, G. Weihs, and A. Zeilinger. Experimental entanglement purification of arbitrary unknown states. *Nature*, 423:417, 2003.
- [20] V. Scarani, H. de Riedmatten, I. Marcikic, H. Zbinden, and N. Gisin. Four-photon correction in two-photon bell experiments. *Eur. Phys. Journ. D*, 32:129, 2005.
- [21] R. Horodecki, P. Horodecki, M. Horodecki, and K. Horodecki. Quantum entanglement. *Arxiv*, page 0702225, 2007.
- [22] A. Peres. Separability criterion for density matrices. *Phys. Rev. Lett.*, 77:1413, 1996.
- [23] A. C. Doherty, P. A. Parrilo, and F. M. Spedalieri. A complete family of separability criteria. *Arxiv*, page 0308032, 2003.
- [24] P. Hyllus, O. Guhne, D. Bruss, and M. Lewenstein. Relations between entanglement witnesses and bell inequalities. *Phys. Rev. A*, 72:012321, 2005.
- [25] M. Lewenstein, B. Kraus, J. I. Cirac, and P. Horodecki. Optimization of entanglement witnesses. *Phys. Rev. A*, 62:052310, 2000.

- [26] F. G. S. L. Brandao and R. O. Vianna. Witnessed entanglement. *Arxiv*, page 0405096, 2008.
- [27] M. Stobinska and K. Wodkiewicz. Witnessing entanglement of epr states with second-order interference. *Arxiv*, page 0508146, 2006.
- [28] I. Marcikic, H. de Riedmatten, W. Tittel, H. Zbinden, M. Legré, and N. Gisin. Distribution of time-bin entangled qubits over 50 km of optical fiber. *Phys. Rev. Lett.*, 93:180502, 2004.
- [29] J. F. Clauser, M. H. Horne, A. Shimony, and R. A. Holt. Proposed experiment to test local hidden-variable theories. *Phys. Rev. Lett.*, 23:880, 1969.
- [30] D. F. V. James, P. G. Kwiat, W. J. Munro, and A. G. White. Measurement of qubits. *Phys. Rev. A*, 64:052312, 2001.
- [31] M. Larqué, I. Robert-Philip, and A. Beveratos. Bell inequalities and density matrix for polarization-entangled photons out of a two-photon cascade in a single quantum dot. *Phys. Rev. A*, 77:042118, 2008.
- [32] D. C. Unitt, A. J. Bennett, P. Atkinson, D. A. Ritchie, and A. J. Shields. Polarization control of quantum dot single-photon sources via a dipole-dependent purcell effect. *Phys. Rev. B*, 72:033318, 2005.
- [33] A. Imamoglu, D. D. Awschalom, G. Burkard, D. P. DiVincenzo, D. Loss, M. Sherwin, and A. Small. Quantum information processing using quantum dot spins and cavity qed. *Phys. Rev. Lett.*, 83:4204, 1999.
- [34] T. M. Stace, G. J. Milburn, and C. H. W. Barnes. Entangled two-photon source using biexciton emission of an asymmetric quantum dot in a cavity. *Phys. Rev. B*, 67:85317, 2003.
- [35] F. Troiani, J. I. Perea, and C. Tejedor. Cavity-assisted generation of entangled photon pairs by a quantum-dot cascade decay. *Phys. Rev. B*, 74:235310, 2006.
- [36] P. M. Visser, K. Allaart, and D. Lenstra. Entangled photons from small quantum dots. *Phys. Rev. B*, 66:053805, 2003.
- [37] J. I. Perea and C. Tejedor. Polarization entanglement visibility of photon pairs emitted by a quantum dot embedded in a microcavity. *Phys. Rev. B*, 72:035303, 2005.
- [38] R. Seguin, A. Schliwa, S. Rodt, K. Pötschke, U. W. Pohl, and D. Bimberg. Size-dependent fine-structure splitting in self-organized inas/gaas quantum dots. *Phys. Rev. Lett.*, 95:257402, 2005.
- [39] U. Hohenester, G. Pfanner, and M. Seliger. Phonon-assisted decoherence in the production of polarization-entangled photons in a single semiconductor quantum dot. *Phys. Rev. Lett.*, 99:047402, 2007.
- [40] A. J. Hudson, R. M. Stevenson, A. J. Bennett, R. J. Young, C. A. Nicoll, P. Atkinson, K. Cooper, D. A. Ritchie, and A. J. Shields. Coherence of an entangled exciton-photon state. *Phys. Rev. Lett.*, 99:266802, 2007.
- [41] C. Becher, A. Kiraz, P. Michler, A. Imamoglu, W. V. Schoenfeld, P. M. Petroff, Lidong Zhang, and E. Hu. Nonclassical radiation from a single self-assembled inas quantum dot. *Phys. Rev. B*, 63:121312(R), 2001.

- [42] R. M. Thompson, R. M. Stevenson, A. J. Shields, I. Farrer, C. J. Lobo, D. A. Ritchie, M. L. Leadbeater, and M. Pepper. Single-photon emission from exciton complexes in individual quantum dots. *Phys. Rev. B*, 64:201302(R), 2001.
- [43] A. Kiraz, S. Falth, C. Becher, B. Gayral, W. V. Schoenfeld, P. M. Petroff, L. Zhang, E. Hu, and A. Imamoglu. Photon correlation spectroscopy of a single quantum dot. *Phys. Rev. B*, 65:161303, 2002.
- [44] M. Paillard, X. Marie, P. Renucci, T. Amand, A. Jbeli, and J. M. Gérard. Spin relaxation quenching in semiconductor quantum dots. *Phys. Rev. Lett.*, 86:1634, 2001.
- [45] S. M. Ulrich, M. Benyoucef, P. Michler, N. Baer, P. Gartner, F. Jahnke, M. Schwab, H. Kurtze, M. Bayer, S. Fafard, Z. Wasilewski, and A. Forchel. Correlated photon-pair emission from a charged single quantum dot. *Phys. Rev. B*, 71:235328, 2005.
- [46] R. Hafenbrak, S. M. Ulrich, P. Michler, L. Wang, A. Rastelli, and O. G. Schmidt. Triggered polarization-entangled photon pairs from a single quantum dot up to 30k. *New. J. Phys.*, 8:315, 2007.
- [47] R.J. Young, R. M. Stevenson, P. Atkinson, K. Cooper, D. A Ritchie, and A. J. Shields. Improved fidelity of triggered entangled photons from single quantum dots. *New. J. Phys.*, 8:29, 2006.
- [48] R. J. Young, R. M. Stevenson, A. J. Hudson, C. A. Nicoll, D. A. Ritchie, and A. J. Shields. Bell-inequality violation with a triggered photon-pair source. *Phys. Rev. Lett.*, 102:030406, 2009.
- [49] A. Acin, N. Brunner, N. Gisin, S. Massar, S. Pironio, and V. Scarani. Device-independent security of quantum cryptography against collective attacks. *Phys. Rev. Lett.*, 98:230501, 2007.
- [50] J.M. Gérard, O. Cabrol, and B. Sermage. Inas quantum boxes: Highly efficient radiative traps for light emitting devices on si. *Appl. Phys. Lett.*, 68:3123, 1996.
- [51] W. Langbein, P. Borri, U. Woggon, V. Stavarache, D. Reuter, and A. D. Wieck. Control of fine-structure splitting and biexciton binding in inxga1-xas quantum dots by annealing. *Phys. Rev. B*, 69:161301(R), 2004.
- [52] R. J. Young, R. M. Stevenson, A. J. Shields, P. Atkinson, K. Cooper, D. A. Ritchie, K. M. Groom, A. I. Tartakovskii, and M. S. Skolnick. Inversion of exciton level splitting in quantum dots. *Phys. Rev. B*, 72:113305, 2005.
- [53] D. J. P. Ellis, R. M. Stevenson, R. J. Young, A. J. Shields, P. Atkinson, and D. A. Ritchie. Control of fine-structure splitting of individual inas quantum dots by rapid thermal annealing. *Appl. Phys. Lett.*, 90:011907, 2007.
- [54] A. Hogele, S. Seidl, M. Kroner, K. Karrai, R. J. Warburton, B. D. Gerardot, and P. M. Petroff. Voltage-controlled optics of a quantum dot. *Phys. Rev. Lett.*, 93:217401, 2004.
- [55] B. D. Gerardot, S. Seidl, P. A. Dalgarno, R. J. Warburton, D. Granados, J. M. Garcia, K. Kowalik, and O. Krebs. Manipulating exciton fine structure in quantum dots with a lateral electric field. *Appl. Phys. Lett.*, 90:041101, 2007.
- [56] K. Kowalik, O. Krebs, P. Senellart, A. Lemaître, B. Eble, A. Kudelski, J. Gaj, and P. Voisin. Stark spectroscopy of coulomb interactions in individual inas/gaas self-assembled quantum dots. *Phys. Stat. Sol. C*, 11:3890, 2006.

- [57] R. B. Patel, A. J. Bennett, K. Cooper, P. Atkinson, C. A. Nicoll, D. A. Ritchie, and A. J. Shields. Postselective two-photon interference from a continuous nonclassical stream of photons emitted by a quantum dot. *Phys. Rev. Lett.*, 100:207405, 2008.
- [58] M. E. Reimer, D. Dalacu, J. Lapointe, P. J. Poole, D. Kim, G. C. Aers, W. R. McKinnon, and R. L. Williams. Single electron charging in deterministically positioned inas/inp quantum dots. *Appl. Phys. Lett.*, 94:011108, 2009.
- [59] S. Seidl, M. Kroner, A. Högele, K. Karrai, R. J. Warburton, A. Badolato, and P. M. Petroff. Effect of uniaxial stress on excitons in a self-assembled quantum dot. *Appl. Phys. Lett.*, 88:203113, 2006.
- [60] K. Kowalik, O. Krebs, A. Lemaître, S. Laurent, P. Senellart, J. A. Gaj, and P. Voisin. Influence of an in-plane electric field on exciton fine structure in inas-gaas self-assembled quantum dots. *Appl. Phys. Lett.*, 86:041907, 2005.
- [61] R.M. Stevenson, R.J. Young, P. Atkinson, K. Cooper, D.A. Ritchie, and A.J. Shields. A semiconductor source of triggered entangled photon pairs. *Nature*, 439:179, 2006.
- [62] R. Brouri, A. Beveratos, J.-P. Poizat, and P. Grangier. Photon antibunching in the fluorescence of individual color centers in diamond. *Opt. Lett.*, 25:1294, 2000.
- [63] F. Romer and B. Witzigmann. Spectral and spatial properties of the spontaneous emission enhancement in photonic crystal cavities. *Journ. Opt. Soc. Am. B*, 25:31, 2008.
- [64] Se-Heon Kim, Sun-Kyung Kim, and Yong-Hee Lee. Vertical beaming of wavelength-scale photonic crystal resonators. *Phys. Rev. B*, 73:235117, 2006.
- [65] K. Hennessy, A. Badolato, A. Tamboli, P. M. Petroff, E. Hua, M. Atature, J. Dreiser, and A. Imamoglu. Tuning photonic crystal nanocavity modes by wet chemical digital etching. *Appl. Phys. Lett.*, 87:021108, 2005.
- [66] K. Hennessy, C. Hogerle, E. Hu, A. Badolato, and A. Imamoglu. Tuning photonic nanocavities by atomic force microscope nano-oxidation. *Appl. Phys. Lett.*, 89:041118, 2006.
- [67] A. Badolato, K. Hennessy, M. Atature, J. Dreiser, E. Hu, P. M. Petroff, and A. Imamoglu. Deterministic coupling of single quantum dots to single nanocavity modes. *Science*, 308:1158, 2005.
- [68] N. Gogneau, L. Le Gratiet, E. Cambril, G. Beaudoin, G. Patriarche, A. Beveratos, R. Hosten, I. Robert-Philip, J.Y. Marzin, and I. Sagnes. One-step nano-selective area growth (nano-sag) of localized inas/inp quantum dots: First step towards single-photon source applications. *Journal of Crystal Growth*, 310:3413–3415, 2008.
- [69] A. Dousse, L. Lanco, J. Suffczynski, E. Semenova, A. Miard, A. Lemaitre, I. Sagnes, C. Roblin, J. Bloch, and P. Senellart. Controlled light-matter coupling for a single quantum dot embedded in a pillar microcavity using far-field optical lithography. *Phys. Rev. Lett.*, 101:267404, 2008.
- [70] K.H. Lee, F.S.F. Brossard, M. Hadjipanayi, X. Xu, F. Waldermann, A.M. Green, D.N. Sharp, A.J. Turberfield, D.A. Williams, and R.A. Taylor. Towards registered single quantum dot photonic devices. *Nanotechnology*, 19:455307, 2008.
- [71] J. Lefebvre, P. J. Poole, J. Fraser, G. C. Aers, D. Chithrani, and R. L. Williams. Self-assembled inas quantum dots on inp nano-templates. *Journ. Crystal Growth*, 234:391, 2002.

- [72] P. Atkinson, S. Kiravittaya, M. Benyoucef, A. Rastelli, and O. G. Schmidt. Site-controlled growth and luminescence of inas quantum dots using in situ ga-assisted deoxidation of patterned substrates. *Appl. Phys. Lett.*, 93:101908, 2008.
- [73] F. Patell, F. Arciprete, E. Placidi, M. Fanfoni, A. Balzarotti, A. Vinattieri, L. Cavigli, M. Abbarchi, M. Gurioli, L. Lunghi, and A. Gerardino. Single quantum dot emission by nanoscale selective growth of inas on gaas: A bottom-up approach. *Appl. Phys. Lett.*, 93:231904, 2008.
- [74] H. Z. Song, T. Usuki, S. Hirose, K. Takemoto, Y. Nakata, N. Yokoyama, and Y. Sakuma. Site-controlled photoluminescence at telecommunication wavelength from inas/inp quantum dots. *Appl. Phys. Lett.*, 86:113118, 2005.
- [75] L. He. Highly reduced fine-structure splitting in inas=inp quantum dots offering an efficient on-demand entangled  $1.55\mu\text{m}$  photon emitter. *Phys. Rev. Lett.*, 101:157405, 2008.
- [76] S. M. Ulrich, S. Strauf, P. Michler, G. Bacher, and A. Forchel. Triggered polarization-correlated photon pairs from a single cdse quantum dot. *Appl. Phys. Lett.*, 83:1848, 2003.

## Chapter 5

# Fine-tuning of the excitonic splitting

As shown in the previous chapter, if a biexciton state is formed after a short pulsed excitation within a quantum dot, then the system will relax its energy through a radiative cascade which consists of two photons of slightly different energies, which are correlated in polarization. These correlations may lead to the formation of a polarization-entangled 2-photon state. Yet in order to obtain such a maximally entangled quantum state of light, several conditions must be fulfilled by the quantum dot system. As we have demonstrated previously, the deployment of quantum dots in such a polarization entangled photons source is hindered by the fine structure splitting of the intermediate level of the cascade. This splitting of the relay excitonic state opens two distinguishable recombination paths and the 2-photon state cannot be described by its sole polarization components. Spectral information must be included and cannot be factorized with respect to the polarization states. This leads to non-maximally entangled state or even to only polarization-correlated photon pairs.

In this chapter, we will first describe the different mechanisms inducing such fine structure splitting of the excitonic levels in self-assembled quantum dots and solutions that have proposed or implemented to tune finely this energy splitting. We will then discuss in more details on the influence of a vertical electric field applied to the dots to compensate its native asymmetry. The following section will report on our technological and experimental work in this direction.

### 5.1 Fine structure splitting of the exciton

Degeneracy of the bright single exciton spin state is a prerequisite for the production of triggered polarization-entangled photon pairs from the biexciton decay of a quantum dot. Although the polarization-entanglement in biexciton-exciton cascade has been recently demonstrated [1, 2, 3], a reliable technique enabling such a control over quantum dot anisotropy remains highly demanded. If quantum dot anisotropy (measured as fine structure splitting of an excitonic line in photoluminescence or FSS) is larger than the natural linewidth, the rate of entangled photon pairs collected after post-selection gets indeed dramatically reduced. In this section, we shall describe briefly the origin of this splitting and presents investigated strategies enabling a control over quantum dot anisotropy.

#### 5.1.1 Quantum dot anisotropy

The exciton ground state in quantum dots is fourfold (spin-)degenerate since both, electron and (heavy) hole, have two different possible spin configurations (spin up or spin down). The exciton ground state is split into two doublets: the so-called bright doublet consisting of the states with total angular momentum  $\pm 1$  and the dark doublet consisting of with total angular momentum  $\pm 2$ . The bright states couple to the photonic field (i.e. can decay or be created via the emission or absorption of a photon with spin  $\pm 1$ ), while the dark states do not. However, these electron-hole states are

not in general eigenstates of the total Hamiltonian because of the electron-hole exchange. The two doublets are usually separated in energy by  $\Delta_0 \simeq 1meV$ . Since the radiative decay of the dark excitons (i.e. excitons occupying the dark states) is forbidden due to the spin selection rule, only the splitting between the two bright states is experimentally accessible in optical spectroscopy. The first experiments showing the fine structure for excitons in an individual quantum dot was presented by D. Gammon *et al* [4]. Since then, a large number of different experiments using various techniques (microphotoluminescence, transmission, pump and probe or cathodoluminescence for instance) have been conducted in the past in order to resolve the two bright exciton transitions and measure the FSS in different material systems. In the (In,Ga)As/GaAs system, the FSS of the bright exciton states, ranges from zero to  $500 \mu eV$ . When a magnetic field  $B$  is applied, however, dark and bright states intermix and form new excitons for which a decay into a photon is partially allowed. This allows to extrapolate at low magnetic field a value for the splitting between the two dark states which is of the order of  $2 \mu eV$ . In this work, no magnetic field will be applied; hence we will concentrate on the bright excitons.

In the single-quantum dot spectra, the manifestation of the bright exciton splitting is twofold. On the one hand the exciton can occupy one of the two bright states and decay into a photon leaving behind an empty quantum dot. The corresponding transition lines in the spectrum are energetically separated by the FSS. Moreover, since the bright states are a superposition of the states  $| -1 \rangle$  and  $| +1 \rangle$ , the light emitted from a decay of these states is a superposition of circularly polarized photons, i.e. it is linearly polarized. The polarization directions are parallel and perpendicular to the anisotropy axes of the confining potential. On the other hand the biexciton also has two different decay paths. The biexciton ground state cannot undergo degeneracy breaking effects as it is a fully unique state. However, the final state of the transition leads to different resonances in the spectrum. The biexciton can decay into either of the two exciton bright states. Consequently, analogously to the exciton, the biexciton will also display two linearly polarized lines in the spectrum, separated in energy by the FSS.

The origin of the symmetry breakdown governing this fine structure splitting is not fully established. In principle, three different effects can lead to such a symmetry lowering:

- Structural elongation of the quantum dot: If the quantum dot itself is elongated into one direction, the potential is naturally anisotropic; it aligns itself on the quantum dot structure.
- Piezoelectricity: Complicated strain fields are generated in the quantum dot structures due to the different lattice constants of quantum dot and matrix material. The shear strain components lead to a separation of the negative and positive charge centres and therefore to piezoelectric fields [5]. This leads to an anisotropy of the potential along [110] as implied by the spectroscopic data.
- Atomistic symmetry anisotropy: Even for perfectly symmetric pyramids, opposite interfaces are not completely identical on the atomistic level due to the underlying zinc-blende crystal structure. This leads to different interface potentials [6]. This effect is augmented and carried into the quantum dot structure by strain [7].

### 5.1.2 Control of the quantum dot anisotropy

As discussed in the previous chapter, the excitonic fine structure splitting is the key parameter which determines the suitability of quantum dots for the generation of polarization entangled photon pairs. Different strategies can be implemented however to restore entanglement.

Our proposal uses cavity effect. By embedding the dot in a cavity, the exciton linewidth is increased and hides the exciton fine structure splitting. This supposes however the use of dots with

small FSS, smaller than tens  $\mu eV$ . Nevertheless, in practice, the use of cavity effects suffers from its resonant character, since the dot position and emission wavelength are not fully controlled. In order to implement such effects, one solution consists in growing low density arrays of dots (less than  $5 \cdot 10^8 \text{ cm}^{-2}$  i.e.  $5 \mu\text{m}^{-2}$ ) and process a large number of cavities. By a statistical and systematic study of all the cavities, one can hope to find one or more cavities fulfilling all the requirements to produce polarization entangled photons. Yet, Let us give an order of magnitude of the probability to find one cavity satisfying all these requirements. First the exciton must be spatially on resonance with the cavity mode. In modified H1 cavity, this supposes that the dot must be placed at most 10 nm away from the cavity centre. If the dot density is of the order of  $5 \mu\text{m}^{-2}$ , this means that only one cavity over 2000 is suitable. Moreover, the exciton must be spectrally on resonance with the cavity mode. Let us consider a cavity with a quality factor of 1000. Since the spectral inhomogeneous bandwidth of the dots is about  $100 \text{ nm}$ , only one over 100 cavities are spectrally matched. Last but not least, for the Purcell factors obtained with such cavities, the FSS value must be lower than  $5 \mu eV$ , in order to violate Bell's inequalities. We do not have a clear statistic of the excitonic splitting values. Based on previous work by R. Seguin [8], Let us suppose that it is possible to have one over 100 dots with a splitting lower than  $5 \mu eV$ . Eventually, the cavity should display a sufficient mode overlap between the two involved dipole modes. The developed and used process in our laboratory allows to obtain a sufficient overlap for 90 % of the cavities. In this context, only one cavity over  $2000 \times 100 \times 100 \times 0.9 \simeq 2 \cdot 10^7$  is suitable for our measurements. It appears clearly that this approach is not satisfactory and new techniques must be implemented to increase drastically this probability.

First one has to implement deterministic techniques to insure the coupling of the dot to the cavity. This can be obtained either by localized growth [9], by AFM localization [10], or optical techniques [11]. These approaches insure spatial and spectral matching usually in two steps. First the dot position is identified respectively during the growth, by AFM localization or by microphotoluminescence measurements. The dot emission wavelength is also measured. Second, a cavity with a mode in resonance with the dot ground state is processed around the dot. A major difficulty here is to process a cavity at the right position and wavelength despite fabrication imperfections. For instance, in [10], the cavity resonance had to be tuned to the dot wavelength after the whole two-step process by digital etching [12]. However, in such process, the cavities displayed a splitting of the H1 cavity dipole modes, which may be further corrected by AFM oxidation [13]. Combination of this two-step procedure to achieve a deterministic coupling and this AFM oxidation to compensate for the mode splitting has never been implemented. A major difficulty here resides in the fact that AFM oxidation shifts the cavity mode, which is not on resonance any more with the dot.

Second, one has to be able to finely control the fine structure splitting of the exciton by external means, at least in order to reduce its value below few  $\mu eV$ . As mentioned in the previous chapter, different strategies for restoring higher symmetry of the quantum dots were tested, either by influencing material properties of heterostructures (annealing or strain engineering [14, 15]) or by applying external perturbations compensating the native asymmetry: in-plane electric field [16], uniaxial strain [17], and in-plane magnetic field [18] were tried. Using these techniques, only a combination of temporal filtering and growth control or magnetic field has given satisfactory results so far and allowed for Bell's inequality violation [2, 3].

Regarding the expertise of the laboratory on cavity effects [19, 20, 21] and on the fine tuning with an in-plane electric field [22, 23, 24], we chose to study the possibility of combining a Purcell effect and a vertical electric field to implement a source of polarization entangled photons. The following sections will focus on the investigation of the FSS modification induced by external vertical electric field perpendicular to the growth axis, in order to compensate the effects of the low symmetry of native quantum dots and possibly restore a higher symmetry.

## 5.2 Control of fine structure splitting

### 5.2.1 Vertical electric field

Let us first discuss the underlying physics allowing for symmetry modifications achievable by applying an electric field perpendicular to the growth axis.

The observed FSS changes with the applied voltage result always from two effects: the symmetry modification of the wavefunctions and the diminution of the overlap of single carrier wavefunctions. The latter effect always leads to the reduction of the exchange interaction. When applying a vertical electric field, we should not modify strongly the symmetry of the wavefunctions, and the changes in the FSS should be influenced mostly by the spatial separation of an electron and a hole. The full description of the impact of a vertical electric field on the FSS value still lacks for a quantitative theory. We shall give here some quantitative arguments explaining this effect.

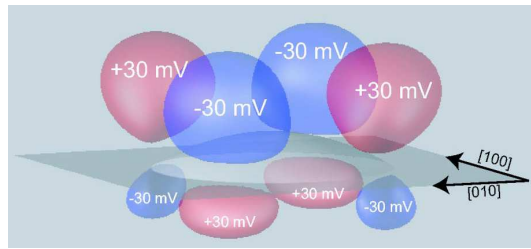


Figure 5.1: Isosurfaces of the piezoelectric potential created by the lens shape of the dot. From [7].

The origin of the influence of a vertical electric field results from the  $C_{2v}$  symmetry of the dot (meaning that directions  $[110]$  and  $[-110]$  are not equivalent), even in dots with cylindrical symmetry about the growth axis. This results from the fact that  $III-V$  dots are made of atoms arranged on the positions of a zinc-blende lattice: the true atomistic symmetry of the dots is affected by interfacial symmetry, atomistic strain, and piezoelectricity. The clear vertical asymmetry of quantum dots has been first considered theoretically by M. Grundmann *et al* [5] and more recently by G. Bester *et al* [7]. It turns out that the effective potential due to the strain varies from the bottom to the top of a quantum dot and a quadrupolar potential of piezo-charge clearly influences the preferential alignment of the carriers along crystallographic axes of the lattice (see Fig. 5.1). This contributes as a perturbation of  $C_{2v}$  symmetry even in the case of a square based pyramid-like quantum dot. The relevance of the piezoelectric potential to the FSS strongly depends on the quantum dot height and as explained in [24] (p.16 in particular). This contribution to the excitonic splitting, often called the long-range exchange contribution, is the dominant one in the case of exciton confinement stronger along the vertical direction than along the in-plane direction. In the expression of this contribution, it is possible to separate the in-plane dependencies to the vertical one, leading to an expression of the splitting  $\delta\omega$  of the form

$$\delta\omega \sim \int \int dq_x dq_y \frac{q_x^2 - q_y^2}{q} F_x(q_x) F_y(q_y) P(q) \quad (5.1)$$

$$P(q) = \int \int dz dz' f(z) f(z') e^{-q|z-z'|} \quad (5.2)$$

where  $F_x(q_x)$  and  $F_y(q_y)$  are the Fourier transform of the in-plane excitonic wavefunctions which describe the in-plane correlated motion of the electron and hole. The function  $f(z)$  describes the vertical dependency of the excitonic wavefunction in the vertical growth axis. The function  $P(q)$  roughly speaking corresponds to the overlap along the growth axis of the electron and hole wavefunctions. An

applied vertical field will modify the function  $f(z)$  and consequently the function  $P(q)$ , by reducing or enhancing the overlap of single carrier wavefunctions<sup>47</sup>. This in-turn modifies the weight  $P(q)$  in the function, the integral of which gives  $\delta\omega$ . The use of a vertical electric field should thus allow the tuning of the FSS value and even in some configuration reduce its amplitude.

This strategy has many advantages, compared to other techniques. First, it allows to address one single dot and compensate deterministically the FSS, conversely to annealing techniques that affect simultaneously all the dots embedded in the structure. Second, it is compatible with the use of compact photonic crystal cavities and thus allows for the engineering of compact sources, conversely to the use of magnetic field (usual magnetic fields used to compensate the FSS are of the order of 2 Tesla). Third, it does not induce (at least theoretically) any mixing between the bright and dark excitonic states that creates new decay paths, conversely to magnetic field or in-plane electric field [24]. Yet, very few theoretical and experimental works has been done in this field up to now. In the following, we shall therefore focus on this technique.

### 5.2.2 Quantum confined Stark effect

By applying an electric field to the dot, we change its eigenstates via the quantum confined Stark effect. The field leads to a bending of the electronic bands of the quantum dot thus influencing the energies of the transitions in the dot. Three different effects are induced by the band bending:

- Electrons and holes follow the electric field both lowering their energy. The recombination energy is thus lowered, leading to a red shift of the corresponding transition.
- Due to the spatial separation of electron and hole the exciton binding energy is reduced. This effect raises the energy of the exciton leading to a blue shift of the corresponding transition.
- The spatial separation decreases the oscillator strength and therefore the time averaged intensity of the corresponding transition.

The first effect dominates over the second one thus leading to an overall redshift of the luminescence with increasing electric field. This energy shift  $\Delta E$  of the dot's eigenstates in an external field  $F$  is for small fields usually described as :  $\Delta E = \mu_{el}F - \alpha F^2$ , where  $\mu_{el}$  and  $\alpha$  are respectively the components of the permanent dipole moment and the polarizability in the direction of the electric field  $F$ .  $\alpha F$  is the static dipole acquired by the electron-hole pair in an electric field  $F$ .  $\mu_{el}$  is the vertical static dipole of the ground state of an electron-hole pair that results from the strong vertical potential asymmetry of the dot.

### 5.2.3 Field-induced carrier escape

In practice the strength of the applied field is systematically limited by the strong reduction of luminescence intensity for high fields. This results from electron-hole separation and carriers escape from the ground state or from a higher state out of a dot. Due to band bending, the electrons and holes get spatially separated; moreover, carriers may tunnel outside the dot. In a simple tunnelling model (see e.g. [96]), one can estimate the carrier escape rate as:

$$\frac{1}{\tau} = \frac{\hbar\pi}{2m_{e,h}^* L^2} \exp\left[\frac{-4}{3\hbar e F} \sqrt{2m_{e,h}^* (E_I^{(e,h)})^3}\right] \quad (5.3)$$

<sup>47</sup>This description is however an approximation. When developing the corresponding perturbations on the single particle wave functions up to second order, it appears that this electric field may also affect the in-plane dependency of the excitonic wavefunction.

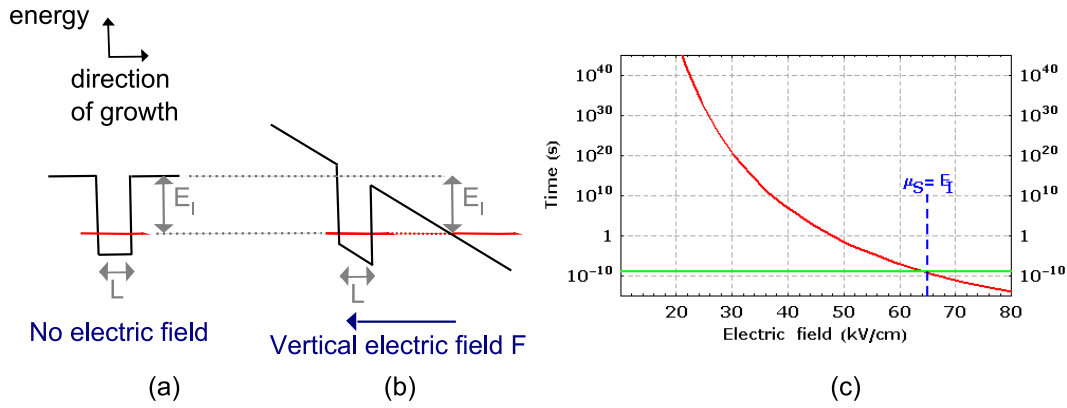


Figure 5.2: Sketch of the potential in the quantum dot when subjected (b) or not (a) to a vertical electric field. (c): Lifetime of the exciton (green line) and electron escape time (red line) as a function of the amplitude of the vertical electric field.

where  $E_I^{(e,h)}$  is the barrier height (or ionization energy) from the electron (resp. hole) level to the wetting layer continuum.  $L$  is the characteristic length of the potential confinement.  $m_{e,h}^*$  are the effective masses of the electron and hole. In usual InAs/GaAs quantum dots, the hole effective mass of the order of  $0.5m_0$  is much higher than the one of the electrons of the order of  $0.06m_0$  and the field-induced tunnelling will preferentially induce electron escape out of the dot. Let us consider a dot, the electron ionization energy of which is of the order of  $100meV$  and confinement characteristic length  $L$  of the order of  $1.4nm$ . Figure 5.2 (c) represents the escape time as a function of the electric field seen by the dot, compared to usual spontaneous emission exciton lifetime of the order of  $1ns$ . It appears that field-induced electron escape will dominate over exciton radiative relaxation for fields, the amplitude of which is higher than  $70kV.cm^{-1}$ .

## 5.3 Device for vertical field

### 5.3.1 Design of the structure

One technique to apply a vertical electric field consists in embedding the dots in a *pin* structure. The quantum dots are located within the intrinsic, undoped region, between the highly doped contact regions. A sketch of the conduction band for this device is shown in figure 5.3. Since we wish to further combine cavity effect and an applied vertical field, the thickness of the *pin* diode is fixed to the one of the suspended membrane of the photonic crystal cavities ( $180nm$ , see § 2.4.3). This *pin* structure is grown on an AlGaAs layer that will act as a sacrificial layer to further suspend the membrane. The growth of the samples was done by Aristide Lemaître in Laboratory for Photonics and Nanostructures-CNRS in Marcoussis. The InAs dots are grown in the middle of the intrinsic GaAs region, the thickness of which is  $100nm$ . This region is enclosed between two doped  $40nm$ -thick layers: *n*-type (Silicon, Si:  $2.10^{18}cm^{-3}$ ) and *p*-type (Carbon, C:  $2.10^{19}cm^{-3}$ ). A sketch of the whole structure is represented on figure 5.4 (b). Two types of multilayer structures were studied: *pin* structure (the substrate and the bottom doped layer are *p*-doped and the upper doped layer is *n*-doped) and *nip* structures (the substrate and the bottom doped layer are *n*-doped and the upper doped layer is *p*-doped). In such structure, the built-in potential is of the order of  $1.45V$ . Consequently, the field in the intrinsic region is of the order of  $\sim 145kV.cm^{-1}$ . This value is much higher than the amplitude of  $70kV.cm^{-1}$ , below which the electrons and holes trapped in the dot are not separated by carriers escape out of a dot. This explains the absence of photoluminescence signal

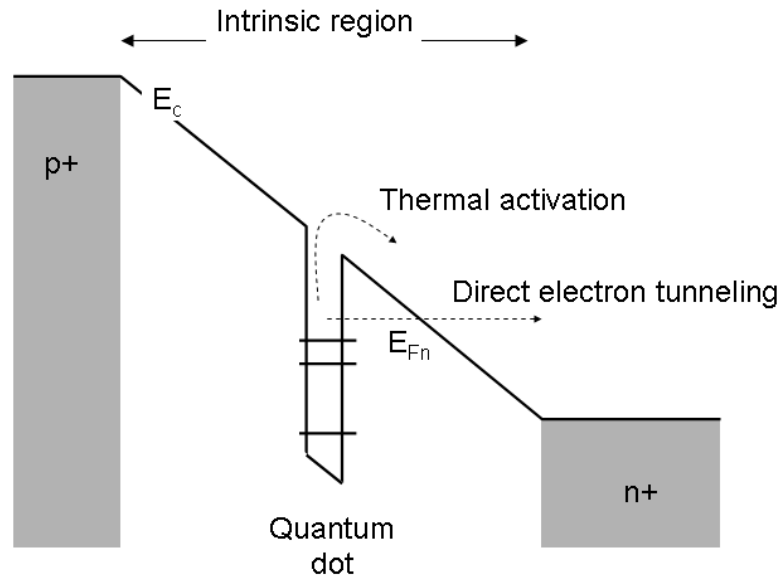


Figure 5.3: Band sketch of a *pin* diode with an embedded array of quantum dots.

emerging from the sample just after growth and without applying any electric field on the diode. The experiments were performed on  $300 \times 300 \mu\text{m}^2$  surface square mesas with  $0.5 \mu\text{m}$ ,  $1 \mu\text{m}$  and  $2 \mu\text{m}$  circular apertures in the top metal contact for optical access. These apertures also allowed us to study one single quantum dot by performing a spatial filtering of the excited dots.

### 5.3.2 Processing of the structure

I will now describe rapidly the overall process I used to fabricate the samples, then focus on the two steps which needed some development: the choice of the metal to realize the top metal contact and the circular apertures patterning.

#### Overall process

The process can be divided into five successive steps after growth, described on figure 5.4 (a):

- **Deposition of the back metal contact:** The metal is evaporated on the back side of the wafer. For contacts on *p*-doped substrate, a bilayer of Ti: 20 nm and Au: 200 nm was used. For contacts on *n*-doped substrate, we use a layer of Ni: 10 nm, Ge: 30 nm, Au: 60 nm, Ni: 20 nm and Au : 100 nm, that is further annealed during few seconds at about  $400^\circ\text{C}$ . These form ohmic contacts. The quality of the back surface proved to be sufficient to not require polishing before the evaporation to obtain a good metallic contact.
- **Realization of the top apertures:** A first electronic lithography forms on the top surface of the sample  $290 \times 290 \mu\text{m}^2$  squared apertures in the resist, in which cylinders of resist are formed. The cylinders height is about 240 nm and their diameters range from 500 nm to 2  $\mu\text{m}$ . This step is followed by a Ti/Au (20/100 nm) deposition and a lift-off which consists in removing the

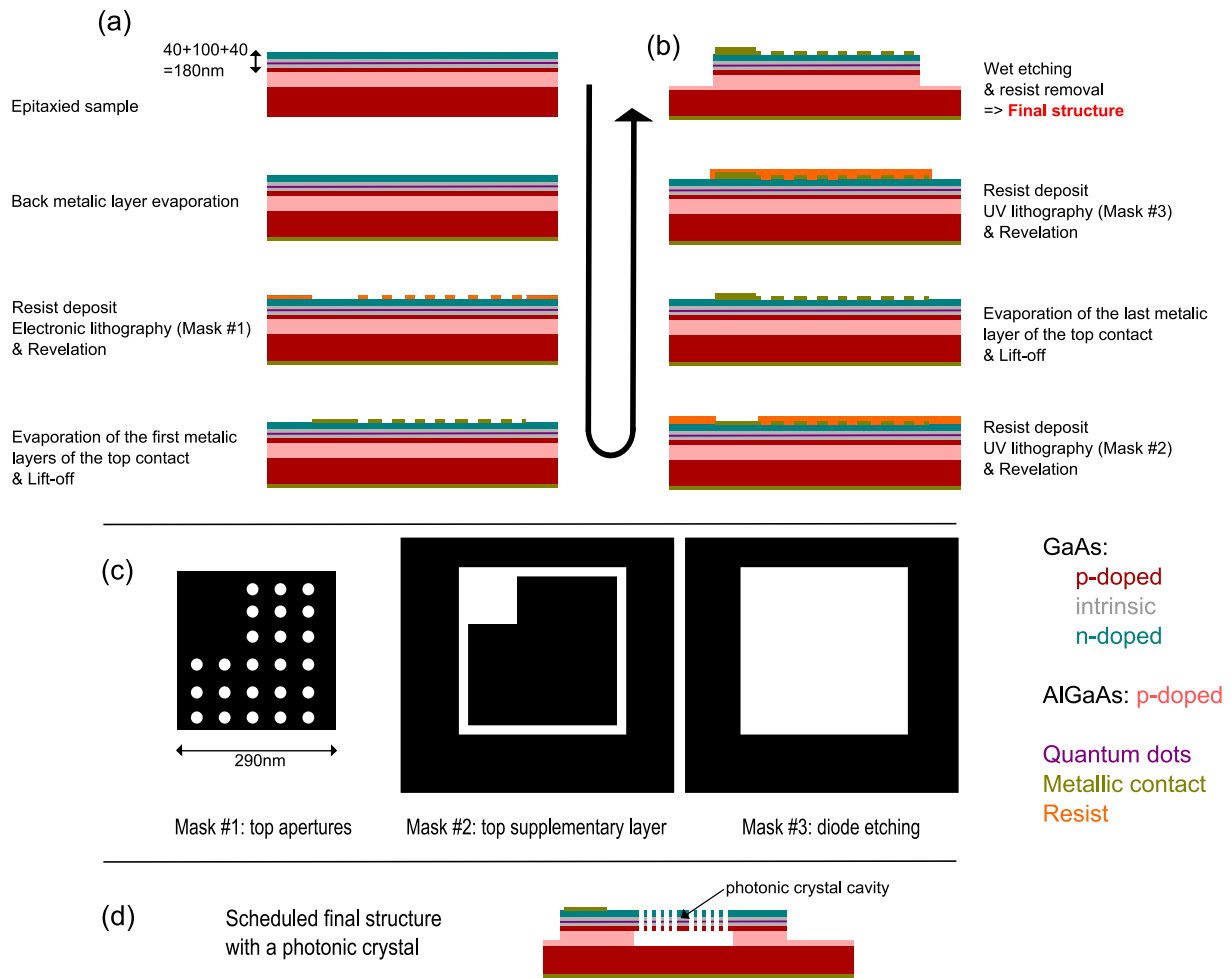


Figure 5.4: (a): Successive processing steps to obtain the studied *pin* structure. (b): Sketch of the final structure. (c): Sketch of the successive lithographic masks (black: resist left after revelation). (d) Sketch of the final structure including the photonic crystal cavity.

resist-metal bilayers by dissolving the remaining resist into acetone. We end up with a squared metallic layer deposited on the top surface and pierced by arrays of holes.

- **Deposition of the top metal contact:** The previous step is followed by a second optical lithography that forms apertures superimposed on the  $290 \times 290 \mu\text{m}^2$  metallic layers, the form of which is described on figure 5.4 (c). The UV resist is AZ5214 used as a negative photoresist. A second layer of  $100\text{nm}$  thick gold layer is further evaporated. This is followed by a second lift-off removing the metal-UV resist bilayers. The resulting  $220\text{nm}$  thick metal layers will form the top contacts sufficiently thick to allow the diode electrical bonding (it is mostly a problem of mechanical solidity).
- **Diode etching:** An optical lithography step defines squares of UV resist (AZ5214 used as a positive photoresist) above the structure (apertures and top contact). Their surface is  $300 \times 300 \mu\text{m}^2$ . After desoxidation of the sample by wet etching (30 seconds in  $\text{HCl}/\text{H}_2\text{O}$  solution with respective proportions 1/4), the sample is etched chemically (by a  $\text{H}_3\text{PO}_4/\text{H}_2\text{O}_2/\text{H}_2\text{O}$  solution with respective proportions 3/1/40) with an etch rate of  $\simeq 100\text{nm}\cdot\text{sec}^{-1}$ . The etching depth is about  $250\text{nm}$ . The protecting resist is then dissolved in acetone and the sampled is cleaned in an isopropanol solution.
- **Diode electrical bondings:** Eventually, in order to make the required electrical bondings, the sample is glued with a silver paste on a ceramic holder making the back contact. The top contact is made by bonding a gold wire thermally compressed on the top metallic surface on one end, and on a metal plot of the ceramic on the other end.

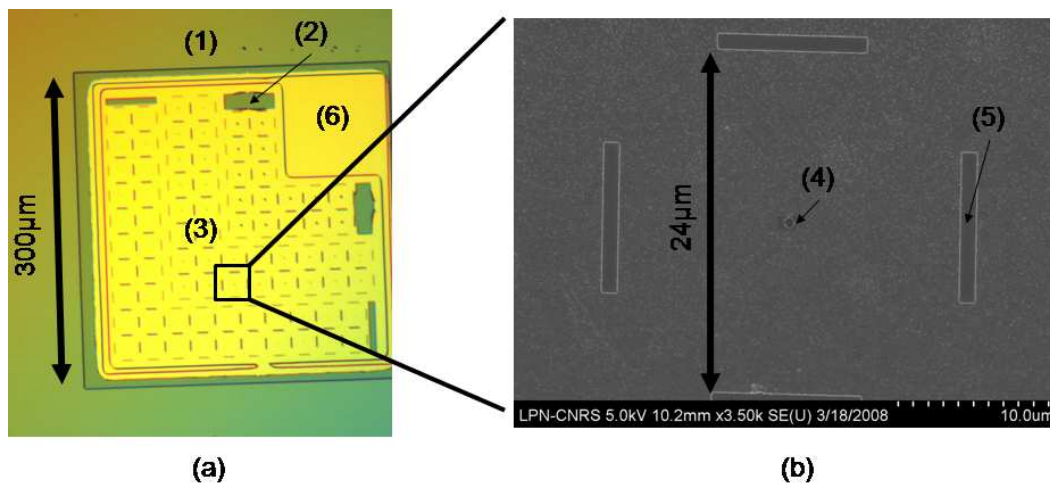


Figure 5.5: (a) Optical microscope top view of a processed *pin* diode. (b) Zoom on an aperture of the top contact: electronic microscope image. The different numbers on the images indicate: (1) the etched surface, (2) the top surface of the diode unrecovered by metal, (3) top metal contact with apertures, (4) aperture, (5) markers to find the apertures positions (processed simultaneously to the apertures), (6) the surface of the upper metallic layer, which is the region where the bonding is made.

### Choice of the metal to realize the top metal contact

Let us first consider the *pin* structure. The top contact is deposited on the *n*-doped layer. Usually, semiconductor metal contacts involve the appearance of a Schottky barrier (a non-linear contact), con-

versely to ohmic contacts with a linear voltage-current characteristic. To achieve low ohmic contacts, annealed  $Au - Ge - Ni$  is usually used for  $n$ -doped GaAs. In our experiments, the metal multilayer to form the  $n$ -type contact consisted of Ni: 10nm, Ge: 30nm, Au: 60nm, Ni: 20nm, Au: 200nm [22, 23, 24]. The upper layer is used to obtain a good bonding with the gold wire. Rapid thermal annealing for few seconds at about 400 °C in nitrogen atmosphere is then performed to induce merging of metals and diffusion inside the sample structure. This creates usually a good ohmic contact. However, diffusion occurs over large depth down to the  $p$ -doped region 140nm below. The current between the two electrodes then flow through a short circuit. By varying the annealing temperature and time, only switching from Schottky type contact (with a voltage threshold) to a short circuit was observed.

Schottky contacts are rectifying contacts formed due to the bending of bands in the semiconductor when a metal comes in intimate contact with its surface. Band bending occurs due to the difference in work functions of the metal and the semiconductor which results in a potential barrier for the flow of carriers at the interface. Although this suggests that Schottky barrier heights would be a strong function of the metal work function, it has been determined experimentally that on a GaAs surface, irrespective of the metal used, a rectifying contact with a Schottky barrier close to 0.8eV is formed. A large density of surface states at the interfacial layer is responsible for this fixed Schottky barrier. Although almost any metal that is placed on GaAs will yield a rectifying Schottky contact, the metal must also exhibit two other characteristics: i) Good adhesion and ii) Thermal stability. Titanium is the most commonly used metal meeting both the above criteria. We have used a metal stack comprising of 20nm of Titanium and 200nm of gold. The gold layer was thick enough to achieve successful electrical bonding. This technique proved to be very satisfying, even if some aspects remain not understood:

- the diode displays a voltage threshold of 1.7V with no leak currents as shown on figure 5.6. The black curve corresponds to the dark current. The diode character of the device is clearly evidenced in reverse bias where the current is very small (a few tens pA), whereas in forward bias the current increases exponentially with applied voltage. When illuminating the sample, we observe photo-current, which dominates the electric properties of the device in the reversed bias region. The value of the threshold (1.7V) is surprising. A usual  $pin$  diode with highly doped regions is expected to sustain a bias about the GaAs gap (1.45V). The higher threshold voltage tends to indicate that the top contact adds up a bias of  $\sim 0.25V$ , which does not correspond to any usual value: the Schottky barrier is 0.8V.
- at room temperature, the I-V characteristic between two distant top contacts on a continuous  $n$ -doped surface (i.e. with no chemical etching between) is a ohmic contact for low currents, and the currents is limited for higher applied tensions (figure 5.7 (a: red curve)). This limitation can be explained as following: strong currents between two surface contacts go deeply into the material, and this deepness increases with the current intensity. In our case the current cannot circulate deeply in the material due to the proximity of the  $p$ -doped layer. This limits the maximally possible current which can be transported into the  $n$ -doped top surface. The top contacts would have been a Schottky barrier as expected from this choice of Ti-Au metal, these two distant top contacts on a continuous  $n$ -doped surface had behaved as two opposite diodes, therefore the current should be blocked for low voltages, as schematized on figure 5.7 (a: blue curve) [24]. Unexpectedly at low current values passing through these contacts, they behave as an ohmic one. In the blocking regime no current is passing through the  $pin$  diode and the loss of voltage induced by the contact is negligible. Above threshold the problem becomes obviously more complicated but is not relevant because we are not interested in this regime. This result also demonstrates the choice of doped layer 40nm thick is at the limit of bi-dimensional currents,

which may be an explanation why the Ti-Au contact does not behave as a Schottky as it is the case for bulk GaAs n-doped contacts.

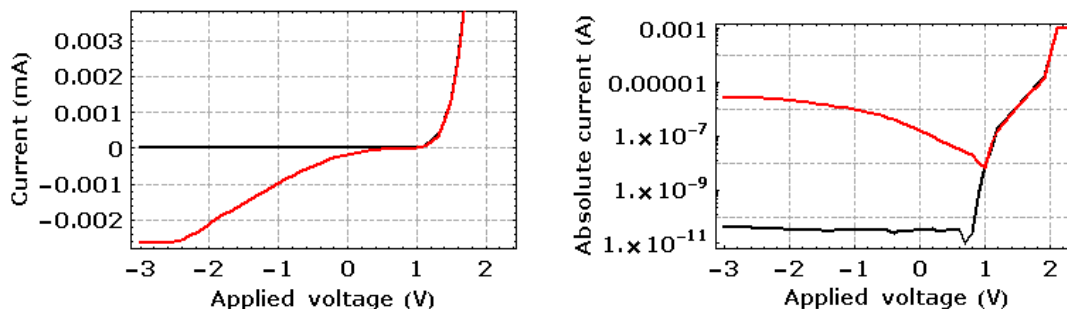


Figure 5.6: Voltage-current characteristics of the *pin* device measured at 4 K in two different conditions. Black curve (without sample illumination) and red curve (illumination with the laser beam tuned to 1.45 eV).

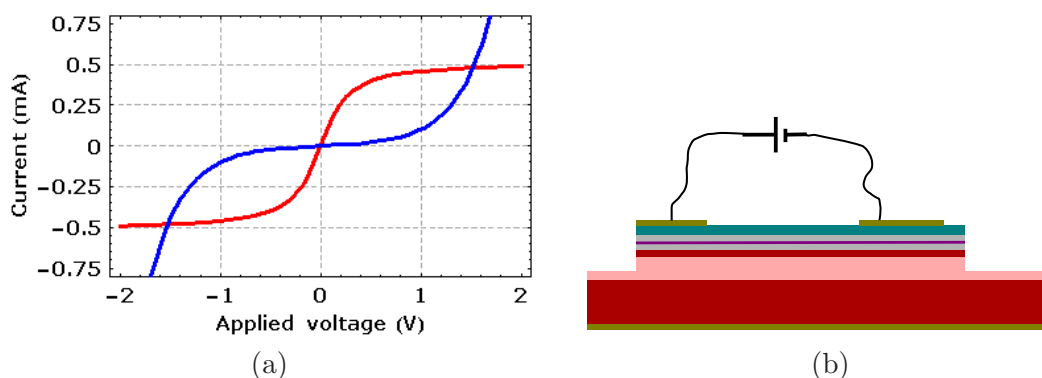


Figure 5.7: (a) Voltage-current characteristics of the structure described in (b): sketch of the measured characteristics (red curve) and of the expected one if the contacts were Schottky (blue curve). (b) Sketch of the studied structure with two Ti-Au contacts on the *n*-doped GaAs layer.

Unexpectedly the *nip* diodes did not behave correctly. Both contacts are expected to be ohmic, leading to a threshold of 1.45V as explained previously. The diode characteristics had the right aspect but the threshold was systematically around 1.0V (at 4K). It is surprising considering that titanium deposit with no thermal diffusion is already a good ohmic contact, at least on a thick p-doped GaAs layer. I nevertheless optically observed the sample at 4K. The optical behaviour varies similarly to the *pin* sample, as for example the voltage at which the dots begin to emit ( $\sim 0.6V$ ), except for the threshold appears sooner when we increase the applied voltage. As for the *pin* structure, the threshold crossing makes appear other lines and quickly degrades the emission of the excitonic and biexcitonic lines. This strongly reduces the interesting range of the applied voltage to about 0.4V, which is quite small.

### Realization of apertures in an optical metal shadow mask

In order to investigate the FSS on a single dot, different techniques can be used to isolate one dot. These are summarized on Figure 5.8. Since the dots density in our sample is too high, metal shadow

masks or mesas have to be applied. Among these two techniques, the use of an optical metal mask is the most appropriate in view of combining it with the *pin* diode process. Here, it consists of a 120 nm thick film of metal (20 nm of Ni and 100 nm of Au) with circular apertures with 0.5, 1 and 2  $\mu\text{m}$  in diameter. They are produced by electronic beam lithography, metal deposition and a lift-off process.

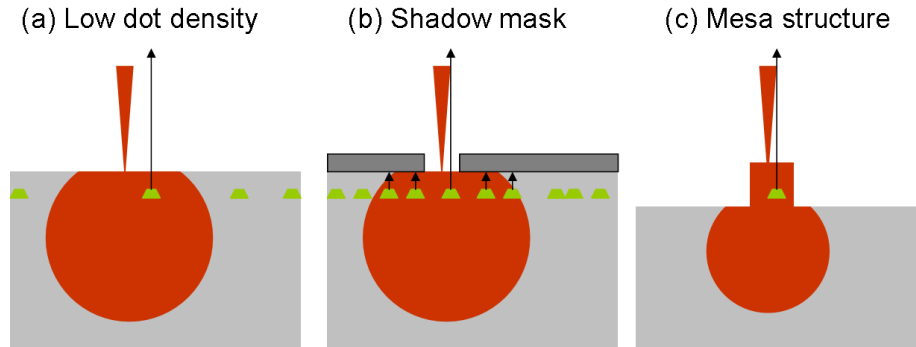


Figure 5.8: Schematics of three different techniques to probe single quantum dots.

Since the apertures diameter is of the same order of the investigated wavelength range, it is necessary to avoid any polarization filtering by making holes with round shapes and no roughness. We used positive resists, in which the portion of resist that is exposed, becomes soluble in a developer, while the portion of resist that is unexposed remains insoluble. The pattern printed by the electron beam consists therefore of square apertures in the resist layer and containing arrays of resist cylinders. After metal deposition and removal of the metal-bilayer regions, we end up with squared layers of metal pierced by circular holes (figure 5.4). After a comparison of the results obtained with two different positive resists (PMMA and ZEP520 resist<sup>48</sup>) with various revelation times<sup>49</sup> and various insulation powers, the ZEP520 proved to be more satisfying. Figure 5.9 illustrates this point. By using the ZEP520 resist, the shape of the apertures is circular and presents very small irregularities on the flanks, compared to apertures obtained with PMMA that presents a more irregular shape and an increased roughness. The surface aspect of the deposited metal is also grainy when using the PMMA resist.

By using this technique, the thickness of the ZEP520 resist is high enough to open apertures in a 220 nm thick metal layer. Let us remind that the top contact will consist of a metallic bilayer with 20 nm of titanium and 200 nm of gold. However, in order to obtain a reproducible process, a two-step process has been used: first the apertures are realized in a 120 nm metallic layer and second a 100 nm layer of Au is deposited. This prevents from any variation in time of the ZEP520 resist thickness (due to aging for instance) or of the thickness of the deposited metal layer (due to change of the metal deposition apparatus). This second layer of metal can be distinguished from the first on figure 5.5 (a).

<sup>48</sup>PMMA stands for polymethyl methacrylate. ZEP stands for Zeon's electron beam positive resist. The matrix resist ZEP520 is a copolymer of methyl chloroacrylate and methyl styrene.

<sup>49</sup>The developers of the PMMA and ZEP520 resists are a solution of Methyl IsoButyl Ketone:1 Isopropanol:3, and a solution of xylene respectively.

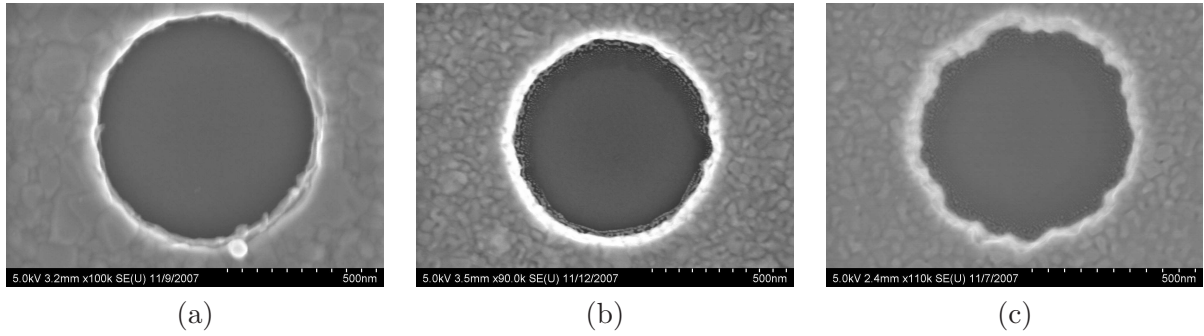


Figure 5.9: Electronic microscope top view of 500 nm diameter apertures formed in the metal layer. (a) Best conditions obtained with the ZEP520 resist. (b) Best conditions obtained with the PMMA resist. (c) Example of apertures obtained if the insulation power is too high.

## 5.4 Experimental results

All the investigation of symmetry-related effect has been performed on *pin* structures. The investigation of single dots was done on 2  $\mu\text{m}$  apertures, where we managed to identify single spectral lines.

### 5.4.1 Experimental setup

A sketch of the whole experimental set-up is shown on figure 5.10.

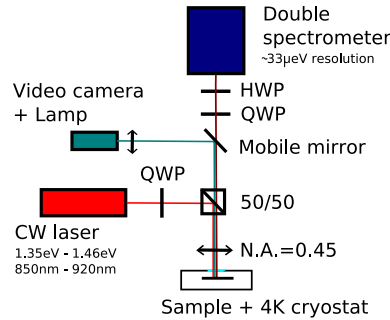


Figure 5.10: Optical setup used to study the spectroscopy of unique quantum dots under vertical electric field.

The sample glued on its ceramic holder is fixed by silver paste on the cold finger of the cryostat and the macroscopic wires connected the ceramic holder with cryostat's electric pins. The sample is cooled at  $\sim 4\text{K}$ . Only one diode is connected at a time, and the current circulating through it is measured. A long working distance microscope, situated in front of the cryostat window and with 0.45 numerical aperture, focus at normal incidence the laser beam on a  $\sim 5\mu\text{m}^2$  area of the sample surface. The cryostat is positioned in front of the objective by use of a 3-axis step motors stage. The Titanium-Sapphire laser used for excitation is tuned at  $1.45\text{eV}$  ( $855\text{nm}$ ). The laser beam is sent into the objective after reflection from a non-polarizing beamsplitter cube. The laser beam polarization is controlled by a set of waveplates and polarizer. The part of the beam which passed through the cube went to a power meter. The photoluminescence signal is collected by the objective and sent through the cube toward the spectrometer. It was first analyzed by a set of polarization waveplates

and spectrally by a double monochromator with a  $33\mu\text{eV}$  resolution. The spectra are recorded using a liquid-nitrogen cooled CCD camera. No mirrors are placed in the optical path from the objective to the spectrometer in order to avoid birefringence. The 50/50 beamsplitter used to separate the laser from the luminescence is birefringence-corrected. In order to see the sample surface a mirror is placed in front of the monochromator (and removed for spectra recording). It sends white light from a halogen lamp and the reflection from the sample to an imaging camera. In order to apply an electric field on the studied diode, an electric source-meter is used.

Spatial filtering of the signal is done in two ways. The metallic arrays of holes on the sample surface limited the excitation/collection area, and additionally with the CDD in imaging mode, one can resolve (vertically only) different luminescence lines originating from different nano-objects in the sample. The set-up resolution (of the order of tens  $\mu\text{eV}$ ) does not allow to directly measure the FSS value. The exciton splitting is inferred by using a Lorentzian curve-fitting procedure [25, 26, 27]. In this context, the accuracy of FSS measurements is limited by spectral diffusion of the lines (a few  $\mu\text{eV}$ 's).

#### 5.4.2 Fine-tuning of the exciton splitting in dots with high asymmetry

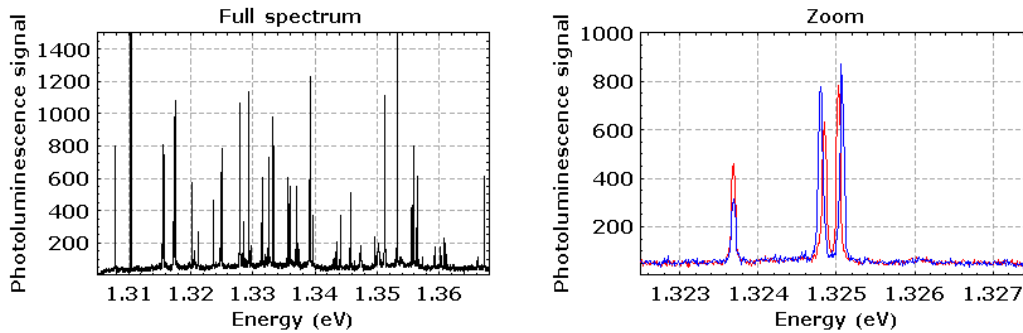


Figure 5.11: Photoluminescence spectrum of an aperture with an applied voltage of  $1.5\text{V}$ , and a zoom on a part of it. The zoom contains the spectrum of both linear polarisations. The three lines corresponds to an exciton, a biexciton and a most probably trion, of the same dot. These three lines are clearly isolated from the rest of the spectrum.

In order to check the action of a vertical field on the FSS value of excitons in dots, first experiments have been done on dots which presented large exciton splitting (around  $80\mu\text{eV}$ , as they can be easily identified. The sample is optically pumped and various spectra over a wide spectral range  $1.30\text{eV}$  to  $1.37\text{eV}$  and under varying applied voltages (from  $0.5\text{V}$  to  $2.0\text{V}$ ) were recorded. Example of such spectra is given on Figure X. These spectra display groups of peaks, each group being attributed to emission from a single dot (the dot density is very low and the number of observed through  $2\mu\text{m}$  aperture is of the order 4-5). In each group of peaks, we identify lines that display a splitting (see figure 5.11). If two split peaks are observed within the group of peaks, the lower energy split peak is attributed to exciton emission from one single dot, as confirmed by its linear intensity dependence as a function of excitation power; the highest energy split peak corresponds to the biexciton line.

We then analyzed on ten dots the variation of the emission wavelength and of the FSS value as a function of the applied voltage. For all the lines, the exciton wavelengths and thus the FSS value is deduced by fitting the split peaks by two Lorentzian curves. This fit also allows us to deduce the width and intensity of each line. By comparison between the H and V polarized spectrum, the excitonic splitting is deduced. This measure is performed for various applied voltages to study these

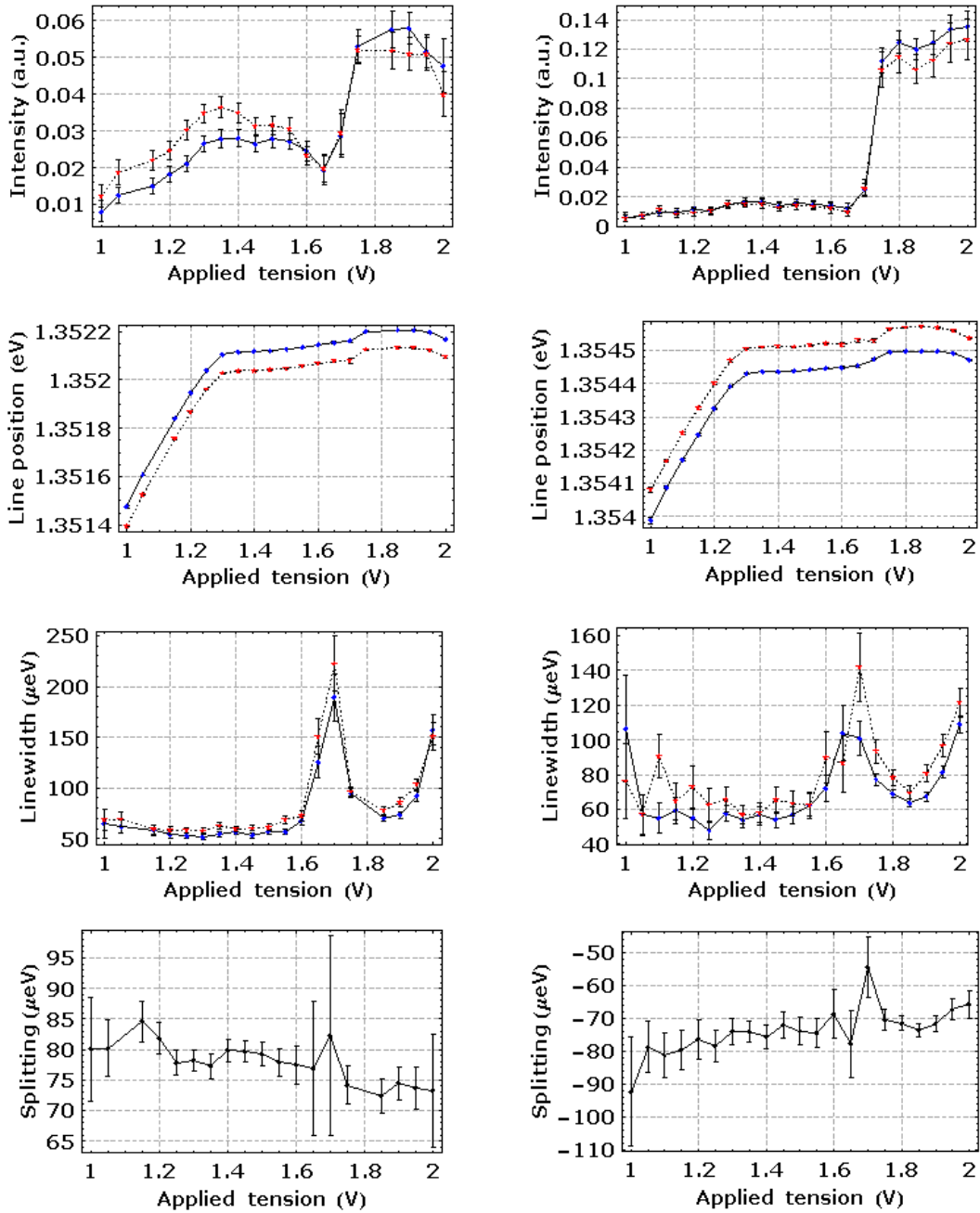


Figure 5.12: Characteristics of the biexcitonic line (column on the left) and the excitonic lines (column on the right) measured on a single dot, as a function of the applied voltage. Blue (resp. red) curves are horizontally (resp. vertically) polarized lines.

characteristics dependencies. One example is shown on figure 5.12. On these curves, six regimes can be distinguished:

- below 1 V far away from the threshold voltage, the dot is not luminescent.  
In this regime, the field applied to the dot is high and the carriers escape the dot before recombining, due to band bending. When increasing the voltage, the amplitude of the total field (built-in field and external field) decreases.
- From 1V to 1.3V the luminescence intensity of both the excitonic and biexcitonic lines increases. This increase comes with a blueshift of the emission lines and a decrease of the absolute FSS value.  
In this regime, the amplitude of the total field is smaller and electron-hole radiative relaxation starts to dominate over carrier escape from the dot. This exciton and biexciton energy shift as a function of voltage, actually results from both the single particle quantum confined Stark shift as well as the subsequent changes of electron-hole Coulomb interaction. We could follow simultaneously the FSS variation for the exciton and biexciton. The bright biexciton and exciton splitting is reduced by  $5 \mu eV$  roughly for a Stark-shift of the order of  $1 meV$ . In this configuration, we should not expect a strong effect since the vertical field does not a priori change the quantum in-plane anisotropy responsible for the FSS.
- From 1.3V to the threshold voltage, the luminescence intensities and the lines position do not change much. The absolute splitting continues to decrease.  
Surprisingly, we should expect a regular blue shift as a function of the electric field due to the Stark effect. This seems to indicate that the amplitude of the electric field does not evolve linearly with the applied voltage as expected. Conversely, the linear evolution of the excitonic splitting, reversely to the biexciton one, tends to confirm the linearity of the field amplitude. No explanation has been found up to now to fully understand this behaviour. Nevertheless, we still observe a linear variation of the excitonic splitting as expected. The exciton FSS value is reduced by  $5 \mu eV$  roughly.
- Around the voltage threshold, the dot emission lines undergoes a fast blue-shift. Their linewidth increases and their intensity decreases.  
At threshold, the bands are flat and the existence of a small current creates free charges which perturb the dot, whereas under tilted bands those charges are expelled away. This effect may explain the short intensity decrease and linewidth increase of the exciton line.
- Just above threshold, the intensity increases abruptly. Other lines appear, corresponding most probably to multiply charged states. The exciton and biexciton linewidths decrease.  
In this region, carriers injection via the photocurrent will add the photoinjection of carriers, thus increasing the number of electron-hole pairs trapped in the dot. The linewidth reduction results from band bending.
- Well above threshold, the biexciton then the exciton lines intensity tends to decrease while their linewidths increase, until the dot is not luminescent anymore. A slight redshift of the lines is also observed.  
Well above threshold the current becomes high and thermal effects may affect the dot characteristics (linewidth and wavelength). For higher voltages, this current becomes too strong for the excitonic and biexcitonic states to be stable enough to remain luminescent.

Figure 5.13 summarizes all the measures performed on different highly asymmetric dots. We first observe as expected that the difference between the biexciton energy and exciton energy (i.e.

binding energy) increases as a function of the exciton energy (i.e. in smaller dots). The native exciton and biexciton splitting are also, as expected, of the same amplitude but with opposite signs. Unlike other work in this field [8, 14], we do not observe a significant reduction of the FSS value as a function of the exciton energy since the dot emission is scanned over a very short spectral range. Usual observed reduction are indeed of the order 1.5 to 2  $\mu\text{eV}/\text{meV}$ .

The absolute value of FSS change amounts up to 10  $\mu\text{eV}/V$ . This confirms that fine-tuning of the exciton structure is possible by applying a vertical electric field. However, the voltage range over which this modification could be used for the exciton FSS fine-tuning in view of producing entangled photon states is relatively limited. One of the reasons already mentioned is the loss of photoluminescence signal due to field-induced carrier escape, accompanied by a strong linewidth broadening when the field increases. The dot luminescence is high enough only over a 0.5 V wide voltage range, allowing for only 5  $\mu\text{eV}$  reduction of the FSS value. This method appears interesting only for quantum dots, displaying a native small asymmetry, with small FSS (below 5  $\mu\text{eV}$ ). In our experiments, the average splitting is of the order of 70-80  $\mu\text{eV}$  around 1.235 eV.

Taking into account the dependency of the FSS value as a function of the exciton energy, such dot with small asymmetry should emit around 1.36 – 1.37 eV. One could argue however that the amplitude of the FSS reduction may depend on the dot wavelength. Different mechanisms (piezoelectricity, shape anisotropy...) affect the value of the FSS. The amplitude of their contributions will depend on the dot size and thus dot wavelength: the impact of the dot shape anisotropy will augment in smaller dots, while the contribution of piezoelectric effect should decrease due the wavefunction expansion outside the dot along the growth axis. One could think that the applied electric field would compensate for only part of these effects. Hopefully, the amplitude of the FSS reduction does not seem to depend on the exciton energy (see Fig. 5.13 (d)). The impact of the different mechanisms participating in the FSS do not indeed contribute independently to the FSS: one must not add the absolute modification of each effect to the whole splitting, but part of them must be added algebraically taking into account the sign of the contributions. This is confirmed by the observed constant value of the FSS tuning per volt.

### 5.4.3 Towards a fine-tuning of the exciton splitting in dots with high asymmetry

A major difficulty in the study of dots with a small asymmetry is to identify lines in the spectrum corresponding to an exciton line, since the splitting is small, below our set-up resolution. It becomes consequently impossible to distinguish a true exciton, from a charged exciton (one exciton plus one hole trapped in the dot or one exciton plus one electron trapped in the dot). One technique consists in exciting the dot on a trapped excited state of the dot, one photon above the exciton transition. The energy of the pumping laser is then tuned, so that the energy of one pump photon is equal to the energy of one phonon plus the energy of the studied lines <sup>50</sup>.

The first advantage of this quasi-resonant pumping technique is that it creates carriers only on a single level of one single dot. The second advantage is the following. The pump creates an electron-hole pair directly in the dot, conversely to non-resonant pumping in which the pair created in the surrounding matrix or in the wetting layer relaxes incoherently in the dot from higher levels. The phonon has a null spin. Therefore the quasi-resonant pump photon spin is transferred to the exciton spin and this information is not erased during a possible damping. Depending on the properties of the dots and the presence of other trapped charges (for instance one electron or one hole), it is possible to deduce the possible polarizations of the emitted photon. The study of the luminescence polarization leads to an identification of the presence of charges and some of the dot's properties.

For example, Let us consider an ideal quantum dot (i.e. no excitonic splitting, no excitonic beating and no incoherent spin-flip processes). The exciton spin polarization is transferred to the

<sup>50</sup>The energy of one optical phonon is  $E_{\text{phonon}} = 8.6\text{meV}/K$ . At 4K:  $E_{\text{phonon}} = 34\text{meV}$  that is about 24nm at 950nm.

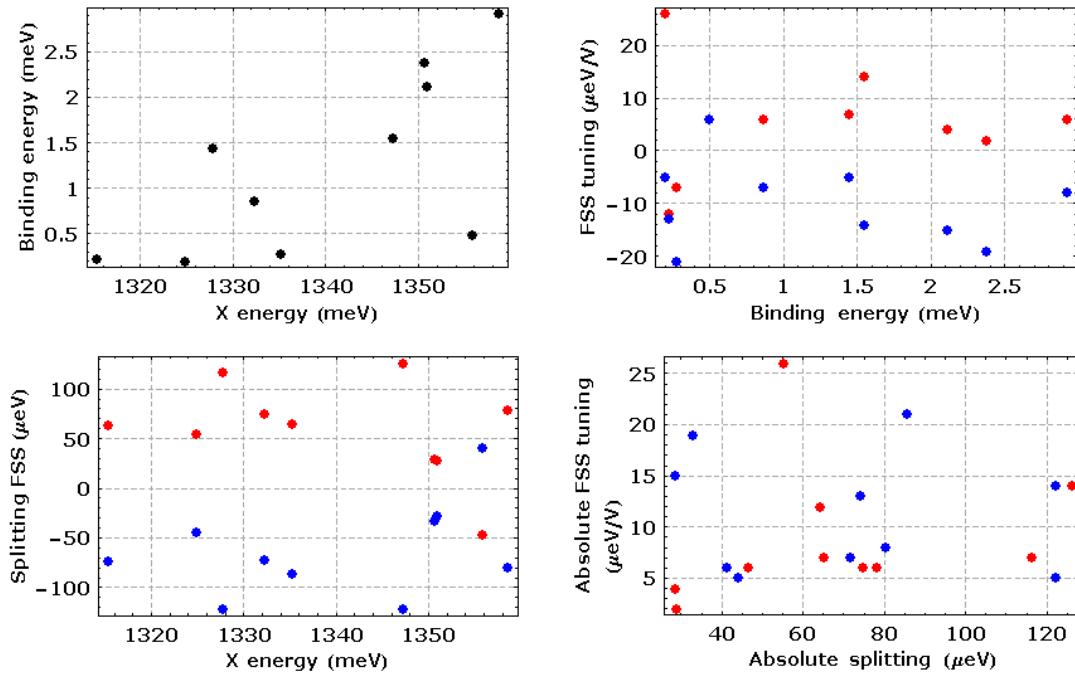


Figure 5.13: Characteristics of ten investigated dots. (a) Variation of the energy difference between the biexciton and exciton as a function of the exciton energy. (b) Amplitude of the native exciton FSS value as a function of the exciton energy. (c) Variation of the FSS tuning per volt as a function of the exciton energy. (d) Variation of the FSS tuning per volt as a function of the exciton native splitting. Blue: biexcitonic line, Red: excitonic line.

polarization of emitted light and the polarization of the excitonic line of such a dot has therefore the same polarization as the pump photon, whatever its polarization. Conversely, for highly split dots, if the polarization orientation corresponds to one of the eigenaxis of the dot, then the polarization is also conserved. But in other cases, we observe polarization beating in time due to a loss of polarization orientation. Consequently, it is possible to distinguish with a good sensitivity quantum dots with small splitting by measuring the exciton emission polarization degree under polarized pump. This technique also allows us to identify trion states (i.e. charged excitons). Let us consider that the additional charge is an electron (the same reasoning stands with holes). The dot contains two electrons and one hole. Pauli's principle implies that the electrons display opposite spins. The spin orientation of the trion is thus only determined by the hole spin, and is obviously circular. Consequently, the polarization degree measured on lines corresponding to trions will be high under circularly polarized pumps but low under linearly polarized pumps.

In our experiment, no dots with a small enough initial splitting were found. The smallest observed splitting were of the order of  $28 \mu eV$ . Smaller splitting may be expected for dots emitting at higher energies. However, the dot emission begins to be masked by the luminescence signal emitted by the wetting layer or the pumping laser. We also tried to anneal the sample in order to reduce the mean native splitting of the exciton [14, 28]. The annealing parameters depend strongly on the growth conditions and thus the native FSS value. We thus proceeded to a step-by-step annealing of the processed diodes, to finely reduce the FSS value of the dots. The annealing of the dots can be obtained either at  $\sim 670 \text{ deg } C$  during a few minutes [14], or at higher temperature during a shorter time (about  $\sim 30 \text{ sec}$  at  $\sim 850 \text{ deg } C$ ). Even at  $850 \text{ deg } C$  during  $3 \text{ min}$ , which is much greater than the requirements, the electrical properties of the sample were not impacted. A major problem here resides in the fact that the annealing temperature is too high and evaporates the gold deposited on the sample. Titanium evaporates more slowly. Tungsten is known to stand at such temperatures. I consequently fabricated diodes with a top contact made of this metal<sup>51</sup>, but their electrical properties were poor due to the reaction of tungsten with the Si doping of the top epitaxial layer (creating most probably  $WSi_2$ ).

## 5.5 Conclusion to this study

In view of fine-tuning the exciton fine structure splitting by applying a vertical electric field, we developed a process allowing for the fabrication of *pin* diodes embedding a low density quantum dot array in the intrinsic region. Small apertures with diameters ranging from  $0.5$  to  $2 \mu m$  were formed on the top of the diode, in order to spatially isolate single dots. By use of these structures, we have demonstrated the possibility of controlling the anisotropic exchange splitting in semiconductor quantum dots by using a vertical electric field. Although the absolute values of FSS changes amount up to  $10 \mu eV/V$ 's, the reduction of the splitting to zero was difficult to achieve, because of the following reasons: i) a strong reduction of luminescence intensity due to the tunnelling out of the carriers, ii) a strong broadening of the lines. However, the FSS change and its constant amplitude as a function of the dot energy and size indicates the possible modification of excitonic wave-function symmetry, promising for future in-situ control of the photon entanglement.

Various improvements should be investigated. From an electric point of view, *nin* structures should be more appropriate. Such structures should allow for a wider change of the field amplitude. The absence of built-in voltage in the intrinsic regions would also allow for photoluminescence study of the dots before diode processing. This last point should open the possibility to reduce the initial

---

<sup>51</sup>Tungsten deposits cannot be lifted. The lift-off step was replaced by a deposit of the tungsten on the whole unprocessed surface, followed by a reactive ion etching to perform the apertures.

excitonic splitting by thermal annealing the sample before processing it. Last, the possibility of controlling FSS using a vertical electric field, combined to the implementation of cavity effect, is presently accessible with available technology. The combination of photonic crystal cavities and electrical contacts has already been implemented, either in view of electrical pumping [29] or in view of shifting the wavelength of the dot by Stark effects and change it from a situation non spectrally resonant to the cavity mode to a resonant one [30, 31].

## Bibliography

- [1] N. Akopian, N. H. Lindner, E. Poem, Y. Berlatzky, J. Avron, D. Gershoni, D. Gerardot, and P. M. Petroff. Entangled photon pairs from semiconductor quantum dots. *Phys. Rev. Lett.*, 96:130501, 2006.
- [2] R. M. Stevenson, A. J. Hudson, A. J. Bennett, R. J. Young, C. A. Nicoll, D. A. Ritchie, and A. J. Shields. Evolution of entanglement between distinguishable light states. *Phys. Rev. Lett.*, 101:170501, 2008.
- [3] R. J. Young, R. M. Stevenson, A. J. Hudson, C. A. Nicoll, D. A. Ritchie, and A. J. Shields. Bell-inequality violation with a triggered photon-pair source. *Phys. Rev. Lett.*, 102:030406, 2009.
- [4] D. Gammon, E. S. Snow, B. V. Shanabrook, D. S. Katzer, and D. Park. Fine structure splitting in the optical spectra of single GaAs quantum dots. *Phys. Rev. Lett.*, 76:3005, 1996.
- [5] M. Grundmann, O. Stier, and D. Bimberg. InAs/GaAs pyramidal quantum dots: Strain distribution, optical phonons, and electronic structure. *Phys. Rev. B*, 52:11969, 1995.
- [6] G. Bester, S. Nair, , and A. Zunger. Pseudopotential calculation of the excitonic fine structure of million-atom self-assembled In<sub>1-x</sub>Ga<sub>x</sub>As/GaAs quantum dots. *Phys. Rev. B*, 67:161306, 2003.
- [7] G. Bester and A. Zunger. Cylindrically shaped zinc-blende semiconductor quantum dots do not have cylindrical symmetry: Atomistic symmetry, atomic relaxation, and piezoelectric effects. *Phys. Rev. B*, 71:045318, 2005.
- [8] R. Seguin. *Electronic Fine Structure and Recombination Dynamics in Single InAs Quantum Dots*. PhD thesis, 2008.
- [9] N. Gogneau, L. Le Gratiet, E. Cambril, G. Beaudoin, G. Patriarche, A. Beveratos, R. Hostein, I. Robert-Philip, J.Y. Marzin, and I. Sagnes. One-step nano-selective area growth (nano-sag) of localized InAs/InP quantum dots: First step towards single-photon source applications. *Journal of Crystal Growth*, 310:3413–3415, 2008.
- [10] A. Badolato, K. Hennessy, M. Atature, J. Dreiser, E. Hu, P. M. Petroff, and A. Imamoglu. Deterministic coupling of single quantum dots to single nanocavity modes. *Science*, 308:1158, 2005.
- [11] A. Dousse, L. Lanco, J. Suffczynski, E. Semenova, A. Miard, A. Lemaitre, I. Sagnes, C. Roblin, J. Bloch, and P. Senellart. Controlled light-matter coupling for a single quantum dot embedded in a pillar microcavity using far-field optical lithography. *Phys. Rev. Lett.*, 101:267404, 2008.
- [12] K. Hennessy, A. Badolato, A. Tamboli, P. M. Petroff, E. Hua, M. Atature, J. Dreiser, and A. Imamoglu. Tuning photonic crystal nanocavity modes by wet chemical digital etching. *Appl. Phys. Lett.*, 87:021108, 2005.

- [13] K. Hennessy, C. Hogerle, E. Hu, A. Badolato, and A. Imamoglu. Tuning photonic nanocavities by atomic force microscope nano-oxidation. *Appl. Phys. Lett.*, 89:041118, 2006.
- [14] R. J. Young, R. M. Stevenson, A. J. Shields, P. Atkinson, K. Cooper, D. A. Ritchie, K. M. Groom, A. I. Tartakovskii, and M. S. Skolnick. Inversion of exciton level splitting in quantum dots. *Phys. Rev. B*, 72:113305, 2005.
- [15] A. I. Tartakovskii, M. N. Makhonin, I. R. Sellers, J. Cahill, A. D. Andreev, D. M. Whittaker, J-P. R. Wells, A. M. Fox, D. J. Mowbray, M. S. Skolnick, K. M. Groom, M. J. Steer, H. Y. Liu, and M. Hopkinson. Effect of thermal annealing and strain engineering on the fine structure of quantum dot excitons. *Phys. Rev. B*, 70:193303, 2004.
- [16] K. Kowalik, O. Krebs, A. Lemaître, S. Laurent, P. Senellart, J. A. Gaj, and P. Voisin. Influence of an in-plane electric field on exciton fine structure in inas-gaas self-assembled quantum dots. *Appl. Phys. Lett.*, 86:041907, 2005.
- [17] S. Seidl, M. Kroner, A. Högele, K. Karrai, R. J. Warburton, A. Badolato, and P. M. Petroff. Effect of uniaxial stress on excitons in a self-assembled quantum dot. *Appl. Phys. Lett.*, 88:203113, 2006.
- [18] R. M. Stevenson, R. J. Young, P. See, D. G. Gevaux, K. Cooper, P. Atkinson, I. Farrer, D. A. Ritchie, and A. J. Shields. Magnetic-field-induced reduction of the exciton polarization splitting in inas quantum dots. *Phys. Rev. B*, 73:033306, 2006.
- [19] S. Varoutsis. *Génération de photons uniques indiscernables par une boîte quantique semi-conductrice dans une microcavité optique*. PhD thesis, 2005.
- [20] S. Laurent. *Cavités à bande interdite photonique bidimensionnelle et application à une source de photons uniques indiscernables*. PhD thesis, 2006.
- [21] R. Braive. *Contrôle de l'émission spontanée dans les cristaux photoniques*. PhD thesis, 2008.
- [22] S. Laurent. *Orientation optique et relaxation du spin du trion dans les boîtes quantiques d'InAs/GaAs*. PhD thesis, 2004.
- [23] B. Eble. *Interaction hyperfine dans les boîtes quantiques d'InAs/GaAs sous pompage optique orienté*. PhD thesis, 2006.
- [24] K. Kowalik. *Symmetry effects in optical properties of single semiconductor quantum dots*. PhD thesis, 2007.
- [25] B. D. Gerardot, S. Seidl, P. A. Dalgarno, R. J. Warburton, D. Granados, J. M. Garcia, K. Kowalik, and O. Krebs. Manipulating exciton fine structure in quantum dots with a lateral electric field. *Appl. Phys. Lett.*, 90:041101, 2007.
- [26] K. Kowalik, O. Krebs, A. Lemaître, J. A. Gaj, and P. Voisin. Optical alignment and polarization conversion of the neutral-exciton spin in individual inas/gaas quantum dots. *Phys. Rev. B*, 77:161305(R), 2008.
- [27] R.M. Stevenson, R.J. Young, P. Atkinson, K. Cooper, D.A. Ritchie, and A.J. Shields. A semiconductor source of triggered entangled photon pairs. *Nature*, 439:179, 2006.
- [28] D. J. P. Ellis, R. M. Stevenson, R. J. Young, A. J. Shields, P. Atkinson, and D. A. Ritchie. Control of fine-structure splitting of individual inas quantum dots by rapid thermal annealing. *Appl. Phys. Lett.*, 90:011907, 2007.

- [29] Hong-Gyu Park, Se-Heon Kim, Soon-Hong Kwon, Young-Gu Ju, Jin-Kyu Yang, Jong-Hwa Baek, Sung-Bock Kim, and Yong-Hee Lee. Electrically driven single-cell photonic crystal laser. *Science*, 305:1444, 2004.
- [30] F. Hofbauer, S. Grimminger, J. Angele, G. Böhm, R. Meyer, M. C. Amann, and J. J. Finley. Electrically probing photonic bandgap phenomena in contacted defect nanocavities. *Appl. Phys. Lett.*, 91:2011111, 2007.
- [31] A. Laucht, F. Hofbauer, N. Hauke, J. Angele, S. Stobbe, M. Kaniber, G. Bohm, P. Lodahl, M.-C. Amann, and J. J. Finley. Electrical control of spontaneous emission and strong coupling for a single quantum dot. *New. J. Phys.*, 11:023034, 2009.

# Chapter 6

## Conclusions and perspectives

### 6.1 Summary

#### 6.1.1 Towards photon entanglement from a single quantum dot

Quantum entanglement expresses the nonlocal correlations allowed by quantum mechanics between distinct systems. It is one of the fundamental concepts embodied in quantum mechanics and challenged the deepest thinkers of the 20th century. Entanglement was first demonstrated in an experiment based on Bell's inequality in 1982 and since then, it has become not only an important element in a "Quantum Toolbox" used in quantum optics, but also an essential resource of Quantum Information Processing and Communications (QIPC). In this context, entangled photons are particularly attractive for applications such as quantum cryptography or quantum relays based on quantum teleportation. Their high robustness against decoherence during transport, has put photonic quantum technologies in a position of great importance in the area of quantum communication.

Some of these protocols have already been experimentally realized. They used generally either polarization entangled photon pairs or energy-time entanglement (or its discrete version, time-bin entanglement). Polarization entangled photons can be produced in an atomic cascade - a two-photon decay process from one state of zero angular momentum to another. Currently, polarization entangled photons or time-bin entangled photons are routinely generated by non-linear processes, such as parametric down-conversion. Spontaneous parametric down-conversion however cannot provide a deterministic source of two-photon entanglement, since the generation of photon pairs per excitation cycle is probabilistic. Multi-pair events lead inevitably to a decreased degree of entanglement of the photon pair. Currently, the engineering of deterministic solid-state compact sources of single entangled photon pairs, which can be used as building blocks for photon-based QIPC systems, is still an open problem.

For this purpose, we investigated a new source using a single emitting dipole. In our experiment, this dipole is a single semiconductor self-assembled quantum dot. Semiconductor quantum dots are attractive: they provide sources of single photons and single pairs of photons on demand. This two-photon cascade process can also produce polarization entanglement, provided an engineering of the dot electronic structure and a spectral/temporal filtering that discards all the non entangled photon pairs. Moreover, these sources suffer from their low quantum efficiency. In our work, we investigated the possibility to engineer the dot electronic structure and exploit cavity effect to restore entanglement. Two schemes were studied: time-bin entanglement and polarization entanglement.

### 6.1.2 Time-bin entanglement

The time-bin scheme uses two sequential single photons emitted by an exciton trapped in a single quantum dot. These two photons are emitted with a time delay greater than their temporal expansion (i.e. the lifetime of the excitonic level). Time-bin entanglement between these two photons is created by sending both of them on one of the input ports of a beam splitter and by post-selecting the configurations in which the two photons leave the beam splitter on different output ports. This produces time-bin entangled photons in the form:  $|\Psi^+\rangle = \frac{1}{\sqrt{2}}(|short\rangle_c |long\rangle_d + |short\rangle_d |long\rangle_c)$ . However, entanglement is created, provided the two photons are indistinguishable: they must be "Fourier transform" limited, which means that their characteristic exciton pure dephasing time  $T_2^*$  must be much larger than the exciton lifetime  $T_1$  ( $T_2^* \gg T_1$ ). My calculations indicate that the key parameter in this scheme is the ratio  $\frac{T_2}{2T_1}$ ,  $T_2$  being the photon decoherence time.

In usual dots under usual non-resonant excitation, the dephasing time is much shorter than the exciton lifetime: entanglement is destroyed by decoherence mechanisms (such as interactions with phonons or fluctuating charge in the dot's surroundings). Hopefully, entanglement can be restored, by lengthening the pure dephasing time and shortening the exciton lifetime. The impact of dephasing processes can be reduced by exciting the dot on trapped excited states of the exciton and by cooling the sample down to 4 K. Spontaneous emission enhancement can also be achieved by embedding the dot in a microcavity (so called Purcell effect). Our calculations indicate that an enhancement by a factor of 30, can restore entanglement, taking into account the impact of dephasing, the impact of the time jitter between the two-photon emission process but also experimental imperfections in the required set-up to violate Bell's inequalities (impact of the balancing between the two required interferometers in a Franson-type set-up).

Different types of cavities can be used. I have focused on cavities formed by etching a two-dimensional photonic crystal in a suspended membrane, since they offer an ultimate confinement of light in time and space. The cavities allow not only to enhance the spontaneous emission rate but also to collect efficiently the emitted photons. However, the cavity must also be designed in order to allow a quasi-resonant excitation of the dot. Different designs have been investigated. Our calculations demonstrate that the most promising structure is double mode cavity, one mode tuned to the excitation wavelength and the other mode tuned to the dot exciton wavelength.

### 6.1.3 Polarization entanglement

The polarisation scheme makes use of the two-photon emission in a cascade manner, when a single dot traps two electron-hole pairs (or a biexciton). In the first step of the cascade, a photon is emitted with random polarisation. In ideal dots, conservation of linear and angular momentum requires that the polarisation of the photon emitted in the second step of the cascade is fixed relative to the first photon: the pair of photons is in a polarization entangled state. However, in real quantum dots, different mechanisms reduce the visibility of entanglement or even destroy entanglement. These mechanisms include mutual dephasing between the two exciton relay levels, incoherent population exchange between these two relay levels and energy splitting between the two excitonic states. Our calculations indicate that the key parameter here is the exciton fine structure splitting.

Different techniques have been investigated to restore entanglement. Up to now, only a combination of growth control and temporal/ spectral filtering has allowed violation of Bell's inequalities. We have investigated the possibility to exploit the Purcell effect to restore entanglement. The Purcell effect should allow the reduction of the spontaneous emission lifetime below the mutual pure dephasing time, the damping time of incoherent population exchange and the quantum beat period between the two excitonic relay levels. However, our calculations indicate that this technique is efficient only for dots with a fine structure splitting smaller than  $5 \mu eV$ , assuming the use of an adequate cavity. Let

us mention that without cavity effects and for dots with null excitonic splitting, Bell's inequalities are hardly violated. Previous experiments therefore added a spectral or temporal filtering, discarding the non entangled pairs and thus reducing the overall efficiency of the source.

An "adequate" cavity for such functionalities must satisfy a large number of requirements. It must accelerate significantly the excitonic transition, without affecting much the dynamics of the biexciton. Both exciton and biexciton lines must be in resonance with the cavity mode, in order to collect efficiently both photons. The cavity mode must be degenerate in polarization and the spatial overlap between these two degenerate modes, in terms of spatial distribution of the intracavity field and of radiation pattern, must be high. This implies to design a cavity displaying one mode degenerated in polarisation, resonant with the excitonic line, quasi-resonant with the biexcitonic one and centred with an accuracy smaller than  $10nm$  around the dot. A design based on a modified H1 cavity is proposed and fulfils all these conditions. However, even in this context, entanglement can be restored if and only if the excitonic splitting is smaller than  $5 \mu eV$ .

Since usual fine structure splitting are of the order of  $10 \mu eV's$ , it is therefore necessary to combine a Purcell effect with techniques allowing for a fine-tuning of the fine structure splitting of the exciton. Different techniques can be used. We investigated the possibility to apply a vertical electric field to reduce the value of this splitting. We therefore fabricated *pin* diodes with apertures and performed measures of the value of the excitonic splitting as a function of the applied voltage. On dots with high asymmetry (with excitonic splitting of the order of tens  $\mu eV$ ), we observed a splitting reduction by  $10\mu eV/V$ . These results are very promising and should be extended to dots with a small asymmetry.

#### 6.1.4 Polarization entanglement versus time-bin entanglement?

In a quantum key distribution prospect, both schemes of coding and entanglement are used. They both suffer from dispersion during fibre propagation (polarization dispersion or velocity dispersion) which both can be compensated accordingly to some demonstrative experiments. Both coding schemes can also be measured and swapped without having to convert from one scheme of coding to the other. These points have also been experimentally demonstrated. However, in the prospect of using quantum dots as deterministic sources of entangled photons, the conditions for obtaining entanglement are much less stringent in the time-bin scheme than in the polarization scheme. In time-bin scheme, indistinguishable single photons with high  $T_2/2T_1$  have already been produced, although the degree of indistinguishability is not high enough to allow for Bell's inequalities violation. Recent progresses in cavity design and processing should allow however to increase the Purcell effect the dot is submitted to and thus the measured degree of indistinguishability. Conversely, for the polarisation entanglement scheme, all the constraints on the cavity mode degeneracy and the dot spatial matching to the cavity mode, are presently far from state-of-the-art fabrication process. Progress in dots growth (for instance localization of the dot and reduction of the native excitonic splitting) and in cavity process (mode degeneracy for example) are still needed.

## 6.2 Perspectives

### 6.2.1 Towards entanglement at telecommunication wavelengths

The investigated dots up to now in this field are InAs dots grown in a GaAs matrix. However, these dots emit around  $950nm$ . Such a wavelength is not appropriate for practical use, in particular due to the poor quantum efficiency of the used detectors. More suitable wavelengths would be the telecommunication ones. Such wavelengths can be reached by using InAsP quantum dots embedded in an InP matrix. However, the InP dots growth is much less mature, compared to techniques to

produce GaAs dots but such a system is still very promising. Accordingly to some theoretical studies, the excitonic splitting of the InAsP dots should also be smaller.

### 6.2.2 Towards entanglement from two single dots

A more prospective application of indistinguishable photons would be to use two single dots each emitting one single photon, instead of one dot producing two sequential single photons. Let us quantify the indistinguishability between two photons emitted by two distinctive sources with same polarization. I use here the formalism developed for the time-bin entanglement. The source  $j = 1, 2$  emits a photon with temporal shape:

$$\mu_j(t) = \sqrt{\Gamma'_j} e^{-i\Omega_j t - \frac{\Gamma'_j}{2} t - i\Phi_j(t)} H(t) \quad (6.1)$$

with, for  $j, k = 1, 2$  and every  $t$  and  $t'$ :

$$\overline{e^{i\Phi_j(t)}} = 1 \quad (6.2)$$

$$\overline{e^{i\Phi_j(t) - i\Phi_k(t')}} = \delta_{jk} e^{-\Gamma_j |t - t'|} \quad (6.3)$$

$\Gamma_j$  and  $\Gamma'_j$  are the pure dephasing and spontaneous emission rates of source  $j$  which emits at the frequency  $\Omega_j$ . The corresponding characteristic times are  $T_1^{(j)}$  (lifetime) and  $T_2^{(j)}$  (coherence time). The photon emitted by the source  $j$  impinges the input of a beam splitter at time  $t_j$ . Let us calculate the probability  $p$  to photodetect one photon at each output of this beam splitter. If we take into account the detection times  $t_\alpha$  and  $t_\beta$  respectively on the output ports  $\alpha$  and  $\beta$ , the probability of cross-detection is:

$$p(t_\alpha, t_\beta) = \overline{\left| \hat{E}_\alpha^{(-)}(t_\alpha) \hat{E}_\beta^{(-)}(t_\beta) (\sqrt{R} \hat{\gamma}_{1,\alpha}^{(+)} + \sqrt{T} \hat{\gamma}_{1,\beta}^{(+)})(\sqrt{T} \hat{\gamma}_{2,\alpha}^{(+)} - \sqrt{R} \hat{\gamma}_{2,\beta}^{(+)} |0\rangle \right|^2} \quad (6.4)$$

$$= \overline{(-R u_1^\alpha u_2^\beta + T u_2^\alpha u_1^\beta)^* (R u_1^\alpha u_2^\beta + T u_2^\alpha u_1^\beta)} \quad (6.5)$$

with  $\hat{\gamma}_{j,x}^{(+)}$  the creating operator of the photon emitted by the source  $j$  and propagating into output  $x = \alpha, \beta$ .  $u_j^x$  is the resulting formula of the destruction on the output  $x$  of the photon  $j$ , which reads if the propagation times are not taken into account:

$$u_j^x = \hat{E}_x^{(-)}(t_x) \hat{\gamma}_{j,x}^{(+)} \quad (6.6)$$

$$= \mu_j(t_x - t_j) \quad (6.7)$$

Let  $\Delta\Omega = \Omega_2 - \Omega_1$  be the spectral mismatch, and  $\tau = t_2 - t_1$  the time delay between the photons. Upon integration of the detection times, the probability reads

$$p = R^2 + T^2 - 2RT \frac{1}{T_1^{(1)} + T_1^{(2)}} \frac{T_2^{(1)} T_2^{(2)}}{T_2^{(1)} + T_2^{(2)}} \frac{1}{1 + \left( \frac{\Delta\Omega}{\Gamma_1 + \Gamma_2 + \frac{\Gamma'_1}{2} + \frac{\Gamma'_2}{2}} \right)^2} g(\delta) \quad (6.8)$$

$$g(\delta) = \begin{cases} e^{-\Gamma'_1 \delta} & \text{if } \delta > 0 \\ e^{-\Gamma'_2 \delta} & \text{if } \delta < 0 \end{cases} \quad (6.9)$$

The photons will bunch if the spectral mismatch is smaller than the sum of their spectral width  $\Gamma_1 + \Gamma_2 + \frac{\Gamma'_1}{2} + \frac{\Gamma'_2}{2}$ , and if they impinge the beam splitter within a delay smaller than the shortest lifetime. In case of a perfect beam splitter, the maximum visibility is a dip of  $\frac{T_2^{(1)} T_2^{(2)}}{(T_1^{(1)} + T_1^{(2)})(T_2^{(1)} + T_2^{(2)})}$  which simplifies into  $\frac{T_2}{2T_1}$  if the sources are strictly identical, as expected.

A major difficulty here in practice is to obtain  $\Delta\Omega = 0$ . My work on the *pin* diode (and similarly A. Laucht's work) allows to tune the dot emission by Stark shift effects. If the cavity mode spectral width  $\delta\omega$  is sufficiently large, it is possible to tune the dot by  $\delta\omega$  and to remain sufficiently resonant with the cavity while maintaining a good ratio  $\frac{T_2^{(j)}}{2T_1^{(j)}}$ . With two such sources, it should be possible to make them interfere.

## Annex: Personal publications

For reference, here is the complete list of the publications made during my PhD. I included the abstract of the article for each of them.

**M. Larqué, A. Beveratos, I. Robert-Philip, *Entangling single photons on a beamsplitter*, Eur. Phys. J. D 47, 119 (2008)** We report on a scheme for the creation of time-bin entangled states out of two subsequent single photons. Both photons arrive on the same input port of a beamsplitter and the situation in which the photons leave the beamsplitter on different output ports is post-selected. We derive a full quantum mechanical analysis of such time-bin entanglement for emitters subject to uncorrelated dephasing processes and apply this model to sequential single photons emerging from a single semiconductor quantum dot. Our results indicate that the visibility of entanglement is degraded by decoherence effects in the quantum dot, but can be restored by use of CQED effects, namely the Purcell effect.

**M. Larque, I. Robert-Philip, A. Beveratos, *Bell inequalities and density matrix for polarization-entangled photons out of a two-photon cascade in a single quantum dot*, Phys. Rev. A 77, 042118 (2008)** We theoretically investigate the joint photodetection probabilities of the biexciton-exciton cascade in single semiconductor quantum dots and analytically derive the density matrix and the Bell's inequalities of the entangled state. Our model includes different mechanisms that may spoil or even destroy entanglement such as dephasing, energy splitting of the relay excitonic states, and incoherent population exchange between these relay levels. We explicitly relate the fidelity of entanglement to the dynamics of these processes and derive a threshold for violation of Bell's inequalities. Applied to standard InAs/GaAs self-assembled quantum dots, our model indicates that spontaneous emission enhancement of the excitonic states by cavity effects increases the fidelity of entanglement to a value allowing for violation of Bell's inequalities.

**M. Larque, T. Karle, I. Robert-Philip, A. Beveratos, *Optimizing H1 cavities for the generation of entangled photon pairs*, New. J. Phys. 11, 033022 (2009)** We report on the theoretical investigation of photonic crystal cavities etched on a suspended membrane for the generation of polarization entangled photon pairs using the biexciton cascade in a single quantum dot. The implementation of the spontaneous emission enhancement effect increases the entanglement visibility, while the concomitant preferential funnelling of the emission in the cavity mode increases the collection of both entangled photons. We demonstrate and quantify that standard cavity designs present a polarization dependent emission diagram, detrimental to entanglement. The optimization of H1 cavities allows us to obtain both high collection efficiencies and polarization independent emission, while keeping the high Purcell factors necessary for high-quality entangled photon sources.

**R. Hostein, R. Braive, M. Larque, K.-H. Lee, A. Talneau, L. Le Gratiet, I. Robert-Philip, I. Sagnes, A. Beveratos, *Room temperature spontaneous emission enhancement from quantum dots in photonic crystal slab cavities in the telecommunications C band*, Appl. Phys. Lett. 94, 123101 (2009)** We report on the control of the spontaneous emission

dynamics from InAsP self-assembled quantum dots emitting in the telecommunications C-band and weakly coupled to the mode of a double heterostructure cavity etched on a suspended InP membrane at room temperature. The quality factor of the cavity mode is  $44 \cdot 10^3$  with an ultra-low modal volume of the order of  $1.2(\lambda/n)^3$ , inducing an enhancement of the spontaneous emission rate of up a factor of 2.8 at 300K.

My contribution on this last one consists of the chapter's 2 annex with the use of electronic microscope view to perform accurate computations of the cavity's characteristics.

Cette thèse étudie l'ingénierie, à partir de boîtes quantiques uniques (BQ), de sources déterministes de paires de photons intriqués selon deux procédés: l'intrication en polarisation lors de la cascade radiative du bi-exciton, et l'intrication temporelle de deux photons indiscernables. Le degré d'intrication est calculé afin d'évaluer quantitativement l'impact de: la levée de dégénérescence de l'exciton (splitting), le renversement de spin, l'interaction de l'exciton avec son environnement. Dans les deux cas l'intrication peut être restaurée en accélérant la durée de vie radiative de l'exciton par effet Purcell. Pour cela, un moyen approprié est une cavité à cristal photonique gravée dans une membrane suspendue (CP2D) contenant la BQ, qui permet aussi une augmentation de l'efficacité de collection. Les requis technologiques d'alignement de la BQ avec la cavité sont aussi étudiés. Cependant les effets de cavité sont insuffisants pour corriger le splitting, qui peut être réduit avec un champ électrique variable vertical. Ceci a été vérifié expérimentalement en développant une technologie pour produire des diodes PIN compatibles avec les CP2D.

This PhD work studies how to generate from unique quantum dots (QD), two kinds of sources of entangled photon pairs: the entangled property is the polarisation of the two photons emitted in the biexcitonic radiative cascade, or is the emission date of two indistinguishable photons. The degree of entanglement is calculated to quantitatively evaluate the impact of the excitonic splitting, the spin flip, and the interaction of the exciton with its surroundings. In both cases the entanglement can be restored by an acceleration of the excitonic radiative life-time with the Purcell effect. A photonic crystal cavity etched on a suspended membrane (CP2D) with the QD embedded within, is an appropriate mean to do so. The CP2D also allows good collection efficiency. The technological requirements to align the QD with the cavity are also studied. The cavity effects are yet insufficient to correct the splitting, which can be reduced with a tuneable vertical electric field. This has been experimentally checked with the process development of PIN diodes compatible with CP2D.